

Use of Additive to Mitigate Deposit and Corrosion Problems in Pulverized Biomass-Fired Boilers

Von der Fakultät Energie-, Verfahrens- und Biotechnik der Universität Stuttgart
zur Erlangung der Würde eines Doktors
der Ingenieurwissenschaften (Dr.- Ing.) genehmigte Abhandlung

vorgelegt von

M.Sc. Manoj Paneru

Aus Setipani, Jhapa, Nepal

Hauptberichter:	Univ.-Prof. Dr. techn. Günter Scheffknecht
Mitberichter:	Prof Dr. -Ing. Hartmut Spliethoff
Vorsitzender:	Prof. Dr. Andreas Kronenburg
Tag der mündlichen Prüfung:	25.10.2021

Institut für Feuerungs- und Kraftwerkstechnik (IFK) der Universität Stuttgart

Dedicated to all in concern

Declaration of authorship

I hereby declare that the dissertation entitled

“Use of Additive to Mitigate Deposit and Corrosion Problems in Pulverized Biomass-Fired Boilers”

is entirely my own work except where otherwise indicated. Passages and ideas from other sources have been clearly indicated.

Signature (Manoj Paneru)

Place, date

Preface

In March 2016, I formally registered the title of my PhD Work. My research area is related to biomass fuel, with main focus on ash. This research work is mainly experimental with numerous combustion test campaigns. Great team work was always essential to run such test campaigns successfully, I would like to express my sincere gratitude to all of my helpful colleagues at IFK.

The scientific supervision of the thesis has been under the guidance of institute's director, Prof. Günter Scheffknecht, to whom I would like to express my utmost gratitude. I express my humble gratitude to Prof. Dr.-Ing. Hartmut Spliethoff, the director of Energy Systems, Technical University of Munich, for his interest in this thesis work as a second examiner. The day to day support and encouragement from Jörg Maier, the head of firing department was a very important and valuable support to finish this thesis work.

My thanks to colleagues Reinhold Spörl, Selahatin Babat, Aaron Fuller and Collins Ndibe for their helpful suggestions to establish the topic of this thesis work. My thanks also goes to Simon Grathwohl, Thomas Matthies, Timo Wagner and Mathias Pagano. My special thanks to Eva Miller and Wolfgang Ross (Laboratory) who supported me with the analytics. Furthermore, I would like to extend my gratitude to Reyhane Youssefi, Alexander Mack and Piotr Plaza who were always open for fruitful discussions. I would like to thank Adolf Neuwirth, Institute Secretariat Marja Steinlechner, Antje Radzuweit, Renate Klein, Beate Koch and Ursula Doctor, the Workshop Ralf Nollert and Thomas Froschmeier and IT system administrator Claus Nagel and Laboratory Kay Mechling. The invaluable assistance received from various students assistant, especially Dependra Uprety and master thesis students within the framework of their research work, especially from Ioannis Polyzois was very pertinent in the completion of this dissertation. I am thankful to my wife and friend Carolin Paneru (Geb. Thesenvitz) who agreed to read through this thesis as an outside reader and Dhiraj Gyawali for final editing. I would like to express my warmest regards to my son Emil Babu Paneru who did his best to remain quiet and playing when I was writing from home desk, my daughter Rosa Krishna Paneru who was there on right time to witness the defense and to my father Benu Prasad Paneru who asked often 'when will you finish', so finally here it is.

Finally, I am thankful to financial support of various research projects and industrial contracts without which the work would not have been possible.

Table of Contents

Preface.....	I
Table of Contents	II
Kurzfassung.....	VI
Abstract	VIII
Nomenclature	X
List of Figures	XIII
List of Tables.....	XIX
1 Introduction.....	1
1.1 General.....	1
1.2 Biomass fuels for energy use.....	2
1.3 Ash-forming matter in biomass fuel.....	5
1.4 Ash related boiler issues	7
2 Present State of Knowledge	9
2.1 Ash formation	9
2.1.1 Specification of inorganic matter.....	9
2.1.2 Release of inorganic matter	13
2.1.3 Ash formation pathway.....	18
2.1.4 Ash system chemistry	21
2.2 Deposition.....	24
2.3 Fireside corrosion	28
2.4 Additive to mitigate deposition and corrosion	32
2.4.1 Ash system chemistry in presence of additives	35
2.4.2 Relation of additive to deposit and corrosion mitigation.....	38
2.4.3 Earlier studies on additive use in biomass boiler.....	40
2.5 Summary of state of the art and thesis statement	41
2.5.1 Part of work already published	43
3 Materials and Methods.....	44
3.1 Combustion test facility.....	44
3.1.1 Pilot scale combustion test rig (KSVA).....	44
3.1.2 Electrically heated combustion test rig (BTS-VR)	47

3.1.2.1	Fuel and additive feeding system	49
3.2	Deposit sampling probes and flue gas measurement device	51
3.2.1	Deposit probes	51
3.2.2	Flue gas measurement device	52
3.3	Fuel, fly ash, and deposit ash analysis	55
3.3.1	Electron Microprobe Analysis (EMPA)	55
3.4	FactSage Software and Database	60
4	Results and Discussion	62
4.1	Characterization of test fuels	62
4.1.1	Compositional ratio relevant to deposition and corrosion	64
4.2	Characterization of test additives	69
4.3	Experiments in pilot scale combustion test facility (KSVA)	71
4.3.1	Result: Demonstration of additive mitigation effect.....	75
4.3.1.1	Evaluation of data obtained from ODS	75
4.3.1.1.1	Deposition rate.....	77
4.3.1.1.2	Deposition propensity.....	80
4.3.1.2	Ash oxide composition and ash fusion temperature.....	84
4.3.1.3	Morphology and composition of outer deposit.....	87
4.3.1.3.1	Miscanthus case (M).....	87
4.3.1.3.2	Miscanthus with additive (M+B).....	89
4.3.1.3.3	Comparative discussion with and without additive.....	91
4.3.1.4	Composition and morphology of inner deposit	91
4.3.1.4.1	Methodology for comparative evaluation of micrographs	92
4.3.1.4.2	Biomass cases	94
4.3.1.4.3	Discussion: Inner deposit growth	99
4.3.1.4.4	Biomass with additive	101
4.3.1.4.5	Discussion: Influence of additive on inner deposit growth	103
4.3.1.5	Influence of salt deposit on fireside corrosion.....	105
4.3.1.5.1	Biomass cases	105

4.3.1.5.2	Biomass with additive	112
4.3.1.5.3	Discussion: Influence of additive in fireside corrosion	114
4.3.2	Summary discussion: Demonstration of additive mitigating effect.....	115
4.4	Experiments in electrically heated combustion test facility (BTS-VR)	118
4.4.1	Result: Mitigative chemistry and optimum additive amount.....	121
4.4.1.1	Additive mitigative chemistry in relation to suppression of molten ash	121
4.4.1.1.1	Outer deposit (OD)	123
4.4.1.1.2	Inner deposit (ID)	125
4.4.1.1.3	Molten history of silicatic ash particles	128
4.4.1.2	HCl as a potential additive control and optimization parameter	133
4.4.1.2.1	HCl concentration at different additive loading	142
4.4.1.2.2	Comparison across different commercial additive	145
4.4.1.2.3	Comparison across different biomass fuels	149
4.4.1.2.4	Equilibrium chemistry and comparability with experimental results.....	151
4.4.1.2.5	Equilibrium chemistry and optimum additive loading	157
4.4.2	Summary discussion: Mitigative chemistry and optimum additive amount.....	161
5	Summary and Conclusion	166
6	Limitations and Recommendations.....	171
7	Annex 1	172
7.1	Standard analysis of test fuels	172
7.1.1	Additional information on fuels.....	180
7.2	Normalized composition of additives and estimation of mineral fraction	181
8	Annex 2.....	182
8.1	Composition of deposit and fly ash	182
8.2	BSE image and element maps of deposit samples from test set B (KSVA)	183
8.2.1	Outer deposit (OD) from M case	183
8.2.2	Outer deposit (OD) from M+B case	185
8.2.3	Inner deposit (ID) from wood (W) case.....	187
8.2.4	Inner deposit from mix (M+W) case	190
8.2.5	Inner deposit (ID) from Miscanthus (M) case	193

8.2.6	Inner deposit (ID) from miscanthus with additive (M+B) case.....	195
8.3	BSE image and element maps of deposit samples from test set C (KSVA)	196
8.3.1	Inner deposit (ID) from straw (S) case	196
8.3.2	Inner deposit from straw with additive (S+D) case	198
8.4	Composition of deposit ash particle/phases corresponding to test set A (BTS).....	200
8.4.1	Outer deposit (OD) from wood (W) case	200
8.4.2	Outer deposit (OD) from wood with additive (W+C) case.....	202
8.4.3	Inner deposit (ID) from wood (W) case.....	204
8.4.4	Inner deposit from wood with additive (W+C) case.....	206
9	Annex 3.....	208
9.1	Input for FactSage calculation.....	208
10	References	210

Kurzfassung

Bei der Substitution von fossiler Kohle durch Biomasse in bestehenden kohlegefeuerten Kesseln sind die aschebedingten Ablagerungs- und Korrosionsprobleme von entscheidender Bedeutung. Problematisch sind die Zusammensetzung und die Eigenschaften der anorganischen Substanz, die später verascht wird und im ursprünglichen Rohstoff der Biomasse vorhanden ist. Die Wechselwirkungen der anorganischen Aschespezies entlang des Verbrennungsprozesses bilden niedrigschmelzende Aschekomponenten wie K-Silikat und korrosive Aschekomponenten wie KCl. Diese Komponenten haben direkte Auswirkungen auf die Kesselablagerung und das Korrosionsrisiko. Daher werden sie als problematische Aschespezies angesehen. Eine Möglichkeit diese Problematik zu verringern ist, die Aschebildungschemie zu modifizieren, sodass die Bildung problematischer Aschespezies gehemmt wird. Aluminosilikate und Tonminerale der Kaolingruppe wie Kaolinit und Halloysite sind bekannte Additive, die geeignet sind, die Chemie derart zu verändern.

In dieser Arbeit wird das Verbrennungsverhalten verschiedener Biomassebrennstoffe, Holz wie krautartig, bezüglich der Ablagerungen und des Korrosionsgrades mit Fokus auf das Ascheverhalten untersucht. Die Verbrennungstests umfassen Szenarien mit reiner Biomasse und Biomasse mit Additiv. Das Additiv wird zusammen mit dem Brennstoff in die Brennkammer eingebracht. Die für die Tests genutzte Anlage simuliert das Szenario eines Feuerungssystems mit staubförmigen Brennstoffen. Der Ort der Aschebeprobung ist vergleichbar mit der Überhitzerzone eines Kraftwerkskessels in Bezug auf Temperatur und Verweilzeit.

Um das Anwachsen der äußeren Ablagerungen quantitativ zu messen, wird ein Online-Depositionssensor (ODS) verwendet. Ferner wird die Morphologie, chemische Zusammensetzung und das Schmelzverhalten der Aschen, die als äußere Ablagerung bezeichnet wird, charakterisiert. Eine temperaturgesteuerte, d.h. gekühlte, Ablagerungssonde wird implementiert, um die morphologische und chemische Charakterisierung der inneren Initialschicht und ihre Auswirkungen auf die Oberflächenkorrosion der Sonde, die das Kesselrohrmaterial repräsentiert, zu untersuchen.

Je nach chemischer Zusammensetzung wird die Asche als silikatische Ablagerung oder Salz-Ablagerung diskutiert. Silikatische Ablagerungen repräsentieren die von Silizium dominierten Aschepartikel bzw. Phasen. Salz-Ablagerung entspricht denen von Schwefel oder Chlor dominierten.

Die abmildernde Wirkung des Additivs wird durch eine geringere Ablagerungsneigung, eine verbesserte Morphologie (z.B. geringeres Sintern) und eine allgemeine Verringerung der ge-

schmolzenen Aschekomponenten sowie den Salzspezies, hier insbesondere KCl, in der Ablagerungsprobe gezeigt. Das Fehlen von KCl erklärt die geringere Korrosionsaktivität bei Additivnutzung verglichen zum entsprechenden Fall mit reiner Biomasse. Das Ergebnis zeigt, dass sowohl für die silikatische als auch für die Salz-Ablagerungen der Blick auf die Spezies des Kaliums am wichtigsten ist. Grundlegend hängt die Verringerung der negativen chemischen Wechselwirkungen mit den Einbindereaktionen von Aluminiumsilikat-Kalium zusammen. In Gegenwart von Aluminosilikat bildet sich im System das von Kalium thermodynamisch bevorzugte, hochschmelzende und nicht korrosive K-Aluminosilikat, das stabil und somit irreversibel ist, anstatt des niedrighschmelzenden K-Silikat oder gar korrosivem KCl.

Die für einen bestimmten Biomassebrennstoff erforderliche Menge an Additiv wird sowohl durch die Aschesystemchemie des zu verbrennenden Biomassebrennstoffs als auch durch das Umwandlungsniveau des reaktiven Minerals, Kaolinit oder Halloysit, in dem gegebenen Reaktionssystem beeinflusst. Die Chemie ist im Wesentlichen eine Gas-Feststoff-Reaktion zwischen der K-Spezies und dem additiven Mineral. Sie verläuft hauptsächlich außerhalb der brennenden Kohlepartikel. Die Kalium-Einbindereaktionen sind thermodynamisch begünstigt und in der Hochtemperaturverbrennungszone nicht kinetisch begrenzt.

Die Chemie des Biomasseaschesystems regelt die Menge der hauptsächlich in der Verbrennungszone freigesetzten, gasförmigen K-Spezies. Andererseits ist der Umwandlungszustand von Kaolinit, d.h. Meta-Kaolin oder Mullit, durch die Wirksamkeit der Additivpartikel zur Adsorption der im System verfügbaren gasförmigen Spezies bestimmt. Anschließend folgt der chemische Einbau von Kalium in die Aluminosilikat-Matrix des Additivminerals. Das KCl verbleibt bevorzugt als gasförmige Spezies in der Hochtemperaturverbrennungszone und ist die letzte Spezies, die von additivem Mineral verbraucht wird. Beim Einbindeprozess entweicht das Chlor als HCl ins Rauchgas. Diese Studie untersuchte die Anwendbarkeit der HCl-Konzentration, gemessen innerhalb geeigneter Temperaturgrenzen im Rauchgas, als geeigneten Kontrollparameter zur Bewertung und Optimierung der brennstoffspezifischen Additivmenge und in wie weit die HCl-Konzentration geeignet ist, die Wirksamkeit der Einbindechemie in einem vorgegebenen Anwendungsszenario mit verschiedenen, im Handel erhältlichen Additiven zu vergleichen.

Abstract

When replacing coal with biomass fuel in existing boilers which are originally designed for coal, ash related deposition and corrosion problems are of critical concern. The problem is inherent to the composition and properties of inorganic matter, namely ash, present in the biomass fuel original feedstock source. The interactive chemistry of ash inorganic species along the combustion process forms low melting ash components, like K-silicate, and corrosive ash components, like KCl. Such components have a direct implication to the boiler deposition and corrosion risk. Therefore, they are considered to be problematic ash species. One of mitigative option is to modify the ash formation chemistry to hinder the formation pathway of problematic ash species. Aluminosilicate minerals from the kaolin group, kaolinite and halloysite, are well known additives suitable to enforce such a mitigative chemistry.

In this work, the combustion behavior of various biomass fuels, woody and herbaceous, were investigated in relation to boiler deposition and corrosion severity associated with ash. The combustion tests include cases of biomass alone without an additive and biomass with an additive. The additive was supplied together with the fuel into the combustion chamber. The employed combustion test facility simulates a scenario of a pulverized fuel firing combustion system. The deposit and ash sampling location represents an environment, i.e. temperature and residence time, comparable to the super heater zone of a power plant boiler.

Online deposition sensors (ODS) are employed to quantitatively measure the outer deposit growth that is bulk ash accumulation. Further, the morphology, chemical composition, and fusion behavior of outer deposit ash bulk was characterized. Temperature controlled (cooled) deposit probe are implemented to investigate inner deposit growth and to evaluate the morphological and chemical composition of inner deposit ash and its implication to boiler tube material corrosion.

According to chemical composition the deposit ash is discussed as silicatic deposit and salt deposit. Silicatic deposit represents the ash particles dominated by silicon while the salt deposit represents the ash/aerosol particles rich in sulfur or chlorine.

The mitigative effect of additive was demonstrated by lower deposition propensity, improved morphology (less sintering), and overall reduction of molten ash components and salt species, especially KCl, in deposit ash. The absence of KCl apparently explains the lower corrosion activity in cases with additives compared to corresponding cases with biomass alone. The result shows that for both, silicatic and salt deposits, the potassium species are of uttermost concern. The mitigative chemistry is fundamentally related to potassium capture reactions driven by aluminosilicate (derive from additive mineral). In presence of aluminosilicate in the system, the

potassium prefers to form refractory (high melting), stable (irreversible capture), and non-corrosive K-aluminosilicate instead of low melting K-silicate or corrosive KCl.

The amount of additives required for a certain biomass fuel is influenced by ash system chemistry of fired biomass fuel and the transformation level of reactive mineral, kaolinite or halloysite, in the given reaction system. The chemistry is essentially gas-solid capture reaction, K-species and aluminosilicate (kaolinite derive), respectively. The reaction basically proceeds outside the burning fuel/char particles. The potassium capture reactions are thermodynamically favored and not kinetically limited in high temperature combustion zone.

The biomass ash system chemistry governs the amount of gaseous K-species primarily released in the combustion zone. The transformation state of kaolinite, meta-kaolin or mullite, governs the effectiveness of additive particles to adsorb the gaseous species available in the system and later the chemical incorporation of potassium within the aluminosilicatic matrix of additive mineral. KCl prefers to remain as gas in the high temperature combustion zone. Therefore, chemically it is the last K-species to be consumed by the additive mineral. In the process, chlorine escapes to the flue gas as HCl.

This study investigates the applicability of HCl concentration in the flue gas measured within appropriate temperature boundaries as a suitable control parameter to evaluate and optimize the fuel specific additive amount. Further, the HCl concentration is a feasible parameter for a benchmark comparison across various commercially available aluminosilicate based mineral additives with regard to the effectiveness of capture chemistry in combustion application scenario.

Nomenclature

Symbols	Unit	Meaning
A_i	m^2	Area
A_λ		Absorbance at specific wavelength
λ	m	Wavelength
b	m	Optical path length
C	mol/L	Molar concentration
D	m	Diameter
D10	μm	Characteristic particle size (10% of particle smaller than given value)
D50	μm	Characteristic particle size (50% of particle smaller than given value)
D90	μm	Characteristic particle size (90% of particle smaller than given value)
D_p	%	Deposition Propensity
ϵ_λ	$m^2 mol^{-1}$	Absorption coefficient at given wavelength
ϑ	$^\circ C$	Temperature
ϑ_{IDT}	$^\circ C$	Initial deformation temperature
ϑ_{DT}	$^\circ C$	Deformation temperature
ϑ_{FT}	$^\circ C$	Fluid temperature
ΔG	kJ	Difference in Gibbs Free Energy
H_u	MJ/kg	Net calorific value
L	m	Length
M_i	kg	Mass of substance i
\dot{M}_i	kg/h	Mass flow of substance i
M_D	g	Mass of deposit
\dot{M}_D	g/h	Deposition rate
\dot{V}_{CA}	m^3/h	Volume flow of combustion air
X_i	wt.-%	Mass fraction of oxide 'i' in fuel ash
x_i	%	Fraction of substance 'i' in reference to certain given amount
$x_{S \rightarrow SO_2}$	%	Fraction of fuel-S released as SO_2
$x_{Cl \rightarrow HCl}$	%	Fraction of fuel-Cl released as HCl

y_i	vol.-% or ppmv	Volumetric concentration of component i
γ_i	wt.-%	Mass fraction of substance i in fuel/sample
$\eta_{\text{Combustion}}$	in %	Combustion efficiency

Abbreviation	Full Name
an.	as analyzed basis
daf	dry ash free basis
db.	dry basis (moisture free)
AFT	Ash Fusion Test
BET	Brunauer-Emmett-Teller
BSE	Back-Scattered Electron
BA	Bottom Ash
CCSEM	Computer Controlled Scanning Electron Microscopy
CFA	Chemical Fractionation Analysis
DIN EN ISO	German nation (DIN), European (EN) and International (ISO) level standard
DT	Deformation Temperature in AFT
EC	Columbian bituminous Coal, El Cerrejon
EDS	Energy-Dispersive X-ray Spectroscopy
EMPA	Electron Microprobe Analysis
ESP	Electrostatic Precipitator
EU	European Union
FA	Fly Ash
FT	Fluid/Flow Temperature in AFT
FTIR	Fourier-Transform Infrared Spectroscopy
HT	Hemispherical Temperature in AFT
IC	Ion Chromatography
ICP-OES/MS	Inductively Coupled Plasma-Optical Emission Spectroscopy/Mass Spectroscopy
ID	Inner Deposit
IDT	Initial Deformation Temperature in AFT
LA	Lab prepared Ash

M	Miscanthus
MB	Methylene Blue sorption
NA	Not Available
NCV	Net Calorific Value
NDIR	Nondispersive Infrared Sensor
NR	Not Reached
OD	Outer Deposit
ODS	Online Deposition Sensor
PF	Pulverized Fuel
PSD	Particle size distribution
S	Straw
SEM	Scanning Electron Microscope
SNCR/SCR	Selective Non-Catalytic Reduction/Selective Catalytic Reduction
TGA	Thermo Gravimetric Analysis
TS	Torrefied Straw
W	Wood
w/	with
w/o	without
WDS	Wavelength Dispersive Spectroscopy
XRD	X-Ray Diffraction
XRF	X-Ray Fluorescence

Indices and ratio	Formula	Unit
Fusion Index	$\frac{[X_{K2O} + X_{Na2O} + X_{P2O5} + X_{SiO2}]}{[X_{CaO} + X_{MgO} + X_{Al2O3}]}$	wt.-%/wt.-%
Corrosion Index	$\frac{2S}{Cl}$	mole/mole
Relevant oxide ratio	$\frac{X_{K2O}}{X_{CaO} + X_{Al2O3}}$	wt.-%/wt.-%
Saturation ratio	$\frac{M_Z + M_{(Si+Al)} + M_S}{M_{(K+Na)} + M_{(Ca+Mg)} + M_{Cl}}$ Where Z refers to kaolinite	g/g

List of Figures

- Figure 1: Schematic ash transformation pathway adapted from literature. In fuel particles, organically associated metals, soluble salts (white), include organic minerals/mineraloids (black) as natural ash. 20
- Figure 2: Schematic of deposit over boiler tube, adapted from [63,64], (i) luv side and (ii) lee side. 24
- Figure 3: Sequence of corrosion reactions with K-Salt. Figure adapted from [21,79] and reaction mechanism sequence from various literature, shows both for *hot corrosion* and *active oxidation*. 30
- Figure 4: Structure of kaolinite and halloysite [94] 33
- Figure 5: Phase diagram of K_2SiO_3 - SiO_2 (a) and $KAlSiO_4$ - SiO_2 system (b) calculated using FactSage 7.3 Phase diagram module. Note: only the change of the chemical form or phase can be observed in the given phase diagram..... 39
- Figure 6: Schematic outline of pilot-scale combustion test facility. 44
- Figure 7: Schematic outline of electrically heated combustion test facility (BTS-VR)..... 47
- Figure 8: (a) Typical calibration curve of fuel-feeding unit (b) Typical mass loss curve of additive feeding unit..... 50
- Figure 9: Schematic outline of online deposition sensor (ODS)..... 52
- Figure 10: Example sequence of data (micro graph) generated from EMPA corresponding to outer deposit (OD) sample. (a) OD sample, ceramic probe section (b) BSE image: (i) area showing sampling ceramic surface (ii) area showing ash deposit. (c) BSE image: magnified BSE image of selected area (a) and (d) Element map. 58
- Figure 11: Example sequence of data (Micro graph) generated from EMPA corresponding to inner deposit (ID) sample. (a) ID sample, metal probe section (b) BSE image: (i) area showing sampling metal surface (ii) area showing oxide scale (iii) area showing ash deposit particle/phases. (c) Element map: as example K element map (deposit ash relevant element) and (d) Element map: as example Fe element map (alloy material relevant element). 59
- Figure 12: Ash deformation temperature versus Fusion index; Wood (W, ●), Straw (S, ■), Torrefied straw (TS, ◇), and Miscanthus (M, ▲). Each data points refer to the analysis of an individual sample. Different colors in given group symbol represent different experimental batches. 65
- Figure 13: Chlorine content (γ_{Cl} in wt.-%, daf.) versus corrosion index. Note: Each data point refers to the analysis of an individual sample. Different color in given group symbol represent

different supply/batch. Wood (W, ●), Straw (S, ■), Torrefied straw (TS, ◇) and Miscanthus (M, ▲).....	67
Figure 14: Temperature profiles by thermocouple measurements along the furnace centerline: (a) Combustion cases from test set A, (b) Combustion cases from test set B. Note: Zero refers to the burner mouth. L11 and L15 denotes deposit sampling location.	75
Figure 15: (a) Cumulative deposit growth (M_D in g) and deposition rate (\dot{M}_D in g/h), (b) the box plot of corresponding deposition rate (\dot{M}_D in g/h)	76
Figure 16: Deposition rate (\dot{M}_D in g/h) corresponding to different combustion cases from test set A (a) L11 and (b) L15.....	77
Figure 17: (a) Deposition rate (\dot{M}_D) versus ash flow (\dot{M}_{Ash}), (b) Deposition rate (\dot{M}_D) versus temperature (ϑ). Legend: the 1 st line refers L11 and the 2 nd to L15.	78
Figure 18: Deposition rate (\dot{M}_D) corresponding to different combustion cases from test set B at (a) L11 and (b) L15.	79
Figure 19: (a) Deposition rate (\dot{M}_D) versus ash flow (\dot{M}_{Ash}) and (b) Deposition rate (\dot{M}_D) versus temperature (ϑ). Legend: the 1 st line relates to L11 and the 2 nd to L15.....	80
Figure 20: (a) Deposition propensity (D_p) versus ash flow (\dot{M}_{Ash}), (b) Deposition propensity (D_p) versus temperature (ϑ). (i) Reference line corresponding to coal (ii) Reference line corresponding to wood. Legend: the 1 st line refers to L11, the 2 nd to L15.	83
Figure 21: (a) Initial deformation temperature (IDT) versus relevant oxide ratio, (b) Deformation temperature (DT) versus relevant oxide ratio (right).....	86
Figure 22: Picture of outer deposit corresponding to M case OD_L15 showing the extent of unburnt particles.....	88
Figure 23: BSE image of ceramic probe cross section OD_L15 corresponding to M.....	88
Figure 24: BSE image and element map of fused deposit ash, sample corresponding to miscanthus (M) case; OD_L15.	88
Figure 25: Picture of OD corresponding to M+B.	90
Figure 26: BSE image of ceramic probe cross-section OD_L15 corresponding to M+B.....	90
Figure 27: BSE image and element map of sintered ash particle in the deposit, OD_L15 corresponding to M+B.	90
Figure 28: Example of micro-graphs (BSE Image) generated from EMPA and their arrangement for the evaluation of ID_L15 from test set B/C.	93
Figure 29: BSE image of sample cross-section ID_L15 corresponding to different biomass cases, including: W, M+W, M, and S.	95

Figure 30: Element map corresponding to wood (W), mix (M+W) and miscanthus (M) cases from test set B. The elements relevant to characteristic composition of silicatic deposit are shown here, corresponding BSE image in Figure 29.	97
Figure 31: Element map corresponding to wood (W), mix (M+W), and miscanthus (M) cases from test set B. The elements relevant to characteristic composition of salt deposit are shown here, corresponding BSE image in Figure 29.	98
Figure 32: Element map corresponding to (straw) S case from test set C. The elements relevant to characteristic composition of silicatic deposit (on top) and salt deposit (below), corresponding BSE image in Figure 29.	98
Figure 33: BSE image corresponding to cases biomass with additive: (a) M+B from test set B and (b) S+D from test set C.	101
Figure 34: Element map corresponding mix M+B case from test set B. The elements relevant to characteristic composition of silicatic deposit (on top) and salt deposit (below). Corresponding BSE image in Figure 33.	102
Figure 35: Element map corresponding straw case with additive (S+D) from test set C. The elements relevant to characteristic composition of silicatic deposit (on top) and salt deposit (below). Corresponding BSE image in Figure 33.	103
Figure 36: HCl concentration (in ppmv, corrected to 6 vol.-% O ₂) measured in flue gas corresponding to straw (S) case and straw pre-mixed with additive (S+D).	104
Figure 37: BSE image (left) and corresponding element map: Fe, Cr, and O relevant to material corrosion (i) Fe-oxide, (ii) Fe+Cr-oxide, (iii) Cr-loss, (iv) surface oxide scale, (v) substrate oxidation, and (vi) ash.	106
Figure 38: BSE image and element map of sulfur (S) shown as pair. Sample probe for ID_L15 cross-section corresponding to W case. Each pair corresponds to different observation locations of a same probe sample.	108
Figure 39: BSE image and element map of sulfur (S) shown as pair. Sample probe for ID_L15 corresponding to mix M+W case. Each pair corresponds to different observation locations of a same probe sample.	108
Figure 40: BSE image and element map of chlorine (Cl) shown as pair. Sample probe for ID_L15 corresponding to M case. Each pair corresponds to different observation locations of a same probe sample.	109
Figure 41: BSE image and element map relevant to oxide scale corresponding to (straw) S case showing (i) chromium depletion and (ii) oxide scale.	111

Figure 42: Element maps of Cr, Cl, and S corresponding to S (straw) case without additive.	111
Figure 43: BSE image and element map relevant to oxide scale and salt deposit species corresponding to M+B.	112
Figure 44: BSE image and element map relevant to oxide scale and salt deposit species corresponding to M+B.	113
Figure 45: BSE image of ID sample corresponding to W+C case showing various points, as an example of point analysis.	121
Figure 46: BSE image OD sample corresponding to (a) W case and (b) W+C case.	123
Figure 47: Average oxide composition of (a) slag from OD and corresponding FA and (b) composition Class A, B, and C from ID. The earth alkalis include: CaO and MgO, the alkalis: K ₂ O and Na ₂ O, and the rest: P ₂ O ₅ , Fe ₂ O ₃ , TiO ₂ , and SO ₃	124
Figure 48: BSE image of ID sample corresponding to case (a) W and (b) W+C.	125
Figure 49: BSE image and element map (WDS) corresponding to case W, ID sample.	127
Figure 50: BSE image and element map (WDS) corresponding to case W+C, ID sample. The number in BSE image represents different points chosen for point analysis as wt.-% oxide.	127
Figure 51: The amount of slag and solid compounds against temperature variation (a) class A, (b) class B, and (c) class C. The solid compound in bold exists at 550 °C, while the solid compound as <i>italic</i> shows transitional existence, i.e. only for a certain temperature range > 550°C.	131
Figure 52: Released versus retention graph corresponding to straw (S) combustion case, corresponding to (a) chlorine and (b) sulfur.	135
Figure 53: Released versus retention graph corresponding to TS and additive variation case, corresponding to the (a) chlorine and (b) sulfur balance.	136
Figure 54: HCl and SO ₂ concentration in ppmv, corrected to 6 vol.-% O ₂ from different measurement locations corresponding to the S combustion case. The column >2.5 m refers to a position outside the influence of reactor wall heating zone (T5).	138
Figure 55: Comparison between case *W-w/o and *W-w/ for (a) HCl concentration and (b) SO ₂ concentration in ppmv, corrected to 6 vol.-% O ₂	140
Figure 56: HCl and SO ₂ concentration in ppmv on the left axis corresponding to a test run with additive B. The fuel feeding was constant ≈ 1 kg/h. The variation in additive feed in g/h is shown on the right axis.	144

Figure 57: $x_{Cl \rightarrow HCl}$ and $x_{S \rightarrow SO_2}$ in % corresponding to the different additive feed in g/h, as fed for the variation of (a) additive A, (b) additive B, and (c) additive D. The fuel feeding is constant at ≈ 1 kg/h.....	146
Figure 58: $x_{Cl \rightarrow HCl}$ in % corresponding to (a) additive loading and (b) kaolinite loading (in % of fuel) for different commercial additives in the combustion cases from test set B.....	148
Figure 59: $x_{Cl \rightarrow HCl}$ and $x_{S \rightarrow SO_2}$ in % corresponding to additive (A) feed rate in g/h, db for the combustion case (a) TS1 and (b) *W. The fuel feeding was constant at ≈ 1.5 kg/h.....	150
Figure 60: $x_{Cl \rightarrow HCl}$ in % corresponding to (a) additive loading and (b) kaolinite loading (in % of fuel) for different biomass fuels and additive A from test set C.....	151
Figure 61: The distribution of potassium $x_{K \text{ as } i}$ in % against temperature variation derived from the FactSage equilibrium calculation: (a) phase distribution and (b) species distribution. The $x_{Cl \text{ as } i}$ refers to the fraction in reference to the respective input.	152
Figure 62: The distribution of potassium $x_{K \text{ as } i}$ in % against the variation of silicon in % derived from the FactSage equilibrium calculation for (a) phase distribution and (b) species distribution.	153
Figure 63: The distribution of potassium $x_{K \text{ as } i}$ in % against kaolinite loading derived from FactSage equilibrium calculation for (a) phase distribution and (b) species distribution. The $x_{Cl \text{ as } i}$, refers to the fraction in reference to the respective input.	154
Figure 64: $x_{Cl \text{ as } HCl}$ versus (a) the additive loading and (b) the saturation ratio derived from equilibrium results corresponding to different input scenario.	159
Figure 65: $x_{Cl \text{ as } HCl}$ versus (a) the additive loading and (b) the saturation ratio.	160
Figure 66: BSE Image (top) and element maps (below) of OD_L15 sample from M case...	184
Figure 67: BSE Image (top) and element maps (below) of OD_L15 sample from M+B case.	186
Figure 68: BSE Image of ID_L15 sample from W case.	187
Figure 69: BSE Image (top) and element map (below) of ID_L15 sample from W case.....	189
Figure 70: BSE Image of ID_L15 sample from M+W case.	190
Figure 71: BSE Image and element map of ID_L15 sample from M+W case.	192
Figure 72: BSE Image of ID_L15 sample from M case.	193
Figure 73: BSE Image and element map of ID_L15 sample from M case.	195
Figure 74: BSE Image showing of ID_L15 sample from M+B case.	195
Figure 75: BSE Image of ID_L15 sample form straw (S) case.	196
Figure 76: BSE Image and element map of ID_15 sample from S (straw) case. After each BSE image follows the corresponding element map.....	197

Figure 77: BSE Image showing surface cross-section of probe metal ring corresponding to straw with additive (S+D) case. (b) Corresponds to the BSE image shown in chapter 4.3.1.5.2 (Figure 44)..... 198

Figure 78: BSE Image and element map of ID_L15 sample from S+D case. After each BSE image follows the corresponding element map..... 199

List of Tables

Table 1: Quality classification of wood pellets for industrial use abstracted from DIN EN ISO 17225-2 [7].	3
Table 2: Ash oxides (typical values) in biomass fuel and bituminous coal.	6
Table 3: Various characterization methods for solid fuel-ash composition.	10
Table 4: The CFA of wood and straw. Abstracted from supplementary data from Zevenhoven et al. [30]. x_i represents the fraction leached in each step in ratio to the total amount of element i in the original sample. The insoluble fraction derives from the difference of water, buffer, and acid soluble fractions to the total amount.	11
Table 5: List of basic and acidic components from primary ash transformation reaction [27].	21
Table 6: ΔG of silicate formation via different reaction pathways.	23
Table 7: Major chemical groups of additives, fundamental mechanism and major mitigation target.	32
Table 8: ΔG of aluminosilicate formation via different reaction pathways.	36
Table 9: Short name index of experiments performed in pilot scale facility (KSVA).	46
Table 10: Short name index of experiments performed in BTS-VR.	48
Table 11: Equipment's and method for flue gas analysis.	53
Table 12: Flue gas components and recommended infrared wave number (cm^{-1}) analytical range.	54
Table 13: Standard analysis method for fuel/fly ash/deposit ash.	55
Table 14: Properties of test fuels.	63
Table 15: Relevant fuel compositions and ash fusion temperatures of wood and KCl doped wood.	66
Table 16: Properties of test additive.	70
Table 17: Fuel feeding rate and combustion air (test protocol and system data).	71
Table 18: Relevant composition and properties of fired fuel (analyzed).	72
Table 19: Relevant composition and properties of fired fuel mix (calculated).	72
Table 20: Fuel gas composition and combustion efficiency, both values correspond to the measurement/FA sample from the end of the combustion chamber.	74
Table 21: Combustion cases with comparable magnitude of deposition propensity.	81
Table 22: Short name index of combustion cases and test system boundary.	118
Table 23: Relevant composition and properties of fired fuel.	119
Table 24: Equilibrium optimum defined corresponding to Figure 63 (a).	154

Table 25: Equilibrium optimum defined corresponding to Figure 63 (b).....	155
Table 26: Standard analysis of bituminous coal.....	173
Table 27: Standard analysis of woody biomass fuel (Wood ‘W’).	174
Table 28: Standard analysis of herbaceous biomass fuel (Straw ‘S’).	175
Table 29: Standard analysis of herbaceous biomass fuel (Miscanthus ‘M’).	176
Table 30: Standard analysis of herbaceous biomass fuel (Torrefied Straw‘TS’).	177
Table 31: Standard analysis of biomass mix (Miscanthus/Wood: 50/50, ‘M+W’), straw premixed with additive (S+D) and KCl doped wood (*W).	178
Table 32: Calculated composition of ‘coal+biomass’ blend and ‘biomass+additive’ mix....	179
Table 33: Supplier information	180
Table 34: Normalized dry (moisture free) composition of additives.	181
Table 35: Normalized ash oxide composition of outer deposit (OD) and fly ash (FA).	182
Table 36: Point analysis of OD sample corresponding to W case.	200
Table 37: Point analysis of OD sample from W+C case.....	202
Table 38: Point analysis of ID sample from W case	204
Table 39: Point analysis of ID sample from W+C case	206
Table 40: Average oxide composition of characteristics ‘silicatic’ deposit particle/phases categorized here as; Class A, Class B and Class C composition.	208
Table 41: FactSage equilibrium input as amount of each component in g per Kg of given fuel (derive from standard analysis of respective fuel).	209

1 Introduction

1.1 General

Coal is the major fuel accounting 27 % of all energy use worldwide and contributes 38 % of electricity generation [1]. The global need to decarbonize the energy (heat and electricity) sector to reduce greenhouse gas emission is becoming clearer and louder every year. It is one of the main contributors to global CO₂ emission, the major greenhouse gases responsible for global warming.

Biomass is an alternative fuel source that could potentially replace/minimize coal usage [2]. Biomass as well, will produce CO₂ during combustion. However, the CO₂ produced from biomass originates from the current earth's atmosphere while CO₂ released from coal and other fossil bound carbon resources add CO₂ from pre-historical storage. Therefore, theoretically, in biomass combustion, there is no net CO₂ addition to the current atmosphere. Additionally, biomass is a renewable source and when/if wisely managed can provide sustainable supply [2].

Biomass has already received attention in many countries, like USA, UK, Germany, Austria, Finland, Denmark and the Netherlands [2,3] and is a part of policy roadmap in many other countries/regions to meet their CO₂ reduction goals. Wood pellets/chips are standardized biomass fuel for energy use. Their usage in large scale power plants however, is coupled with the renewable energy policy specific to the country. For instance, in Germany almost all wood pellets are consumed in smaller units, like domestic stoves [3]. The large scale biomass co-firing application in Germany mostly accounts for the share (nominal up to 3 %) of sewage sludge [3]. While in many other European countries such as the Netherlands, Denmark, Belgium and UK, co-firing wood pellets in large scale coal power plants is already an established practice [3]. Further, in recent years, countries like Denmark and UK are already converting and operating with 100 % biomass in both demonstration and commercial level.

The demonstration/application in large scale, has prepared a reasonable base by screening the potential/available biomass feedstock, establishing production-supply chain and trading of biomass fuel across distances. Experience is also available regarding biomass fuel handling (including milling) and firing it in existing large-scale boilers. Existing infrastructures of coal power plants with certain customized modification could largely handle the biomass fuels up to certain share with coal [3]. Switching of fuel from coal to biomass in existing power plants could be an attractive option to realize CO₂ neutral energy production with existing assets and no huge additional infrastructure investments. Obviously in the long run, to be replaced by other

renewable sources like solar or wind, would be a desirable option. For the transitional phase and as a stable source, similar climate and sustainable benefits could be achieved by replacing coal by biomass. Recently in 2019, Germany's legislator initiated a plan to entirely phase out coal by 2038. Biomass is foreseen as an option to fill some of the space that would be left by the exit of coal. It is relevant for countries which already have a timeline to exit the coal but still have a substantial and stabilized contribution of coal in their domestic energy mix.

1.2 Biomass fuels for energy use

The DIN EN ISO 17225-1 divides biomass into five major sub-categories based on their origin and sources i) woody biomass, ii) herbaceous biomass, iii) fruity biomass, iv) aquatic biomass, and v) defined/undefined mixtures [4]. The DIN EN ISO 17225-2 and 17225-4 includes quality classification of woody biomass pellets and chips. Similarly, DIN EN ISO 17225-6 includes the quality classification of herbaceous biomass pellets. The standard focus lies more on the quality requirement suitable for smaller appliances like oven/stoves used for residential heating. The standard also includes quality classification extended for industrial use. Table 1 shows the quality classification of wood pellets for industrial use according to DIN EN ISO 17225-2.

The quality criteria suggested by the standards are mostly for wood pellets and as a power-plant fuel; the parameter thresholds are often stringent. The biomass fuel producer and the larger-scale end users like power plants can often make their own quality criteria agreement within the general boundaries identified by these standards.

Biomass fuels including wood/wood residues, agricultural residues (e.g. straw), energy crops (miscanthus, coppice), and municipal waste/sewage sludge, are the primary biomass feedstock co-fired in combination with different varieties of coal (anthracite, bituminous and lignite). Some plants fire fruity biomass fuel like palm kern shells and cocoa shells (the Netherlands) and olive palm residue (UK) [5]. In general, the average co-firing share of woody fuel is up to 20 – 30 %, while the co-firing share of other biomass fuels ranges between 3 – 10 % with minor modification of the existing infrastructures [5,6]. The practiced co-firing share varies depending on the chemical and physical properties of biomass fuel, the base coal, boiler type as well as the policy target (de-carbonization aim) of the respective countries or region.

Woody biomass, as pellets or chips, are well-established co-firing fuels. The experience regarding trading, handling, and firing of these wood pellets/chips is continuously growing to become potential reference fuel for biomass (100 %) fired boilers.

Agricultural residue (e.g. straw), energy crops (e.g. miscanthus), and process residues (e.g. palm kern shell) are other feedstock sources for biomass fuels. Comparatively lower price makes the residues attractive feedstock while dedicated energy crops, like miscanthus, provides secure feedstock supply.

In case of a complete fuel switch in large scale power plants, firing biomass fuels originating from various feedstock sources will probably be the operational reality. Use of seasonal and regional biomass reduces the dependency on woody biomass and also minimizes the overall fuel costs.

Table 1: Quality classification of wood pellets for industrial use abstracted from DIN EN ISO 17225-2 [7].

Property Class Analysis method	Unit	I1	I2	I3
Origin and source ISO 17225-1		1.1 Forest, plantation and other virgin wood 1.2.1 Chemically un- treated wood resi- dues	1.1 Forest, planta- tion and other vir- gin wood 1.2.1 Chemically untreated wood residues	1.1 Forest, planta- tion and other vir- gin wood 1.2 By-products and residues from wood processing industry 1.3.1 Chemically untreated used wood
Bulk density ISO 17828	kg/m ³ , ar.	≥ 600		
Net calorific value (H_u) ISO 18125	MJ/kg, ar.	≥ 16.5		
Moisture (M) ISO 18134-1 & 2	wt.-%, ar.	≤ 10		

Property Class Analysis method	Unit	I1	I2	I3
Ash (A), ISO 18122	wt.-%, db.	≤ 1	≤ 1.5	≤ 3
Nitrogen (N), ISO 16948	wt.-%, db.	≤ 0.3		≤ 0.6
Sulphur (S), ISO 16994	wt.-%, db.	≤ 0.05		
Chlorine (Cl), ISO 1699	wt.-%, db.	≤ 0.03	≤ 0.05	≤ 0.1
Arsenic (As), ISO 16968	mg/kg, db.	≤ 2		
Cadmium (Cd), ISO 16968	mg/kg, db.	≤ 1		
Chromium (Cr), ISO 16968	mg/kg, db.	≤ 15		
Copper (Cu), ISO 16968	mg/kg, db.	≤ 20		
Lead (Pb), ISO 16968	mg/kg, db.	≤ 20		
Mercury (Hg), ISO 16968	mg/kg, db.	≤ 0.1		
Zinc (Zn), ISO 16968	mg/kg, db.	≤ 200		
Ash fusion tem- perature, CEN/TS 15370-1	°C	as Informative		

The biomass pre-treatment techniques like torrefaction enhances the quality of raw biomass. Torrefaction increases the energy density, upgrades chemical properties including a decrease in moisture/volatile content, increase of fuel-carbon content, and improves the physical properties like bulk density, durability, and grindability [8]. Because of these upgrades, torrefied biomass

is more comparable to coal and becomes the preferable fuel. Nevertheless, any pretreatment process comes with costs which add to the fuel price.

Torrefaction significantly improves handling and milling behavior and to some extent the combustion behavior [8]. However, it has neutral impact on ash behavior. Besides minor losses of volatile inorganic components the average ash composition, form/association of ash-forming inorganics and its properties (e.g. ash fusion behavior) remains similar to the raw biomass. Therefore, ash related issues with torrefied biomass is also expected to remain similar.

1.3 Ash-forming matter in biomass fuel

Ash is the noncombustible fraction and represents the inorganic part of the fuel. There is an extensive amount of open literature regarding the amount, composition, and properties of ash. The research on ash is mostly driven by the aim to understand the deposition (slagging and fouling) and fireside corrosion issues faced by power plant boilers. The interference of ash on emission control units and particulate emission are some other challenges related to ash. The utilization of fly ash as a product to other industries is also an area of interest in ash research. The physical and chemical properties of ash-forming matter in raw fuel and their interactive chemistry and transformation during combustion to form fly ash has been studied for long, both for coal and biomass fuel. The most fundamental difference between ash-forming matter in coal and biomass is the extent of mineralization of the inorganic matter.

The ash-forming matter in coal is mostly derived by proper mineral species, formed, and accumulated during the coalification process of pre-historic biomass. The coal minerals consist of mineralized inorganic species inherent to the pre-historic plant and minerals incorporated by weather and geology. The ash-forming matter in coal derives from a broad variety of included and excluded minerals [9,10]. ‘Included’ refers to the mineral grains that remain enclosed within fuel carbon matrix and ‘excluded’ refers to those mineral grains that remain outside.

The ash-forming matter in biomass is comprised of inorganic salt species, elements associated with the fuel organic matrix, and mineraloids/minerals [9,11]. Additionally, the soil-borne components, especially soil minerals and more abundantly quartz, are the part of ash-forming matter in biomass. Soil, climate, growing practice (e.g. use of fertilizer, irrigation), plant species/parts, and harvesting-storage practice impact the amount and kind of ash-forming matter.

A detailed overview of composition and properties of organic (combustibles) and inorganic fraction (ash) of biomass has been published in series by Vassilev et al. [12–16]. The ash-forming matter in biomass can be divided as natural and technogenic [12]. The natural ash-forming

matter can be further divided as authigenic and detrital [12]. Authigenic is in-organic matter accumulated by biomass (cell and tissues) during its life cycle while detrital is in-organic matter formed outside the biomass but incorporated within biomass (cell and tissues) during its life cycle [12]. The technogenic refers to the external contaminants or impurities added to biomass in the process outside its life cycle, i.e. by the process to become a fuel [12].

The amount of ash in biomass varies widely with the feedstock source [16]. Woody biomasses have very low ash content in general. The ash fraction is lower than 0.5 % in stem wood derived pellets [16]. Industrially available wood pellets have higher ash concentration, around 1 – 2 %, because of mixing other parts, like bark, branches, or leaves, in the feedstock during pellets production [16]. Also, forest or logging residues, used or demolition wood can increase the ash content to a higher range, $\approx 3 - 4$ % [16]. Typically, herbaceous biomasses have a higher ash content than woody biomass. The ash content in industrially available non-treated straw pellets is in the range of $\approx 7 - 10$ % and in miscanthus pellets is in the range of $\approx 5 - 8$ % [16].

Table 2: Ash oxides (typical values) in biomass fuel and bituminous coal.

wt.-% in ash, db.	Wood [17]	Miscanthus [18]	Straw [18]	Coal [18]
$X_{Al_2O_3}$	2.6	1.0	0.6	28.3
X_{CaO}	18.0	9.9	9.7	5.3
$X_{Fe_2O_3}$	1.5	1.2	1.20	10.1
X_{K_2O}	6.6	25.1	18.5	3.6
X_{MgO}	4.7	1.9	1.8	2.8
X_{Na_2O}	1.4	0.6	0.2	1.2
$X_{P_2O_5}$	2.0	2.5	2.3	0.5
X_{SO_3}	1.9	1.0	0.9	4.5
X_{SiO_2}	32.0	59.1	67.0	44.2
X_{TiO_2}	1.0	0.1	0.1	1.1

Potassium (K), phosphorous (P), calcium (Ca), and silicon (Si) contribute to the major composition of ash in biomass fuels from woody and herbaceous feedstock [16]. K and P are mostly of a natural origin [11,12,16]. Si is mostly of technogenic origin and it may exceed the most abundant ash element Ca, for the exception of wood pellets [12]. Most of the calcium is of a natural origin. Elements like sodium (Na) and magnesium (Mg) are mostly lower. Typically, in woody biomass fuels earth-alkalis are more abundant than alkalis while in herbaceous biomass

fuel alkalis are more dominant than earth-alkalis. In biomass, aluminum (Al) and iron (Fe) are typically lower than in coal and this is the major distinction to the element composition of coal ash. Table 2 shows the typical ash oxide composition of biomass fuels and coal found in open literature.

1.4 Ash related boiler issues

The ash related boiler issues relate to the interference of combustion-generated ash with the boiler components or equipment. A certain fraction of combustion-generated ash falls off as *bottom ash* which are the heavy, large ash particles. They cannot follow the flue gas velocity and therefore drop off. The fraction of bottom ash depends on boiler geometry, firing systems, and burner arrangements. The bottom ash fraction in pulverized boilers ranges between 10 – 20 % [19]. The fraction of combustion-generated ash flying out with the flue gas is *fly ash*. In pulverized boilers, fly ash accounts for 80 – 90 % of the total combustion generated ash [19]. Eventually, fly ash is collected by the particulate control equipment (e.g. ESP) downstream in the flue gas cleaning section.

The volatile ash species and fly ash condense and accumulate over the boiler's heat exchanger surfaces, i.e. tubes. This ash fraction is referred to as *deposit ash*. The furnace wall, the burner tip (*eyebrow deposit*), and the bottom hopper zone are as well susceptible to deposition. The whole phenomenon of deposition is unavoidable as any solid fuel, coal or biomass, contain fractions of ash.

Conventionally, boiler deposition is categorized as slagging and fouling. *Slagging* is the deposition in the radiative section of the boiler, i.e. in furnace combustion chamber, particularly in the furnace or evaporator wall. *Fouling* is the deposition over the surface of boiler tubes, including super heaters, reheaters, and economizer. Additionally, deposit ash can interact with boiler tube surfaces at the oxide scale or with metal-alloy elements. Such reactions are referred to as *fireside corrosion*. The higher temperature boiler tubes, i.e. the super-heater zone, is most vulnerable to fireside corrosion.

Deposition phenomena reduce the overall transfer of fuel released heat to the boiler fluid (steam). Excessive local deposition blocks the flow path of flue gas while accumulated ash on the bottom hopper regime obstructs the removability of bottom ash. Deposits on burner mouth, also referred to as *eyebrow deposits*, influence the flame behavior and its stability. Additionally, corrosive deposits formed on super-heaters reduce boiler lifetime and availability.

Many large-scale boilers are equipped with soot blowers to dislodge deposits and to minimize deposit growth. The deposition rate, the strength of deposit in terms of removable and not removable by soot blowers, and the corrosivity of deposit ash, is coupled with the chemical and physical properties of the deposit ash components or species [20]. The combustion system boundaries, the transport of molten or solid ash components, and condensation of volatile ash species from flue gas to the receptive surface govern the severity of the problem [20].

Molten or partially molten ash particles are sticky. Thus they can adhere to the receptive surface on impaction to facilitate the deposit growth and sintering. Historically, the ash fusion temperature is an important criterion to assign the *furnace exit temperature* $\vartheta_{f, \text{exit}}$. This was assigned lower than the ash softening temperature, determined by ash fusion test standard, to avoid sticky ash particles reaching and adhering to convective heat exchanger surfaces.

The first concern arises here because ash fusion temperatures of biomass fuels are substantially lower than most of the coals. The typical softening temperature, this term also referred to as *deformation temperature*, of woody fuel is in the range of 1000 °C – 1200 °C and for herbaceous biomass, like straw and miscanthus, in the range of 800 °C – 1100 °C. The sintering temperature, also referred to as *initial deformation temperature*, would be even lower. Therefore, with similar furnace-exit temperature severe deposition will be faced. Firing biomass in boiler designed for coal will be operationally challenging.

The second concern with biomass fuel is the retention of chloride salts in deposit ash and associated corrosion risk [21].

Co-firing biomass is widely employed over the last 10 – 20 years in large scale power plants. The biomass replaces a certain amount of coal during co-firing. The co-firing power plants already recognized this challenge which was one of the major reasons to limit the share of biomass fuel, specifically for pulverized boilers.

To summarize, biomass increases the risk of deposition and fireside corrosion in comparison to coal [22–25]. Both situations are fundamentally inherent to physical and chemical properties of ash. The severity may vary with the firing system, boiler geometry or design, and the process conditions. From experience, the ash related boiler issues, namely deposition (slagging and fouling) and corrosion, are noticed as the major challenges [2,26] to address when biomass is introduced to an existing boiler designed for coal. These issues will directly affect the day-to-day operation and cumulatively the overall boiler performance, availability, and efficiency.

2 Present State of Knowledge**2.1 Ash formation**

The mineral transformation approach cannot satisfactorily explain the fundamentals of ash transformation chemistry related to biomass fuel [9,22]. Instead, major ash-forming matter in biomass are not proper minerals: they are dissolved salts and organically associated elements or mineraloids. The composition of ash generated from biomass combustion derives from the release of volatile inorganic species and homogeneous or heterogeneous chemical interaction among these species [27].

The differentiation of biomass with coal starts with the specification of inorganic matter, their release during combustion, followed by their interactive chemistry, and the major pathway of ash particle evolution. These four main aspects in relation to woody and herbaceous biomass fuel are discussed in the following sections.

2.1.1 Specification of inorganic matter

Huggins [28] provided a detailed overview of various analytical methods to determine ash composition of fossil based solid fuels and discussed the advantages and limitations associated with these different methods. Similar methods are in practice for biomass fuels. Table 3 summarizes the widely practiced methods to determine the ash composition of solid fuel.

Defining the ash composition as major and minor inorganic ash elements is a standardized method. Customarily, the ash elements are presented as their oxides. However, this method does not provide any specification of the chemical form of ash-forming matter as it is present in the raw fuel.

The Chemical Fractionation Analysis (CFA) is argued to be a more suitable method for biomass fuels [29,30]. In CFA, the fuel is leached in water, ammonium acetate (buffer solution), and hydrochloric acid in sequential steps. The elements soluble in the given solvents are considered to associate together in the fuel. Based on CFA data of varieties of biomass fuels, Vassilev et al. [16] reported three major kinds of associations of inorganic elements in biomass fuel including: the K-P-S-Cl-Na association as mainly water soluble, the Ca-Mg-Mn association as buffer or acid soluble, and the Si-Al-Fe-Ti association as non-soluble.

Table 3: Various characterization methods for solid fuel-ash composition.

Characterization method	Short description	Detection and Quantification	Remark
Bulk composition characterization	Thermal digestion of fuel sample	ICP-OES/MS XRF	Composition reported as ash elements [mg/Kg, db. in fuel] or as ash oxides [%, db. in ash] Standards available Widely used and common method
Solubility characterization	Chemical fractionation analysis (CFA): Sequential leaching of fuel by water, buffer solution, and acid	ICP-OES/MS IC MB	Composition reported as fraction of soluble ash elements in water, buffer, and acid and the fraction of insoluble ash elements Standard procedure available Preferred for biomass fuel
Mineral characterization	Fuel sample or lab prepared ash	XRD CCSEM	Composition reported as various minerals or compounds in crystalline phase and amorphous phase Widely used for coal but not common for biomass fuel

Table 4 shows chemical fractionation data abstracted from Zevenhoven et al. [30]. The data show the solubility of inorganic elements present in biomass fuel, namely wood and straw. The general assumption is that the water-soluble fraction represents easily soluble alkali salts like chlorides, sulfates, phosphates, and carbonates. The buffer soluble fraction indicates the inorganic elements associated with fuel organic matrix. The acid soluble fraction stands for included as well as organic minerals and earth alkali carbonates and sulfates. The remaining residual, the insoluble fraction, represents the mineral species, soil minerals, mainly quartz or silica.

Table 4: The CFA of wood and straw. Abstracted from supplementary data from Zevenhoven et al. [30]. x_i represents the fraction leached in each step in ratio to the total amount of element i in the original sample. The insoluble fraction derives from the difference of water, buffer, and acid soluble fractions to the total amount.

x_i in %	Wood				Straw			
	Water soluble	Buffer soluble	Acid soluble	Insoluble	Water soluble	Buffer soluble	Acid soluble	Insoluble
x_K	64	0	36	0	76	21	1	2
x_{Na}	57	0	0	43	66	19	15	1
x_{Cl}	100	0	0	0	97	3	0	0
x_P	64	0	36	0	74	17	8	1
x_S	11	0	12	76	45	10	12	33
x_{Ca}	5	58	37	0	16	63	17	4
x_{Mg}	10	90	0	0	26	56	13	5
x_{Mn}	7	72	21	0	15	48	37	0
x_{Si}	7	0	7	87	5	12	9	74
x_{Al}	0	22	38	41	3	2	29	66
x_{Fe}	11	0	74	16	7	3	71	19
x_{Ti}	0	0	0	100	4	4	14	79

Werkelin et al. [29] propose a quantitative model for the specification of ash-forming matter, an extension of the CFA analysis method. The specification is based on the ion charge balance of leachate and the residual, solid fraction obtained from each CFA step. Chloride (Cl^-), sulfate (SO_4^{2-}), phosphate (PO_4^{3-}), oxalate ($C_2O_4^{2-}$) are the ions under consideration. According to Werkelin et al. [29] the major specification of ash-forming inorganic mater are K-salts which are

soluble in water: Potassium chloride (KCl), Potassium phosphate (K_2HPO_4/KH_2PO_4) and Potassium sulfate (K_2SO_4), minerals which are soluble in acid: Calcium oxalate ($CaC_2O_4 \cdot nH_2O$) and Opal ($SiO_2 \cdot nH_2O$). Additionally, organically associated metals: ionically bonded Ca^{2+} , Mg^{2+} , Mn^{2+} , K^+ , Na^+ , Al^{3+} and Fe^{3+} which are soluble in buffer and covalently bonded P and S which are acid-soluble or insoluble. They pointed out a large fraction of silicon remains as insoluble fraction is, apparently present as quartz and other soil minerals.

The quantitative model proposed by Werkelin et al. [29] corresponds to the previously reported association and specification of ash-forming matter in biomass fuel. Balancing the ion charges is not only tedious but also contains substantial uncertainty [29]. Information derived from chemical fractionation analysis does provide the specification to the ash-forming elements but the quantification of each species is largely impossible and possibly unrealistic [16].

Nevertheless, the information from CFA are considerably useful and more elaborate than the information derived from standard ash analysis where they are seen as oxides. The information derived from CFA is extended to justify the reactivity of ash-forming matter in biomass fuel [27]. The water-soluble fraction is expected to be released as volatile species and are most reactive in ash formation reactions. The buffer and acid soluble fractions, oxalates and opal, are considered reactive. The insoluble fraction, mainly silicon, as quartz or other soil minerals, is considered to show partial reactivity [27].

The specification of ash-forming inorganic matter as minerals is widely preferred for coal. However, the poorly mineralized ash in biomass is hard to identify by X-ray fluorescence (XRD). In many cases, the specification is limited to report the majority of amorphous phase including salts (sulfates, chlorides and carbonates) and quartz. Another concern regarding mineral specification, as they are present in raw fuel, is related to the interaction that occurs during the ashing procedure which changes the original chemical specification in the raw fuel.

Especially, the fraction of inorganic elements associated with the organic fuel-matrix probably changes their initial association as they interact with each other during ashing and could exhibit a different chemical form. Low-temperature plasma ashing (100 – 250 °C) is an option to minimize such effect. Knowing their poor state of mineralization, the identification of ash-forming matter in biomass fuel as mineral species is inconclusive.

2.1.2 Release of inorganic matter

The combustion process is broadly categorized into three main steps viz. drying, volatile combustion and char combustion. The inorganic matter is released during the combustion stages and eventually forms the ash.

Inorganic ash elements like K, Na, S, and Cl primarily escape the char surface as gas phase species while the elements including Ca, Mg, Si, Al, and P retain as solid or liquid species within the char surface [31] and are released once the char surface is collapsed along the combustion process.

Dayton et al. [32,33] directly observed the gas-phase potassium species released during biomass combustion using Molecular Beam Mass Spectrometry (MBMS). Davidsson et al. [34] measured the alkali emission from biomass fuel particles, beech wood, during rapid pyrolysis using surface ionization (SI) technique. More recently, Mason et al. [35] use Emission Spectroscopy Detection Method (ESDM) to detect and quantify the release of gas-phase potassium from 13 different kind of biomass fuels. Other authors [36–40] quantify the release of gas-phase potassium indirectly by a mass balance of inorganic elements present in the raw fuel and later in the ash sample generated after combustion.

The evaluation is further supported by equilibrium chemistry. The potassium release is of the main concern. Following summary for woody and herbaceous biomass is based on [32–41].

1. For *chlorine lean woody biomass* such as: spruce, beech, and bark, about 20 % of potassium is released in the gas-phase at 800 °C. This increases to 30 – 40 % for bark and spruce at 1000 °C and 70 % for beech. At a higher temperature, 1150 °C, potassium reaches 70 – 90 % for all fuels [39,40]. Mason et al.'s [35] quantification of the gas phase show that gas phase potassium accounts for about 70 % of the total potassium present in the observed woody fuel (all chlorine lean).
2. For *chlorine rich herbaceous biomass* such as straw from rice, barley, and wheat, Knudsen et al. [38] experiments show little or no potassium release to gas phase below < 700 °C. At 800 °C the potassium release accounts for 40 – 50 % for barley and rice straw, but less than 20 % for wheat straw. At higher temperature, 1150 °C, the gas phase K reach \approx 50 % for rice straw, \approx 60 % for wheat straw and \approx 80 % for barley straw. The quantification results from Mason et al. [35] demonstrated that gas phase potassium for wheat straw and miscanthus which both are chlorine rich herbaceous fuels are below < 50 %.

The general understanding regarding the release of potassium with respect to its chemical form and association in raw biomass fuel is summarized below. The amount of another alkali element sodium (Na) is very low in biomass fuel and essentially releases analogous to potassium (K).

1. The potassium release is significantly *influenced by other inorganic elements*, mainly chlorine and silicon. Additionally, the experimental approach (heating rate, test equipment, sample mass and particle size, solid and gas sampling method) and quantification method (direct measurement and quantification, indirect quantification from solid samples) impacts the result. Nonetheless, the common agreement is that major fraction of potassium releases to the gas phase at high temperature, the peak release rate occurring during char-combustion stage and Cl promotes while Si demotes the release.
2. The *chemical form of released gaseous potassium* species is associated with the original mode of its occurrence in the given fuel. It is considered that the K (g), KOH (g) and KCl (g) are the major species in the released gaseous potassium. In chlorine lean fuel, like woody biomass, K (g), KOH (g) dominate while in chlorine rich fuel, straw and miscanthus, KCl (g) dominates.
3. The *potassium release is driven by two distinct origins*: from organically bound potassium and from potassium salt species. The organically bound potassium releases at low temperature during de-volatilization. The release from inorganic species, mainly K-salt, requires high temperatures mostly during char combustion.
4. As the *fuel organic matrix thermally degrades the organic-K releases* [34]. This typically occurs in the temperature interval of 300 – 500 °C [34]. The thermal degradation of alkaline carboxylate results in release of elemental K (g) which escapes from the char and further forms KOH (g) in presence of water-vapor. The direct gaseous alkali measurement [35] suggested that only the minor fraction ($\approx 10\%$ of total fuel-K) is detected during de-volatilization stage. The secondary reaction of K (g) with species like P_2O_5 (g) or SO_3 (g) originating from thermal degradation of organic containing P, S which occur in the char surface results in partial retention of potassium as solid salt, K-phosphate and K-sulfate [34]. Such secondary reactions may as well account for the lower release of potassium during de-volatilization.
5. The *inorganic potassium exists as salts* like K-chloride, K-carbonate, K-sulfate, and K-phosphates. These salts precipitate as solid particles within the char surface during de-

volatilization. Some salts may be freshly formed during de-volatilization. The evaporation and decomposition of these salts species explain their release behavior. Evaporation of KCl is a widely agreed and established release mechanism. The melting temperature of KCl is 770 °C. The evaporation of KCl present in biomass fuel starts well below its melting temperature [41] and is the major pathway of alkali release from chlorine rich biomass. Most of fuel-KCl releases to the gas-phase in the temperature interval of 700 – 830 °C [38].

Knudsen et al. [38] suggest that the gas phase release of K in a temperature range of 700 – 950 °C is associated with the decomposition of K-carbonates. The temperature of K_2CO_3 decomposition almost overlaps with KCl evaporation. The TGA curve of pure K_2CO_3 presented in [42] shows that under a dry N_2 atmosphere the significant mass loss is observed only at a high temperature interval of 1150 – 1450 °C. The estimated and measured evaporation rate is based on mass loss of heated salt samples. Knudsen et al. and Zhao et al. [38,43] show that under dry conditions the evaporation rate of K_2CO_3 at 900 – 1200 °C is similar to K_2SO_4 at 900 – 1200 °C but in presence of water vapor the evaporation rate of K_2CO_3 improves significantly and shifts to the temperature interval of 700 – 1000 °C. With this, it is comparable to KCl evaporation. In reference to earlier literature, Knudsen et al. [38] argued that instead evaporating, the K_2CO_3 decomposes at the presence of water vapor which initiates above the melting temperature ≈ 890 °C of K_2CO_3 . The initial decomposition of K_2CO_3 releasing K (g) and further forming of KOH (g) in presence of water vapor is a mechanism as proposed by Knudsen et al. [43]. Zhao et al. [43] proposed the decomposition is followed by a direct K_2CO_3 (s) and H_2O (g) interaction. Despite differences in the actual explaining mechanism, the common agreement is that K_2CO_3 decomposes and releases as KOH (g). For chlorine and phosphorous lean woody biomass fuel the decomposition behavior of K_2CO_3 is of substantial importance as it is the primary potassium salt.

K-sulfates (K_2SO_4) are expected not to vaporize but melt and decompose at higher temperature and eventually release K (g) either in form of KOH owing to the availability of water vapor or KCl owing to availability of HCl. The melting and boiling temperatures of K_2SO_4 is respectively ≈ 1070 °C and ≈ 1690 °C.

The literature regards K-phosphates and its contribution to gas phase potassium release as limited. K_2HPO_4 and KH_2PO_4 , K_3PO_4 are the proposed chemical form of K-phosphates present in biomass fuel [29,30]. K_3PO_4 has a high melting point (≈ 1340 °C [44]).

As pure salt K_3PO_4 does not evaporate at temperatures as high as $1150\text{ }^\circ\text{C}$ [38]. The KH_2PO_4 dehydrates at temperatures between $210 - 350\text{ }^\circ\text{C}$ [45], it releases water and converts to KPO_3 . KPO_3 melts at $\approx 812\text{ }^\circ\text{C}$ and evaporates above $> 900\text{ }^\circ\text{C}$ [45]. The K_2HPO_4 melts above $> 465\text{ }^\circ\text{C}$ and decomposes [45]. In combustion generated residual ash the phosphates are in general discussed as Ca-/Mg-phosphates and Ca-K-phosphates [46,47]. Grimm et al. [47] suggest the shift of phosphate from potassium to calcium as it forms Ca-phosphate and contributes to the gas phase release of K-species. The fact that the pathway of gas phase potassium release originates from K-phosphate salts is still ambiguous, and phosphates are generally considered to retain in residual ash.

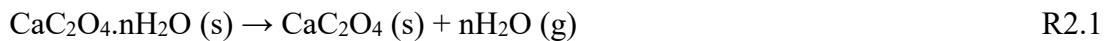
The general understanding of the release of sulfur (S), chlorine (Cl) and phosphorous (P) with respect to their chemical form or association in raw biomass fuel are summarized below.

1. The organically associated sulfur (S) releases to the gas phase already during de-volatilization [36,37] while the fuel-S fraction that exists as sulfate salt requires higher temperature. The fractionation of fuel-S as organic and inorganic S is largely fuel dependent. For woody fuel like spruce, beech, and bark, the sulfur release was almost $\approx 70\%$ already at $500\text{ }^\circ\text{C}$. It remains below 80% in the temperature interval of $500 - 800\text{ }^\circ\text{C}$ and abruptly increases to 100% in the temperature interval of $800 - 1150\text{ }^\circ\text{C}$ [40]. For herbaceous fuels as straw like rice, barley, and wheat, $25 - 35\%$ of the total fuel-S released to the gas phase at $500\text{ }^\circ\text{C}$, increased to $40 - 50\%$ in the temperature interval of $500 - 800\text{ }^\circ\text{C}$ and reached almost 100% at $1150\text{ }^\circ\text{C}$ [38]. Most of fuel-S is converted to $SO_2\text{ (g)}$ in an oxidizing combustion atmosphere.
2. Much of the chlorine present in biomass fuel is assumed to exist as water-soluble salt [41], namely KCl. For chlorine rich herbaceous biomass fuel (straw) $\approx 50\%$ of total chlorine already releases at $500\text{ }^\circ\text{C}$ and increases to almost 100% in the temperature interval of $800 - 1150\text{ }^\circ\text{C}$ [37,38]. Dayton et al. [33] undertook direct measurements. They confirm the HCl (g) peak during the de-volatilization stage while most of KCl (g) was observed during char burnout. This is explained by the chlorine released during early de-volatilization. HCl (g) is formed due to the interaction of KCl (s) and the carboxylic group and the later release associated with evaporation of KCl [37,41] at higher temperatures.
3. The organic fraction of phosphorus is probably released as phosphorus oxide, P_4O_{10} or $P_2O_5\text{ (g)}$, during thermal degradation of phosphorous containing organic compounds

[27]. Werkelin et al. [29] report that almost one quarter of phosphorous in woody biomass is present as organic-P. The remaining three quarters are present as water soluble K-phosphate salts [29].

The release is an ambiguous term with regard to solid and/or molten species: they possibly remain in the char surface even after their primary detachment from organic matrix, i.e. during de-volatilization. It may react with gaseous species while escaping the char and hold them in solid or liquid phase. Further, they are potentially involve in reactions with other solid or molten species on physical contact. The release of refractory ash inorganic elements is viewed here as their detachment from the organic matrix or the thermal transformation and decomposition of organic mineraloids and minerals.

1. The calcium in biomass is principally present as calcium oxalate ($\text{CaC}_2\text{O}_4 \cdot n\text{H}_2\text{O}$). The calcium oxalate mineral decomposes in three successive steps according to the following equation [48]. The TGA mass loss result of natural whewellite mineral ($\text{CaC}_2\text{O}_4 \cdot \text{H}_2\text{O}$) shows the mass loss associated with dehydration at 120 – 251 °C, associated with CO at 427 °C and the loss of CO_2 at 603 °C [48]. The lower temperatures with respect to CO_2 release probably indicate that freshly formed CaCO_3 decomposes earlier than pure CaCO_3 mineral grain. Additionally, the thermal decomposition conditions, especially the heating rate as well, influences the reported temperature regime. CaO mostly remains as solid particles due to its refractory nature, the melting temperature of CaO is 2572 °C. Another earth-alkali element, magnesium (Mg), in biomass fuel remains rather independently to calcium minerals nevertheless like calcium it forms MgO (s) [27]. Considering the temperature interval, it probably occurs at later stage during de-volatilization.



2. The Opal ($\text{SiO}_2 \cdot n\text{H}_2\text{O}$) is a mineral of biological or else natural origin. The water content in opal is differentiated as *molecular water* and *silanol-group water* (Si-OH) [49]. The TGA derived mass loss curve suggests that water losses in opal start during the temperature interval of 100 - 400 °C [49]. The higher temperature is potentially associated with the removable of silanol-group water. Opal dehydrates and releases amorphous SiO_2 (s)

particles. Considering the temperature interval, it probably occurs already during the de-volatilization stage. Boström et al. [27] suggested the reduction of SiO_2 in a high temperature and reducing atmosphere and its subsequent release as vapor or fumes, i.e. SiO (g). The reduction of SiO_2 particles outside the char particle is limited but the high temperature and locally reducing atmosphere may exist within a burning char particle.

3. The aluminum (Al) content in biomass is typically low. Water soluble $\text{Al}(\text{OH})_3$, as it is found e.g. in pine [29], is the aluminum species present in biomass fuel and originates biologically or else naturally. The $\text{Al}(\text{OH})_3$ loses water at a temperature range of 300 – 340 °C [49] and apparently forms alumina (Al_2O_3) (s). Considering the temperature interval, it occurs during de-volatilization.
4. The technogenic originating minerals like quartz, feldspar like soil minerals, remain outside the fuel organic matrix. They go through temperature-related phase transformation and decomposition. In parallel, they are also involved in heterogeneous reactions with the species released from the fuel.

2.1.3 Ash formation pathway

Fuel particles which are injected into the hot furnace release moisture (drying). This is followed by the release of fuel volatiles (de-volatilization). Both drying and de-volatilization are endothermic processes i.e. they require heat. De-volatilization is followed by combustion. The combustion is divided into volatile (gas) and char (solid) combustion. The heat bounded in the fuel is released by oxidation during combustion. The temperature at the combustion zone can reach > 1300 °C in pulverized fuel flames. The temperature within the burning char particle may locally peak at even higher values than the average combustion zone temperature.

The burnout time of fuel particles in pulverized furnaces is significantly faster in comparison to (fluidized) bed and grate furnaces [20]. The average heating rate experienced by a particle injected inside the pulverized furnace ranges between $10^3 - 10^6$ K/s [20]. Typically, drying and de-volatilization is completed below < 1 second and within 2 – 3 seconds, most of the combustion (volatile + char) is completed. The fuel's physical and chemical properties (like ash, volatile content, particle size distribution, furnace/burner geometry/aerodynamics, etc.) impact the completed burnout time, decisively. If two particles are of a similar size, a biomass particle is expected to combust significantly faster due to higher volatiles in comparison to a coal particle. Typically, the particle size distribution of pulverized biomass particles fired in pulverized systems ranges between 1 – 2 mm. This is substantially higher in comparison to pulverized coal

particles which are typically below $< 100 \mu\text{m}$. The larger particle size distribution of pulverized biomass may further extend the burnout time.

The ash formation proceeds parallelly with the whole combustion process. Figure 1 shows the simplified schematic of ash formation pathway widely reported in literature [20,25,50]. All aspects of the physical transformation are not included in the sketch. Especially, the fragmentation of char particle is not shown. In general, the fragmentation is crucial for the number and the degree of fineness of ash particles which evolve by burning an individual fuel particle [20]. Generally, fragmentation is expected to be common for larger size biomass particles due to a higher de-volatilization rate owing to higher fuel volatile content [20,51]. But typically, biomass does not contain large size mineral grains within the char particles. So fragmentation does not influence the ash particle evolution [20].

Path I is the pathway of ash particle evolution from volatiles inorganic ash species. These are mostly fine ash or aerosol particles (sub-micron) originating from gaseous inorganic species or species formed by the homogenous reaction which eventually condense as the temperature drops. The fine ash or aerosol particles composition is characterized by K-salts. Sipilä et al. [52] pointed out that due to a small fuel particle size (pulverized fuel) part of the refractory ash species (apparently, CaO , SiO_2) contribute to aerosol formation which is uncommon for conventional biomass firing systems like grate firing and fluidized bed.

KCl-aerosol is expected to evolve directly from condensation of the gas phase of KCl. K_2SO_4 aerosol is formed by sulfation of a stable gas phase K-species especially, KOH and KCl. The sulfation reaction is typically favored $< 900 \text{ }^\circ\text{C}$ and is limited by the availability of SO_3 [53,54]. K-carbonates/phosphates may contribute to fine particle or aerosol fraction. But to the author's knowledge there is no common agreement among literature regarding their contribution as for K-chlorides/sulfates.

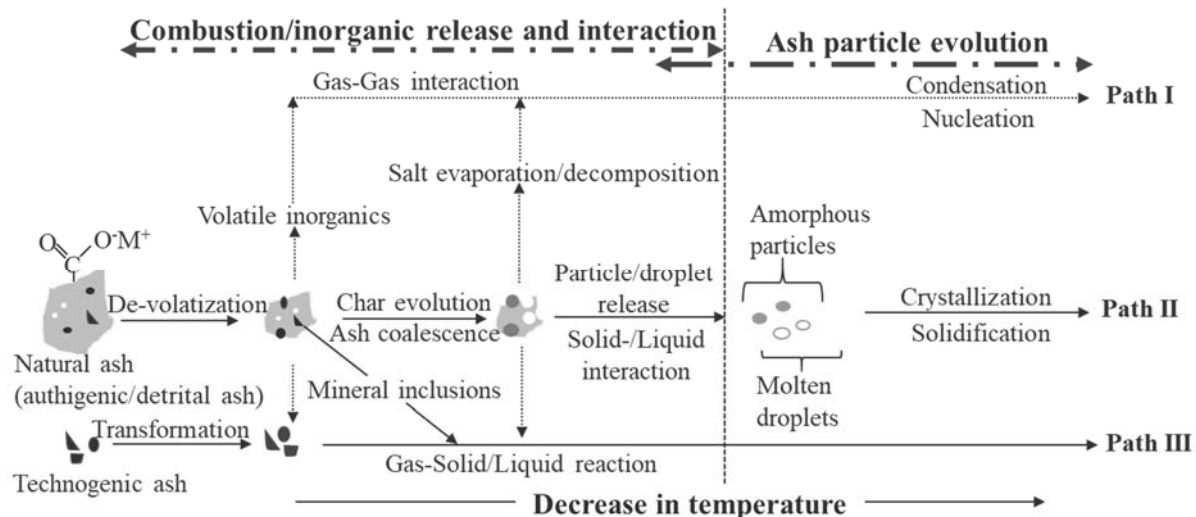


Figure 1: Schematic ash transformation pathway adapted from literature. In fuel particles, organically associated metals, soluble salts (white), include organic minerals/mineraloids (black) as natural ash.

Path II represents the pathway of ash evolution from char retained ash in-organic species. Such ash particles (micron size) originate from the heterogeneous reactions between refractory and volatile ash species and may as well go through subsequent phase transformation (solid \leftrightarrow liquid). Such ash particles are largely silicon dominated and represents the majority of amorphous phase present in biomass generated fly ash.

Wornat et al. [31] studied the structural and compositional transformation of biomass chars during combustion. The char particles (75 - 106 μm) produced from pyrolysis (625 $^{\circ}\text{C}$) of two feed stock pine (woody biomass) and switch grass (herbaceous biomass) were used. The combustion of char was carried out in a laminar flow reactor which operates at a mean gas temperature of approximately 1600 K and an excess of 6 to 12 vol. % oxygen. The combustion conditions simulate the upper furnace region of pulverized-fuel-fired boilers. The char/ash samples were extracted from the reactor at difference residence times using a He-quenched sampling probe.

Wornat et al. [31] observed a significant fraction of inorganic metal retained in the biomass char surface which successively depletes with an increasing residence time of char combustion. The alkali elements (K, Na) depleted drastically due to vaporization. While earth-alkali metals (Ca, Mg), silicon (Si), and aluminum (Al) are largely retained within the char surface. They point out that surface migration, coalescence, and the incorporation of metals into silicate structures are the major inorganic transformation during char particle burnout. The silicate formation reduces vaporization losses associated of given metal species, especially Ca and K. Comparatively, the increasing dominance of Ca-Si association and subsequently diminishing presence

of K-Si association with increased level of char conversion [31] indicate that the Ca-silicate formation is the major chemical interaction within the char particle while potassium (K) evaporates and escapes the char surface with increasing particle temperature. The spherical nature of Si-rich beds developing over the char surface is evident while scanning electron micrographs [31] suggested the K-/Ca-silicates evolve as molten components.

Path III basically represents the pathway of ash particle evolution from ash species or minerals that remains independent of the fuel organic matrix. In most biomass fuels silicon (as quartz) is the most abundant external ash species/mineral and other mineral like feldspar. Both are soil-borne impurities. They independently go through their thermal transformation and/or are partially involve in heterogeneous reactions with the primarily released volatile ash species.

2.1.4 Ash system chemistry

Boström et al. [27] explained ash formation chemistry by categorizing the ash inorganic interaction into primary and secondary reactions. The primary reaction summarizes the phase and form of ash inorganic species released from fuel as basic and acidic components. The secondary reaction is the interaction among these species. The theoretical approach of Boström et al. [27] understands the release of inorganic ash-forming matter as primary reactions. The secondary reaction includes gas-gas homogeneous reaction and heterogeneous reactions (gas-liquid-solid). The gas-gas reaction includes the formation of alkali (K) species. It is widely agreed, at high temperature KCl and KOH are the main species. If species escape the heterogeneous reaction (mainly with SiO₂), as the temperature drops, mainly K-salt species are formed. The K-salt species are expected to be present as such in the fuel itself. Therefore, this chemistry can be viewed as release (eventual to escape with the flue gas) and retention (eventually to remain in ash) of elements present in respective salt compounds.

Table 5: List of basic and acidic components from primary ash transformation reaction [27].

Basic components	Acidic components
KOH (l, g) (K ₂ O), NaOH (l, g) (Na ₂ O), CaO (s), MgO (s)	P ₂ O ₅ (g), SO ₂ /SO ₃ (g), HCl (g) (Cl ₂), CO ₂ (g), H ₂ O (g), SiO ₂ (s)

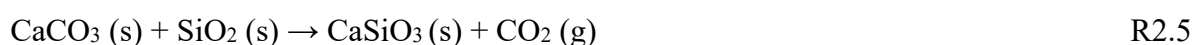
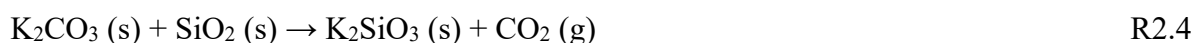
The potassium, calcium, and silicon in biomass fuel remain as independent compounds which apparently meet each-other during the combustion process to form the compounds found in combustion generated ash. The interaction among these species represents the main ash system chemistry where compounds, which do not originally exist in raw biomass fuel, are formed

during the combustion process. The heterogeneous chemical reactions between potassium and calcium species with SiO₂ lead to the formation of K-/Ca-silicates. KCl (s), K₂SO₄ (s), K₂CO₃ (s), K-phosphate (s), and CaCO₃ (s) are species relevant during de-volatilization while KCl (g), KOH (g), and CaO (s) are species relevant during the combustion stage.

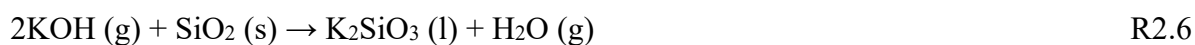
R 2.4 to R 2.7 show the silicate formation reactions divided as silicate formation during de-volatilization stage and during combustion stage. Many of these reactions are reported, see e.g. Boström et al. [27] and others [17,25]. Only the heterogeneous reactions related to silicate formation are organized here.

The change in Gibbs free energy (ΔG , see Table 6 calculated by using FactSage) of each reaction per mole of K/Ca-silicate formation are compared at temperature 500 °C and 1000 °C. The lower temperature represents the de-volatilization temperature (end regime) and the higher represents the combustion temperature regime (begin regime). The ΔG comparison is made per unit mole of given silicate compound (see Table 6). The FactSage reaction module was used to abstract the ΔG of each balanced reaction. It is important to note that with KCl (s), K₂SO₄ (s), and KCl (g) the formation of K-silicate is not favorable. The pathway of K-phosphate and SiO₂ direct chemical interaction is not discussed in concern to biomass ash system silicate chemistry [27]. Phosphates are argued to evolve outside silicate chemistry as Ca-K-Mg phosphates [55].

K/Ca-silicate formation in de-volatilization temperature regime



K/Ca-silicate formation in combustion temperature regime



K-silicates as pure compounds exist in various chemical forms. K-silicates in general can be represented as K₂O.nSiO₂. The chemical form of K-silicate varies with the mole of SiO₂ namely, K₂SiO₃ (n=1), K₂Si₂O₅ (n=2), and K₂Si₄O₉ (n=4).

The solid or liquid species may or may not leave the char surface until the char (organic) matrix is completely consumed by combustion. When all the reactants are solid species, the reactions are speculated to proceed within the char surface where the contact is facilitated by coalescence.

Under such scenario, various reactants come in contact. Therefore, non-stoichiometric compounds or solutions are formed instead of simple stoichiometric compounds. Many authors consider the formation of K-Ca-silicate, Ca-Mg-silicates or silica-based slag.

Table 6: ΔG of silicate formation via different reaction pathways.

Silicate compound	K/Ca-compound	ΔG in kJ/mole at 500 °C	ΔG in kJ/mole at 1000 °C
K-silicate	KOH (g)	<i>Not considered</i>	-207
	K ₂ CO ₃ (s)	-15.5	<i>Not considered</i>
Ca-silicate	CaO (s)	<i>Not considered</i>	-89.9
	CaCO ₃ (s)	-34.8	<i>Not considered</i>

From a thermodynamic point of view, K-silicate formation is favorable over Ca-silicate by comparing ΔG among the reactions. Beside, individual K-silicate and Ca-silicate, the formation of mixed silicates, K-Ca-silicate is also discussed by many authors [27,56]. In general, comparing ΔG simplifies the hierarchy among a set of reactions. But, obviously, the equilibrium conditions may not always be achieved in an actual combustion facility. The reactivity of involved species, contacts among species, inadequate reaction time, or reaction kinetics are factors limiting the reaction to reach the level of thermodynamic equilibrium. Especially, the condensed (solid/liquid) reactions are far from reaching thermodynamic equilibrium [57].

The chemistry based prediction of the chemical form of ash species is often justified and validated by the crystalline compounds identified by X-ray diffraction (XRD), seen at Boström et al. [27] and others [15,58]. To the author's knowledge and pointed out by others [27] K-silicates or K-Ca-silicates are not identified by XRD, which on contrary is speculated to be the major compound formed. The common explanation is that K-silicate or K-Ca-silicates mostly remain in the amorphous phase and are therefore difficult to be identified by XRD. The Scanning Electron Microscope (SEM) generated BSE image shows spherical fly ash particles which are presented in various literature [59–61]. The spherical shape of particles relates to the particle molten history and such particles are abundantly found in biomass generated fly ash [20]. The SEM-Energy-Dispersive X-ray Spectroscopy (SEM-EDS) composition is helpful to justify the silicate based composition of amorphous ash particles. They are expected to derive from solidification of silicate based slag and ash compounds are K-/Ca-silicates or their solutions.

The fine/aerosol ash (mostly K-salt species) and the amorphous fly ash (mostly K-/Ca-silicates) due to its molten history are biomass specific. These particles are critical ash components with regard to fire-side corrosion and deposition. The formation of such species is inherent to ash-forming matter in biomass feedstock and ensured by biomass ash system chemistry.

2.2 Deposition

Deposition refers to the transport, adhering, and accumulation of ash particles to the furnace wall and the boiler heat-exchanger surfaces. The main transport mechanisms leading to ash deposition are [20,62]

- **inertial impaction** including eddy impaction,
- **thermophoresis** and diffusional aerosol transport due to the gradient in temperature and concentration, respectively, of the flow, and
- **diffusion** of inorganic vapors followed by condensation.

Inertial impaction is the dominant mechanism for the deposition of coarse particles, i.e. solid or molten ash components. Deposition modeling studies generally consider particles $> 10 \mu\text{m}$ to deposit via inertial impaction [20]. The condensation over the boiler heat exchanger surface and/or the particle transport due to temperature gradient (thermophoresis) and concentration gradient (diffusion) are mechanisms responsible for deposition of finer size, i.e. gas phase volatile and aerosols, ash components.

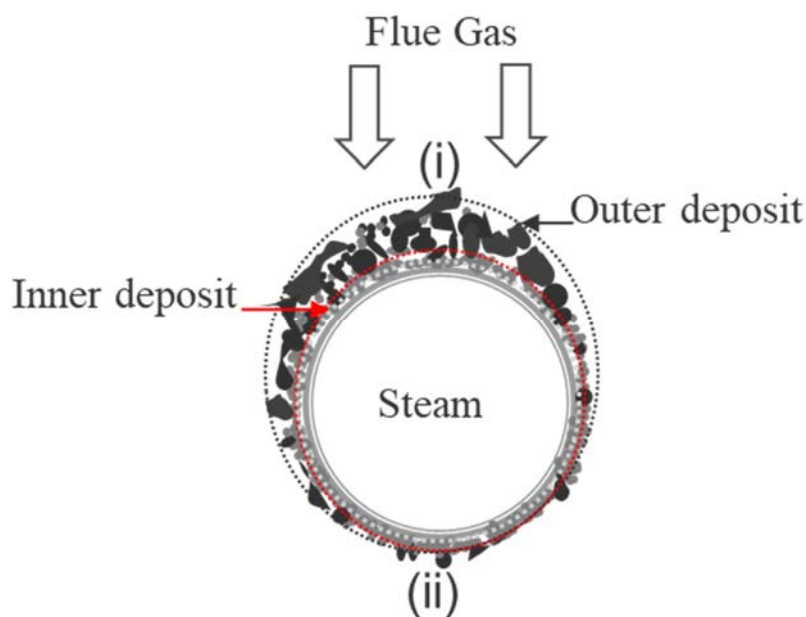


Figure 2: Schematic of deposit over boiler tube, adapted from [63,64], (i) luv side and (ii) lee side.

In ash deposit dedicated experimental studies [59,63,65], temperature controlled deposit probes (simulating boiler tube surface) are exposed inside an operating boilers/combustion test facility for certain duration. Over time ash accumulates, and a deposit layer develops over the probe surface. The ash deposit layer is generally distinguished as inner layer and outer deposit layer. The inner layer is composed of finer ash particles deposited by thermophoresis and diffusion while the outer is of coarser ash deposited by inertial impaction. A further distinction is due to the direction of the flue gas flow, mainly as luv (upwind) and lee (downwind) side deposit.

Ash deposition behavior of biomass fuel in reference to coal is discussed thoroughly [18,64,66]. These references mostly undertake co-firing studies. The severity of critical deposition behavior differs with the kind of biomass and the base coal. But, biomass fuel increases deposition and ash particle sintering, in general. This is explained by the low melting properties of biomass generated ash. Considering this behavior, Heinzl et al. [18] suggest that the risk of furnace slagging to be more critical than the boiler fouling during biomass co-firing. Another highlighted concern, is the retention of chlorine in fly ash/deposit which is mostly observed for chlorine rich herbaceous biomass (like straw).

Wu et al. and Bashir et al. [59,65] studies with 100 % biomass combustion report that the bulk composition of outer deposit is almost similar to the fly ash composition. The outer deposit primarily consists of Si, Ca, and K rich, mostly spherical and clustered particles [59,65]. The inner deposit is dominated by alkali salt species. K, S, and Cl rich particles dominate the inner and lee side deposit in both studies. Evaluating the molar balance and ratios among water soluble K, Na, S, and Cl, from wood deposit Wu et al. [59] suggest the considerable presence of potassium in form, other than sulfate and chloride, apparently K_2CO_3 . Both K_2CO_3 and KOH was detected by XRD in fly ash (sample from ESP) as reported by Wu et al. [59]. In general, K_2SO_4 dominates the inner deposit from woody fuels if it is mostly chlorine lean [59] while KCl dominates the deposit from straw fuels because it is mostly chlorine rich [63,65,67]. Despite of the very low chlorine content in woody biomass fuel, the majority of the chlorine tends to retain in the ash as KCl. KCl is critical irrespective to the amount due to its high corrosiveness [59].

The concentration of certain ash elements or species in fly ash and deposit differs distinctly depending on the firing system. The point of concern here, is the higher fraction of refractory species (like Ca, Si) in fly ash/deposit (super heater) from pulverized fuel boilers [60,65] in comparison to fly ash/deposit (super heater) from grate boilers for similar fuel [68,69]. Potassium and chlorine species represent the majority in fly ash/deposit (super heater) composition:

almost 60-70% together in a grate boiler study by Zhou et al. [68]. However, silicon represents the majority in fly ash/deposit (super heater) composition from pulverized combustion boiler, almost 40-50% alone in the pulverized boiler study by Bashir et al. [60]. The smaller fuel particle size, higher heating rate, and higher fly ash loading in the flue gas contribute to a higher fraction of refractory elements, like Si and Ca, [20] in pulverized boiler deposit.

The volatile ash species, mostly K-salt species, form the inner deposit with other fine ash (aerosol particles) via diffusion-condensation transport pathway. Especially, due to fine size distribution of thus formed particles; they are prone to deposit, irrespective to particle stickiness. It is arguable, therefore, that the melt induced particle stickiness may not be of high relevance for diffusion and direct condensation driven mechanism. However, as the surface temperature rises with respect to increased deposit thickness, the melting of the salt-rich initial deposit layer may enhance the probability to capture other impacting coarser ash species. The sticky salt layer is often argued as a prerequisite for bulk deposit growth [20] and determines the capture efficiency of the receiving surface. To summarize, the melt induced stickiness of salt-rich ash particle may not be relevant for the deposition of salt species themselves but for the capture of incoming/impacting coarser ash particles.

The bulk ash melting behavior has long been recognized as a boiler design parameter to avoid excessive ash deposition in super heater region. It is further recognized that the fly ash generated from biomass is characterized by low ash melting temperatures.

Instead of having a specific temperature, ash particles melt congruently. At individual particle level, the melt co-exists with solid components over a wider temperature range. The melt fraction decreases as the particle temperature decreases, for instance during the process of deposition, i.e. when particles entrained by the hot flue gas enter the boundary layer of the heat exchanger surface. The search for a critical melt fraction, when ash particles are expected to adhere to the impacting surface, has gained attention in biomass ash deposition modeling [20].

Mueller et al. [70] argue, particles must have a melt fraction $> 15\%$ to stick to the surface. They performed an experiment in an entrained flow reactor with furnace temperature of $1000\text{ }^{\circ}\text{C}$ and deposit probe surface temperature of $550\text{ }^{\circ}\text{C}$ with salt mixture, K/Na sulfate and K/Na chloride, of three different size fraction ($75\text{ }\mu\text{m}$, $75 - 150\text{ }\mu\text{m}$, and $150 - 250\text{ }\mu\text{m}$). The temperature of the assumed critical melt fraction (15%) lies in the range of $520\text{ }^{\circ}\text{C} - 790\text{ }^{\circ}\text{C}$. Mueller et al. [70] point out that the critical sticking range of $15 - 70\%$ fits well for particles $< 75\text{ }\mu\text{m}$. For bigger size particles, the physical phenomenon of particle rebounding appears rather important. The extension of a critical melt criteria to other composition, for instance to silica-rich ash, is

still unclear and maybe misleading due to the difference in physical properties, especially viscosity, of salt-melt and silicate melt [20].

For most coal ash deposition modelling, the critical viscosity is widely used to define the particle stickiness. Kleinhans et al. [20] reviewed extensively the various deposition models discussing the stickiness criteria used in ash deposition modelling. Based on their comparative evaluation, Kleinhans et al. [20] argue that, for salt-rich ash the critical melt defined criteria appears more reliable while for silica-rich ash the critical viscosity appears more reliable. The sticking criteria among different ash compositions and process conditions are not universal, instead it needs to be chosen case by case [20]. Kleinhans et al. [20] performed a comparative evaluation of different sticking criteria, both melt fraction and viscosity, reported in previous studies. The soda lime glass particles are considered to simulate silica-rich ash particles. The viscosity range between $10^5 - 10^8$ Pa.s is considered to be the critical viscosity regime for the calculation and the approach used by Srinivasachar et al. [71].

The inertial impaction is the main deposition mechanism for coarser particles. Such particles are the main contributor in bulk deposit growth. The amount of melt fraction and viscosity of impacting particles are interrelated by the same chemistry and governs the sticking probability. On impaction, the soft molten particles dissipate the kinetic energy due to deformation and adhere to the surface while the hard solid particles rebound back and join the flue gas flow [20]. In real boilers, both, capture efficiency of the deposit front and stickiness of impacting particles, are dynamic and change in relation to the frequency of soot blowing and natural deposit shedding. Some studies [59,65,68] used advanced deposition probes to evaluate the dynamic and real time deposition behavior inside a boiler. The common approach is to measure the ash mass accumulating over the probe surface. These quantitative numbers (ash deposition rate) are influenced by the ash chemical and physical properties and the conditions specific to the given boiler/test facility operation conditions. Bashir et al. [65] concluded that the deposition rate increases with increase in flue gas temperature while the probe surface temperature have no significant impact on the measured deposition rate. Their conclusion is drawn from measurements in a pulverized boiler, firing straw, wood, and their blends. A similar study from grate boilers [68] suggests, the higher flue gas temperature reduces deposit weight. Lower flue gas temperature increases deposit weight. The influence of probe surface temperature was similar, i.e. higher probe surface temperature results in lower deposition rate and vice versa.

The comparison of quantitative deposition behavior among different firing systems considering different combustion boundaries (especially temperature, residence time) and different exposure conditions (flue gas temperature, flow condition/velocity, fly ash loading), discloses substantial differences. The contradicted dependency of flue gas temperature and/or probe surface temperature on deposit growth may relate to the composition of fly ash at the probe exposure location. The silica-rich fly ash drives the bulk deposit growth in case of pulverized boiler [65,72] where a significant fraction of silicatic ash passes through the boiler as fly ash. The bulk deposition rate is mainly governed by inertial impaction. With increase in flue gas temperature, the melt induced stickiness of silicatic-ash increases. In response, the deposition rate increases. For potassium and chlorine dominated fly ash, the deposition is driven by condensation/aerosol formation. In case of grate boiler [68], most of the silicatic ash remains as bed ash and does not reach the boiler heat-exchanger area. Generally, the bulk growth is due to thermophoresis and diffusion-condensation. The condensation/aerosol formation is promoted at lower temperature as a response to which the deposition rate increase. Most importantly, the comparison clearly highlights the differences in deposition behavior among the firing systems. Though the fundamental ash formation chemistry and the critical behavior associated with certain ash species remains similar, the fraction of the fly ash reaching the boiler heat exchanger area differs from one firing system to other therefore exhibit different level of severity even when the same fuel is fired. It indicates that the general experience of grate boilers with regard to quantitative deposition is probably not transferable to pulverized boilers even for the similar biomass fuel.

2.3 Fireside corrosion

The interaction of flue gas components and deposit ash species, mainly salts, with boiler tube surfaces, i.e. the boiler tube alloy material, is referred to as fireside corrosion. The presence of sulfate and chloride salt is well known to accelerate corrosion [9]. Chloride salts are considered more corrosive in comparison to sulfate salts. The presence of molten salts further accelerates the interaction which then further enhances the severity of corrosion. The corrosion mechanism which is related to sulfate salts is known as *hot corrosion* and the mechanisms connected to chloride salts as *active oxidation* [21,73].

These mechanism and their chemistry are outlined with alkali salts as sodium sulfates and chlorides [74,75] as well as with alkali's salt as potassium sulfates and chlorides [76,77]. In general, there are no practical difference in relation to alkalis, i.e. potassium or sodium, as the basic drivers of corrosion mechanism are sulfur (sulfate) and chlorine (chloride).

Eliaz et al. [74] divided *hot corrosion* into type I and type II. They are discussed in terms of gas turbine engines. Hot corrosion involves the specific role of salt melt and the formation of metal sulfidation. The type I mechanism occurs in temperatures ranging from 850 °C to 950 °C. Type II ranges between 650 °C to 800 °C [74]. They are morphologically characterized by a depletion region beneath the porous non-protective scale as well as by pitting or localized corrosion [74].

For *active oxidation*, the presence of salt melt is not a prerequisite. It includes the role of molecular chlorine and is explained as metal chloride formation. Its outward migration and oxidation thus again releases molecular chlorine [75]. The mechanism is understood as a cyclic process where the chlorine continuously diffuses into the material and continuously brings new metal molecules to the surface to oxidize [75]; a situation of accelerated metal oxidation. The accelerated oxidation is associated with the volatile nature of metal chlorides, especially Cr-chlorides, and the possibility of Cl trapped in a close loop within the alloy matrix. Morphologically it is characterized by the loss of alloy elements, especially Cr, and a chemically destroyed and physically porous oxide scale [75]. Many studies [21] pointed out the synergy between chloride salt and SO₂, especially in relation to sulfation and release of HCl in the process as a potential chlorine source to trigger active oxidation while some [78] pointed towards the direct alkali chloride (salt)-oxide interaction and formation of alkali-chromates.

Formations of metal sulfides (hot corrosion) and metal chlorides (active oxidation) are undesired corrosion effects. In contrast, oxidation is essentially helpful if it generates a protective oxide scale formation. The oxide scale is acting as barriers to stop diffusion of corrosive species into the alloy matrix. Metal sulfides are thermodynamically less stable than oxides and have low melting points while metal chlorides are characterized by their higher volatility [73]. Due to higher volatility, metal chlorides are highly mobile and accelerate the oxidation leading to a catastrophic corrosion rate. The metal sulfides are comparatively less mobile and may not establish accelerated metal oxidation. Nonetheless, their presence signifies a non-protective oxide scale and a breakaway corrosion.

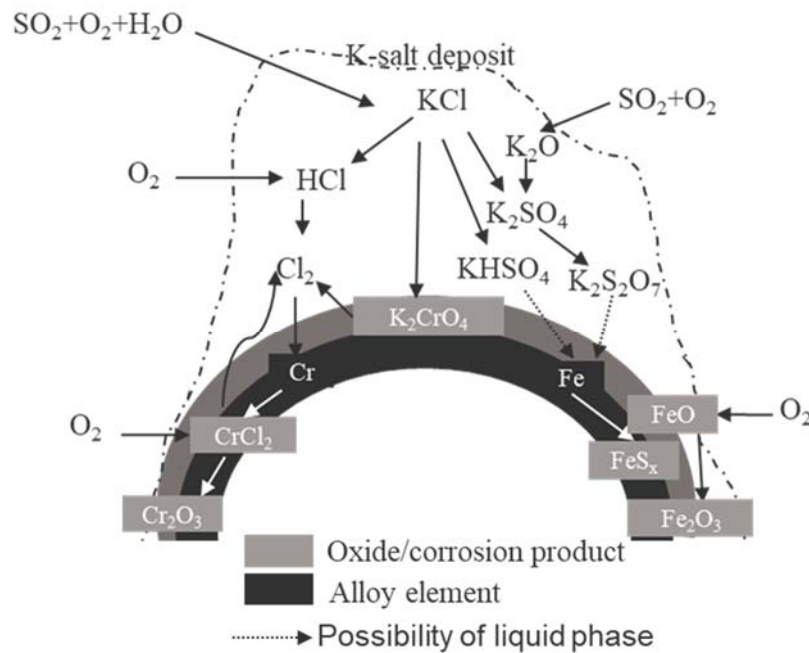


Figure 3: Sequence of corrosion reactions with K-Salt. Figure adapted from [21,79] and reaction mechanism sequence from various literature, shows both for *hot corrosion* and *active oxidation*.

Historically, boiler heat exchanger alloy material development focused on the increase of high temperature creep strength [80,81]. The martensitic 9 – 12 % Cr steel (Fe-alloy) is widely used as high temperature boiler heat exchanger material. It has a maximum temperature range of 610 – 620 °C [80]. Austenitic ≥ 15 % Cr steels (Fe-alloy) are considered for temperature up to 650 °C. For advanced ultra-super critical power plants ≥ 20 % Cr, Ni-based alloys are proposed to stand temperatures up to 700 °C [80]. Beside steam temperature, the steam pressure is to be considered. Additionally, the reported maximum temperature refers to ideal conditions whereas in boiler atmosphere/conditions, the maximum applicable temperature is also coupled with the extent of fire-side corrosion.

Corrosion resistivity is another concern in the development of boiler heat exchanger material [81]. The chromium content is often correlated to the corrosion resistivity provided by the material which is related to selective oxidation of chromium and the formation of protective Cr-oxide scale. In general, the austenitic steel shows more corrosion resistivity than martensitic steels. The Cr-oxide is proven protective against sulfur/sulfate related corrosion in an oxidizing atmosphere but in chlorine/chloride containing atmosphere the Cr-oxide layer could fail to remain protective [82]. The observations made from corrosion exposure studies using pure sulfate and chloride salt show that the protectiveness of a Cr-oxide layer is destroyed in the presence of chloride salt whereas maintained in presence of K₂SO₄ alone [78,83].

G. Sorell [79] and Nielsen et al. [21] summarized the implication and major mechanism of chlorine-associated fireside corrosion in relation to waste and biomass fuels. The fireside corrosion risk related to biomass fuel mostly revolves around the condensation or deposition of chloride salt (KCl) over boiler tube surfaces and a corrosion mechanism referred as active oxidation.

The protectiveness of chromium oxide layer is poor to hinder active oxidation apparently due to higher affinity of chlorine towards chromium (Cr) in comparison to other alloy element (Ni) and/or the bulk metal (Fe) itself [84]. The cyclic mechanism of chlorine triggered active oxidation suggests that once a chlorine molecule is entrapped within the alloy matrix, the corrosion process is self-sustained. It implies that the risk of such corrosion is not related to the amount of salt but rather to the mere presence of chloride salt (KCl) in the deposit.

The fuel-Cl is released as KCl (g) and HCl (g) at combustion/furnace temperature regime. KCl (g) is a condensable species in the boiler temperature regime while HCl is a condensable species only below the acid dew point ($< 80\text{ }^{\circ}\text{C}$ for HCl and $< 150\text{ }^{\circ}\text{C}$ for SO_3 as reference in typical flue gas composition), i.e. well outside the boiler temperature regime. The corrosivity of HCl which remains in the gas phase in the boiler temperature regime is not of high risk [21,85]. The main risk is associated with chloride (KCl) in deposit/ash. The retention as KCl in ash/deposit is expected when firing biomass fuel due to one or more of the reasons listed below;

- The lower fuel-S content in biomass limits SO_x and therefore sulfation to release chlorine (as HCl in the flue gas).
- Flue gas temperatures (super-heater region) are higher than optimum temperature of KCl sulfation.
- KCl sulfation is inhibited by CaO sulfation.
- Thermodynamic limitation of KCl-SiO₂ interaction to release chlorine (as HCl in the flue gas).

Pettersson et al. [83] and Lehmusto et al. [86] pointed out that K_2CO_3 could be equally corrosive as KCl. Lehmusto et al. [86] further discussed the differentiation in severity of K_2CO_3 for Fe-based and Ni-based alloys and as well as synergies with the presence of water vapor. The role of K_2CO_3 and its possible decomposed product in the boiler atmosphere, KOH, may as well be of concern for fireside corrosion for chlorine lean biomass fuel, like wood.

2.4 Additive to mitigate deposition and corrosion

Wang et al. [87] reviewed additives and their application to reduce ash related operational issues. The major kind of additives tested and proposed for deposition and corrosion mitigation are grouped and their major mitigation mechanism are summarized in Table 7.

The ability of aluminosilicate based additives to capture alkali, here potassium, species in the high temperature regime to form stable and non-corrosive K-aluminosilicate is a widely reported mechanism. The efficiency to capture may vary with the mineralogy (additive related properties) and alkali species (fuel related properties) and application conditions (temperature, residence time, atmosphere, application zone etc.) but the associated chemistry is well agreed. The positive effect of aluminosilicate based additive has been highlighted in open literature [25, 58, 67, 88–92].

The underlying idea of using aluminosilicate based additives is to alter the biomass ash system chemistry to form less problematic ash species which are less critical with regard to deposition and corrosion. Alkalis are irreversibly captured by aluminosilicates to form stable (noncorrosive) and refractory compounds (high melting temperature) K-aluminosilicate.

Table 7: Major chemical groups of additives, fundamental mechanism and major mitigation target.

	Aluminosilicate based	Sulfur based	Calcium based
Additive material	Kaolin Coal fly ash	Ammonium sulfate	Dolomite Calcium phosphate
Fundamental mechanism	Chemical/physical adsorption of potassium species as high melting K-aluminosilicate compounds.	Sulfation of K-chlorides to less corrosive K-sulfates	Promoted formation of high melting Ca-silicates and/or dilution of K-silicate slag to improve its crystallization/solidification.
Mitigation target	Deposition and corrosion	Corrosion	Deposition

Aluminosilicate belongs to the clay mineral group. According to Handbook of Clay Science, [93] different aluminosilicate minerals are found in nature. They are categorized as *1:1 clay minerals* and *2:1 clay minerals*. Aluminosilicate minerals which efficiently capture and incorporate other elements, here metals, within their structure are beneficial for the purpose as a mitigative additive. Aluminosilicate minerals of the 1:1 clay mineral group, generally reported as kaolin, are the base aluminosilicate mineral of interest as a mitigative additive.

The kaolin minerals have different crystalline forms, these poly types include kaolinite, dickite, nacrite, and halloysite. They are generically referred to as hydrous aluminum phyllosilicates and chemically $\text{Al}_2\text{Si}_2\text{O}_5(\text{OH})_4$ [93]. A single crystal consists of siloxane group (Si-O-Si) tetrahedral layer and aluminol octahedral layer (Al-OH) [93]. Kaolinite and others typically occur in platy morphology while halloysite contains additional water molecules between the layers and can exhibit tubular, spheroidal, as well as platy morphology [93,94]. Chemically, halloysite is reported as $\text{Al}_2\text{Si}_2\text{O}_5(\text{OH})_4 \cdot 2\text{H}_2\text{O}$ and sometimes regarded as the hydrated kaolinite phase [93].

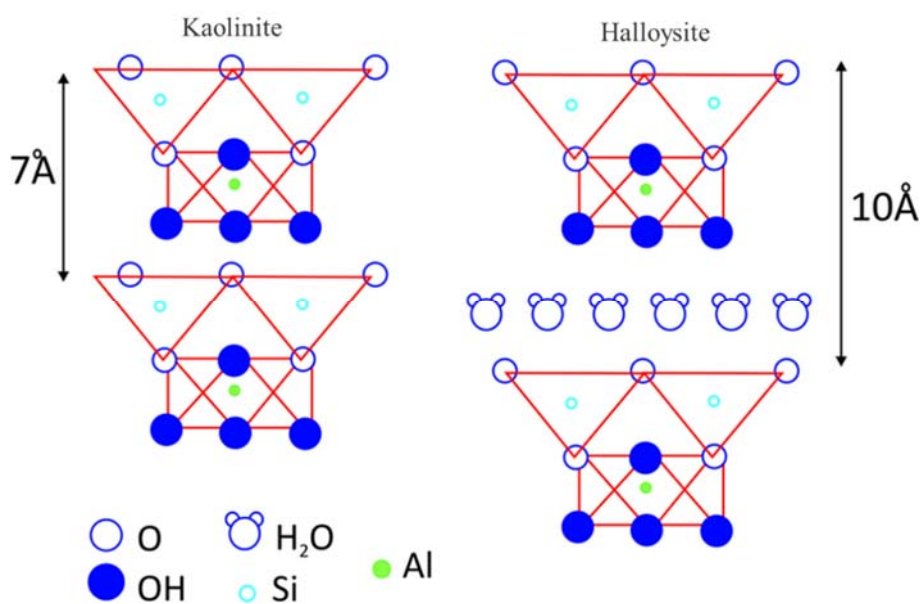


Figure 4: Structure of kaolinite and halloysite [94]

Kaolin is commonly used as an additive to modify the biomass ash system chemistry. Therefore, the additive is often referred to as *aluminosilicate based additive* or *kaolin based additive*. As an additive, coal fly ash is discussed in the same category. However, the difference in relation to mineralogy is evident.

When coal fly ash is used, the aluminosilicate is derived from the clay minerals present in the coal. The positive consequence of aluminosilicate rich coal ash is well noted by many biomass co-firing studies. In coal, aluminosilicatic clay minerals are abundant [95,96] and found mainly as Kaolinite, Illite, Muscovite, Chlorite, and Montmorillonite. Beside kaolinite, other clay minerals already contain alkalis/earth alkalis or other metals in their chemical structure. Thereby, they do not provide an active site to incorporate additional alkalis within its structure. In contrast, kaolinite only contains aluminum and silicon. Thus it provides the active site to chemically incorporate alkali species.

The aluminosilicates present in coal fly ash are a product of the transformation of clay minerals. Depending on the temperature observed during the coal combustion, kaolinite may be present in amorphous phase, like meta-kaolin, and/or crystalline phase, like spinel and mullite.

Beside kaolin group minerals other mineral impurities are as well present in commercially available aluminosilicatic mineral additives. Muscovite and quartz are the most common impurities. Iron is present mostly when halloysite is the main kaolin mineral [93,94].

It is pointed out that the adsorption of gaseous species on the surface of halloysite particles is more effective than it is by kaolinite particles. The argument behind this is the additional active site available when the surface water molecules which are only present in halloysite, see Figure 4, are removed. Additionally, halloysite minerals are known to have higher porosity than kaolinite. This characteristic is explained as a consequence of its tubular structural arrangement [94]. Halloysite adsorption behavior provides superior performance to capture alkalis in comparison to kaolinite [89,97].

In a combustion system application scenario, the thermal transformation state of base mineral is probably more relevant for capture reactions. Halloysite loses its additional water in a temperature range of 70 – 100 °C and chemically remains $\text{Al}_2\text{Si}_2\text{O}_5(\text{OH})_4$ as kaolinite. $\text{Al}_2\text{Si}_2\text{O}_5(\text{OH})_4$ loses the hydroxyl group in a temperature range of 450 – 600 °C [98] to form $\text{Al}_2\text{Si}_2\text{O}_7$. $\text{Al}_2\text{Si}_2\text{O}_7$ is the amorphous, also disordered, phase and referred as *meta-kaolin*. On further heating, the amorphous aluminosilicate forms spinel phase ($\text{Si}_3\text{Al}_4\text{O}_{12}$) at 980 °C accompanied by crystalline mullite ($\text{Al}_6\text{Si}_2\text{O}_{13}$) which largely forms above 1250 °C [98]. The reported mullite crystallization temperature varies in the range of 100 – 200 °C. Mullite is a stable aluminosilicate which melts well above 1840 °C. Zhou et al. [98] reported that thermal decomposition behavior of kaolinite is influenced by other mineral impurities. They argued that the transformation of pure kaolinite to mullite is more readily achieved.

$\text{Al}_2\text{Si}_2\text{O}_5(\text{OH})_4 \rightarrow \text{Al}_2\text{Si}_2\text{O}_7 + 2\text{H}_2\text{O}$	R 2.8
$2\text{Al}_2\text{Si}_2\text{O}_7 \rightarrow \text{Si}_3\text{Al}_4\text{O}_{12} + \text{SiO}_2$	R 2.9
$3\text{Si}_3\text{Al}_4\text{O}_{12} \rightarrow 2\text{Al}_6\text{Si}_2\text{O}_{13} + 5\text{SiO}_2$	R 2.10

Amorphous meta-kaolinite ($\text{Al}_2\text{Si}_2\text{O}_7$) is the primary component derived from kaolinite. And is the main reactive aluminosilicate that would drive the alkali metal capture reactions [99]. The vacant sites due to the removal of water, i.e. hydroxyl molecules, are the capture sites. As it owes the additional surface H_2O , it is argued that halloysite offers better capture efficiencies than kaolinite. It is also reported that the meta-kaolin phase derived from halloysite possess additional porosity and surface area because of its tubular structure [100]. This is further beneficial to capture reactions. The capture effectivity of the spinel phase is not much discussed in literature. Further, mullite is considered less effective [99] as far as the capture reaction is concerned, because of its tight crystalline structure.

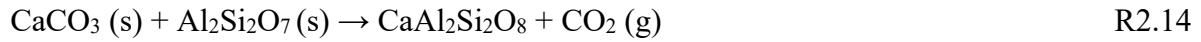
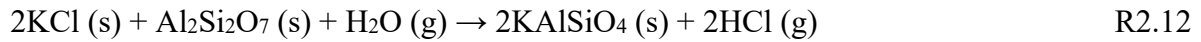
Coal fly ash is also successfully used as additive in many studies [91,101]. The idea behind is to exploit the excess aluminosilicatic minerals present in coal fly ash. The original minerals in coal which are largely clay minerals, like kaolinite, have already gone through transformation resulting in fly ash. In comparison per unit gram, coal fly ash is expected to be less effective than pure mineral additives [99]. The lower price on the other hand is an ideal benefit.

2.4.1 Ash system chemistry in presence of additives

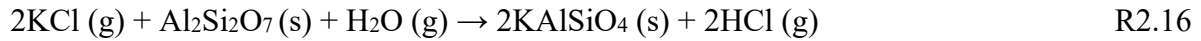
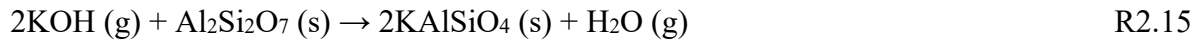
Meta-kaolin ($\text{Al}_2\text{Si}_2\text{O}_7$) is mostly considered [99] as an aluminosilicate to discuss the alkali capture reactions and in some literature [58] the reactions are outlined with kaolinite. The possible ash species and additive reactions are summarized here, see R 2.11 to 2.17. In literature mostly the gas phase K-species, mainly KCl and KOH reactions are considered.

From a thermodynamic point of view, when comparing ΔG in Table 6 and Table 8, the K-aluminosilicate formation is comparatively favorable over the K-silicate formation. Additionally, the K-aluminosilicate formation is favored with KCl and K_2SO_4 which does not show a thermodynamic drive to form K-silicates. Ca-aluminosilicate is as well comparatively favorable over the Ca-silicate formation.

K-aluminosilicate formation in a devolatilization temperature regime



K-aluminosilicate formation in a combustion temperature regime



K-aluminosilicate as pure compounds exist in various chemical forms [58]. The chemical form of K-aluminosilicate varies with the mole of SiO₂ including KAlSiO₄ (Kalsilite), KAlSi₂O₆ (leucite), and KAlSi₃O₈ (microcline). Wang et al. [102,103] performed experiments at temperatures > 1000 °C in a heated entrained flow reactor with pure salts and kaolin additive. Based on XRD, they evaluate the solid product. They report KAlSiO₄ to be the major K-aluminosilicate when KOH and K₂CO₃ are involved and KAlSi₂O₆ as the major K-aluminosilicate when KCl and K₂SO₄ are involved [102,103]. Beside the crystalline K-aluminosilicate, Wang et al. [103] discussed the presence of amorphous K-aluminosilicate which could be originating from KAlSi₃O₈ which melted at high temperatures and formed amorphous K-aluminosilicate.

Table 8: ΔG of aluminosilicate formation via different reaction pathways.

Aluminosilicate compound	K-species	Δ G in kJ/mole at 500 °C	Δ G in kJ/mole at 1000 °C
K-aluminosilicate	K ₂ CO ₃ (s)	-207.6	<i>Not considered</i>
	KCl (s)	-106.6	<i>Not considered</i>
	K ₂ SO ₄ (s)	-73.3	<i>Not considered</i>
	KOH (g)	<i>Not considered</i>	-306.5
	KCl (g)	<i>Not considered</i>	-176.2
Ca-aluminosilicate	CaO (s)	<i>Not considered</i>	-397.9
	CaCO ₃ (s)	-342.7	<i>Not considered</i>

In biomass+additive studies [58,104,105], KAlSiO₄ and KAlSi₂O₆ are commonly reported as K-aluminosilicate and identified by XRD. Steenari et al. [58] discussed the various chemical

forms of K-aluminosilicate and argue that KAlSiO_4 is the direct or primary product and incorporation of further mole of silica results in KAlSi_2O_6 and KAlSi_3O_8 . They [58] also reported the weak diffraction product of muscovite is mainly characterized as a non-crystalline K-aluminosilicate. Most kaolin based additives contain impurities, like muscovite ($\text{KAl}_3\text{Si}_3\text{O}_{10}(\text{OH})_2$) and the non-crystalline K-aluminosilicate which may itself be original to muscovite [58].

Davidsson et al. [106] reported a significant presence of KAlSi_3O_8 and a small amount of KAlSiO_4 in an ash sample. In their experiment, the ash is sampled from a loop seal of a circulating fluidized-bed boiler firing wood with the kaolin additive. It is still an open issue if KAlSi_3O_8 is possibly derived from capture reactions. The possibility of KAlSi_3O_8 as a capture derived product depends on excess availability of SiO_2 and also on other reaction conditions, including temperature, contact possibility, or available reaction time. The (most) relevant distinction between KAlSi_3O_8 and other K-aluminosilicate (KAlSiO_4 and KAlSi_2O_6) is their melting point. As a pure compound KAlSi_3O_8 melts incongruently above 1150°C . In contrast, other K-aluminosilicate are high melting compounds which need temperatures $> 1500^\circ\text{C}$.

The reaction between fuel ash species and additive mineral (aluminosilicate) is pictured as capture reactions and mainly discussed in a context for gaseous alkali (K/Na) species [104,107]. This reaction is understood as an absorption of gaseous alkali species over the surface of mineral particle followed by chemical reaction by which the cationic part (K/Na) is incorporated irreversibly within the solid aluminosilicate matrix and in the process the salt anionic part (Cl, S, OH) escapes as respective gaseous species. Factors, like the chemical form of the alkali species, their concentration, particle size of the additive, its physical properties (mainly BET surface area), and the reaction temperature, influence the capture rate. Additionally, the fixed bed scenario [104] or the entrained capture scenario [107] influence the capture rate constant derived from these experiments. The main points regarding alkali capture reactions driven by additive are:

- The gaseous alkali species prefer to react or to be captured by aluminosilicate in a reaction system where silica (SiO_2) is abundantly present, for which the thermodynamic favorability is the main driver.
- Alkali-additive capture studies [102,103] which performed experiments with individual salt species note that the kinetics is not a limitation to proceed the capture and mostly remain predictable by equilibrium thermodynamic chemistry.

- Comparatively, KOH is captured more effectively than KCl/K₂SO₄ [102,103,107]. Tran et al. [104] report a similar capture efficiency of KCl and KOH and lower for K₂SO₄. Tran et al. [104] experiments are conducted in a fixed bed capture scenario and at lower temperature of 850 °C. Others [102,103,107] perform in an entrained capture scenario at high temperature between 950 – 1300 °C.

2.4.2 Relation of additive to deposit and corrosion mitigation

The relation of additive to ash deposit mitigation relies on the fact that K-aluminosilicate are stable and refractory, i.e. high melting, compounds in comparison to K-silicates. Figure 5 shows the phase diagram of K₂SiO₃-SiO₂ and KAlSiO₄-SiO₂ systems in relation to temperature and component ratio. The phase diagram clearly shows that the liquidus area is significantly smaller in the KAlSiO₄-SiO₂ system in comparison to the K₂SiO₃-SiO₂ system, see L in Figure 5 (b) and (a), respectively. The liquidus temperature in K-silicate system is as low as 755 °C while in K-aluminosilicate system is 990 °C. K₂Si₂O₅ is most stable as solid K-silicate ($\vartheta_{\text{melt}} \approx 1142$ °C) while KAlSiO₄ is the most stable solid K-aluminosilicate ($\vartheta_{\text{melt}} \approx 1750$ °C).

Increased ash fusion temperature, decreased ash sintering, and easier deposit removability are reported in many biomass-additive comparative studies [58,59,97,108]. Such positive improvement is argued to be related to the promoted formation of K-aluminosilicate [58] and consequently increased fraction of high melting components in the resulting ash system.

The relation of additives to corrosion mitigation relies on the readily absorption of gaseous KCl by aluminosilicate to form K-aluminosilicate. In the process, chlorine is released as HCl. The retention of chlorine in ash/deposit/aerosol (as KCl) is hindered thereby and salt associated corrosion risk will be reduced. The decrease of KCl (chloride salt) as well as the decrease of the water soluble potassium fraction in deposits, ash, and aerosols are confirmed by many biomass-additive comparative studies [59,67]. Note here, K-aluminosilicates are water insoluble while KCl is water soluble.

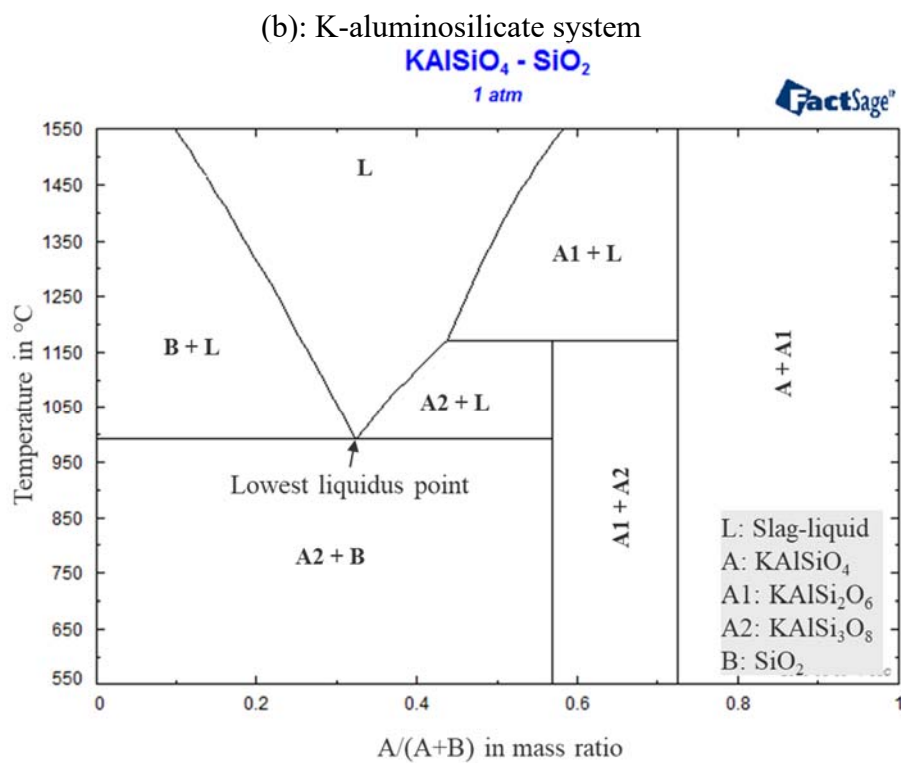
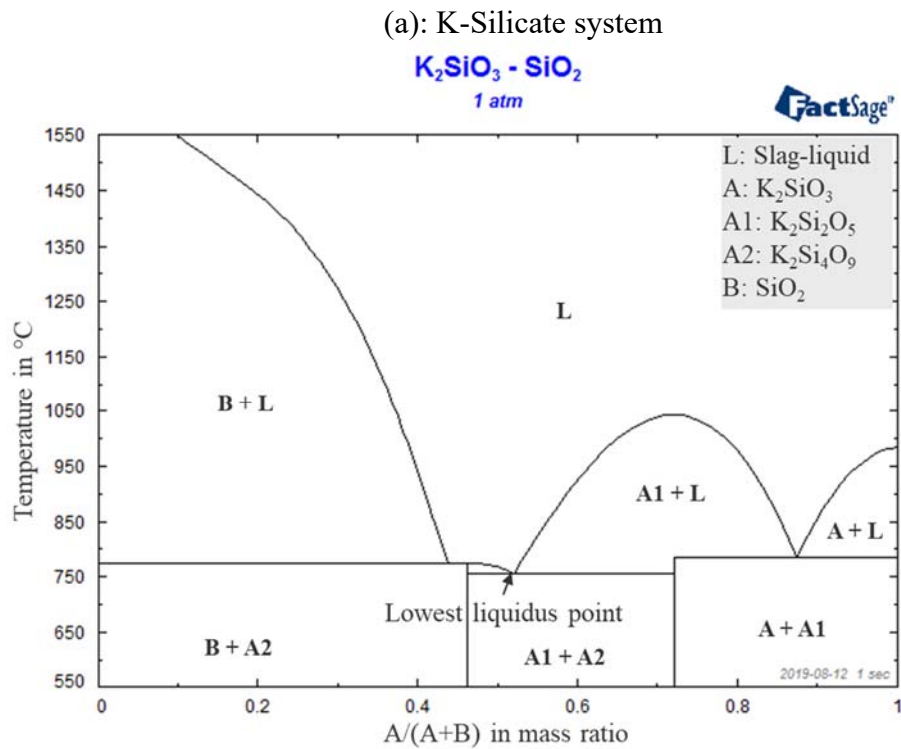


Figure 5: Phase diagram of $K_2SiO_3-SiO_2$ (a) and $KAlSiO_4-SiO_2$ system (b) calculated using FactSage 7.3 Phase diagram module. Note: only the change of the chemical form or phase can be observed in the given phase diagram.

2.4.3 Earlier studies on additive use in biomass boiler

Due to historical preference of firing system and the choice for biomass feedstock, most of the experiences regarding boiler deposition and corrosion with 100 % biomass fuel derives from grate and fluidized firing system. Consequently, earlier additive application experience comes from grate and fluidized combustion systems and fundamental studies in temperature regimes and reaction conditions comparable to these combustion systems.

A relevant study of additive application in grate boilers is published by Madhiyanon et al. [109] and Kubica et al. [110]. For grate boilers, bottom ash sintering along with deposition and corrosion are major ash related concerns. Additive is reported as beneficial to address these ash related problems. The favorable change is explained as a result of alkali-aluminosilicate interaction which changes the ash composition and consequently increases the melting temperature of bottom ash. Increased fraction of high melting aluminosilicate compounds in the bottom ash and decrease in chlorine content in deposit/fly ash are the mitigative benefits associated with the additive.

Relevant studies of additive use in a fluidized biomass boiler are reported by Davidsson et al. [106,111] and Öhman et al. [112]. For fluidized boilers, bed particle agglomeration along with deposition and corrosion are the major ash related concerns. The interaction of volatile alkalis (fuel-ash species) with the bed material (most case silica) is identified as the underlying mechanism of bed agglomeration. The additive is helpful to mitigate bed particle agglomeration. The agglomeration temperature with additive can be held above, in comparison to biomass alone. It is explained as an outcome of preferred alkali-aluminosilicate interaction for high melting compounds over alkali-silica interaction for low melting compounds. In addition, the decrease in chlorine retention in fly ash or deposit is commonly observed in presence of additives.

In comparison to grate and fluidized combustion system, the pulverized combustion system is characterized by finer fuel particle size, higher furnace temperature, and short residence time and entrained reaction conditions. The fly ash loading in pulverized boilers is significantly higher than in grate boilers. Moreover, the fly ash composition significantly differs even for similar fuels among grate and pulverized boilers. Relevant comparative studies with similar fuel are published by Hansen et al. [113] and Bashir et al. [60].

Wu et al. [67] reported the influence of aluminosilicate based additive with straw while Paneru et al. [17] reported the influence of aluminosilicate based additive with wood. Their experi-

ments were performed at an electrically heated combustion test facility simulating the conditions of pulverized boiler conditions. Wu et al. [67] reported lower deposition flux and reduction in amount of water soluble KCl in fly ash/deposit as the positive consequence of additive.

Large scale experience on the topic of ash, deposit, and corrosion with 100 % biomass firing in large scale pulverized combustion system comes from DTU (Denmark) research group and includes the results from series of measurement campaigns conducted at Avedøre Power Plant unit 2 (AVV2) owned by DONG Energy. The fired biomass fuels includes; wood, straw, straw/wood mix [60,65,72] as well as wood with coal fly ash [59]. The coal fly ash (from bituminous coal) is used as an additive. The coal fly ash was directly injected into the boiler at the two highest burner levels. The coal fly ash is reported to contain aluminosilicate species that are able to capture/adsorb the alkali species originating from the fired fuel. The influence of coal fly ash addition on deposition and chlorine retention behavior is reported by Wu et al. [59]. The fired fuel (wood) has ash content of ≈ 1.1 wt.-% (db.) and chlorine content of 0.007 wt.-% (db.). The coal ash as additive is applied ≥ 4 times higher than the ash content in the fired fuel.

2.5 Summary of state of the art and thesis statement

There is more than 100 years of research and thousands of openly accessible literature related to fuel ash and related boiler issues. The earlier focused on coal and is still in continuation. Later the biomass related ash issues came into focus. At utility scale, biomass has been conventionally used in grate and in fluidized boilers. With few exceptions instead of power (electricity), biomass feedstock dedicated utilities mostly function as combined heat and power (CHP) plants and, in some cases, as incinerators for biogenic waste/residues. The choice of the combustion system is related to the physical and chemical inhomogeneity and lower heating values of biomass feedstock. This is historically developed. The biomass firing utilities are more tilted towards heat and operate at lower final steam temperature to comply with the operational problems, especially related to ash, deposition and corrosion.

The pulverized combustion utilities are mostly dedicated for the production of power (electricity). The temperature at the main combustion zone (furnace) is in a range of 1300 – 1500 °C and the final steam conditions are pushed up to super-critical and ultra-super critical level. Replacing coal with biomass in a pulverized boiler without derating existing efficiency is a challenging task. Biomass co-firing research and actual experiences recognize, the major challenges are deposition and corrosion.

The mineral transformation approach cannot fundamentally explain the ash formation chemistry for biomass fuels simply because the ash composition is not representative as proper minerals but as water soluble salts, organically associated inorganic metals and organic mineral/mineraloids. During combustion, the ash-forming inorganic matter present in biomass releases in variety of forms and all phases, gas, liquid and solid. The interactive and individual contributions of these released species drive the ash system chemistry. Among all, potassium species play a leading role irrespective to the type of firing system. The evolution of low melting *silicates* is traced back to the interaction between potassium species and silica (SiO_2). Further, KCl is a well-known corrosive *salt*.

The *silicatic* species are formed by interactive chemistry among potassium, calcium, and silicon species. The formation of silicatic species proceeds mainly within the burning char particle. The silicatic species which remain in molten phase at combustion temperature regime solidifies as amorphous ash particles as the flue gas temperature drops. The quenching along deposition process may not be enough to solidify the droplet thus leaving such particle to have melt induced stickiness. The melt fraction in the impacting ash particle and associated viscosity determine the deposition severity related to such silicatic ash particles.

The potassium in biomass fuel remains as *salt* species like K-chlorides, sulfates, phosphates, and carbonates. The salt species are released in the gas phase during the combustion by vaporization or by decomposition along the combustion stage. The potassium species that are not involved in silicatic species formation escape to the gas phase of which KOH and KCl are the most dominant chemical forms. The gaseous alkali species are transported to heat exchanger surface mainly by diffusion-condensation. The flux of gaseous K-species reaching the heat exchanger surface determines the severity related to fouling. The sulfation predominantly occurs along the diffusion condensation process. The sulfation of KCl (g) is largely limited in relation to biomass ash system chemistry and is eventually deposited as salt (aerosol) particles. This is of uttermost concern because of the high corrosivity associated with it.

The ash related problems to a certain level can be handled by dedicated burner-boiler design and specific boiler material selection to avoid corrosion. Nevertheless, the problem is principally inherent to fuel-ash composition and properties. This is ensured by the ash system chemistry, itself. It is well agreed that potassium species are the lead contributor to either melt induced deposition or chlorine induced corrosion for biomass fuel. Adsorbing alkali (K) species in the aluminosilicate matrix to form high melting and non-corrosive K-aluminosilicate instead

of low melting K-silicate and corrosive KCl is an applicable option to engineer the ash system chemistry itself at its origin.

The mitigative advantage of aluminosilicatic additive is well reported and the underlying chemical mechanism is agreed. The magnitude of the mitigative effect however may differ depending on the combustion system, the additive application scenario or else boundaries, the fired fuel ash composition and content, the additive composition and properties, and the amount of additive (additive loading) in use.

This experimental work tested various biomass fuels and examined the ash related deposition and corrosion behavior in biomass co-firing scenario, biomass mono-firing scenario, and biomass with additive scenario. The experiments were performed in combustion test facility (rig) simulating the conditions of pulverized combustion system. This thesis work has three major objectives:

1. To evaluate and understand the severity of ash related boiler problems, namely deposition and corrosion, in biomass (100 %) fired pulverized combustion systems.
2. To demonstrate the mitigation effect of additive with respect to deposition and corrosion.
3. To evaluate the optimum additive amount corresponding to given biomass fuel and additive.

2.5.1 Part of work already published

Parts of results shown in this thesis have already been published in a journal and presented at conferences by the author of this thesis which is clarified below.

Journal publication [17]: The results presented in section 4.4.1.1.1-2 are part from this publication. In this work the main author planned the experiment, evaluated the results and scientifically derived conclusion from it. The paper has been prepared by the author, documented and submitted.

Conference paper [114]: The results related to torrefied straw presented in section 4.4.1.2.3 are part from this conference paper. In this work the main author planned the experiment. The evaluation of results and the scientific conclusion presented in the conference paper were prepared by the author.

3 Materials and Methods

3.1 Combustion test facility

3.1.1 Pilot scale combustion test rig (KSVA)

Figure 6 shows the schematic outline of the combustion test facility at the Institute of Combustion and Power Plant Technology (IFK), located at the University of Stuttgart in Stuttgart, Germany. It is a down fired atmospheric pulverized fuel combustion test facility that is extensively used for pilot scale testing. In this thesis, hereafter the test facility is simply referred as, pilot scale facility. The pilot scale facility is optimized for investigation of pulverized fuel combustion process. The upper section of the combustion chamber simulates the furnace zone and below the boiler zone with regard to temperature and residence time. It also simulates the flue gas side of a power plant including different ash separation units, namely Air Pre-Heater (APH) ash, Electrostatic Precipitator (ESP) ash, and Bag Filter (BF) ash. For the combustion test relevant to this thesis, the Selective Catalytic Reduction (SCR) unit was kept in bypass.

The combustion air is provided by a Force Draught (FD) fan while Induced Draught (ID) fan insures the transport of the flue gas through the flue gas duct towards the stack.

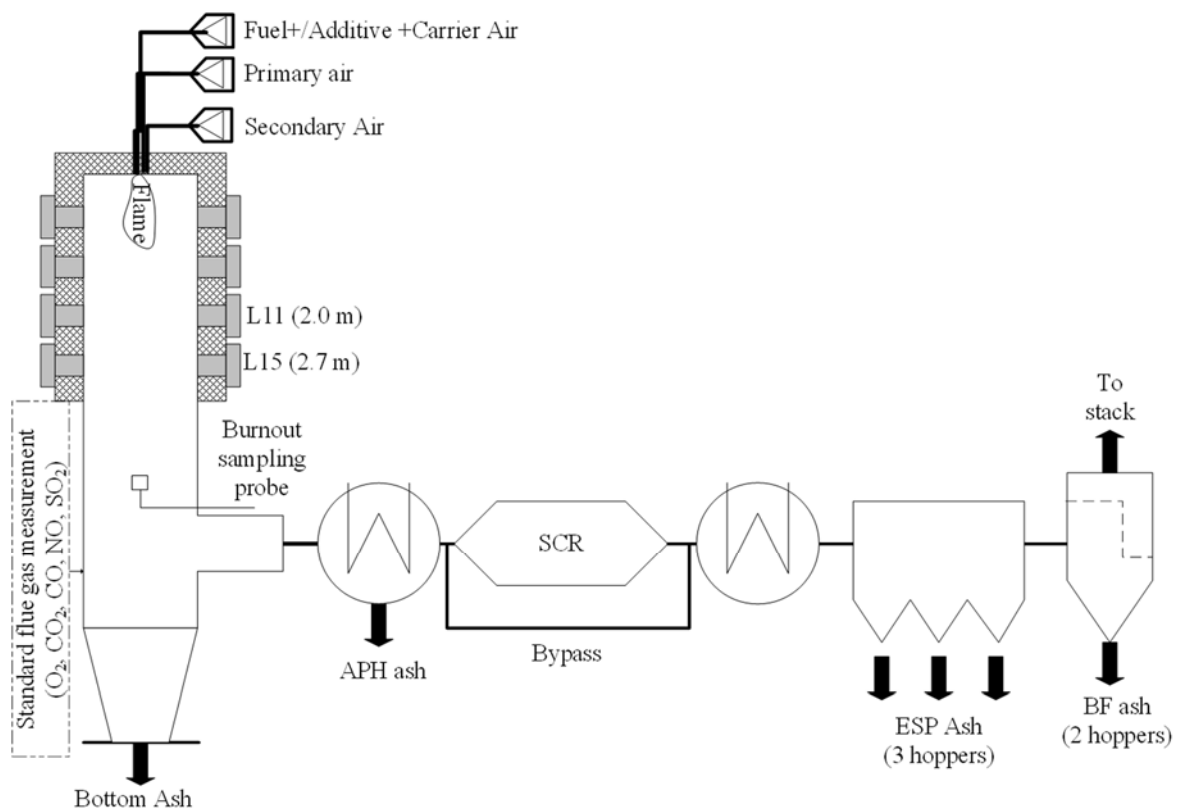


Figure 6: Schematic outline of pilot-scale combustion test facility.

The vertical combustion chamber consists of six cylindrical segments. It has a total length of 7 m and an inner diameter of 0.8 m. The refractory lining covers the inner surface of the upper 4 m of the combustion chamber. The remaining section below is water cooled. Numerous measurement openings are integrated into the wall of combustion chamber each at a level between 0.15 to 0.17 m. In some segments three ports per level are integrated to the wall, shifted by 90° to one another.

The fuel feeding rate was gravimetrically controlled by a dosing system. An individual dosing system was employed for coal, biomass, and additive. The fuel and additive transport to the burner was ensured pneumatically. Corresponding to co-firing and independently fed additive case, the mixing occurs along the fuel transport line prior to burner injection.

During the experiments, the combustion was continuously monitored at the end of the combustion chamber. The burnout, fly ash (FA) samples were collected by a suction probe later to evaluate and compare the combustion efficiency across different cases. This sampling location at the end of the combustion chamber is hereafter referred to as L27 (5.5 m down) and the burnout fly ash sample is referred as FA_L27.

The deposit sampling probes were implemented from a port referred as L11 (2.0 m down the burner) and L15 (2.7 m down the burner).

The short name index of test sets, combustion cases, and firing sets corresponding to experiments in pilot scale facility (KSVA) are listed in Table 9. Each test set refers to one measurement campaign. The firing set is a general grouping of the individual test cases with respect to type of fuel, fuel mix, or additive in the mix. The combustion case refers to the fuel or fuel-mix and represents each individual test as reported in the result and discussion section later. Each test set is briefly described below.

Test set A: The experiments include biomass co-firing cases. The Columbian bituminous coal was the reference coal and the straw (cereal/mixed straw feed stock) was the co-fired biomass. Each combustion case runs more than 8 h. The measurement program includes online deposition sensor (ODS) for the deposition rate measurements, deposit probe exposures (cooled and uncooled), FA sampling, flue gas/temperature profile measurement, heat flux measurements, ash balance, hopper ash sampling, continuous standard flue gas measurements, and Fourier-Transform Infrared Spectroscopy (FTIR). This thesis includes the results corresponding to ODS (deposit rate) measurements. Reference to other measurements are reported when necessary.

Table 9: Short name index of experiments performed in pilot scale facility (KSVA).

Test set	Combustion case	Firing set	Remark
A	EC	Coal	100 % Columbian bituminous coal
	25S	Biomass co-firing	25 % thermal share of straw + 75 % thermal share of coal (mixed at burner)
	40S		40 % thermal share of straw + 60 % thermal share of coal (mixed at burner)
	60S		60 % thermal share of straw + 40 % thermal share of coal (mixed at burner)
	S		100 % thermal share of straw
B	M	Biomass mono-firing	100 % Miscanthus
	W		100 % Wood
	M+W		50 % Miscanthus + 50 % Wood (premixed during milling)
	M+B	Biomass with (w/) additive	Miscanthus + Additive B-independently fed during test
S+D	Straw + Additive D-pre-mixed		
C	S		Straw without additive Reference mono-firing case

Test set B: The experiments include biomass mono-firing cases and a biomass with additive case. The wood, miscanthus, and a mix of both (50/50) were the fired biomass fuels. It also includes the miscanthus case with additive. The additive was fed independently. Each combustion case runs more than 8 h. The measurement program was set up similar to test set A. This thesis includes the results corresponding to ODS (deposit rate) and deposit/FA samples. References to other measurements are reported when necessary.

Test set C: The experiments include biomass mono firing and biomass with additive cases. Straw was the fired biomass fuel. The additive was premixed with straw (fuel as received). The straw mono-firing case (S) in test set C has different fuel feeding rate and combustion air than

straw mono firing case (S) in test set A (see Table 17). The straw mono firing case (S) in test set C is a comparative reference to corresponding case with additive (S+D) within the same test set. This thesis includes the results corresponding to deposit/FA samples. Reference to other measurements are reported when necessary.

3.1.2 Electrically heated combustion test rig (BTS-VR)

Figure 7 shows the schematic outline of the electrically heated combustion test facility at the IFK, located at the University of Stuttgart in Stuttgart, Germany. The functionality is similar to a drop tube furnace. It simulates an entrained down-fired pulverized combustion scenario but with the temperature profile maintained by external electrical heating.

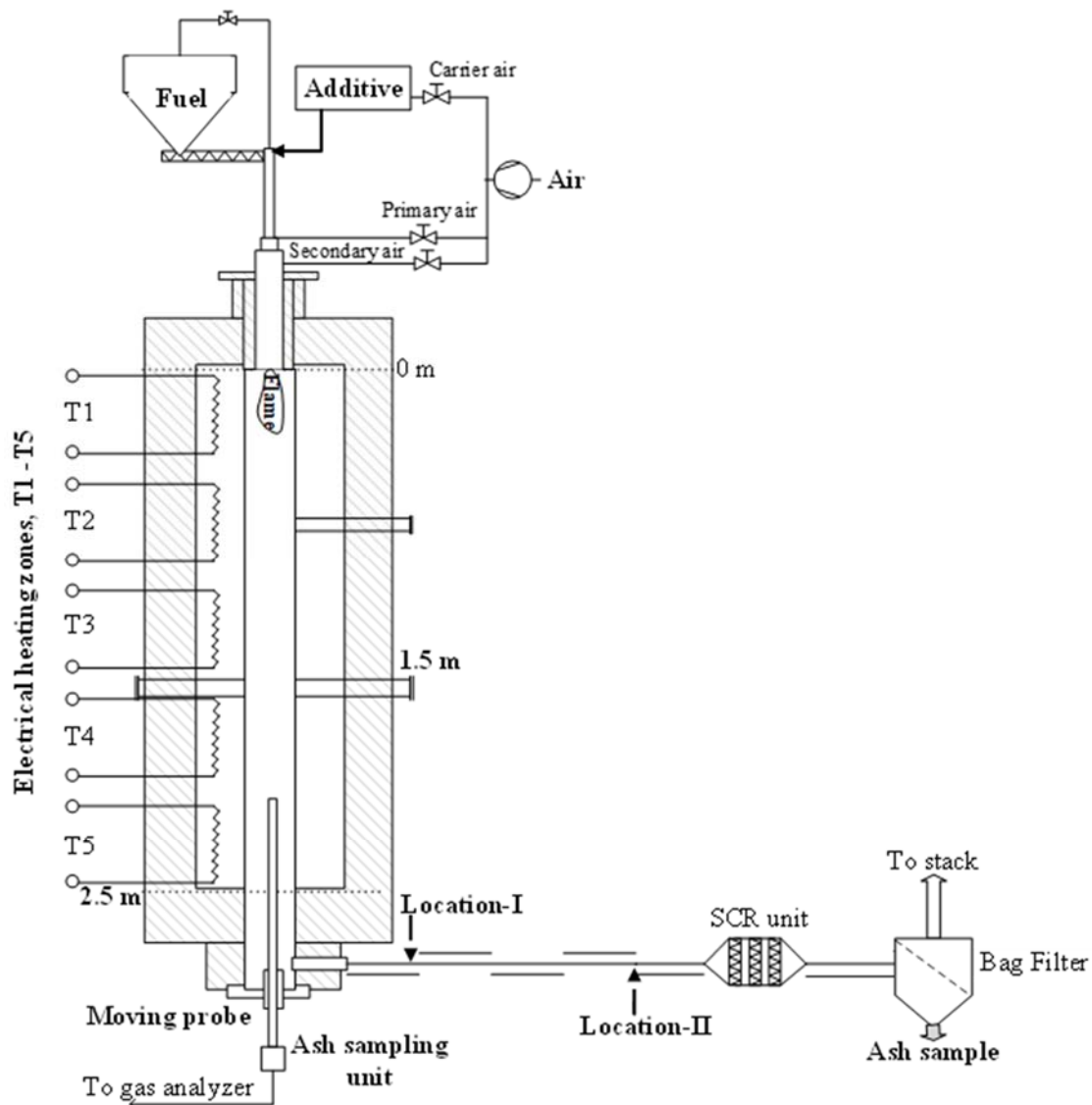


Figure 7: Schematic outline of electrically heated combustion test facility (BTS-VR)

The vertical ceramic tube functions as combustion chamber embossed to maintain the wall temperature up to 1300 °C. The ceramic tube is 2.5 m long and of 0.2 m inner diameter. There are later excess ports to the inside of the ceramic tube at 0.9 m and 1.5 m which facilities to introduce the sampling/measurement probes. A vertical moving probe can be introduced inside the ceramic tube at the desired location to extract fuel gas, FA, or char samples. The temperature of the vertical probe was maintained ≥ 180 °C by oil cooling.

The experiments in the electrically heated facility consist of tests with biomass fuel as well as with additive. The fuel and additive were fed together to the system through the top mounted burner. The combustion air was divided as carrier air, primary and secondary air. At the end of the combustion chamber the flue gas was directed to the flue gas duct (heated and insulated) by the suction (ID fan) which operates from the end of the flue gas duct (after filter).

There are various access ports along the flue gas duct which facilitate to extract flue gas from different locations. The location-I, outside the combustion chamber and location-II, before the SCR unit, are relevant measurement locations, later discussed in this thesis.

Table 10: Short name index of experiments performed in BTS-VR.

Test set	Combustion case	Remark
A	W	Wood (without additive)
	W + C	Wood with additive (pre-mixed)
B	TS+ A TS + B TS + D	Torrefied straw (TS) with variable loading of different additive
C	TS + A *W + A	Torrefied straw (TS) and KCl doped wood (*W) with variable loading of given additive
D	S	Straw combustion (without additive)

Table 10 summarizes the test set and combustion cases conducted in BTS-VR. Each test set is briefly discussed below.

Test set A: The combustion case includes wood and wood pre-mixed with additive. This thesis includes the results corresponding to deposit samples. Reference to other measurements are reported when necessary.

Test set B: The combustion case includes torrefied straw and with additive cases. Three different additive types are tested and each was independently varied while the fuel fed was constant.

This thesis mainly includes the results corresponding to HCl (FTIR) measurements. Reference to other measurements are reported when necessary.

Test set C: The combustion case includes torrefied straw and wood (doped with KCl) with additive variation. This thesis includes the results corresponding to HCl (FTIR) measurements. Reference to other measurements are reported when necessary.

Test set D: The combustion case includes straw. This test set did not include additive. This thesis includes the result corresponding to FA samples and HCl (FTIR) measurements obtained from different locations inside the combustion chamber.

3.1.2.1 Fuel and additive feeding system

The pulverized fuel ($< 500 \mu\text{m}$) was fed from the hopper by a screw feeder. Corresponding to each fuel, a feeding curve was generated. Figure 8 (a) shows a typical calibration curve (as example) of the fuel-feeding unit. The amount of fuel-fed was constant for any given test case. The fuel feeding rate was chosen in range of 1 – 2 kg/h depending on the fired fuel. The additive was supplied by a dust disperser system (SAG-Solid Aerosol Generator [115]).

The system comprised of two steps: the rotating toothed belt brings the powder (additive) and the amount of powder in the gap of each tooth gap is sucked and removed from the belt by the injector nozzle. From the nozzle the powder is transported to the point in the fuel feeding system (outlet of screw) where it is mixed with the fuel and transported together to the burner. The air supply to the injector nozzle also functions as the carrier air for the mix of fuel and additive. The feeding arrangement gives a possibility to change the additive amount of choice without changing the total air fed to the system, set for a certain air-fuel ratio of choice.

The amount of additive was independently varied during the test. For a given case the additive amount is here defined as additive loading (in %) according to Eq. 3.1. Proper metering of additive fed to the system was important for the experiments. The amount of additive dispersed by the injector nozzle was varied by the belt speed. The speed can be conveniently varied in the feeder control unit in desired steps as % of allowable (max) belt speed. The additive feeding unit was kept over a scale connected to the computer and the mass loss over a feeding duration was recorded continuously, every second.

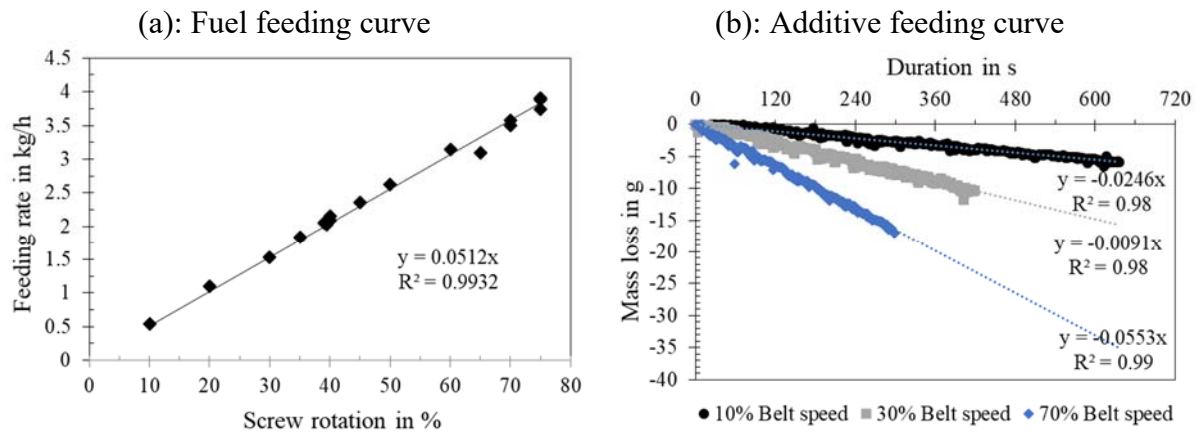


Figure 8: (a) Typical calibration curve of fuel-feeding unit (b) Typical mass loss curve of additive feeding unit.

Figure 8 (b) shows a typical mass loss curve corresponding to various belt speed. From the mass loss, the corresponding additive feed rate was derived. For each additive case, feed rate corresponds to an individual mass loss curve, recorded during the respective test run. A smaller unit (max. air to injector 1 - 1.5 m³/h) was employed in BTS-VR and a larger unit (max. air to injector 10 – 15 m³/h) in KSVA.

$$\text{Additive loading} = \frac{\dot{M}_{\text{additive}}}{\dot{M}_{\text{fuel}}} \cdot 100 \quad (3.1)$$

3.2 Deposit sampling probes and flue gas measurement device

3.2.1 Deposit probes

Two kinds of probe were used to sample the deposit ash. The deposit probes were categorized as uncooled deposit probe and cooled deposit probe according to their functionality.

- **Uncooled deposit probe:** The uncooled deposit probe samples ash over a ceramic tube surface. The temperature of the ceramic tube surface remains in equilibrium with the exposure surrounding. The accumulation of ash over the ceramic tube surface is driven by internal impaction and is considered to represent a deposit scenario when the temperature of a boiler (tube) heat exchanger deposit front approaches the temperature of the surrounding flue gas. Such deposit is hereafter referred as outer deposit (OD).
- **Cooled deposit probe:** The cooled deposit probe samples the ash over a metal (alloy) tube surface. A piece cut or rings of actual/candidate boiler tubes is mounted at the head of the probe. The temperature of the metal tube ring surface is maintained at the desired level with pressurized air as cooling media. The thermocouple is attached to the tube ring from inside which feeds the desired set temperature to the control loop. This regulates the flow of cooling media. Once the probe is exposed inside the combustion chamber, the desired temperature is set and regularly checked. The accumulation of ash over the ceramic surface is driven by diffusion-condensation, thermophoresis and by inertial impaction and is considered to represent a deposit scenario over a boiler (tube) heat exchanger surface. Such deposit is hereafter referred to as inner deposit (ID).

After successful exposure, both probes were extracted from the combustion chamber. The surface of the probe with the deposit ash was carefully embedded and further prepared for EMPA analysis. The morphology and composition of deposit ash were evaluated from such samples. The metal (alloy) cross-section beneath the ‘inner deposit’ were the samples to evaluate corrosion. This sampling, post sample preparation and evaluation method was extensively used/discussed by previous researchers at IFK and is a method widely used for deposit [96] and corrosion [116] studies.

An online deposition sensor (ODS) developed in-house in IFK and patented by Babat et al. [117] was used for quantification of ash accumulation. The sensor is able to continuously measure and record the amount of ash accumulated over a ceramic tube surface.

The ODS system consists of a metal housing in which a strain gauge load cell is mounted. The metal housing is air cooled to avoid overheating of the sensor. The load cell is basically a deformation element with strain gauges glued upon it. These strain gauges change their electrical resistance depending on the material strain.

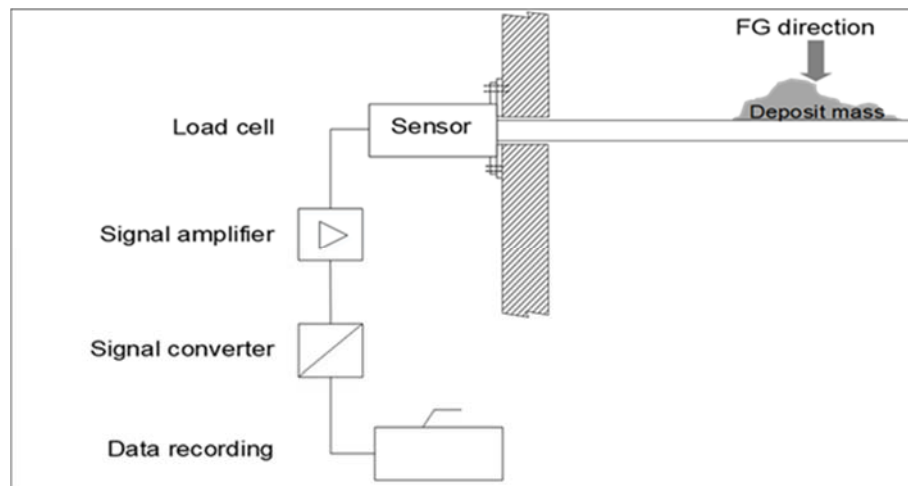


Figure 9: Schematic outline of online deposition sensor (ODS).

A ceramic tube is connected to the load cell at the other end. The forces that are acting on the probe, the deposition weight and the flow forces, cause the elongation of the strain gauge. The electrical resistance changes as a function of the elongation. The sensor output as weight of the exposed probe is continuously recorded over time. The ODS system is able to record the mass difference of 0.1 g and gives an output every second.

The ODS system was implemented during the combustion test performed at KSVA. The sensor output is the cumulative mass over the ceramic tube surface at a given time. The deposit bulk also serves as OD sample for the corresponding exposure case.

3.2.2 Flue gas measurement device

The flue gas was extracted from different locations inside the combustion chamber or along the flue gas duct. The flue gas was filtered for ash and aerosol separation and dried before analysis. Table 11 summarizes the standard measurement technique and analyzers used for fuel gas measurements.

Table 11: Equipment's and method for flue gas analysis.

Component	Measurement technique	Manufacturer
O ₂	Paramagnetism	ABB EL 3020
CO ₂	NDIR	ABB EL 3020
CO	NDIR	Siemens/Ultramat 23
NO _x	Chemiluminescence	ECO physis
SO ₂	NDIR	Siemens/Ultramat 23
HCl	FTIR	Gasmet/Ansyco

The HCl in flue gas was one of the major concerns for this thesis. The device used in this study was a Gasmet DX4000 portable FTIR gas analyzer [118]. The measurement unit as a whole consists of Gasmet DX4000, a portable sampling system with heated filter head and transport lines that bring sample gas to the FTIR measuring cell and a laptop equipped with Calcmet software from Ansyco for concentration quantification out of the measured spectrum.

When the infra-red radiation passes through the sample a gas, certain amount of radiation is adsorbed, and a certain amount is transmitted. The Lambert-Beer law (see Eq. 3.2) describes the quantitative relationship between the absorption and the concentration of a gas [119].

$$A_{\lambda} = \varepsilon_{\lambda} \cdot b \cdot C \quad (3.2)$$

Where,

A_{λ} : absorbance at specific wavelength

ε_{λ} : absorption coefficient at given wavelength

b : path length through the sample

C : concentration of the absorbing material

For a given measurement system, the path length (b) and for a given molecule at given wavelength the absorption (ε_{λ}) coefficient is constant. Both variables combine into a single constant (K_{λ}). Thus by measuring the absorbance of an unknown molecule in appropriate wavelength the concentration of a given gas molecule derives by Eq. 3.3.

$$C = \frac{A_{\lambda}}{K_{\lambda}} \quad (3.3)$$

Table 12: Flue gas components and recommended infrared wave number (cm^{-1}) analytical range.

Components	Analyzing area
H ₂ O	3200-3401
CO ₂	910-1150
	2000-2250
CO	2000-2222
	2540-2590
NO	1875-2138
NO ₂	2700-2950
SO ₂	1050-1250
	1220-1366
HCl	2440-2542
	2856-2879

The quantification process is automated by the Calcmet software [119]. The user provides following inputs:

- A sample gas spectrum,
- A background spectrum corresponding to a N₂ filled measurement chamber which is compared with the sample spectrum to determine the percent transmittance of each frequency, thus removes any spectral features common to the background, and
- The spectral range of each component of interest and the reference calibration spectrum.

The library of Calcmet Software includes the reference spectrum of gas components at various concentration.

Theoretically, beside diatomic molecules, like O₂ or N₂, all gaseous components could be detected by the measurement cell.

Table 12 shows the list of gas components included for FTIR analysis. The chosen fuel gas components represents the major species present in the flue gas. A fraction of sample gas was directed to an O₂ analyzer to measure the corresponding O₂ concentration.

The concentration of components could be influenced by the user choice. To avoid this, the choice was selected as recommended or as default by the Calcmet software. The same setting was applied for all analysis with the background generated at regular intervals which is performed for most cases before each test run. The components of interest were standard flue gas

species therefore profound measurement experience is available with FTIR analyzer. Within the software recommended settings, the measured concentration is expected to be reliable.

3.3 Fuel, fly ash, and deposit ash analysis

Fuel, FA, and deposit were analyzed according to standard analysis method by the in-house lab at IFK. The DIN EN ISO standard corresponding to the analysis are listed in Table 13.

Table 13: Standard analysis method for fuel/fly ash/deposit ash.

Analysis	Component	Standard (DIN EN ISO)
Proximate	Water, Ash and Volatiles	18134-3, 18122 and 18123
Ultimate	C, H, N	16948
Sulfur and Chlorine	S and Cl	16994
Major ash elements	Al, Ca, Fe, Mg, P, K, Si, Na, Ti	16967
Ash fusion test	IDT, DT and FT	ISO/CD 21404

The ash elements can either be determined directly from the fuel sample specimen or the fuel sample specimen can be first ashed at 550 °C. For most fuel analysis, the ash elements were determined from the fuel sample itself without pre-ashing. The element concentration as mg/kg in the fuel sample is mathematically converted to ash oxides as % in reference to the ash content in the given fuel. For FA and deposit samples, a direct analysis without pre-ashing from the sample itself follows. In case of an ash fusion test, the sample specimen was first ashed at 550 °C to avoid interference from the unburnt samples also for FA and deposit samples.

3.3.1 Electron Microprobe Analysis (EMPA)

The ID and OD samples were subjected to EMPA analysis. Each deposit sample is later identified as ID or OD_XX where XX denotes the sampling location. The EMPA requires sample preparation prior to analysis. It includes cutting a piece out of the probe, embedding the cut piece with epoxy in a desired shape and size, further grinding, and polishing the surface. To avoid the loss of soluble ash species, especially chlorides, mainly for the ID samples, the pre-preparation process was done water free.

Two different EMPA systems were used in this work:

1. System equipped with SEM and Energy-dispersive X-ray Spectroscopy (EDS).
2. System equipped with SEM and Wavelength Dispersive Spectroscopy (WDS).

The choice depends on the availability of the system, cost, and time requirements for analysis. The EDS mapping is faster and cheaper and considered to be adequate to provide the required information for this work.

Both systems work on a similar fundamental analysis principals [120]. The data derived from EMPA analysis are Back-Scattered Electron (BSE) images (micro graph), element maps (micro graph), and point analysis (composition as oxide in wt.- %).

- BSE image: The primary electron beams hitting the sample surface in vacuum are scattered by near surface atoms. The atoms with higher average atomic weight scatter back with a higher signal intensity. Additionally, depending on surface topography, the electron scatter in different directions. The detector placed at the appropriate position detects these signals and with the surface scanned in a raster pattern, the position of beam and intensity is combined to generate a BSE image (Gray scale micro graph) corresponding to the scanned sample surface cross-section. The gray scale of BSE image gives information as an average composition of all elements present in the sample (scanned area) but does not distinguish between elements.
- Element map: An element map shows the spatial distribution of elements in the sample. Element maps are generated by EMPA analysis technics, EDS or WDS. The main difference between EDS and WDS analysis technic is that for EDS a single detector is employed while for WDS various detectors are used, each specific to certain wavelength of X-ray radiation. With different detectors specific to certain wavelength range the resolution and accuracy is better with WDS system. The element map corresponding to samples acquired from pilot scale combustion test uses an EMPA system equipped with EDS while the element map corresponding to sample acquired from the electrically heated combustion system uses EMPA system equipped with WDS.
- Point analysis: The principle is similar to the generation of an element map. Instead of the element distribution as semi-quantitative way in textural context, the point analysis refers to the quantified chemical composition of a certain area or point of choice. The chemical composition is determined by the peak-height ratio relative to the standard with the help of software and is presented as oxides (normalized).

The micrograph EMPA generated data were generated at different magnification. For each magnification a scale in μm is automatically generated. The general procedures followed for each sample under observation were:

-
1. The generation of multiple BSE images of the sample area showing the sampling surface and the deposit/ash,
 2. The generation of multiple magnified BSE images of a selected area, i.e. sampling surface or deposit/ash,
 3. The generation of element maps corresponding to a selected area, and
 4. The marking of selected points or areas in BSE images for point analysis to generate the chemical composition of characteristic particle/phase.

Figure 10 shows various micro graphs generated from EMPA corresponding to outer deposit samples as an example sequence. From OD samples, the evaluation of the morphology and composition of deposit ash is the basic objective.

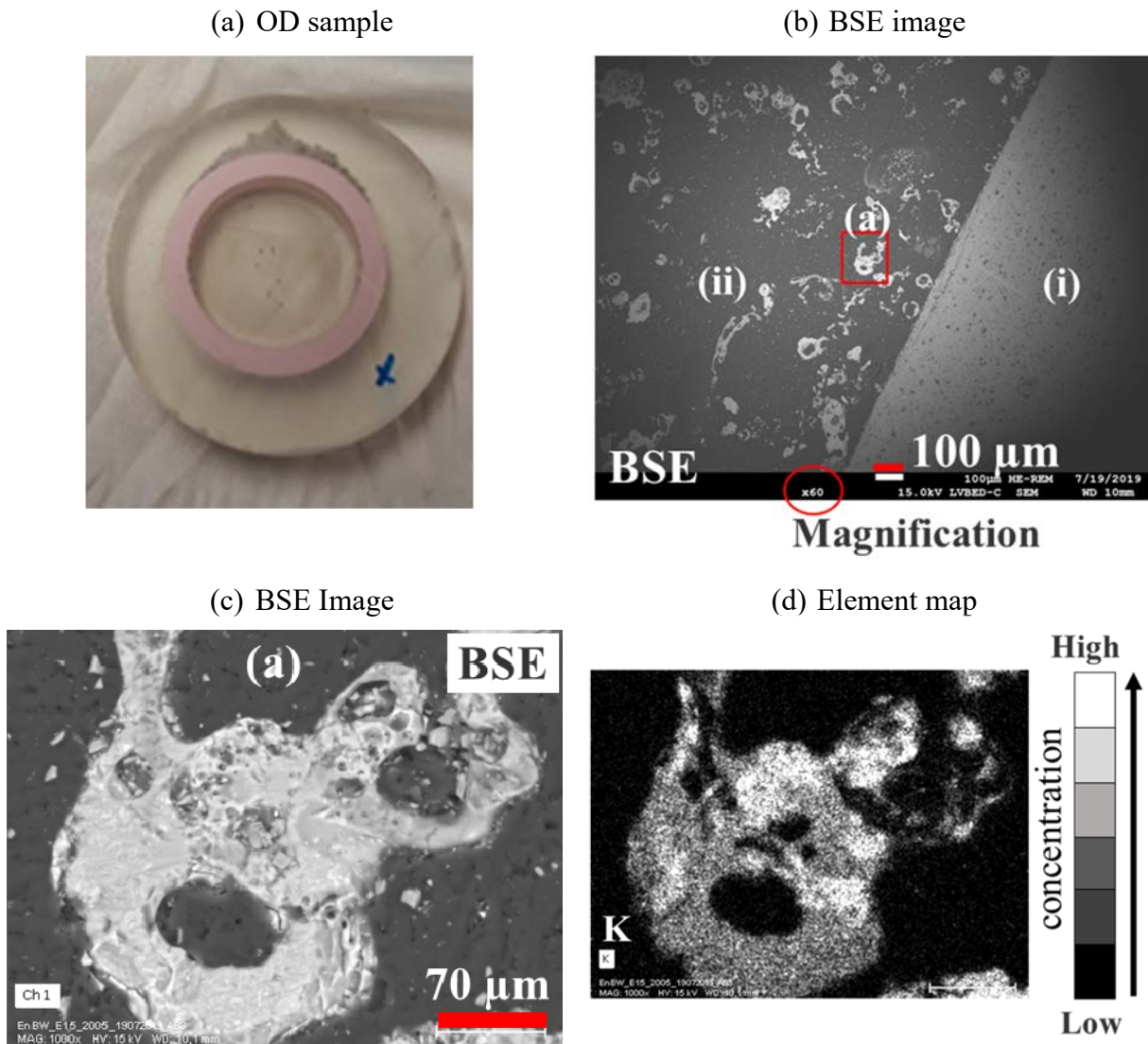


Figure 10: Example sequence of data (micro graph) generated from EMPA corresponding to outer deposit (OD) sample. (a) OD sample, ceramic probe section (b) BSE image: (i) area showing sampling ceramic surface (ii) area showing ash deposit. (c) BSE image: magnified BSE image of selected area (a) and (d) Element map.

Figure 11 shows various micro graphs generated from EMPA corresponding to ID as an example sequence. From ID samples, the evaluation of the morphology and composition of the deposit ash and of the sample (alloy metal) surface is the basic focus. A clear demarcation between oxide scale and inner deposit ash species does not exist in many cases. The evaluation methodology followed across different micro graphs adapted for the purpose of this thesis is further clarified, specifically for ID, in the result and discussion section (see section 4.3.1.4.1).

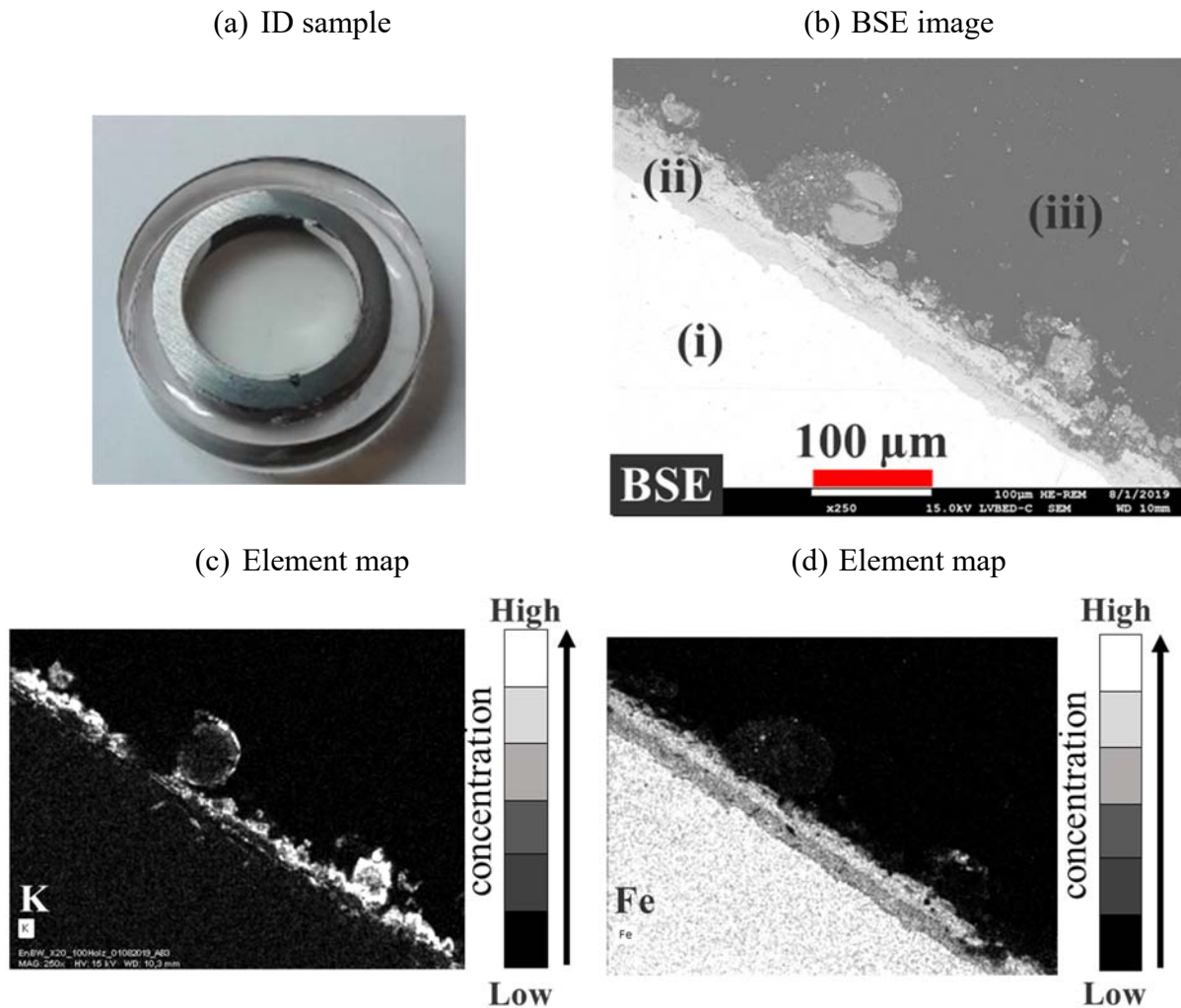


Figure 11: Example sequence of data (Micro graph) generated from EMPA corresponding to inner deposit (ID) sample. (a) ID sample, metal probe section (b) BSE image: (i) area showing sampling metal surface (ii) area showing oxide scale (iii) area showing ash deposit particle/phases. (c) Element map: as example K element map (deposit ash relevant element) and (d) Element map: as example Fe element map (alloy material relevant element).

The visual quality of a micro graph is influenced by the quality of the sample surface polishing and the optical conditions, such as focus, brightness, and magnification, during its capture. Such

parameters vary from one sample or area under observation to another. The same holds for the visual quality of the given BSE images. Therefore, a comparison between different samples should be performed carefully.

3.4 FactSage Software and Database

The thermodynamic database and software FactSage 7.3 was used for equilibrium calculation. The FactSage database contains parameters for the Gibbs energy calculation of various compounds and solutions as a function of temperature and pressure. For the given set of input, the software calculates the equilibrium output (i.e. compound and/or solution and their state, gas, liquid and solid) by minimizing the total Gibbs energy of the system. Further information on the principle, functionality and database in FactSage is found in Bale et al. [121] and its applicability as a tool to understand and evaluate biomass ash system chemistry is found in Lindberg et al. [122].

In this thesis, the equilibrium calculation was performed corresponding to the composition of ash particles found in deposit to evaluate their molten history (in section 4.4.1.1.3) and corresponding to given fuel composition with various amount of kaolinite to evaluate the influence of additive loading (in section 4.4.1.2.4-5). The equilibrium results for each run were extracted as excel file and further evaluation graphs of interest were prepared.

The boundaries for a given equilibrium calculation, or run, are listed as follows:

- All equilibrium calculations were performed at 1 atm pressure. Depending upon the case, the temperature or the input of a certain component was varied. The objective of variation and the input varied are reported in the section where the equilibrium output results are discussed.
- FactPS, FTOxide, and FTsalt were the databases chosen for the thermodynamic equilibrium calculation. FactSage contains two different kinds of database groups, namely (i) the COMPOUND database for stoichiometric compounds of a fixed composition and the (ii) SOLUTION database for liquid and/or solid solution.
- For gas and solid species, the COMPOUND database was used. For liquid species the SOLUTION database was used namely, Slag liquid A from the FTOxide database and Salt liquid F from the FTsalt database. The slag liquid solution is a mixture of various metal oxides while Salt liquid F is a mixture of various alkali salts. Additionally, 'Mullite' from FTOxide database was used. 'Mullite' is the solid solution of aluminosilicate compounds.

The choice of the database, especially SOLUTION, impacts the equilibrium output. The database choice employed in this work represents the general database choice considered suitable to evaluate biomass ash chemistry [122]. Additionally, the following arguments are primal for the made choice:

- Slag Liquid A: Such a liquid solution is representative to the silicatic slag composition relevant to the biomass ash system chemistry.
- Salt liquid F: Such a liquid solution is representative to alkali salt eutectics relevant to biomass ash system chemistry.
- Mullite: Such a solid solution is representative to the aluminosilicate from kaolinite (additive mineral).

4 Results and Discussion

4.1 Characterization of test fuels

During the study duration, fuel samples from the same batch or supply were analyzed multiple times. The fuel samples which are sent to the lab include pellets, milled (< 1 mm), and sieved (< 0.5 mm) samples. A certain variation is observed from one analysis to other. These variations are mostly random. The sample storage time in the fields (in source) and in the fuel storage (below roof/open) influence the amount of moisture and water soluble ash species. Additionally, the fuel sample form (pellet, milled and sieved) could also contribute to these variations. The values are presented as a range, including minimum-maximum. The fuel composition/properties relevant to this study are presented here. The ash content, ash oxides (K_2O , CaO , P_2O_5 , SiO_2 and Al_2O_3), and ash fusion temperature are most relevant for this study. Further the chlorine (Cl) and sulfur (S) content in the fuel is of interest. Table 14 shows the composition or properties obtained from standard fuel analysis of different biomass fuels used during this study. The complete standard analysis is organized in Annex 1 (see section 7.1). When necessary, the values corresponding to the fired fuel are reported and they refer to the fuel sample taken corresponding to the combustion case (from feeding hopper).

The fuels are grouped according to biomass source group, i.e. Woody biomass (W) and herbaceous biomass, including Straw (S), Miscanthus (M), and Torrefied straw (TS). The non-treated straw (S) and torrefied straw (TS) are acquired from different suppliers and feedstock sources. Between them, only a general comparison is valid.

Corresponding to standard fuel analysis, the following general observations are made:

- Sulfur and Chlorine: In general, biomass fuels are characterized by a low sulfur content, either woody or herbaceous. Woody fuels are chlorine lean compared to herbaceous fuels. Among the test fuels, straw (S) shows the highest amount, up to 0.34 wt.-%, daf. The amount of chlorine varies by 2 – 3 times between the same herbaceous feedstock groups.
- Calcium and Potassium: The woody biomass fuels are characterized by higher CaO content while the herbaceous biomass is characterized by higher K_2O content. Despite of variations, $CaO > K_2O$ in wood and in herbaceous biomass mostly $CaO < K_2O$.
- Phosphorous: The amount of P_2O_5 in woody biomass is lower in comparison to herbaceous fuels. In miscanthus (M) P_2O_5 is 2 – 3 times higher than in straw (S, TS).

Table 14: Properties of test fuels.

Source group	Woody	Herbaceous		
Feedstock source	Saw dust/Mix wood	Cereal straw/mixed	Wheat straw	Energy crop
Fuel Name	Wood (W)	Straw (S)	Torrefied Straw (TS)	Miscanthus (M)
H_u [MJ/kg, an]	16 – 17	14 – 15	16 – 17	16 – 17
Proximate analysis				
γ_{H_2O} [wt.-%, an]	6 – 8	5 – 10	7 – 10	6 – 8
γ_{Ash} [wt.-%, db.]	1 – 3	10 – 13	4 – 6	2 – 3
$\gamma_{Volatiles}$ [wt.-%, daf.]	79 – 81	79 – 81	75 – 76	80 – 81
Ultimate analysis [wt.-%, daf.]				
γ_C	50 – 52	49 – 51	52 – 54	49 – 50
γ_H	5 – 6	6 – 7	5 – 6	6 – 7
γ_N	0.02 – 0.63	0.91 – 1.44	0.52 – 0.67	0.26 – 0.36
γ_S	0.01 – 0.09	0.09 – 0.18	0.09 – 0.11	0.06 – 0.08
γ_{Cl}	0.02 – 0.03	0.16 – 0.34	0.05 – 0.10	0.03 – 0.09
Ash oxides [wt.-%, db.]				
X_{K_2O}	6 – 14	10 – 19	17 – 26	17 – 28
X_{CaO}	13 – 30	9 – 13	17 – 20	8 – 10
$X_{P_2O_5}$	2 – 3	2 – 4	2 – 3	7 – 9
X_{SiO_2}	28 – 61	50 – 66	40 – 49	48 – 58
$X_{Al_2O_3}$	1 – 9	4 – 6	1 – 2	1 – 3
As analyzed $\Sigma\gamma_i$, Ash oxides, db.	Approx. ≥ 80	Approx. ≥ 90	Approx. ≥ 90	Approx. ≥ 90
Ash fusion temperatures				
ϑ_{IDT} [°C]	960 – 1170	700 – 740	720 – 780	700 – 790
ϑ_{DT} [°C]	1170 – 1250	1070 – 1130	840	830 – 920
ϑ_{FT} [°C]	1190 – 1300	1240 – 1300	1160	1260 – 1310

- Silicon: SiO₂ is the most abundant ash oxide, in general. The absolute amounts vary the most compared to other ash oxides. Most of SiO₂ in biomass fuel are soil originated. The supply chain practices from field to fuel influence the extent of external impurities. In woody fuels which are dominated by stem parts, the amount of CaO may exceed SiO₂ as individual ash oxide. In general, it is considered that the fraction of SiO₂ inherent to plant tissues (accumulated during growth) is higher in herbaceous feedstock than in woody feedstock [12,29].
- Ash fusion temperatures: The ash fusion temperatures of herbaceous fuels are significantly lower in comparison of woody fuels. The conventional understanding is that the deformation temperature (DT) represents the start of the recognizable melting of the test ash sample bulk. Others suggest the actual melting initiating well before DT. The initial deformation temperature (IDT) of herbaceous biomass is significantly low, 700 – 800 °C.

4.1.1 Compositional ratio relevant to deposition and corrosion

The biomass ash is characterized by lower ash fusion temperatures in comparison to typical bituminous coal. The DT is one of the important ash related properties considered in pulverized fuel (PF) boiler design to select the furnace exit temperature, i.e. the zone of first super-heaters banks. Lower ash fusion temperatures are generally associated with higher deposition severity. The fusion behavior of ash depends largely on its composition and the interactive contribution of individual components. Sommersacher et al. [123] propose the molar ratio $(K+P+Si) / (Ca+Mg)$ as ash fusion indicator dedicated to biomass fuel. They reported a statistically relevant linear co-relation with the ash sintering temperature (prCEN/TS 15370-1). A low ratio corresponds to high sintering temperatures and vice versa. The published work [123] includes various woody based biomass fuels.

The fusion index applied here is adapted from the ratio proposed by Sommersacher et al. [123]. In standard fuel analysis, the ash composition is generally reported as oxides. For simplicity, the ratio here is discussed as a ratio of oxides (as wt.-%, db.). Figure 12 shows the relation of the ash fusion temperature as DT with the ash oxide ratio defined as fusion index (see Eq. 4.1).

$$\text{Fusion index} = \frac{[X_{K_2O} + X_{Na_2O} + X_{P_2O_5} + X_{SiO_2}]}{[X_{CaO} + X_{MgO} + X_{Al_2O_3}]} \quad (4.1)$$

The fusion index is derived corresponding to the normalized ash oxide content of the respective fuel. The numerator ash oxides (K_2O , Na_2O , P_2O_5 , and SiO_2) are considered to decrease the ash fusion temperature while the denominator ash oxides (CaO , MgO , Al_2O_3) are considered to increase the ash fusion temperature. A significant fraction of silica (SiO_2) in biomass fuels are apparently soil minerals, like quartz. The quartz is a solid compound even at higher temperature and supposed to show only partial melting. Nevertheless, SiO_2 being the frame of silicatic composition which is determining the formation of low melting silicates compounds, it is included with the numerator oxides.

The biomass fuels (see Figure 12) show the tendency of lower ash fusion temperature with an increasing magnitude of ash fusion index and the variation in ash fusion temperatures among the same feedstock group is marginal.

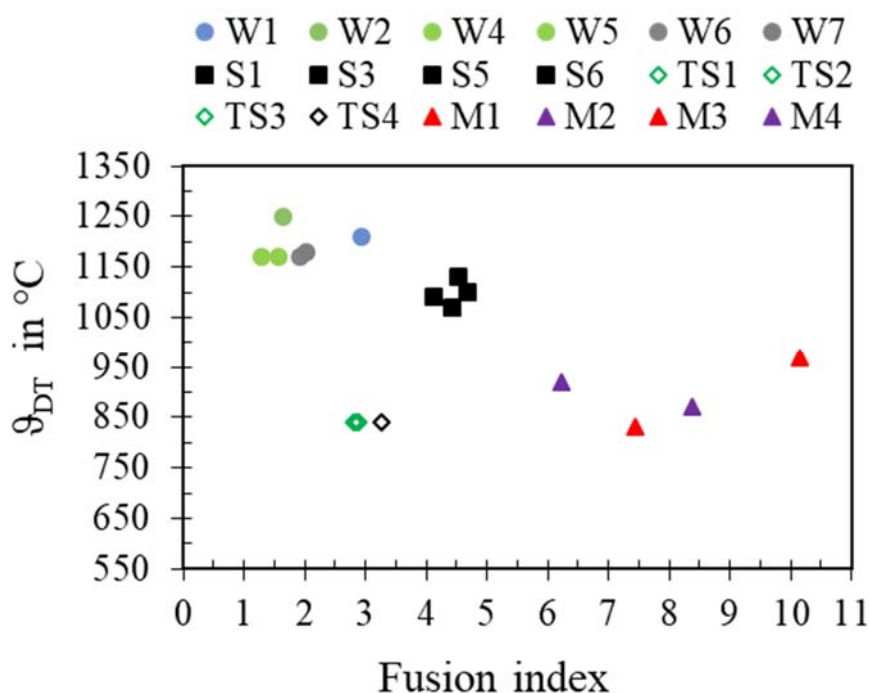


Figure 12: Ash deformation temperature versus Fusion index; Wood (W, ●), Straw (S, ■), Torrefied straw (TS, ◇), and Miscanthus (M, ▲). Each data points refer to the analysis of an individual sample. Different colors in given group symbol represent different experimental batches.

The general trend suggested by Sommersacher et al. [123] is observed. But, a single trend line, including for biomass fuel from different biomass feedstock is not realizable. Especially, the torrefied straw shows substantial offset to the general trend. Author speculates that a certain fraction of silica impurities may separate in the fuel preparation steps of the torrefaction in favor

to lower the magnitude of fusion index. However, the ash fusion behavior driven by interactive chemistry of inorganics inherent to biomass, apparently remains similar.

The contribution of salt components, especially KCl, is of concern for chlorine rich herbaceous fuel. One possibility is that the KCl that remains in 550 °C ash (AFT test sample) escapes as vapor during gradual heating (AFT procedure) or it proceeds to form eutectic melts with other salt components, like sulfate/carbonates/phosphates that are as well present in the ash.

Table 15 shows the ash fusion temperature and relevant fuel components, corresponding to wood fuel doped with KCl. The KCl (as solution) is carefully sprayed over the pulverized wood powder (<500 μm). The KCl doped sample (Fuel Name: *W) is then supplied to the laboratory for standard fuel analysis (see Annex 1, Table 31).

In comparison to original wood, the chlorine content increases 3 – 4 times in absolute numbers which is almost comparable to the herbaceous fuel (TS and M). The IDT is lowest at 930 °C, corresponding to doped wood (see Table 15). The contribution of KCl doping to the DT is non-significant. The standard ash fusion temperatures largely reflects the melting behavior of silicates present in the test ash sample or that are formed along the AFT heating procedure. The KCl which may retain in the test ash sample (550 °C ash) rather evaporates as the test sample is heated and escapes in vapor phase. However, it cannot be generalized to imply that the IDT of herbaceous fuel which is rich in chlorine is not associated with melting of KCl or its eutectic salt mixture.

Table 15: Relevant fuel compositions and ash fusion temperatures of wood and KCl doped wood.

	Wood	KCl doped Wood
γ_{Cl} [wt.-%, daf.]	< 0.03	0.13 – 0.14
X_{K_2O} [wt.-%, daf]	8 – 9	17 – 19
Fusion Index	1.3 – 1.6	≈ 1.9
ϑ_{IDT} [°C]	960 – 1050 °C	930 – 950°C
ϑ_{DT} [°C]	≈ 1170 °C	1160 – 1180°C
ϑ_{FT} [°C]	1190 – 1220 °C	1230 °C

The molar ratio 2S/Cl is widely used as corrosion index for biomass fuels [123]. Generally, a fuel with a ratio < 4 is considered to pose a high corrosion risk while > 8 is considered to pose low corrosion risk [123]. The ratio simply considers the molar stoichiometry of KCl sulfation [123].

The argument to support the significance of the ratio (2S/Cl) to corrosion risk is that with a decrease in the 2S/Cl ratio, the fraction of K-chlorides increases in aerosols, on the other hand at higher 2S/Cl loading which satisfies the sulfation demand of KCl, the aerosol is mostly rich in K_2SO_4 [123]. And it is well established that KCl is a highly corrosive salt in comparison to K_2SO_4 .

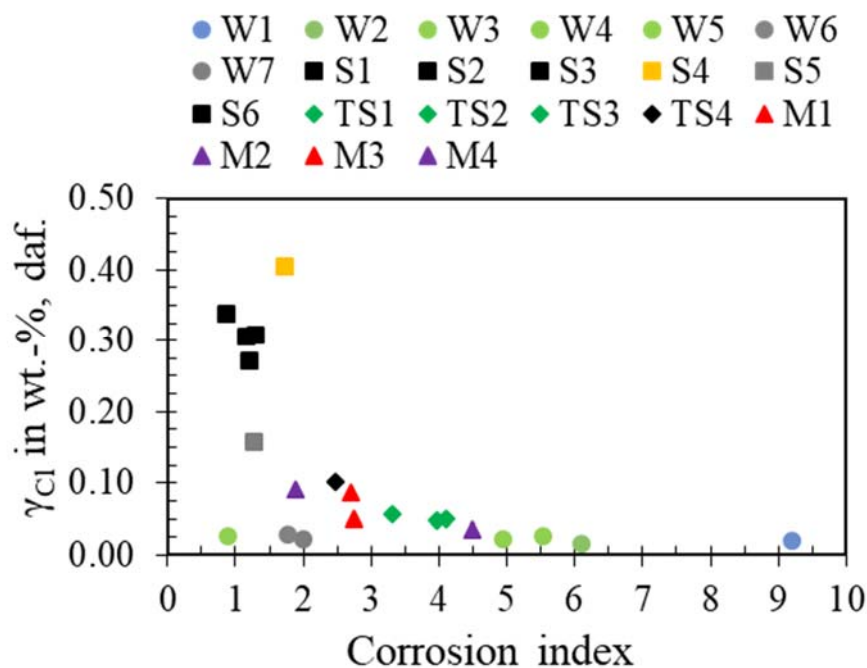


Figure 13: Chlorine content (γ_{Cl} in wt.-%, daf.) versus corrosion index. Note: Each data point refers to the analysis of an individual sample. Different color in given group symbol represent different supply/batch. Wood (W, ●), Straw (S, ■), Torrefied straw (TS, ◇) and Miscanthus (M, ▲).

Figure 13 shows the chlorine content (γ_{Cl} in wt.-%, daf.) versus corrosion index corresponding to test biomass fuels. The corrosion index corresponding to woody fuels extends over the whole range (see Figure 13). Among herbaceous fuels, the corrosion index corresponding to straw (S) lies well below 2, corresponding to torrefied straw (TS) and miscanthus (M) it remains in a range 2 – 4.

For comparative reference, the absolute chlorine (Cl) content in all woody fuels lies within the limit (<0.1 wt.-%, db.) for industrial use according to DIN EN ISO 17225-2 quality classification (see Table 1). The absolute Cl content in both, torrefied straw (TS) and miscanthus (M), remains in the boundary of the highest limit while for straw (S) it clearly exceeds.

Following are the general summary points with regard to the compositional ratio based categorization of deposition and corrosion risk.

- When the biomass fuels from various feedstock sources are included, the statistically relevant single linear correlation of ash fusion temperature with fusion index is far to realize. The fusion index nevertheless indicates a specific trend of ash composition to its fusion or melting behavior. Its use is limited for general assessment of ash fusion temperature corresponding to given ash composition. As it, captures mainly the aspect of silicatic chemistry typical to biomass ash, the fusion index is certainly superior to conventional coal based slagging or fouling indices.
- The use of corrosion index is limited for a general assessment of the corrosion risk. In a combustion system neither all fuel-Cl is released as KCl nor all fuel-S species (SO_x) are selectively consumed for KCl sulfation. The competition of other primarily released ash inorganics species, like KOH (g) and CaO (s), to get available SO_x , overwrites the corrosion risk level assessment based on stoichiometry of chlorine and sulfur alone. Additionally, beside the ratio the absolute amount of chlorine content as well contributes to the magnitude of corrosion risk.
- The simplicity of fuel composition based indices; either fusion index or corrosion index as discussed in this section, signifies their usefulness as well as the limitation owing to complexity of ash compositional chemistry.

4.2 Characterization of test additives

The moisture content in additives represents the mass loss of a sample at 105 °C. The crystal water represents the total mass loss within the temperature range of 105 – 910 °C. The chemical composition as oxide of additives is determined by ICP-OES following the standard for ash oxide analysis.

The crystalline mineral phases in additive are identified by XRD. Also, preliminary information is provided by the additive supplier. Kaolinite ($\text{Al}_2\text{Si}_2\text{O}_5(\text{OH})_4$) is the main aluminosilicate mineral of interest in this study. In the additives, A, B, and C, Kaolinite is the major aluminosilicate present. Additive B is mostly kaolinite while additives A and C include a fraction of muscovite and quartz. The main aluminosilicate mineral in additive D is halloysite. It contains a considerable fraction Fe_2O_3 .

The chemical formula of kaolinite is $\text{Al}_2\text{Si}_2\text{O}_5(\text{OH})_4$. For halloysite, it is $\text{Al}_2\text{Si}_2\text{O}_5(\text{OH})_4.n\text{H}_2\text{O}$. The quantitative XRD or mineralogy was not always available to the author. The mineral fractions in % are estimated from the molar mass balance corresponding to the ash oxide composition, (see Annex 1, section 7.2).

The BET surface area is a measure to specify the surface area of materials. A high BET surface area is associated with a better adsorption of gaseous molecules over the solid surface. The BET is determined by N_2 -Physisorption. For the additives, A and C, it ranges between 10 – 13 m^2/g while additive D shows substantially higher BET surface area (72 m^2/g). Due to the richness in halloysite, additive D has a higher BET surface area than the other investigated, kaolinite rich additives.

The additive mineral as pure compounds is characterized by its high melting temperature. The additives as raw samples were subjected to standard ash fusion test (AFT) procedure. The sample height shows no substantial drop that could be related to the fusion/melting of the test sample within the maximum AFT temperature, i.e. until 1500 °C. A minor decrease in sample height observed in early stage at 900 – 1000 °C is apparently related to the loss of crystal water and associated mineral transformation.

Table 16: Properties of test additive.

Supplier	Imery Ceramics, France		Kaolin und Tonwerke SalzMünde GmbH, Ger- many	Intermark, Poland
Additive identity	A	B	C	D
as an, in wt.-%				
γ Moisture	13	< 1	1	2
γ Crystal water	10	14	11	14
γ Al ₂ O ₃	24.5	36.2	27.6	22.7
γ SiO ₂	37.2	47.3	49.3	36.1
γ K ₂ O	1.8	0.1	1.1	0.2
γ Fe ₂ O ₃	1.0	0.5	0.7	16.0
¹ Main minerals [%]				
Kaolinite	63	92	67	-
Halloysite	-	-	-	60
Muscovite	20	1	10	2
Quartz	11	5	18	10
Others	6	2	5	28
D10 in μm	2.2	1.8	2.2	1.8
D50 in μm	10.0	5.6	5.3	9.1
D90 in μm	61.0	15.0	11.3	31.4
BET surface area [m²/g]	10.8	-	13.4	72

¹ Estimated from molar mass balance of oxides, see Annex 1 section 7.2, Table 34.

4.3 Experiments in pilot scale combustion test facility (KSVA)

The test set, case identity and test boundaries corresponding to pilot scale combustion test facility are summarized in Table 17. The combustion cases (see also Table 9 in section 3.1.1) refer to the fuel or fuel-mix and is the case identity as reported in the result section and graphs hereafter. Table 17 shows the fuel (in kg/h) and combustion air (in m³/h) flow corresponding to different cases. The fuel feeding rate was chosen to keep a thermal output of $\approx 280 - 300$ kW. The total combustion air is chosen to represent the air ratio of $\approx 1.15 - 1.20$. The values reported below are typical to stable operating durations.

Table 17: Fuel feeding rate and combustion air (test protocol and system data).

Test set	A					B				C	
Case identity	EC	25S	40S	60S	S	W	M+W	M	M+B	S	S+D
\dot{M}_{coal} [kg/h]	≈ 39	≈ 29	≈ 24	≈ 15	-	-	-	-	-	-	-
\dot{M}_{biomass} [kg/h]	-	≈ 17	≈ 27	≈ 24	≈ 66	≈ 65	≈ 64	≈ 63	≈ 45	≈ 70	≈ 72
\dot{V}_{CA} [m ³ /h]	≈ 294	≈ 288	≈ 286	≈ 303	≈ 306	≈ 330	≈ 310	≈ 300	≈ 320	≈ 324	≈ 364

Table 18 shows some important composition/properties of fired fuel relevant for the result and discussion that follows. The composition and properties (Table 18) refer to the analysis corresponding to the sample taken directly from the feeding hopper. The complete analysis of fuel (S) as fired is in Annex 1 (see Table 28). For test set C, S+D, refers to the straw premixed with additive. The fuel was received as additive pre-mixed fuel (pulverized). The complete analysis of fuel (S+D) as fired is in Annex 1 (see Table 31).

Table 18: Relevant composition and properties of fired fuel (analyzed).

Test set	A		B			C	
Fuel	EC	S	W	M+W	M	S	S+D
γ_{ash} [wt.-%, db.]	12.1	10.2	1.36	1.68	3.40	12.9	13.9
γ_{Cl} [wt.-%, daf.]	0.02	0.27	0.03	0.05	0.09	0.31	0.33
Corrosion index	89	1.2	1.9	1.7	1.9	1.2	0.9
Fusion index	1.3	3.3	2.0	2.9	6.2	4.5	2.9
ϑ_{DT} [°C]	1310	1090	1175	1080	920	1130	1210
Test set A: Straw: S (S2)							
Test set B: Wood: W (W6 and W7) and Fuel Name: Miscanthus: M (M2)							
Test set C: Straw: S (S6)							

During co-firing cases in test set A, the coal and biomass was independently fed. The number of the combustion case identity refers to the thermal share of straw in the resulting mix. For co-firing cases (25S, 40S and 60S) the composition of the resulting co-firing blend is calculated from the corresponding mass share. The compositions relevant to the result and discussion are given in Table 19 (also see Annex 1, Table 32).

In test set B, during the M+B combustion case, the additive was independently fed by a separate feeder. The average feeding rate was 1.75 kg/h with average carrier air $\approx 8 \text{ m}^3/\text{h}$. It corresponds to $\approx 4 \%$ of the additive loading in reference to the fuel feed. The composition of ‘fuel+additive’ mix is calculated corresponding to the mass flow of the fired fuel miscanthus (Fuel Name: M3, see Annex 1 Table 29) and additive mass flow corresponding to respective combustion case. The calculated compositions relevant to the result and discussion are given in Table 19 (also see Annex 1, Table 32).

Table 19: Relevant composition and properties of fired fuel mix (calculated).

Test Set	A			B
Fuel	25S	40S	60S	M+B
γ_{ash} [wt.-%, db.]	11.4	11.1	10.7	5.7
γ_{Cl} [wt.-%, daf.]	0.11	0.15	0.21	0.05
Corrosion index	11.1	6.6	3.4	2.7
Fusion index	1.7	2.0	2.5	2.2

The combustion stability was continuously monitored at the end of the combustion chamber with maintaining the excess O₂ of 3 – 3.5 vol.-%. The FA was sampled at the end of the combustion chamber for each combustion case. Table 20 shows the average flue gas concentration typical to stable combustion duration. The combustion efficiency (Eq. 4.2) is derived corresponding to the ash content in the FA sample in reference to the ash content in the fired fuel.

$$\eta_{\text{combustion}} = \frac{\left(1 - \frac{Y_{\text{ash,fuel}}}{Y_{\text{ash,sample}}}\right)}{\left(1 - \frac{Y_{\text{ash,fuel}}}{100}\right)} \cdot 100 \quad (4.2)$$

To maintain the flame stability and the temperature profile, a support gas, with ≤ 90 kW, was provided corresponding to the tests with additive. It is important to note that the compromised combustion stability in relation to increased solid fraction from the additive in the flame zone is of concern and requires a separate specific study. The influence of gas is expected to be minimal with regard to the deposit/ash samples later discussed in the result section.

Figure 14 shows the temperature profiles along the furnace centerline corresponding to (a) test set A and (b) test set B. The magnitude of temperature varies from one case to other but the trend is similar, the peak temperature is shifted downward which is a notable difference to the temperature profile in comparison coal flame. This behavior is apparently related to the peak heat release which probably shifts in relation to the larger particle size of pulverized biomass. The D₉₀ of pulverized coal (EC) and straw (S) fired in test set A is respectively, 55 μm (see Annex 1, Table 26) and 622 μm (see Annex 1, Table 28).

Table 20: Fuel gas composition and combustion efficiency, both values correspond to the measurement/FA sample from the end of the combustion chamber.

Test set	A					B				C	
	EC	25S	40S	60S	S	W	M+W	M	M+B	S	S+D
yO ₂ [vol-%]	2.9	3.7	3.2	2.4	3.7	3.4	3.3	3.3	3.1	3.4	3.5
yCO ₂ [vol-%]	15.7	15.2	15.8	16.9	16.2	16.8	17.1	17.1	17.3	16.4	14.4
yCO [ppm]	275	118	103	80	98	126	76	93	122	317	660
yNO [ppm]	758	755	785	554	307	97	168	137	154	238	332
ySO ₂ [ppm]	349	280	187	97	14	< 1	< 1	30	11	24	104
$\eta_{\text{combustion}}$ [%]	98.83	99.05	99.70	99.97	99.54	99.88	99.82	99.84	99.78	-	-

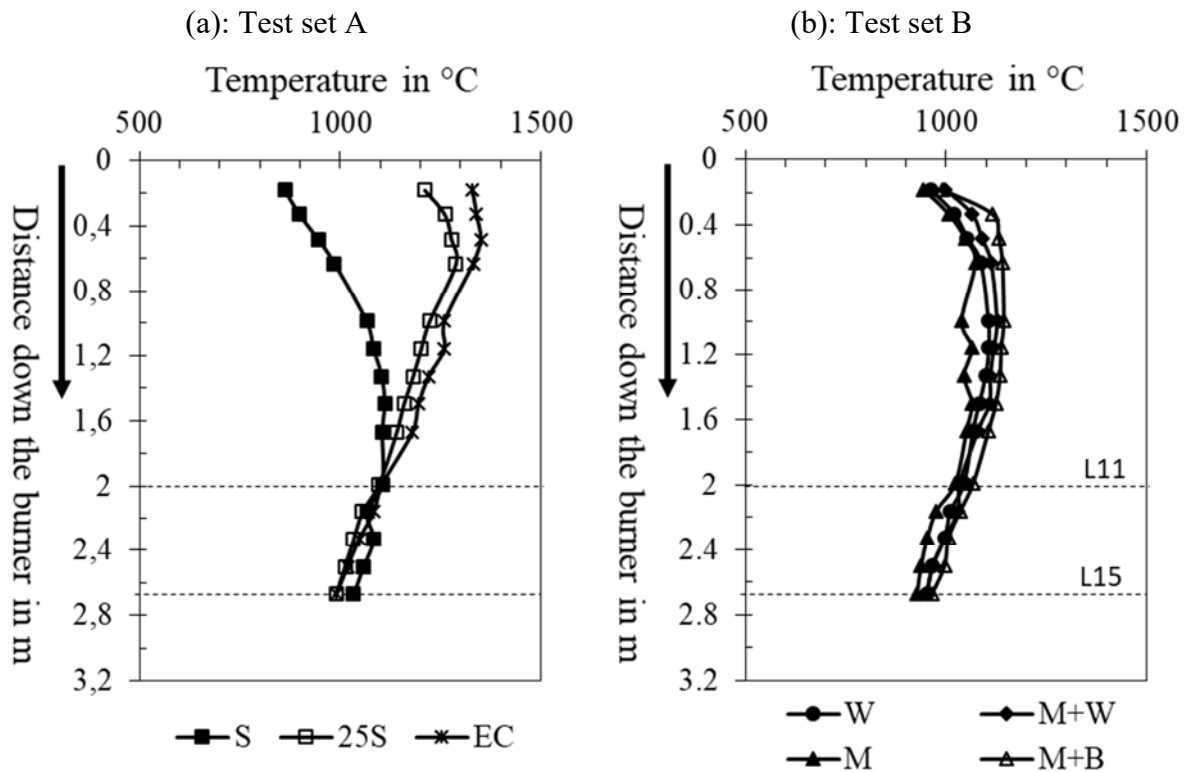


Figure 14: Temperature profiles by thermocouple measurements along the furnace centerline: (a) Combustion cases from test set A, (b) Combustion cases from test set B. Note: Zero refers to the burner mouth. L11 and L15 denotes deposit sampling location.

The temperature at the sampling/measurement location (L11 and L15) is of most concern. The measurement refers to the furnace centerline temperature (thermocouple measurement). Most importantly, the temperature at L11 is always higher by 100 – 150 °C than the temperature at L15.

4.3.1 Result: Demonstration of additive mitigation effect

The results that follow include the evaluation of online deposition sensor (ODS) measurements, the outer deposit (OD) and inner deposit (ID) samples, and for some cases the fly ash (FA) samples. The measurement/sampling boundaries specific to certain case are discussed individually when necessary.

4.3.1.1 Evaluation of data obtained from ODS

The ODS is implemented at the exposure location L11 and L15 and refers to the position 2 m and 2.7 m below the burner position. The ODS continuously records the mass of ash accumulated over the ceramic probe (tube) surface. Figure 15 (a) shows the cumulative deposit mass (M_D in g) and the deposition rate (\dot{M}_D in g/h), an example case corresponding to the M+W case.

Figure 15 (b) shows the box plot of the corresponding deposition rate (\dot{M}_D in g/h). The deposition rate (\dot{M}_D in g/h) is calculated corresponding to each consecutive half hour measurement. The data corresponds to a continuous exposure for a duration of 6.5 h, for all cases discussed hereafter.

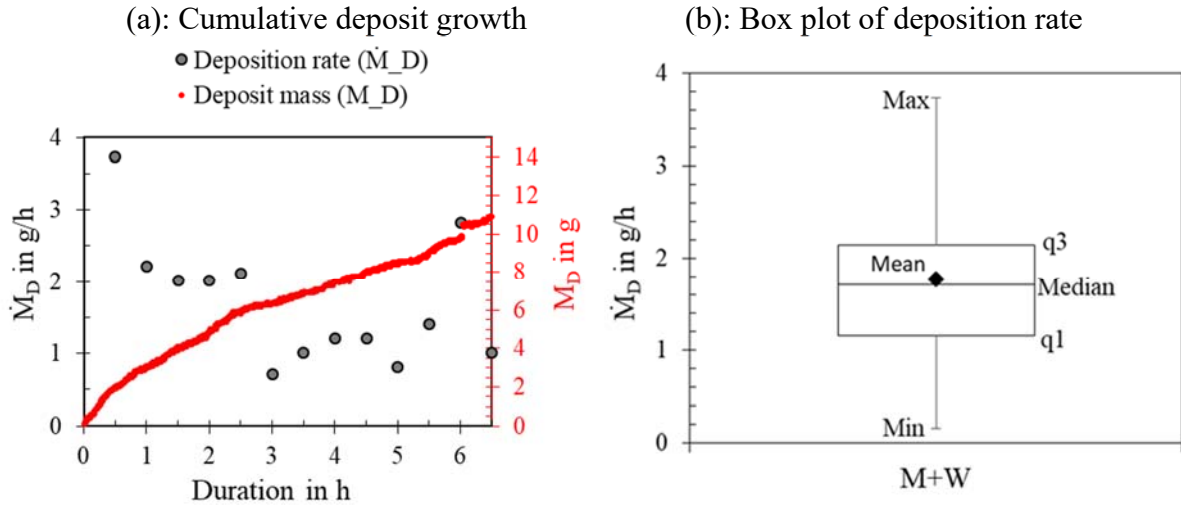


Figure 15: (a) Cumulative deposit growth (M_D in g) and deposition rate (\dot{M}_D in g/h), (b) the box plot of corresponding deposition rate (\dot{M}_D in g/h)

Deposition propensity (D_p in %) is derived from the measured deposition rate (\dot{M}_D) and is calculated by the following mathematical formula (Eq. 4.3).

$$D_p = \frac{\dot{M}_D}{\dot{M}_{Ash}} \cdot \frac{A_{furnace}}{A_{probe}} \cdot 100 \quad (4.3)$$

Where,

\dot{M}_{ash} is the ash flow the calculated from fuel feeding rate and ash content corresponding to the given fired fuel

$A_{furnace}$ is the furnace cross-sectional area at the exposure plane (0.503 m², with furnace D = 0.80 m)

A_{probe} is the receptive area (rectangular assumption) of the probe in the exposure plane (0.013 m², with probe L = 0.4 m and D = 0.032 m)

4.3.1.1.1 Deposition rate

Coal (EC), Co-firing (25S, 40S, 60S) and Straw (S)

Figure 16 (a) and (b) show the deposition rate corresponding to L11 and L15, respectively. Coal shows the lowest deposition rate among all. The share of straw induced substantial increase of the deposition rate. Apparently, a substantial increase by already 25 %th co-firing case suggests that the deposition rate is largely dictated by the straw ash system. The average rate of increase in reference to coal is 0.3 – 0.5 g/h and 0.2 - 0.4 g/h per unit share of straw, at L11 and L15, respectively. The ratio of straw to coal ash (calculated corresponding to the ash flow in respective cases) is 0.5, 0.9 and 2.2, respectively for 25S, 40S and 60S. It means on a mass basis, the fraction of straw derived ash exceeds the coal derived ash above 40 %th straw share.

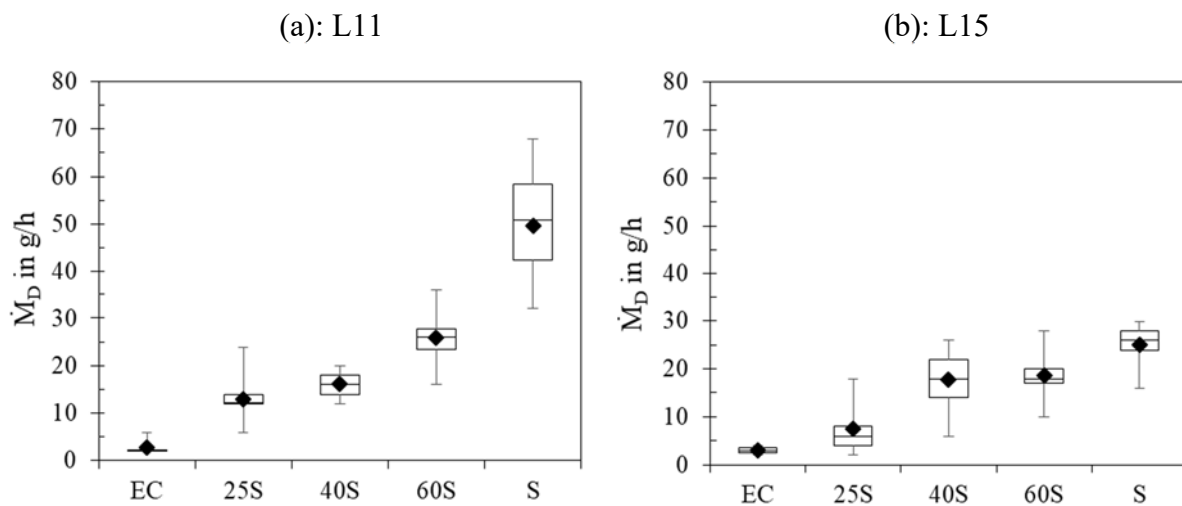


Figure 16: Deposition rate (\dot{M}_D in g/h) corresponding to different combustion cases from test set A (a) L11 and (b) L15.

The ash flow in the system, the temperature at the exposure location, and the properties of ash in the system are the three main parameters influencing the deposition rate. Figure 17 (a) shows the relationship between deposition rate and ash flow in the system. The total calculated ash flow in the system increases with the share of straw and is directly linear to the measured deposition rate. Figure 17 (b) shows the relationship between deposition rate and temperature of the probe exposure location. For a given case the temperature at L15 is always lower than at L11 and so does the deposition rate. The temperature at a given location does not vary substantially. The variation is < 50 °C with the share of straw and among cases it remains comparable. Within the same exposure location, the influence of temperature among cases is non-specific.

The straw ash system at the exposure temperature regime is expected to be dominated by molten or semi-molten ash particles. This situation leads to melt induced stickiness and therefore accumulations due to impaction result in substantial deposit growth. In contrast, the coal fly ash is dominated by solid ash particles which do not pose melt induced stickiness to accumulate on impaction. The properties of impacting ash particles apparently influence the system more regarding the deposition rate.

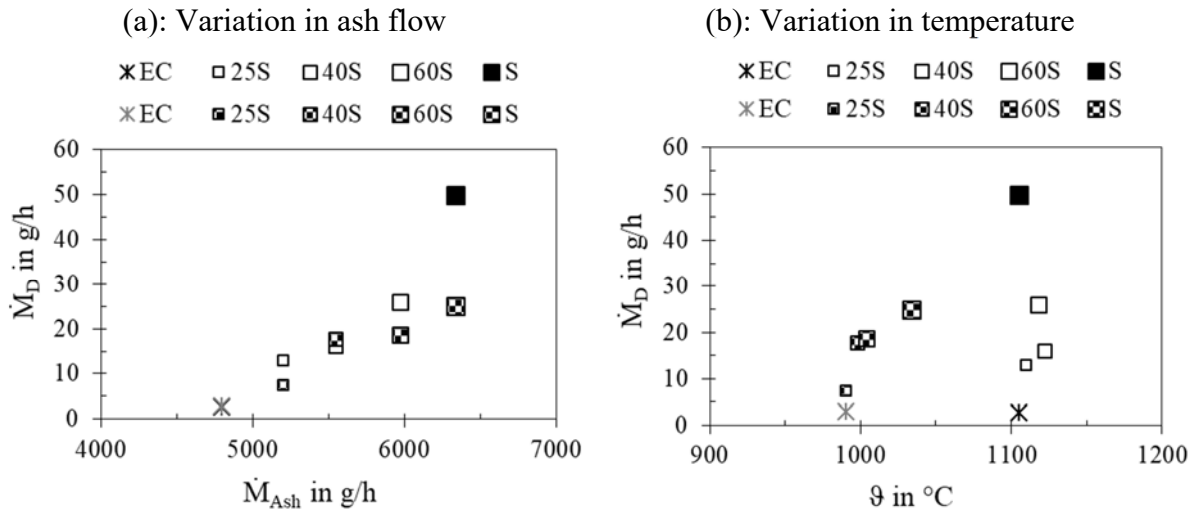


Figure 17: (a) Deposition rate (\dot{M}_D) versus ash flow (\dot{M}_{Ash}), (b) Deposition rate (\dot{M}_D) versus temperature (θ). Legend: the 1st line refers L11 and the 2nd to L15.

The co-firing shares in this study represent the cases in which the deposit growth is largely governed by the biomass ash system. The positive effect of coal ash is highlighted in many co-firing studies. The argument behind is the biomass ash and coal ash, especially aluminosilicatic ash, interaction. The fired coal is rich in aluminosilicatic ash and therefore represents the ideal quality as a base coal for co-firing. The extent of the positive effect is limited only for lower co-firing shares or low ash containing biomass fuels. The ash content (γ_{Ash} : 11 wt.-% db.) in straw co-fired during this study is comparable to coal (γ_{Ash} : 12 wt.-% db.). The visual observation as well suggests that molten or semi molten ash which originates from the straw share dominates the outer deposit bulk already at 25 %th share of straw.

Wood (W), Miscanthus (M), Mix (M+W), and Miscanthus with additive (M+B)

Figure 18 (a) and (b) shows the deposition rate from L11 and L15, respectively corresponding to test set B combustion cases. The deposition rates are substantially lower than both of the straw test set A, mono- or co-firing, which is largely explained by the substantially lower amount of ash in the biomass fuel fired in test set B.

The deposition rate of W is lowest, mix M+W remains in middle while M shows the highest among all, see Figure 18. In comparison to the corresponding case without additive, the deposition rate corresponding to case with additive, see M compared to M+B, remains comparable or lower depending on the exposure location. The solid particle flow (mass basis) is higher corresponding to the case with additive. Despite of higher solid (ash) flow in the system the comparable or lower deposition rate signifies that the solid minerals from the additive do not substantially contribute to deposit growth.

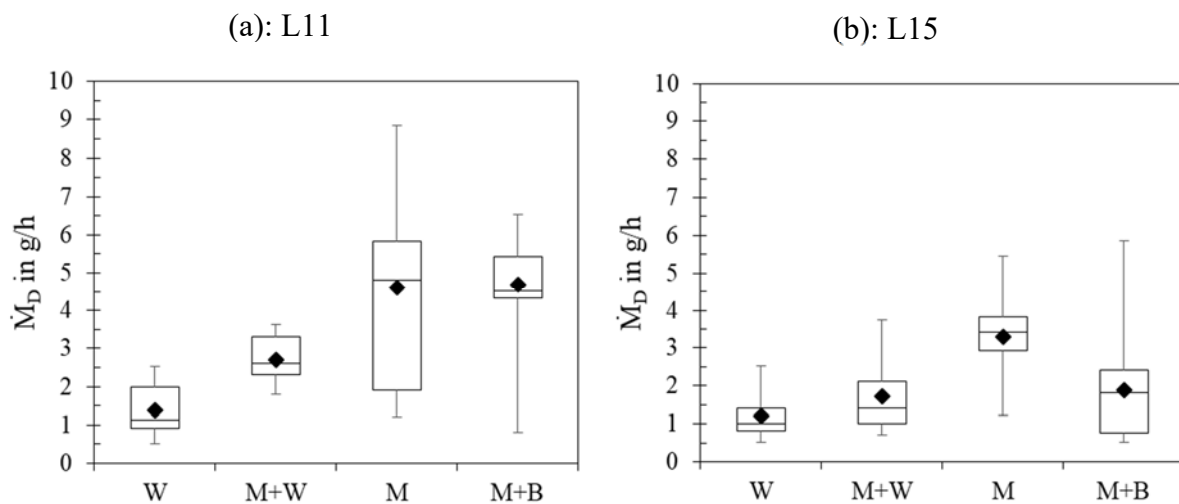


Figure 18: Deposition rate (\dot{M}_D) corresponding to different combustion cases from test set B at (a) L11 and (b) L15.

Figure 19 (a) shows the relationship between deposition rate and ash flow in the system. The break in the direct linear relation in case with additive, suggests that the deposit growth reduces in the case with additive. This suppression is related to the reduction of molten or semi molten ash in the corresponding ash (biomass+additive) system. The contribution due to mere physical dilution relates to the refractory mineral components, i.e. solid particles, introduced with the additive or the contribution of the expected biomass ash-additive interactions is however non distinguishable from the mass data. The eroding effect of impacting solid minerals which originate from additive may also contribute to lower the deposit growth.

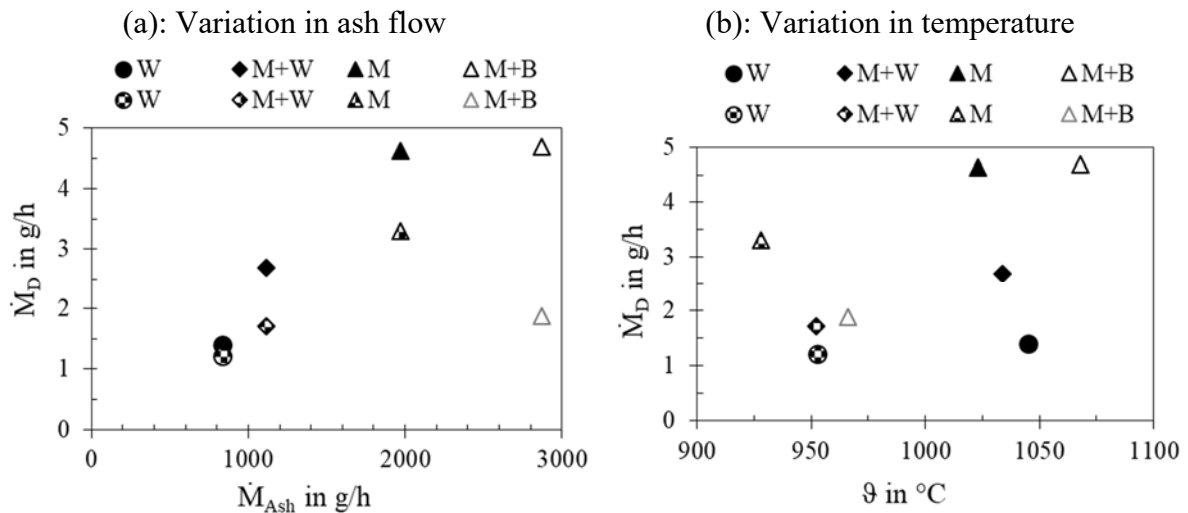


Figure 19: (a) Deposition rate (\dot{M}_D) versus ash flow (\dot{M}_{Ash}) and (b) Deposition rate (\dot{M}_D) versus temperature (ϑ). Legend: the 1st line relates to L11 and the 2nd to L15.

Figure 19 (b) shows the relationship between deposition rate and temperature at the exposure location. The temperature at a given location does not vary substantially among biomass/mix cases. The temperature during additive case is marginally higher which is apparently related to additional heat input from gas. Within the test temperature range at a given location, not any specific relationship to the deposition rate is observed.

4.3.1.1.2 Deposition propensity

The ash properties in the given exposure surrounding (combustion system) have the most significant impact on outer deposit growth. Due to variations in the ash flow inside the system across different cases, a comparison based on the deposition rate is not applicable. The down fired test rig (test facility used) even more highlights the correlation to ash flow because all combustion generated ash (FA) passes through the probe exposure plane. To harmonize the influence of ash flow among the cases the discussion is made according to Deposition Propensity (D_p). D_p is a measure to evaluate the % of ash accumulation over the unit receptive surface area in reference to the total ash flux in the exposure (plane) surrounding. The influence of flue gas flow/directions and velocity of ash particle impaction are presumed comparable owing to similar combustion setting. Basically, the measured deposition rate observed among the cases is related to the ash flow in the system coupled with the properties of ash in the exposure surrounding corresponding to the given cases.

With D_p the variation in ash flow is harmonized, see Figure 20 (a). Therefore, the difference among cases is basically related to the properties of ash, especially melt induced stickiness. The

phase, solid or liquid, of a given ash component is related to its melting or else fusion temperature.

D_p is plotted against the temperature of the respective exposure location and shown in Figure 20 (b). The ash content in wood (1.4 wt.-% db.) is almost 10 times lower than in coal (11 wt.-% db.). In contrast, D_p is $\approx 3\%$ and $\approx 6\%$ corresponding to coal and wood, respectively. This twofold increase in deposition propensity, i.e. ash accumulation, despite of lower temperature (see Figure 20 (b)) indicates higher stickiness associated with biomass ash in comparison to coal ash. Deposition propensity corresponding to M, mix M+W case, and co-firing case is within or substantially above both references, coal and wood.

The deposition propensity corresponding to S is the highest among all. Across different cases and measurement locations, different D_p are grouped with comparable magnitude and summarized in Table 21. The groups are arbitrary defined and specific to the test results discussed here. The objective is to compare the severity of deposition among different cases in reference to coal and wood. The deposition severity corresponding to the cases of group I are comparable to coal reference. Group II is comparable to the wood reference. Other groups exceed both, coal and wood, see Figure 20 and Table 21. The D_p corresponding to the case with additive M+B is lower in comparison to the same fuel case without additive M and shows a similar drop at both measurement locations, L11 and L15.

Table 21: Combustion cases with comparable magnitude of deposition propensity.

Group	I	II	III	IV	V
D_p	≈ 3	≈ 6	≈ 10	≈ 16	≈ 32
L11	EC	W M+B	40S 25S M M+W	60S	S
L15	EC M+B	W M+W W M 25S	25S 40S	S 60S	

It is well known that kaolinite in the system promotes the formation of refractory K-aluminosilicate compounds in the expense of low melting K-silicate compounds. Thereby it reduces the fraction of molten or semi-molten ash components. As a consequence of this chemistry shift, the melt induced stickiness of the ash particles is lower and thereby their accumulation on impaction. Additionally, the fraction of refractory solid components from additives exhibits eroding effects. Both effects essentially contribute to lower deposition propensity (D_p).

The straw to coal ash ratio (mass flow basis) corresponding to the lowest co-firing share 25S case and miscanthus ash to additive ratio corresponding to M+B case are respectively, 0.5 and 0.7. Despite of higher ash flux in the system the deposition propensity (D_p) corresponding to 25S case remains comparable to other biomass cases. The fired coal ash is known to contain significant amount of kaolinite and expected to induce a similar chemistry effect as mineral additive. Nonetheless, it is rather speculative to compare the effectiveness of mineral derived kaolinite versus coal ash derived kaolinite based on deposit growth behavior.

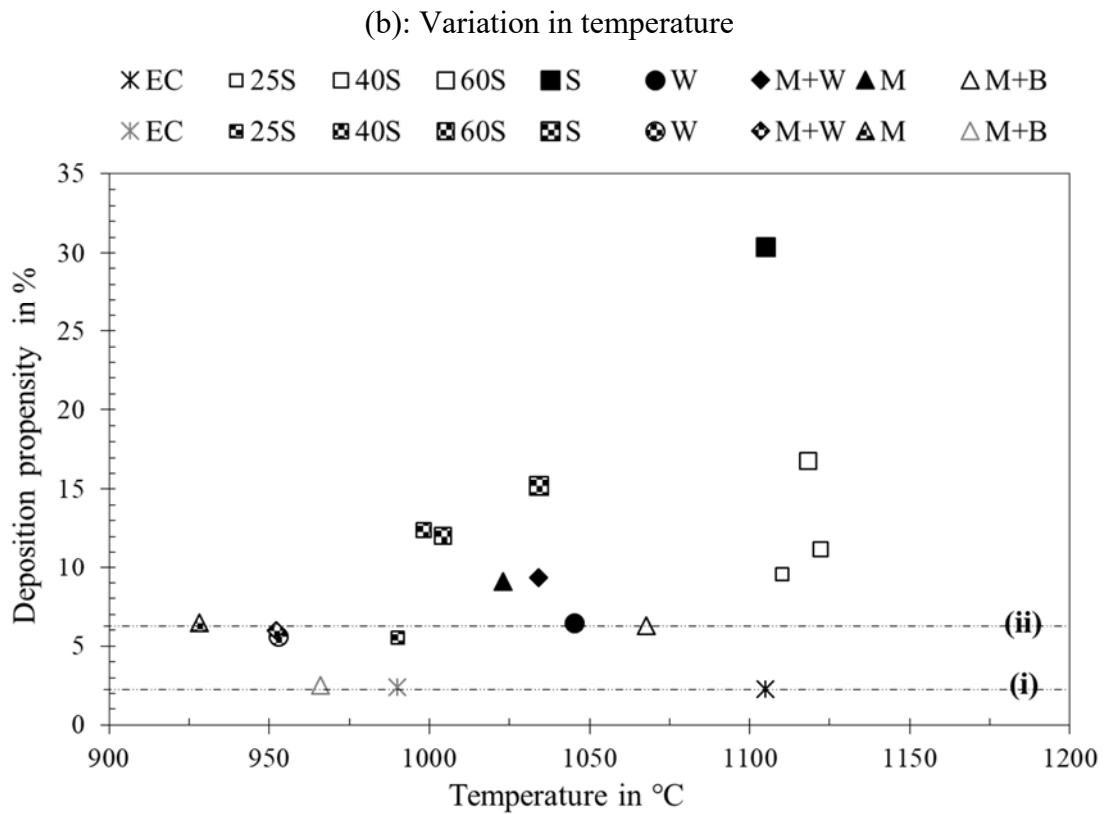
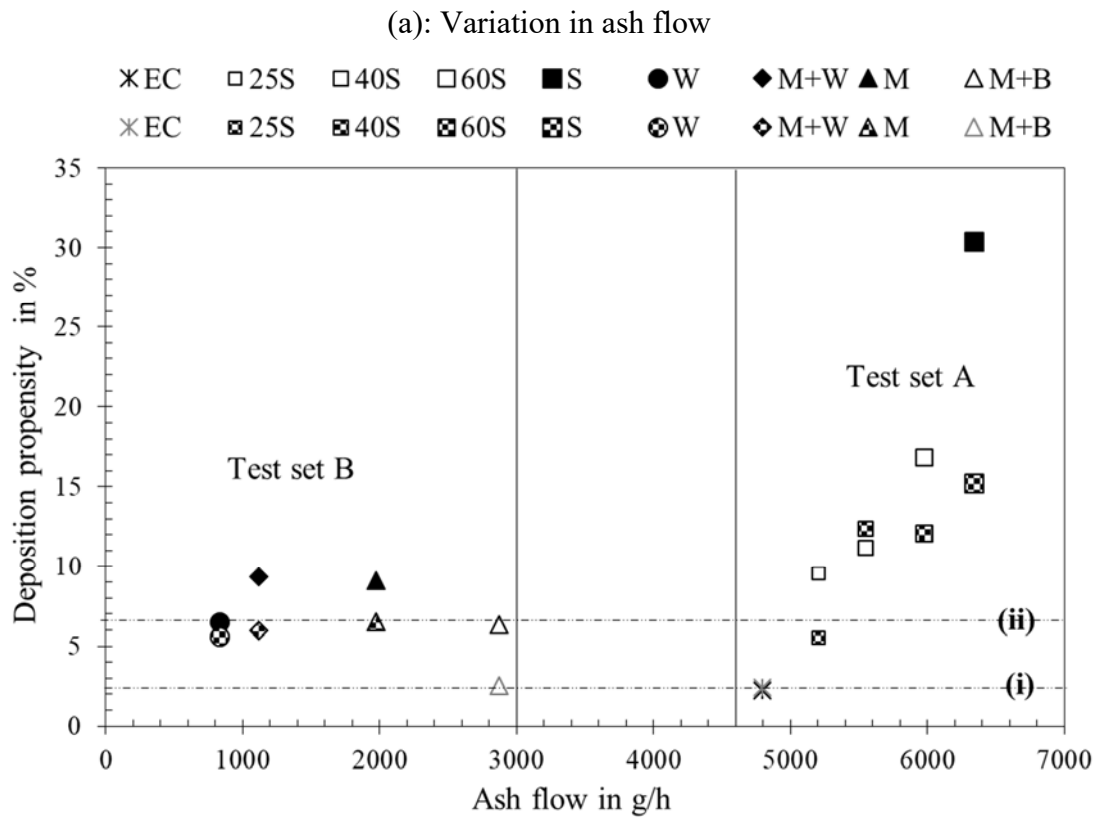


Figure 20: (a) Deposition propensity (D_p) versus ash flow (\dot{M}_{Ash}), (b) Deposition propensity (D_p) versus temperature (θ). (i) Reference line corresponding to coal (ii) Reference line corresponding to wood. Legend: the 1st line refers to L11, the 2nd to L15.

4.3.1.2 Ash oxide composition and ash fusion temperature

The deposit ash was scratched off manually from the ceramic probe (tube) surface after the exposure. To harmonize the difference in unburnt fuel particles in deposit ash bulk, the samples are ashed at 550 °C in lab air atmosphere prior to ash fusion test. OD_L11 and OD_L15 refers to the deposit sample from the measurement position L11 and L15, respectively. FA_L27 represent the ash sample collected by suction probe sampling at position L27 and represents a homogeneous fraction of combustion generated ash sample. FA samples is also ashed at 550 °C in lab air atmosphere prior to ash fusion test. Fuel ash refers to the ash sample generated from the fuel according to standard, 550 °C in air atmosphere. The oxide composition and characteristic ash fusion temperature of each deposit/FA sample is organized in Annex 2 (see section 8.1).

Following general observations are made from the ash fusion test results.

- The ash fusion temperature of combustion generated FA shows a similar hierarchy as the fuel-ash, at 550 °C sample, among biomass fuel, i.e. $W > M+W > M$.
- The ash fusion temperature corresponding to case with additive M+B is substantially higher in comparison to corresponding case without additive M.
- Comparatively, the fuel ash sample (550 °C) shows a lower ash fusion temperature than combustion generated ash (deposit/FA). This is believed since alkali salt components and their decomposition are still present in the fuel ash (lab prepared). The release and the interactions with other ash components proceeds along the gradual heating of the test sample during the AFT procedure. Consequently, the influence is reflected in the ash fusion temperatures. In contrast, the combustion generated ash (deposit/FA) experienced that process in the combustion system itself. Basically, the ash fusion temperatures of combustion generated ash reflect the melting or else re-melting behavior of amorphous particles, i.e. silicatic slag derived particles, while the fuel ash largely represents the melting behavior of silicate slag precursors, like K/Ca-silicates and of alkali salt components.

The sum of the oxides K_2O , CaO , and SiO_2 represents > 70 – 80 % of the ash oxide composition. For the additive case, the amount of Al_2O_3 becomes relevant. The SiO_2 alone contributes more than 50 % of the total oxide composition, except for the wood case FA where $CaO > SiO_2$.

The ash fusion temperatures are plotted against the relevant oxide ratio and shown in Figure 21, where the relevant oxide ratio derives from Eq 4.4.

$$\text{Relevant oxide ratio} = \frac{X_{K_2O}}{X_{CaO} + X_{Al_2O_3}} \quad (4.4)$$

The idea behind the relevant ratio is similar to that of the fusion index (Eq. 4.1) discussed earlier. Here, the contribution of other ash oxides is not considered for the correlation with the ash fusion temperature of combustion derived ash sample. The bulk composition of such sample is dominated by silicatic slag derived components (amorphous particles). With SiO_2 as the frame of slag, the dominant oxide in the slag are K_2O , CaO and Al_2O_3 . Among them, the K_2O is responsible to lower the melting temperature while CaO and Al_2O_3 is responsible to increase. A similar correlation is to be expected also for the fusion index.

The relevant oxide ratio has an inverse relationship with ash fusion temperature. The deposit/ash samples corresponding to biomass+additive cases show substantially higher ash fusion temperatures in comparison to all biomass (alone) cases. The conventional conviction in PF boiler design is that if the flue gas temperature in the boiler zone is above or near the DT of fired fuel, a deposition risk is to be expected. The deposit growth in such case is expected to melt induced stickiness of impacting ash particles.

Among biomass cases, DT flattens out at around $\approx 1150 - 1200$ °C corresponding to wood ash/deposit and is the highest among all biomass fuels tested during this work. DT of the cases with additive M+B is higher ≥ 1300 °C and clearly outside the linear trend of all biomass fuels. Despite of a similar or even lower ratio compared to wood, a substantial lift in ash fusion temperature is observed. The shift outside the general correlation (valid to biomass) suggests that it is not merely a dilution effect owing to increased Al_2O_3 fraction as aluminosilicate but also reflects the contribution of high melting compounds, possibly K-aluminosilicate.

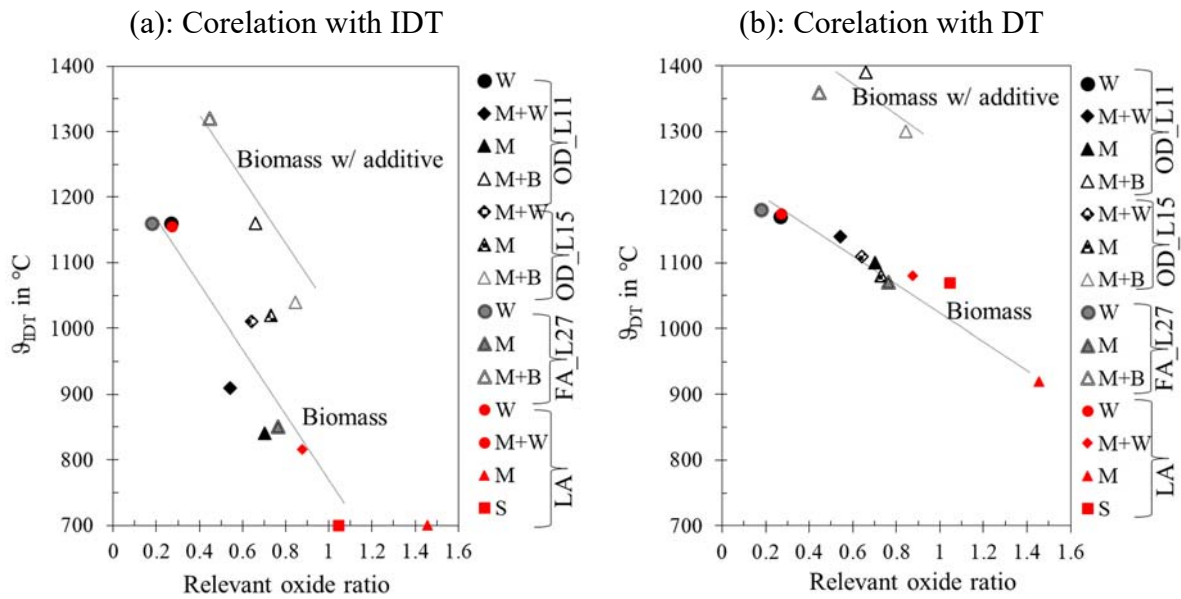


Figure 21: (a) Initial deformation temperature (IDT) versus relevant oxide ratio, (b) Deformation temperature (DT) versus relevant oxide ratio (right).

The characteristic temperature defined by AFT standard procedure is based on the change in height or else size of the test ash sample specimen. Both initial deformation temperature and deformation temperature is a subjective conformation. The melting of a test ash sample specimen initiates and proceeds along the AFT procedure. The component in the given ash sample with the lowest melting temperature is the first to melt. The melting behavior of bulk ash sample is apparently analogous to the silicatic slag, i.e. with SiO_2 as frame, and the variation of K_2O , CaO , and Al_2O_3 in the ash largely dictates the behavior. A strong correlation to the given ratio probably signifies this.

The compounds like K-/Ca-silicates, K-/Ca-aluminosilicate, and their mixtures constituting the slag composition and their melting behavior governs its liquids temperature. Such compounds are not presented as such in fired biomass fuel but evolve from ash inorganic interactions which proceed along the combustion process. The formation of K-/Ca-silicates is evident for most biomass fuels. The kaolinite (from additive) hinder this chemistry and instead favor the formation of K-aluminosilicatic. The K-aluminosilicate is a high melting compounds in comparison to K-silicate. The consequent observation is a higher ash fusion temperatures of ash/deposit for cases with additives.

4.3.1.3 Morphology and composition of outer deposit

For all biomass fuels the outer deposit bulk is characterized by molten or semi-molten ash. The visual judgement by naked eye is influenced by the thickness of the deposit bulk which varies according to the amount of ash flow in the corresponding case. The ceramic probe cross-section, i.e. OD bulk, was subjected to SEM observation (EMPA analysis) to generate micro-graphs for closer observation. Here, the micrographs, BSE image and Element maps, from case M (miscanthus without additive) and M+B (miscanthus with additive) are discussed.

4.3.1.3.1 Miscanthus case (M)

Figure 23 shows the BSE image corresponding to miscanthus case OD_L15. The deposit ash appears fused to the sampling surface confirming its molten state/history. In addition, the unburnt char accumulation was distinct at the deposit front. The molten ash may facilitates its accumulation over the sampling surface. Basically, the char transport and accumulation is a consequence of the abundance of molten ash in the exposure surrounding. The BSE image and elemental map of a fused deposit ash where the area is chosen for closer view, is shown in Figure 24. The fused layer is characterized by the regular distribution of Si, K, and Ca, apparently K-/Ca-silicates. The Ca distribution is characterized by the localized concentration in combination with P and probably remains as discrete particles, means in an independent chemical phase, within the fused phase, apparently as Ca-phosphates.

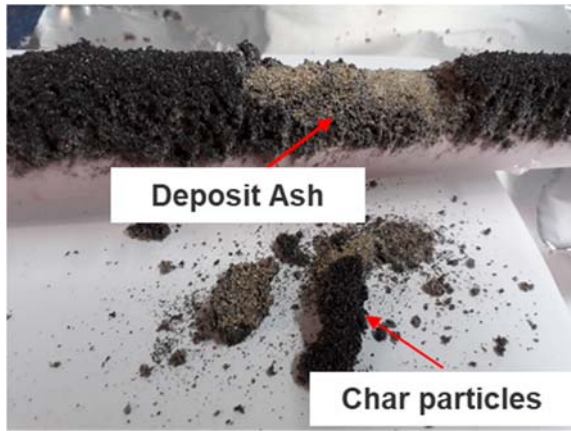


Figure 22: Picture of outer deposit corresponding to M case OD_L15 showing the extent of unburnt particles.

Figure 23: BSE image of ceramic probe cross section OD_L15 corresponding to M.

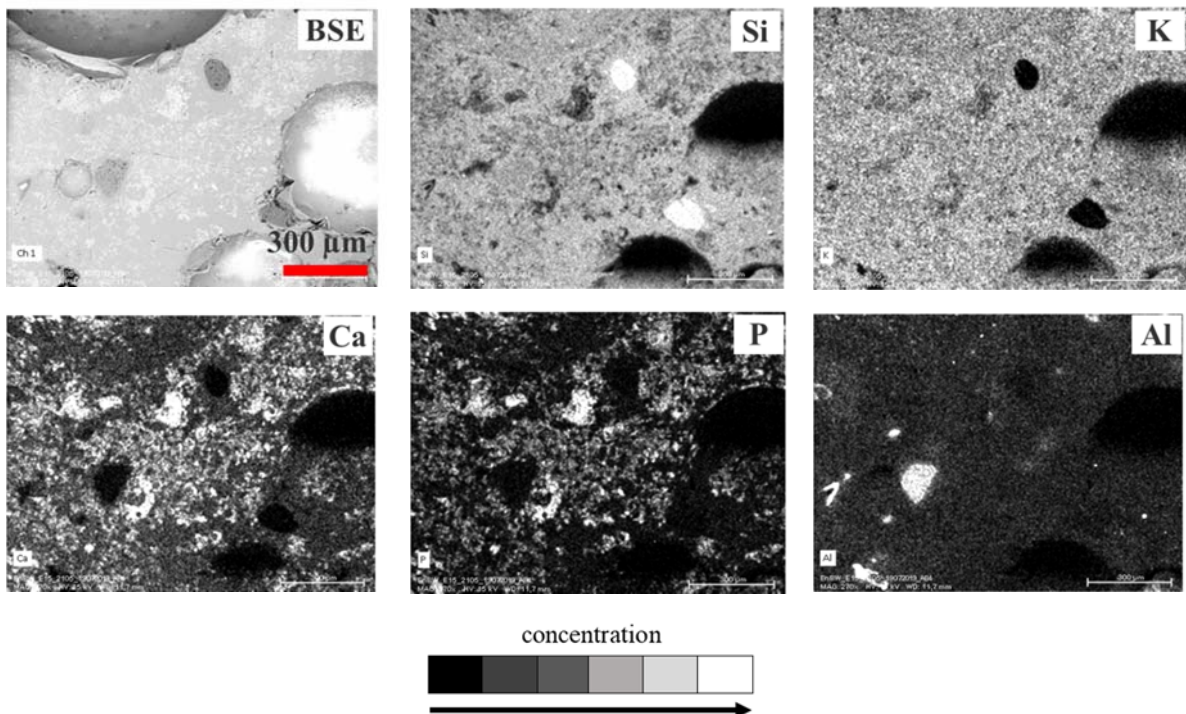


Figure 24: BSE image and element map of fused deposit ash, sample corresponding to mis-canthus (M) case; OD_L15.

4.3.1.3.2 Miscanthus with additive (M+B)

The OD corresponding to the case with additive M+B shows a completely different color: white which is similar to the color of additive as fed, Figure 25. The additive minerals largely dilute the resulting ash system. This is the main reason behind the difference in color.

In general, the deposit is less sintered and loose which signifies the lower contribution of molten or semi-molten ash. Additionally, the presence of unburnt char is significantly suppressed in comparison to the corresponding case without additive, see Figure 22 in comparison to Figure 25.

Figure 26 shows the BSE image of ceramic probe cross-section of OD corresponding to M+B. The surface is almost free of fused deposit and characterized by desecrated individual ash particles, suggesting loose deposit morphology. The individual particles and sintered particles which are big size particle cluster signify that the evolution of molten or semi-molten ash is not completely hindered but the fractional contribution to bulk deposit growth is certainly reduced, in comparison to case M without additive, compare Figure 23.

Figure 27 shows the elemental distribution in a sintered particle, selected here for closer observation. The distribution of Al is observed as concentrated pockets in the silicate slag frame in association with K and Si. These particles are probably K-aluminosilicatic and may include into a molten silicate slag on physical contact.

The presence of aluminum or else aluminosilicatic particles within the silicatic phase is a stochastic outcome because these inclusions are largely governed by the physical contact during flight or over deposition. The choice of the observational area exhibits variation (see Annex 2, section 8.2.2) with regard to the extent of such inclusions. In general, the aluminosilicate inclusion is considered to improve the crystallization or solidification behavior of the silicatic phase. The ash fusion temperature of OD (ash sample) corresponding to the additive case is significantly higher (see section 4.3.1.2) and exceeds the average temperature in the surrounding. The higher ash fusion temperature also justifies the differences in OD morphology which is in accordance to higher contribution of refractory aluminosilicatic compounds.



Figure 25: Picture of OD corresponding to M+B.

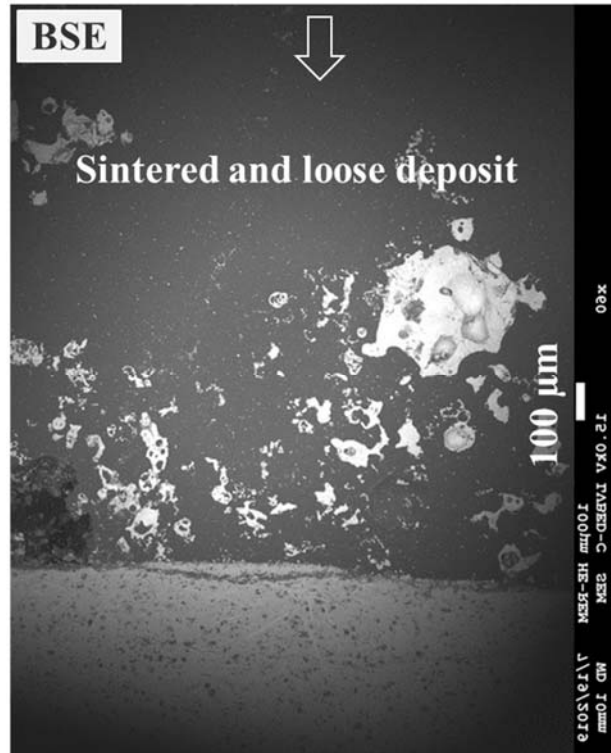


Figure 26: BSE image of ceramic probe cross-section OD_L15 corresponding to M+B.

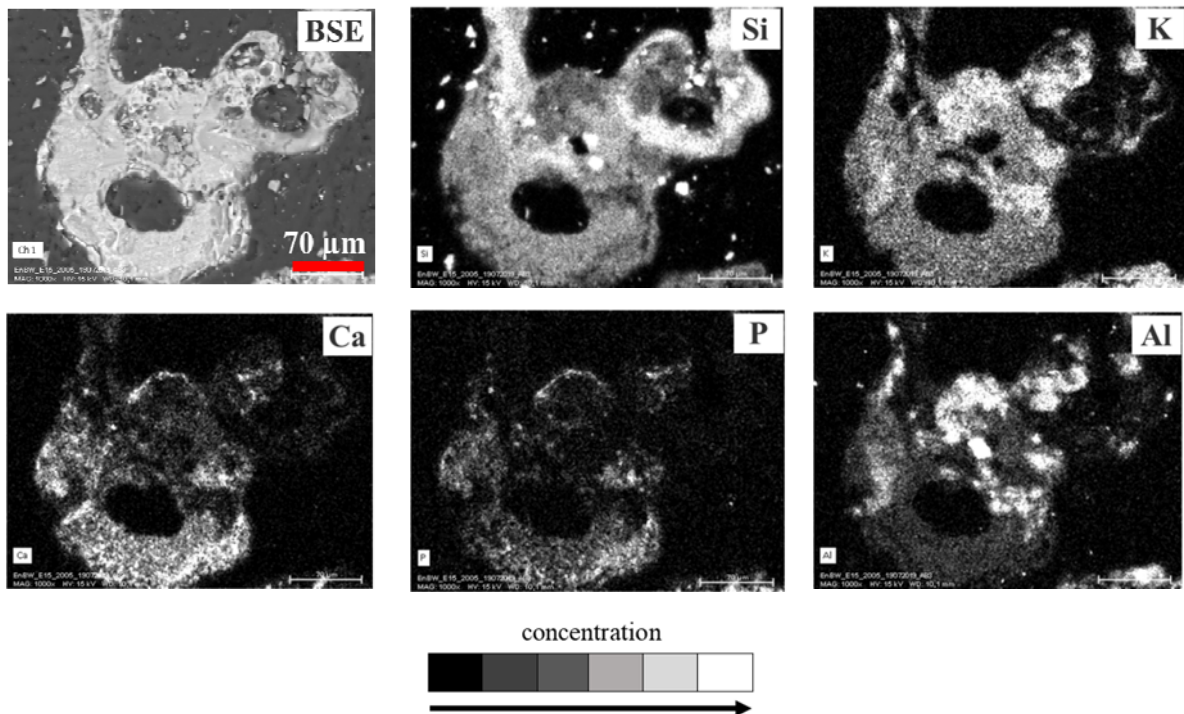


Figure 27: BSE image and element map of sintered ash particle in the deposit, OD_L15 corresponding to M+B.

4.3.1.3.3 Comparative discussion with and without additive

The reduction in char accumulation corresponding to the additive case is likely a consequence of the reduction in molten or semi-molten ash (slag) and accordingly to a lower inclusion-transport-accumulation of unburnt char. The availability of aluminosilicate from the additive in the system inhibits the gaseous potassium-silica (SiO_2) reaction and thus suppresses the formation of potential slag precursors, like low melting K-silicates. Instead, solid K-aluminosilicates are formed. This shift in the ash system chemistry contributed to the change in deposit morphology from fused deposit to loose deposit and as well as substantial difference in the level of unburnt char accumulation. A one to one comparison regarding the level of unburnt char accumulation is biased due to introduction of gas, ≈ 90 kW, during the additive case. The presence of gas could also improve the burnout level at the upper combustion zone which potentially contributes to this. Nevertheless, the ash system of the fired fuel miscanthus remains similar even in presence of gas. Solely the additive mineral may interfere with the ash system chemistry of the fired biomass fuel. The presence of molten or semi-molten ash is clearly suppressed for additive cases. Both, dilution of refractory additive minerals which is irrespective to chemical reaction and the chemical interference of additive mineral kaolinite, contribute to this. Additionally, the impacting solid components which are introduced from the additive erode the sampling surface and thus the growth of a fused layer is avoided.

4.3.1.4 Composition and morphology of inner deposit

The inner deposit (ID) is sampled over a temperature controlled metal surface. Inertial impaction, thermophoresis, and diffusion-condensation contribute to the formation of ID. Coarse ash particles are deposited by inertial impaction. Fine ash or aerosols particles are deposited by thermophoresis and diffusion-condensation. The ID corresponding to test set B and C are discussed in this chapter.

The martensitic grade alloy (X20CrMoV12-1) was the probe material employed for test set B. The surface temperature is maintained at 550 ± 10 °C as set temperature during exposure of ≈ 8 h inside the combustion chamber. The temperature at the exposure location L15 is in the range of 900 – 1000 °C. The austenitic grade alloy 310S is employed for test set C. The surface temperature is 600 ± 10 °C during an exposure of ≈ 5 h. The corresponding temperature at the exposure location (L15) is in the range of 800 – 900 °C.

The influence of the variation of the sampling conditions among cases is rather non-significant. The difference between the cases as discussed here is largely related to the ash system chemistry corresponding to the fired fuel.

The results are organized under two groups namely:

- Biomass cases and
- Biomass with additive cases.

4.3.1.4.1 Methodology for comparative evaluation of micrographs

Figure 28 shows the example micrographs (BSE image) corresponding to metal probe (ID sample). The metal probe (ID sample) is embedded along with the deposit ash over the surface. The epoxy resin (liquid) applied over the probe surface shifts the placement of ash particles which means a wash off, especially of the loose particles along the circumference. The differentiation as luv and lee side in relation to flue gas direction may not make further sense. Therefore, the sampling surface was observed along the whole circumference dividing it in different o'clock sections. To avoid the selectivity or observational bias regarding the choice of the micro-graph in evaluation, the following considerations were applied for each probe sample.

- The sample circumference was observed from multiple directions dividing it in different o'clock sections (see Figure 28 (a)) and corresponding BSE image are generated, see example of 12 o'clock position in Figure 28 (a) and 5 o'clock position in (d).
- All micro-graphs generated corresponding to various o'clock position are rotated to keep the sampling surface beneath, see example rotated BSE image Figure 28 (e) in comparison to BSE image in Figure 28 (d).
- The down arrow in each BSE image denotes the direction of impaction. Within the circle is the magnification corresponding to each BSE image.
- Micro-graphs are generated on different levels of magnification, see example in higher magnification (Magnification x750) in Figure 28 (c) in comparison to Figure 28 (b) (Magnification x60).
- Representative BSE images and element maps are shown along the result and discussion chapter and other micro-graphs are organized in Annex. The scale shown in micro-graphs (BSE image) are harmonized. The variation in scale length from one to other is related to the magnification.
- The main objective here is to outline comparative observations among cases in terms of chemical composition (element maps, qualitative) and morphology (non-scale).

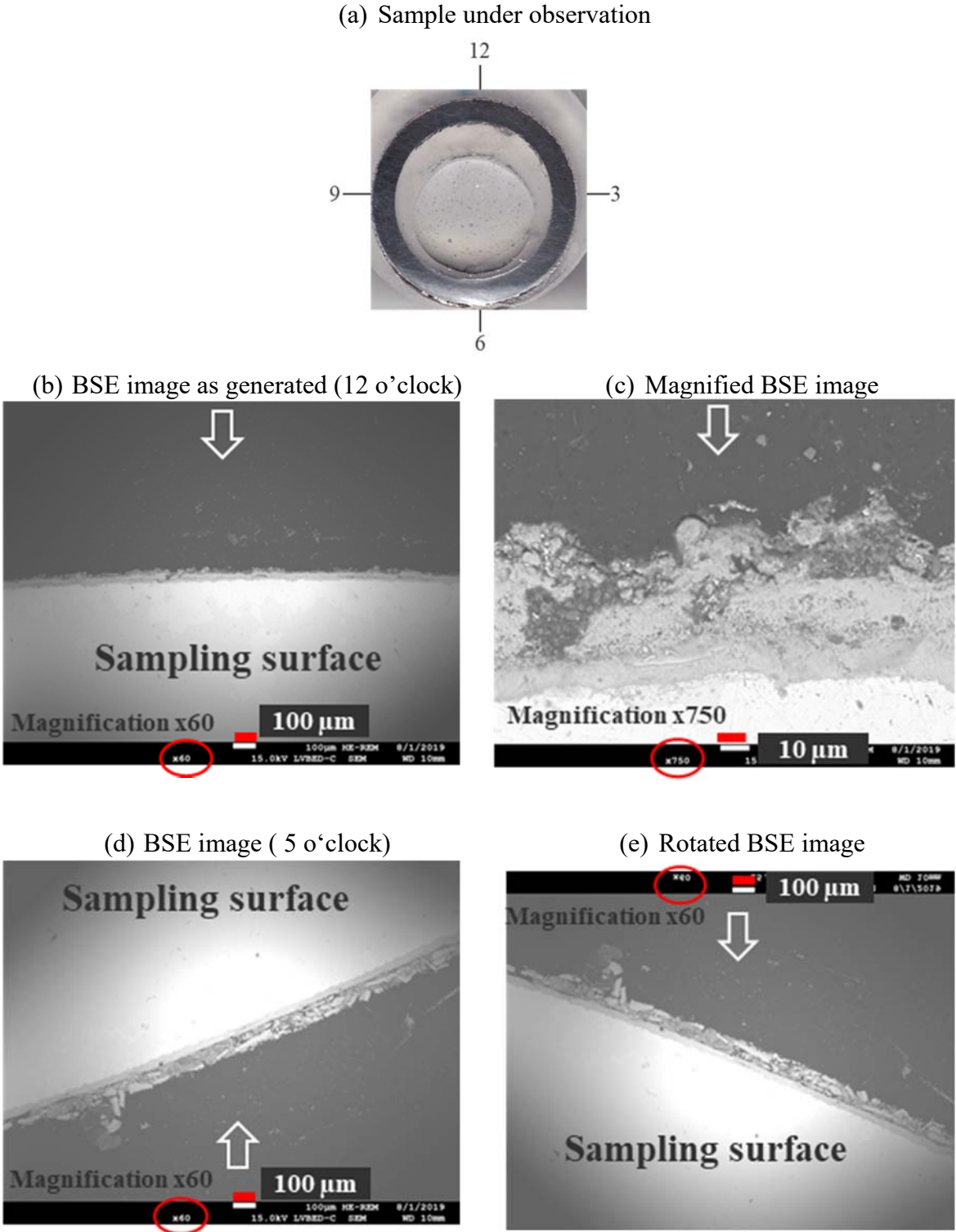


Figure 28: Example of micro-graphs (BSE Image) generated from EMPA and their arrangement for the evaluation of ID_L15 from test set B/C.

4.3.1.4.2 Biomass cases

A clear demarcation of the sampling surface and deposit bulk is often difficult to establish owing to surface oxidation of the alloy-metal of the sampling surface. In this section, the discussion is focused on the morphology and chemical composition of ash particles or else phases found in ID. The difference between those observed across various biomass and biomass blends, as discussed here, is largely related to the ash system chemistry of the fired fuel. The variation imposed by combustion system boundaries, the ash input from fuel, and the sampling bounding conditions including temperature, duration, sampling, or surface conditions, is expected to remain comparatively less relevant to the chemical composition of characteristic ash particles or phases. Figure 29 shows the BSE image and Figure 30 shows the corresponding element map. The evolution of ash particles from molten silicatic slag and condensation of alkali salt vapor species is the main concern regarding ID growth. The ID is here discussed as silicatic deposit and salt deposit.

The silicatic deposit refers to the deposit particle/phases rich in Si and are mostly coarser in size. The silicatic deposit remains as discrete particles exhibiting individual morphological appearance. Spherical particles, particles deformed on impaction, sintered particles, and irregular shape-compact particles constitute the silicatic deposit. The difference between the biomass cases is rather ambiguous. The general and widely formulated understanding related to silicatic deposit particle morphology observed from biomass cases are as follows:

- Spherical particles have a molten history and have solidified prior to impaction.
- Deformed particles suggest a molten or semi-molten phase during impaction.
- Sintered particle cluster signifies at least one of the particle in cluster was in molten or semi-molten state during impaction.
- Compact particles represent the ash particles which escaped the flame zone in solid phase.

The salt deposit refers to the deposit particle or phase rich in either S or Cl. They are mostly fine ash particles or aerosol. The salt deposit is often mentioned as a layer growing outward adjacent to the sampling surface. Nielsen et al. [63] argued that the morphological appearance of salt deposit as layer is a subject of picture magnification. In sufficiently magnified SEM pictures the K_2SO_4 appears to be a sponge-like matrix of sub-micron particles. KCl remains as individual angular particles of primarily 1 – 2 μm [63].

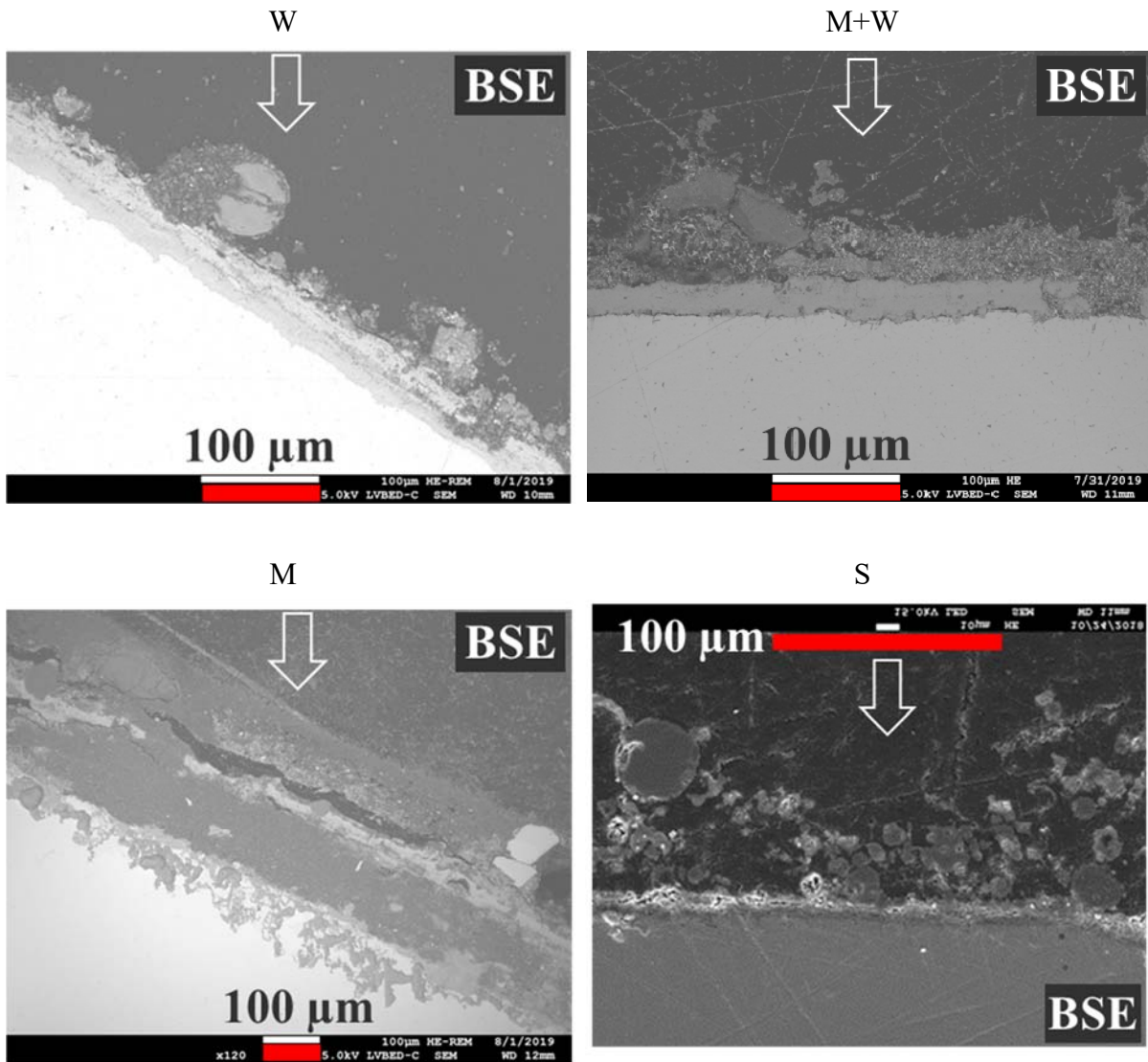


Figure 29: BSE image of sample cross-section ID_L15 corresponding to different biomass cases, including: W, M+W, M, and S.

Figure 30 and Figure 31 show element maps corresponding to wood (W), mix (M+W), and miscanthus (M) case from test set B, respectively. They show the elements relevant to characteristic composition of silicatic deposit and salt deposit. Figure 32 shows the element map corresponding to straw (S) case from test set C showing elements relevant to characteristic composition of both silicatic deposit, Si, Al, Ca and K, and salt deposit, S and Cl. Other BSE images and element maps are organized in Annex 2 (see W case section 8.2.3, M+W section 8.2.4, and M section 8.2.5 and see S case 8.3.1).

The observation made across different cases with respect to characteristic composition of silicatic and salt deposit are listed below:

- Si rich particle/phase are observed in combination with one or many of the elements like K, Ca, or Al. Such particles or else phase are expected to derive from the silicatic slag phase and the characteristic particle is found in all cases. It is generally observed that beside Si and K, the composition of spherical particles is often associated with higher distribution of Ca or Al. While the sintered non-spherical particles are mostly dominated by distribution of K and Si. The silicatic particles which may remain attached to the sampling surface in the exposure condition lose their attachment as the probe is pulled out after exposure and cooled to the room temperature. It is observed that silicatic ash particles which remain as deposit ash has a tendency to displace and wash off when liquid epoxy resin is applied over the sampling surface. It is noted that the visual impression regarding the dominance of silicatic particles across different samples therefore do not provide any quantitative understanding. Deposit layers rich on Si are observed, distinctively in miscanthus (M) cases. There is no overlapping presence of any other element suggesting it to be a collection of fine silica (SiO_2) particles. Similar, silicon (Si) rich discrete particles are also observed in W case (see element maps in Annex 2 section 8.2.3) and mix (M+W) (see element maps section 8.2.4 in Annex 2) but their overall dominance is clearly less than in M case (see element maps section 8.2.5 in Annex 2).
- The overlaying presence of K and S characterizes the salt deposit corresponding to W case (see element maps in Annex 2 section 8.2.3) and M+W case (see element maps in Annex 2 section 8.2.4) and see respective cases in Figure 31. The overlaying presence of K and S appears mostly as a layer grown adjacent to the metal surface. Overall observation suggests that salt deposits corresponding to W and M+W cases is K-sulfate dominated. The M case shows strong presence of Cl while S is largely limited (see element maps in Annex 2 section 8.2.5) and see respective cases in Figure 31. The overall observation suggests that salt deposits corresponding to M cases is dominated by K-chloride. The K-chloride does not appear specifically as layer grown adjacent to the sampling surface but as continuous individual phase alongside the silicatic deposit. The straw (S) case shows the presence of both S and Cl (see element maps in Annex 2 section 8.3.1) and see Figure 32. The salt deposit appears for both as distinct layer grown adjacent to the sampling surface, over the surface of coarser ash particles which are mostly as K-sulfate and as continuous

phase of fine individual particles which are mostly as K-chloride. Overall observation suggests that both K-sulfate and K-chloride constitute the salt deposit. For all cases, S appears also in combination with Ca while Cl is specifically in combination with K.

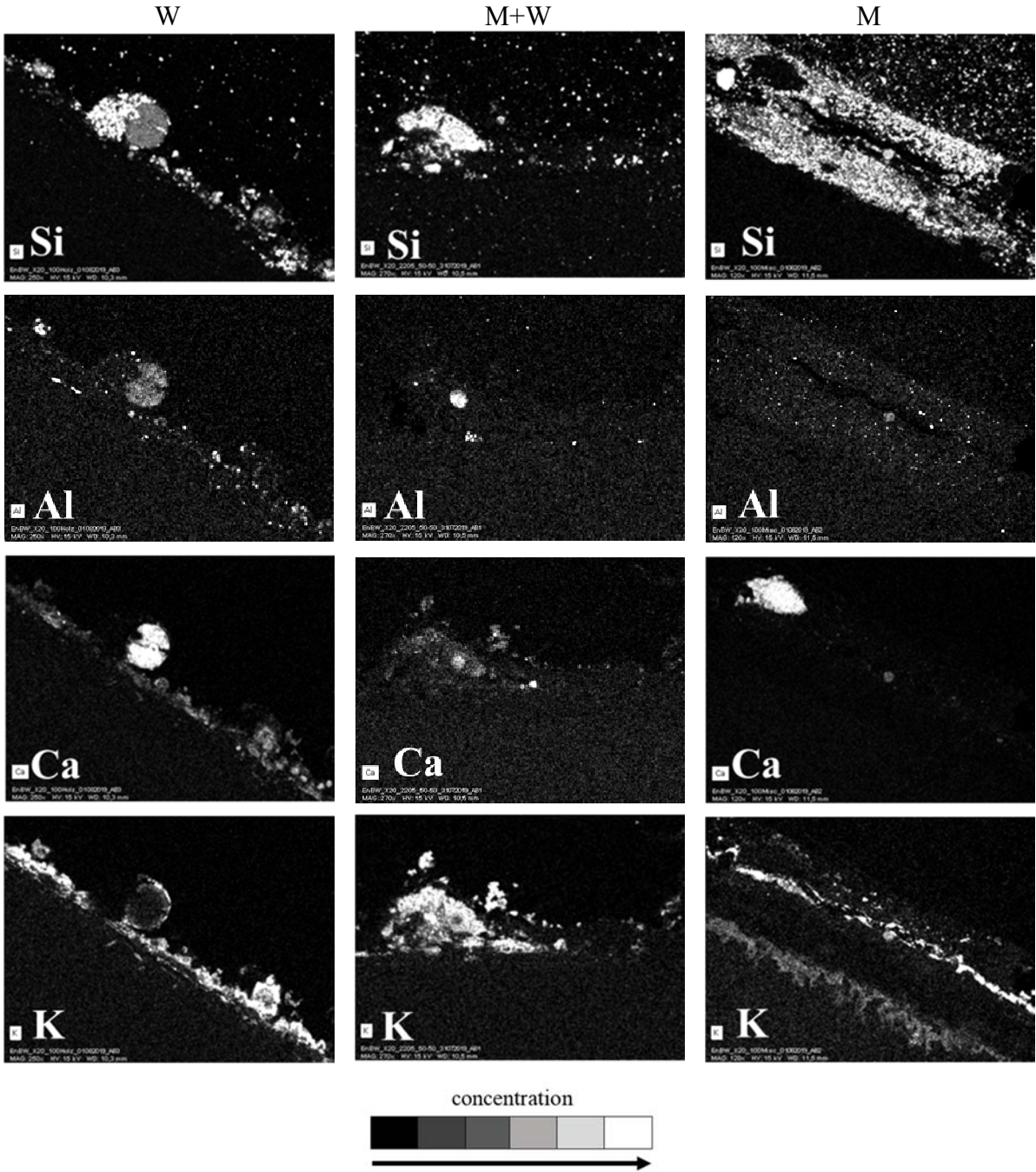


Figure 30: Element map corresponding to wood (W), mix (M+W) and miscanthus (M) cases from test set B. The elements relevant to characteristic composition of silicatic deposit are shown here, corresponding BSE image in Figure 29.

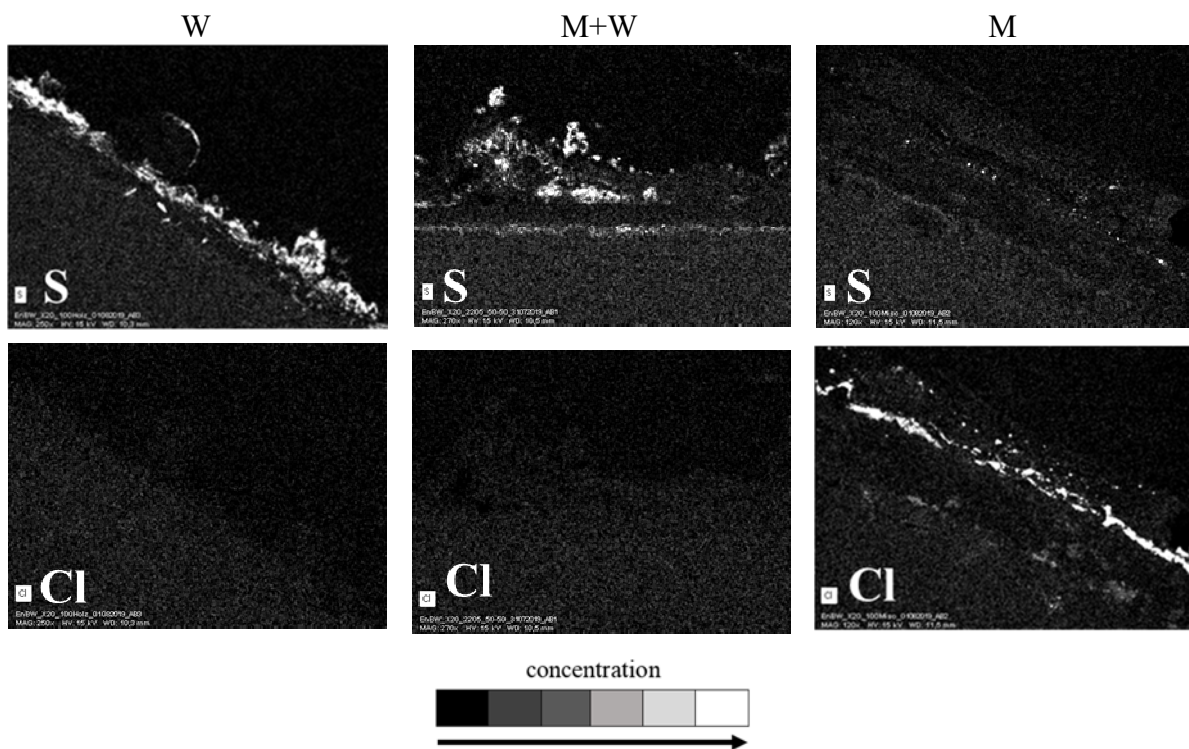


Figure 31: Element map corresponding to wood (W), mix (M+W), and miscanthus (M) cases from test set B. The elements relevant to characteristic composition of salt deposit are shown here, corresponding BSE image in Figure 29.

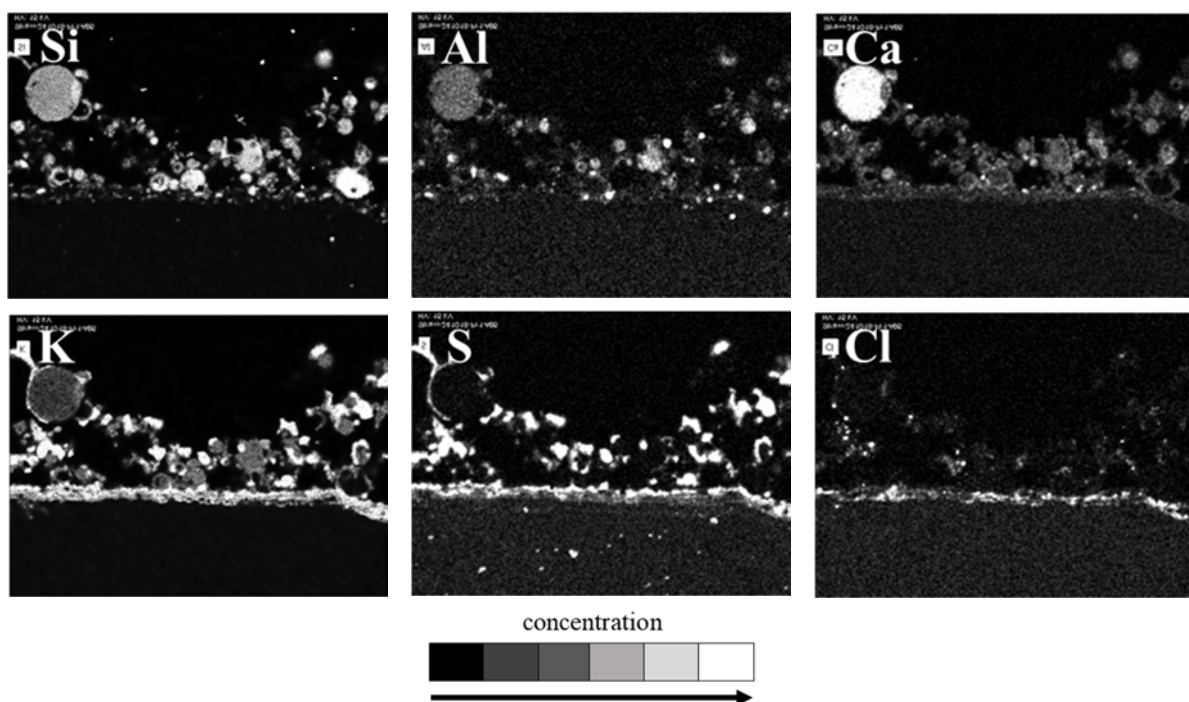


Figure 32: Element map corresponding to (straw) S case from test set C. The elements relevant to characteristic composition of silicatic deposit (on top) and salt deposit (below), corresponding BSE image in Figure 29.

4.3.1.4.3 Discussion: Inner deposit growth

The transport of alkali salt species to the sampling surface is mainly considered to be diffusion-condensation driven as they remain in the gas phase in the surrounding hot flue gas. The sulfation reaction overlaps with this diffusion-condensation process. The sulfation reaction is favored near the vicinity of the sampling surface compared to the surrounding (global) atmosphere. This probably would explain the dominance of K-sulfate as salt deposit over the sampling surface.

The gaseous K-species reaching the sampling surface eventually convert to K_2SO_4 . The sulfation could occur near the vicinity of the sampling surface prior to deposition (homogeneous sulfation) or over the sampling surface in-situ, over time (heterogeneous sulfation) [124]. The KCl (g) which could have escaped the sulfation reaction along the diffusion-condensation process may remain as K-chloride (s). The sulfur to chlorine ratio (as $2S/Cl$) is lower than 4 for all test fuels suggesting that the stoichiometric demand for sulfation of all available KCl is not fulfilled. Nonetheless, the K-sulfate dominates the salt deposit corresponding to W and mix M+W case. K-chloride is almost completely absent. The K-chloride is distinctive only in M and S (straw) case. Comparatively, the K-chloride is more prominent² in M case while the K-sulfate is still relevant³ in S (straw) case. The chlorine content is 0.03, 0.05, 0.09, and 0.27 (wt.-%, daf.) in W, mix M+W, M, and S (straw), respectively.

It is observed that the presence or absence of K-chloride in salt deposits does not show a direct correlation to the absolute chlorine content or the sulfur-chlorine stoichiometry of the fired fuel. And there is no apparent reason why KCl in M case is not converted to K-sulfate along the diffusion-condensation process as it does during W, mix M+W, and partly during S (straw) case.

It may be, that the uniqueness of the M case is the consequence of unburnt char accumulation in the deposit front. The significance of char accumulation is highlighted in OD growth corresponding to M case and as well observed visually distinct in the S (straw) case. The ID growth is also a consequence of a similar ash system and the deposit growth front is essentially impacted by similar particles. The difference to OD growth is that the ID growth exhibits the phase

² Qualitative observational conclusion: None of the observational areas shows substantial presence of sulfur (S)

³ Qualitative observational conclusion: At some observational area K-chloride is absent, the area occupied by sulfur (S) distribution is bigger than the area occupied by chlorine (Cl) in a given micro-graph and K-sulfate as layer is thicker than K-chloride in all observational areas.

transition of impacting ash components, i.e. solidification of molten ash (slag) droplets and condensation of vapor K-species.

Apparently, the level of unburnt char in the exposure surrounding among cases should be comparable. The difference in the particle size of the fired fuel and the combustion boundaries could not satisfactorily justify why the char transport or accumulation is distinctly specific to miscanthus (M) or partly for straw (S) case. The substantial char transport-accumulation is a consequence of its molten ash dominated exposure surrounding.

The temperature at the probe exposure location (≈ 950 °C) is closely comparable to the ash fusion temperature of miscanthus fuel ash with ϑ_{DT} : 870 – 970 °C which is lowest among all combusted fuels. The molten ash, mostly silicatic slag derived, creates a sticky ash layer as a growing deposit front. The solid ash particles and/or un-burnt char impacting the surface is prone to accumulate. The thick and continuous layer of SiO₂ particles as a silicatic deposit also unique to M cases is probably as well the consequence of such deposit growth as well as a reason for KCl in the salt deposit.

Another herbaceous fuel straw also shows distinct presence of KCl salt. In comparison to miscanthus (M), the ash fusion temperature of straw lab ash is higher at ϑ_{DT} : 1070 – 1130 °C. The temperature at the probe exposure location corresponding to S (straw) cases is ≈ 900 °C and little below the ash fusion temperature. The char borne KCl may as well contribute to inner deposit growth in the straw case, comparatively to a lesser extent as observed from the deposit samples discussed here.

Much of KCl is considered to be released during char combustion. The unburnt char therefore brings KCl along. The organic fraction of char is eventually consumed over the probe surface where $\vartheta_{surface} \approx 550$ °C. KCl (s/l) remains along with other ash inorganics. This pathway of KCl (s/l) deposition is mainly driven by internal impaction and along this pathway the sulfation is probably limited.

The amount of fuel-Cl in a given biomass fuel, the extent of sulfation allowed by sulfur-chlorine stoichiometry, the melting behavior of the corresponding ash system, and the temperature of exposure surrounding are important parameters that contribute to the growth of inner deposit. The molten ash facilitated char associated KCl transport is apparently a concern for herbaceous fuel characterized by low ash fusion temperatures.

The total flux of vapor alkali species reaching the surface is most relevant in salt deposit growth other than the content of sulfur and chlorine in the fuel. With lower flux, the vapor alkali species

are eventually sulfated. With the flux high enough to exceed the achievable sulfation, K-chloride may remain in deposit along with K-sulfate. The ash system chemistry globally (at flue gas temperature regime) keeps the chlorine as KCl (g) as the 2S/Cl molar ratio corresponding to all fired fuel is <4 . It probably implies that the sulfation is locally favorable near the sampling surface. The sulfation of KCl achievable near the sampling surface along with diffusion-condensation or in-situ over time determines the co-existence of K-sulfate and K-chloride or dominance of one or other. Christensen et al. [124] studied the formation of sub-micron particles in straw fired boiler (experimental and equilibrium modeling study) and as a conclusion stated that the eventual content of SO_2 and HCl in the flue gas and the content of KCl and K_2SO_4 as fine-mode aerosol is determined by equilibrium of sulfation reaction at $812 \pm 10^\circ\text{C}$. The temperature of the exposure surrounding is higher than this equilibrium temperature which suggests that the sulfation largely proceeds near the vicinity of the sampling surface.

4.3.1.4.4 Biomass with additive

Figure 33 shows the BSE image corresponding to cases biomass with additive, namely M+B from test set B and S+D from test set C. Figure 34 and Figure 35 show the element maps, respectively. Additional BSE images are organized in Annex 2 (see M+B case section 8.2.6 and S+D case section 8.3.2).

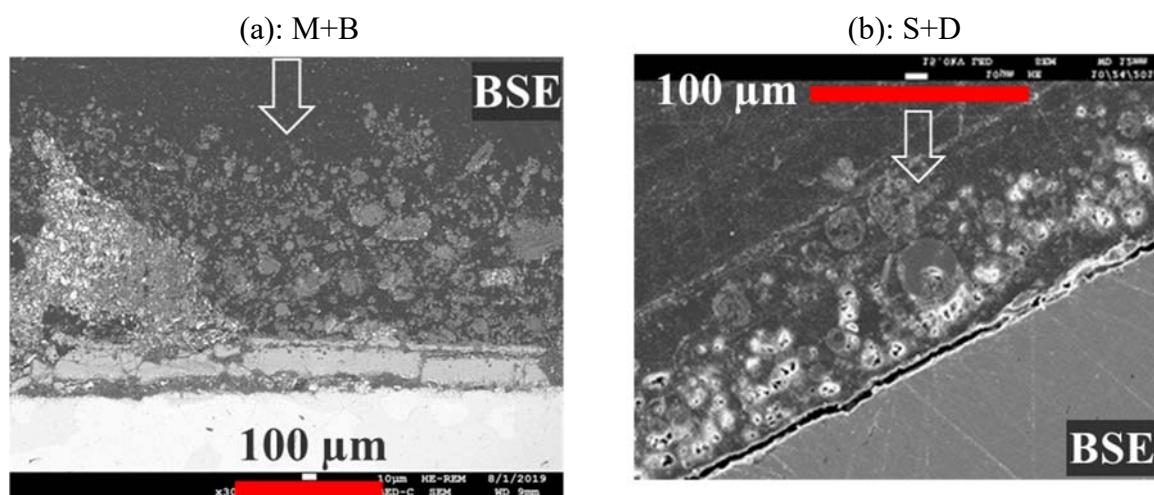


Figure 33: BSE image corresponding to cases biomass with additive: (a) M+B from test set B and (b) S+D from test set C.

Overall, the following general observation can be made corresponding to cases with additive, i.e. M+B and S+D.

- The Si dominated silicatic deposit in M case (see earlier discussion in 4.3.1.4.2) is replaced by K-Al-Si dominated distribution in M+B. In the S+D case, the most noticeable difference in comparison to S case (see earlier discussion in 4.3.1.4.2) is the increased intensity of Al distribution in discrete particle or phases showing presence of Si, K, or Ca. In some locations, fine particles characterized by K-Al-Si distribution are also a distinct observation. Additive adds refractory aluminosilicate minerals to the system and is ideally expected to promote high melting K-aluminosilicate formation instead of K-silicates. The significance of slag derived silicatic particles are expected to reduce. The expected influence can be qualitatively justified but the distinction between the mere dilution of additive originated aluminosilicate mineral particles and ash-additive mineral interaction remains rather speculative.
- The influence of additive on salt deposit is rather conclusive. The chlorine (Cl) is almost completely absent in additive cases while sulfur (S) distribution is still distinctive. The overall observation suggests that the significance of salt deposit growth is lower in case with additive and the composition is characterized by the absence of K-chloride.

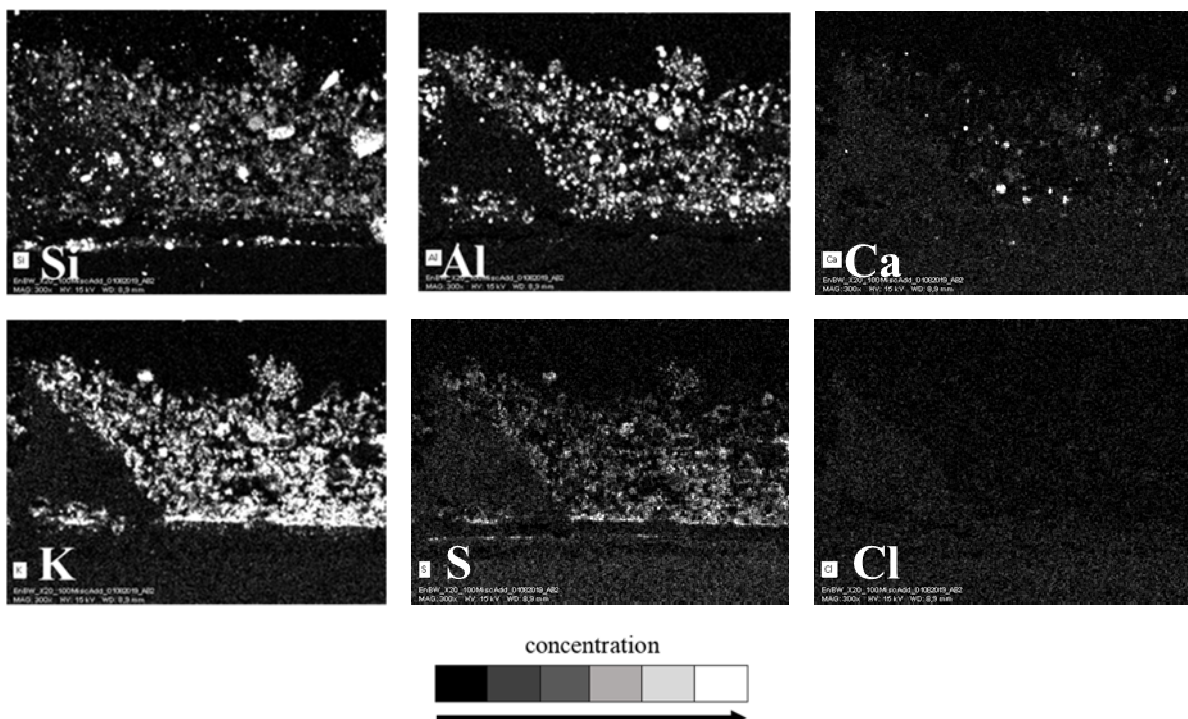


Figure 34: Element map corresponding mix M+B case from test set B. The elements relevant to characteristic composition of silicatic deposit (on top) and salt deposit (below). Corresponding BSE image in Figure 33.

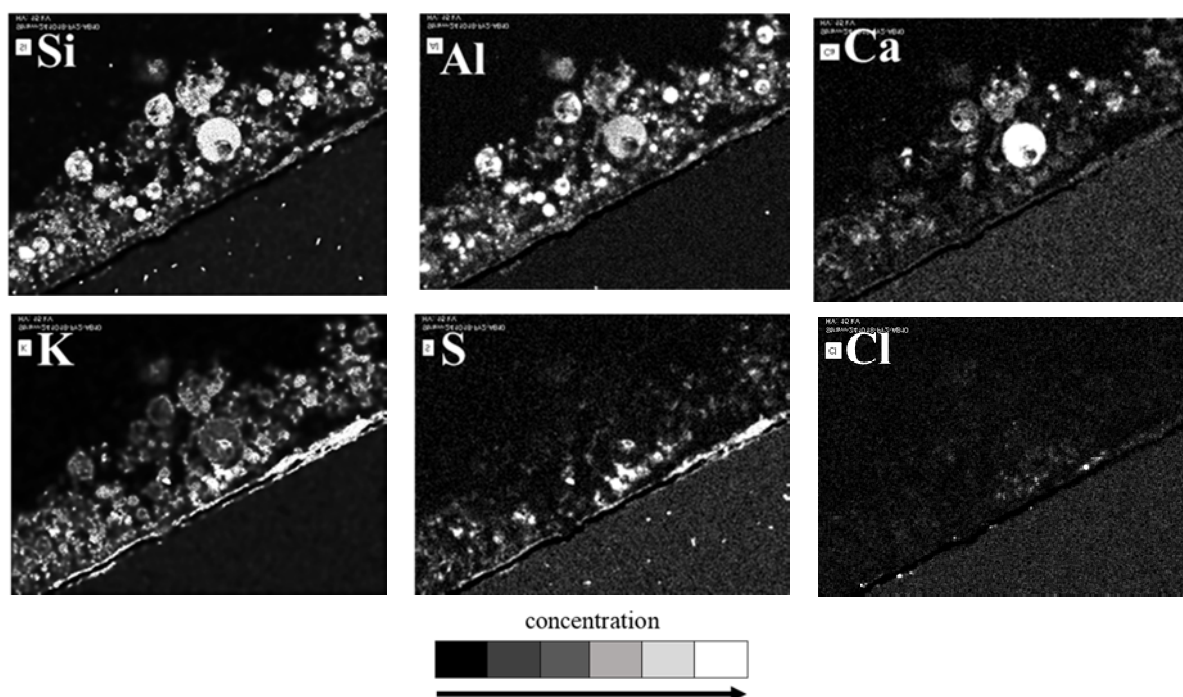


Figure 35: Element map corresponding straw case with additive (S+D) from test set C. The elements relevant to characteristic composition of silicatic deposit (on top) and salt deposit (below). Corresponding BSE image in Figure 33.

4.3.1.4.5 Discussion: Influence of additive on inner deposit growth

The conclusion with respect to silicatic deposit is ambiguous due to substantial dilution of the existing biomass ash system by additive derived mineral components. Nonetheless, it can be fairly conclusive with regard to suppression of chlorine in ash/deposit and is largely explained by the alkali capture reactions.

The salt deposit growth is mainly diffusion-condensation driven supported by the flux of condensable alkali vapor species reaching the sampling surface. The capture of gaseous alkali species reduces the overall amount of alkali vapor in the system and associated salt deposit growth over the sampling surface. The capture reaction is not only specific to KCl (g) but also to other gaseous alkali species, like KOH (g) . Consequently, the ratio of K-species/available SO_2 in the system is lower in comparison to the corresponding case without additive. This situation favors the sulfation that occurs along the course of deposition. Either by direct capture or by indirectly promoted sulfation the presence of additive pushes the chlorine to the gas phase in the process, thereby its retention in ash is reduced.

The co-feeding of additive with the fuel facilitates the capture of gaseous alkali species as soon as they are released, i.e. already in the combustion zone. This early capture reaction suppresses the formation of slag precursors, mainly K-silicate, at its origin. Consequently, the fraction of

molten ash in the system is lower. This means the probability of char transport and the accumulation to the deposit front is minimized and so does the amount of K-chloride deposition via this pathway.

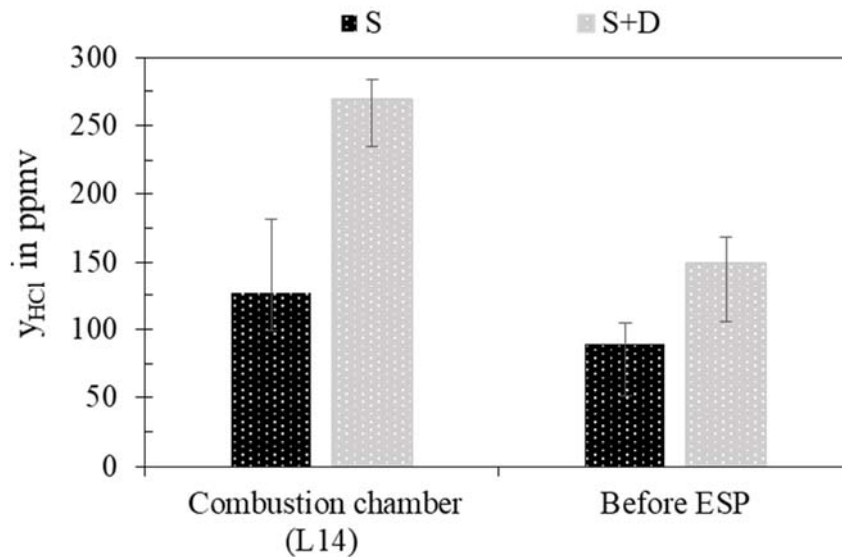


Figure 36: HCl concentration (in ppmv, corrected to 6 vol.-% O₂) measured in flue gas corresponding to straw (S) case and straw pre-mixed with additive (S+D).

Introduction of kaolinite to the biomass ash system is known to change the fate of chlorine. It is well established that the escape of chlorine as HCl to the flue gas is promoted owing to KCl-additive (kaolinite) capture reaction. Figure 36 shows the HCl concentration measured inside the combustion chamber (L14, i.e. ~0.17 m above L15) and before ESP corresponding to straw (S) case and straw pre-mixed with additive (S+D) case. The increase in HCl concentration justifies the possibility of lower chlorine retention in ash/deposit in presence of additive in the system. It is noted that the flue gas measurement location significantly influences the concentration of HCl. The author believes that the decrease in HCl concentration outside combustion chamber is related to its recapture of HCl in ash probably by free CaO.

4.3.1.5 Influence of salt deposit on fireside corrosion

The corrosion resistance of the given metal-alloy depends on its ability to form or maintain the protective surface oxide scale. In iron (Fe) based alloy, the alloying element chromium (Cr) is expected to provide the protective oxide scale. The corrosion resistivity offered by the surface oxide scale is related to the type of alloy. In test set B, the probe metal is a martensitic alloy X20CrMoV12-1 and in test set C austenitic alloy 310S. The martensitic grade alloy are characterized by mixed oxide scale, i.e. Fe-/Cr-oxides, while austenitic grade alloy are characterized to selectively form Cr-oxide scale.

The growth of oxide scale is influenced mainly by the surrounding flue gas atmosphere, surface temperature and the duration of exposure. Fireside corrosion refers to the interference of flue gas and salt deposit in the growth of surface oxide scale. The corrosion severity is related to the chemical or physical integrity of the oxide scale.

In this chapter, the corrosion behavior is discussed corresponding to the alloy-metal probe surface after exposure. The discussion is categorized according to the alloy material, Martensitic alloy corresponding to test set B, and Austenitic alloy corresponding to test set C. To discuss the corrosion severity and mechanism related to salt deposit species, for each case the results are organized as:

- Biomass cases
- Biomass with additive cases

4.3.1.5.1 Biomass cases

Martensitic alloy (sample from Test set B)

Figure 37 shows the BSE image and element map of alloy-metal probe cross-section from W, M+W, M cases.

The fired fuel does not contain substantial amounts of Fe and Cr. Fe and Cr observed outside the oxide scale are likely to be the pieces (spall) from the material surface, broken off probably in the sample preparation process, grinding and polishing. The tendency of such spall is more visible for samples which experience substantial corrosion during exposure. The lack of overlaying oxygen (O) signifies that spall are consequence of sample preparation. The general understanding is that the alloy elements (Fe, Cr) that move out of the alloy-metal substrate in the exposure environment would be oxidized or remain in combination with some ash borne elements. The oxide scale thickness from one to another case is out of scope for the discussion made here.

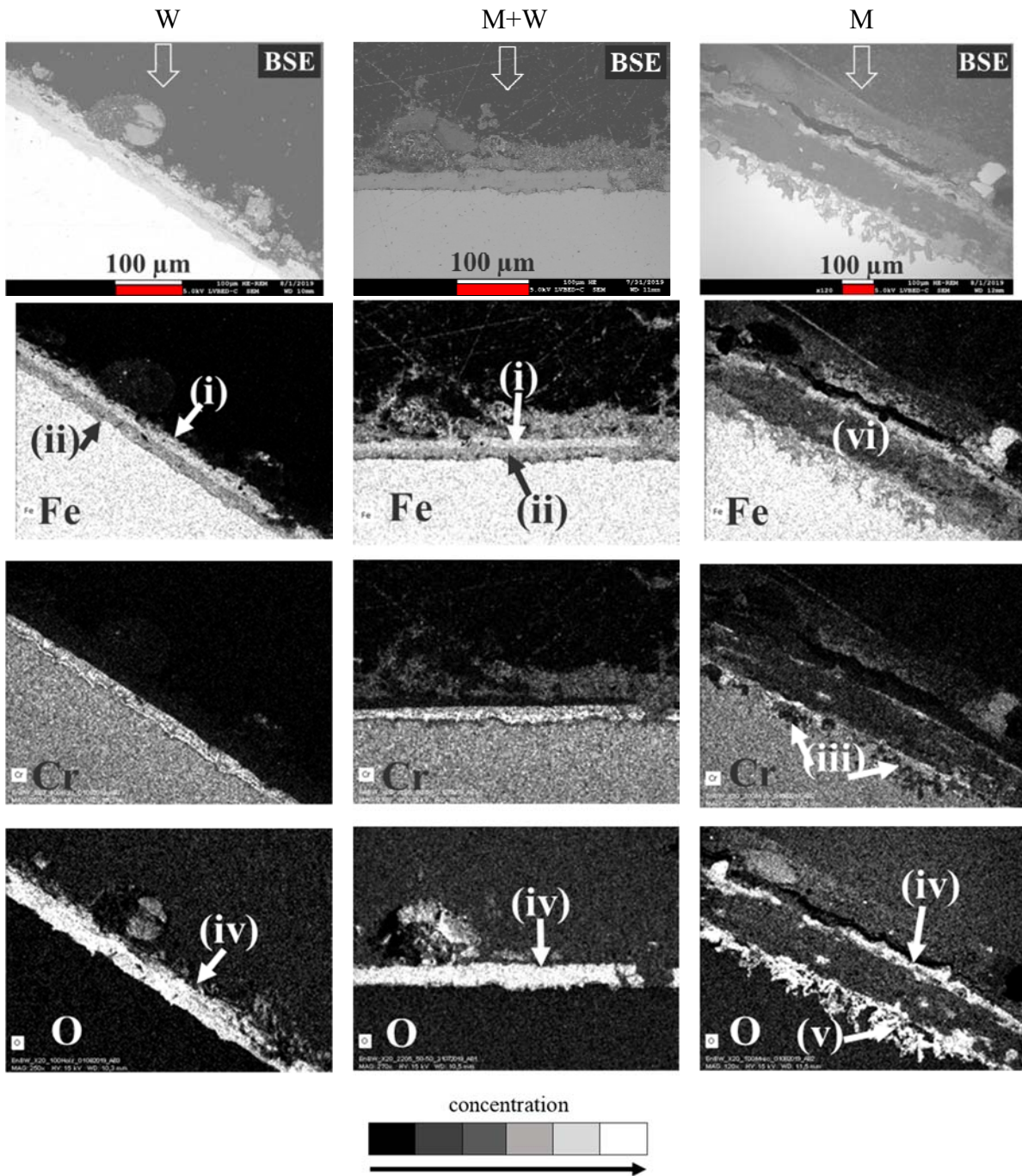


Figure 37: BSE image (left) and corresponding element map: Fe, Cr, and O relevant to material corrosion (i) Fe-oxide, (ii) Fe+Cr-oxide, (iii) Cr-loss, (iv) surface oxide scale, (v) substrate oxidation, and (vi) ash.

The following comparative discussion is made with regard to chemical and physical integrity of oxide scale knowing that the two layered oxide scales are typical for the test material X20, martensitic grade steel. Following observations can be made:

- The corrosion (surface oxidation) in the exposure atmosphere is characterized by outer Fe-oxide scale and a Cr+Fe-oxide beneath. Both, W and M+W, fundamentally show similar oxide scale composition.
- The detachment of oxide scale with the alloy substrate is relatively more visible for mix M+W case.
- The oxide scale corresponding to M case is destroyed and is completely detached from the alloy substrate. The loss of chromium from the alloy substrate and Fe-oxide at such areas signifies accelerated internal oxidation.

The moisture content in the fired fuel is in a range of 6 – 8 %, significant variation in H₂O concentration in the flue gas among cases is therefore not expected. The maximum calculated HCl concentration assuming all fuel-Cl conversion to HCl is 25, 52, and 91 ppmv and the maximum calculated SO₂ concentration assuming all fuel-S conversion to SO₂ is 23, 45, and 86 ppmv for W, mix M+W, and M, respectively. The concentrations of corrosion relevant flue gas species (fuel born) are lower to satisfactorily explain the difference in corrosion activity and severity among the cases. The author argues that the difference in corrosion activity among cases is basically related to the salt deposit and its chemical form i.e. K-chloride and/or K-sulfate.

The BSE images from different observation positions are shown, see Figure 38 (W case), Figure 39 (M+W case), and Figure 40 (M case), in pair either with S or Cl to signify the chemical form salt deposit in corresponding cases. Following observation/arguments are presented.

- Figure 38 shows the BSE image and corresponding element map of S as pair from W case. As discussed earlier the presence of chlorine is non-significant in W case. The oxide scale corresponding to W case appears to retain its integrity with some local discontinuity. The observation does not support any substantial interference of salt components from deposit with the oxide layer or alloy substrate, beneath. There is no substantial indicated sulfur combination with the metal-alloy element, Fe or Cr. The sulfur element map overlaps with potassium element map and basically corresponds to the presence of K-sulfate as salt deposit.
- Figure 39 shows the BSE image and corresponding element map of S as pair from mix M+W case. As discussed earlier the presence of chlorine is non-significant in mix M+W case. The attachment of oxide scale to the alloy substrate corresponding to mix M+W case appears to be weaker for oxide scale detachment. The sulfur (S)

above the oxide layer remains in combination with K, apparently K-sulfate. S beneath the oxide layer remains in combination with metal-alloy element, mainly Fe. The overall observation suggests the formation of metal, i.e. Fe, sulfide beneath the oxide scale in the inner oxide-substrate interface. This signifies the sulfur corrosion attack in relation to the presence of K-sulfate salt.

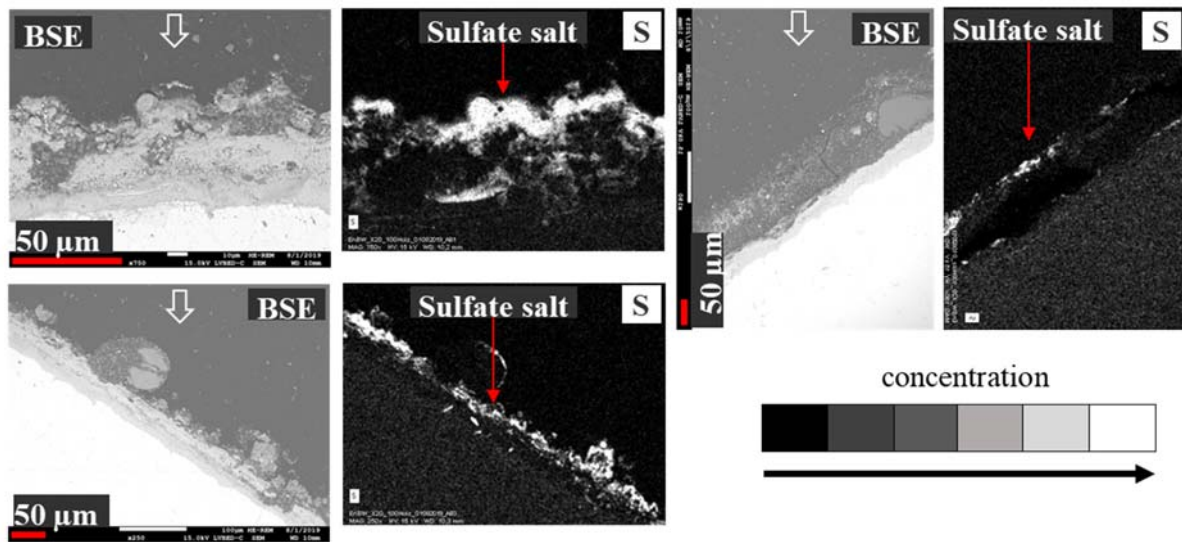


Figure 38: BSE image and element map of sulfur (S) shown as pair. Sample probe for ID_L15 cross-section corresponding to W case. Each pair corresponds to different observation locations of a same probe sample.

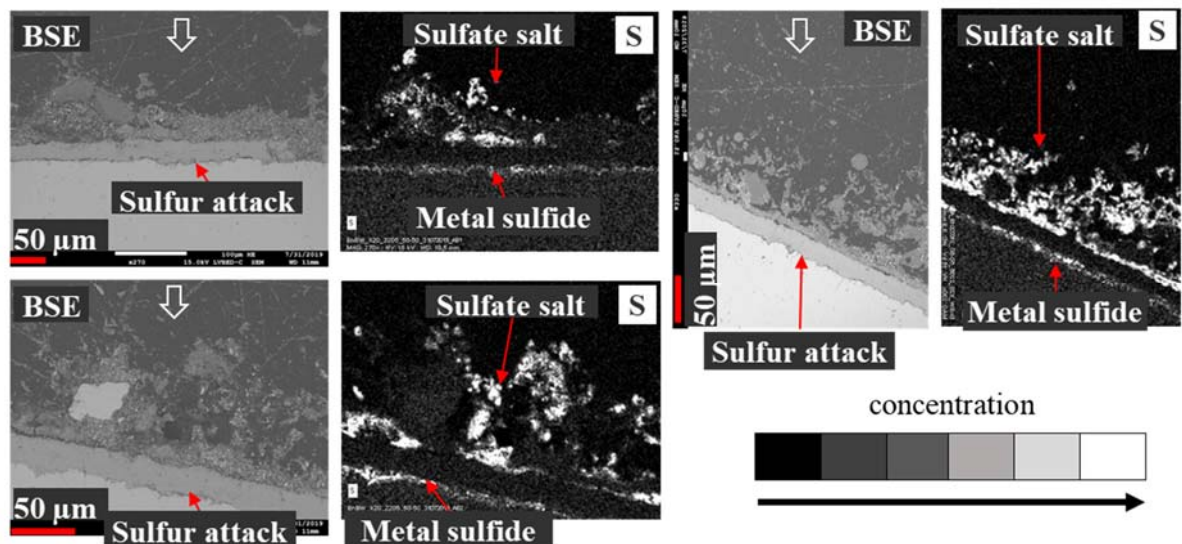


Figure 39: BSE image and element map of sulfur (S) shown as pair. Sample probe for ID_L15 corresponding to mix M+W case. Each pair corresponds to different observation locations of a same probe sample.

- Figure 40 shows the BSE image and corresponding element map of Cl as pair from M case. As discussed earlier the presence of Cl is distinct for the M case. The oxide scale corresponding to M case is destroyed and completely detached from the alloy substrate. This loss of uniform oxide scale over the surface signifies the Cl corrosion attack in relation to the presence of K-chloride. The corrosion mechanism is characterized by the loss of Cr from the alloy substrate which is a typical case of accelerated *active oxidation*. The ash element potassium, see element map K in Figure 30 for M case, appears to be in combination with the alloy-metal element suggesting a direct salt-alloy interaction.

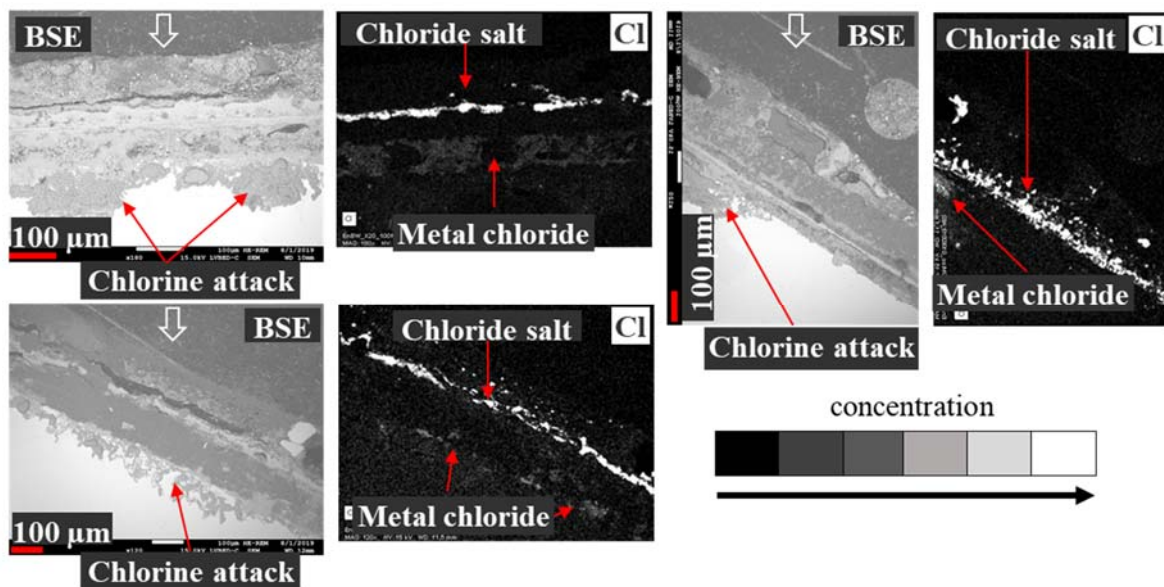


Figure 40: BSE image and element map of chlorine (Cl) shown as pair. Sample probe for ID_L15 corresponding to M case. Each pair corresponds to different observation locations of a same probe sample.

The corrosion severity related to biomass fuels is often categorized based on the $2S/Cl$ molar ratio. The $2S/Cl$ molar ratio of the test biomass fuel is ≤ 2 and represents high corrosion severity related to the fuel. Nonetheless, the overall observation suggests that the corrosion activity across the cases clearly shows different levels of severity. The corrosion severity probably correlates with the Cl content in the corresponding fuel and more to the flux of condensable K-salt species reaching the material surface in corresponding case or exposure condition.

The W and mix M+W cases which show regular surface oxide scale do not show a substantial difference with regard to oxide thickness. But the attachment of oxide scale with the alloy substrate appears to be compromised in mix M+W case which is probably related to the formation

of metal sulfides beneath the oxide scale. In both, W and mix M+W, the exposure scenario shows that the sulfation of KCl apparently occurs along the deposition process. The HCl release near the vicinity of oxide scale may provide molecular Cl and increases the oxidation rate but appears not to invoke *cyclic oxidation*. Thereby, the oxidation front does not penetrate into the alloy substrate. The vertical cracks and local discontinuity is probably due to thermal or mechanical stress during exposure or in the sample preparation process. Eventually, in both, W and mix M+W, K-sulfate exhibits the ash related fire side corrosion risk. And such K-sulfate is expected largely originating from the sulfation of KCl along the deposit growth.

The M case shows a typical case of *active oxidation* and induced by molecular Cl. The distinct presence of KCl in deposit is a severe corrosion risk as it can establish a direct salt-alloy interaction thus leaving the molecular chlorine in-trapped within the alloy matrix to establish a close loop of metal-chloride and metal-oxidation formation. The transport of KCl via char (earlier discussion in 4.3.1.4.2) and further oxidation of glowing char over the sampling surface further accelerates the risk by creating local peak temperatures and corrosive atmosphere (lack of oxygen).

Austenitic alloy (sample from Test set C)

Figure 41 shows the BSE image and element map of alloy-metal probe cross-section from straw (S) case. The surface oxide scale corresponding to austenitic is significantly thinner in comparison to martensitic oxide scale. This difference mainly signifies the alloy oxidation behavior, i.e. lower oxidation rate with increasing alloy grade and higher Cr content. The oxide scale of austenitic are selectively Cr-oxide. The exposure duration during test set C is less (≈ 5 h).

The straw case salt deposit is characterized by the distinct presence of K-chloride as well as K-sulfate. The aim is to evaluate the corrosive resilience of austenitic alloy against chlorine corrosion. Knowing that the chlorine corrosion is characterized by loss of alloy element, especially Cr, from the alloy substrate. The Cr element map from different observation positions are shown, see Figure 42, in pair with S and Cl to signify the chemical form salt deposit in corresponding case. Other element maps and additional BSE images are organized in the Annex 2 (see section 8.3.1). In some observation locations the Cr-oxide scale is completely detached from the alloy substrate. Further, the detached oxide scale shows a thin Fe-layer beneath, possibly in combination with sulfur. The overall observation suggests that the chromium loss is also typical in austenitic alloy in presence of K-chloride in the deposit.

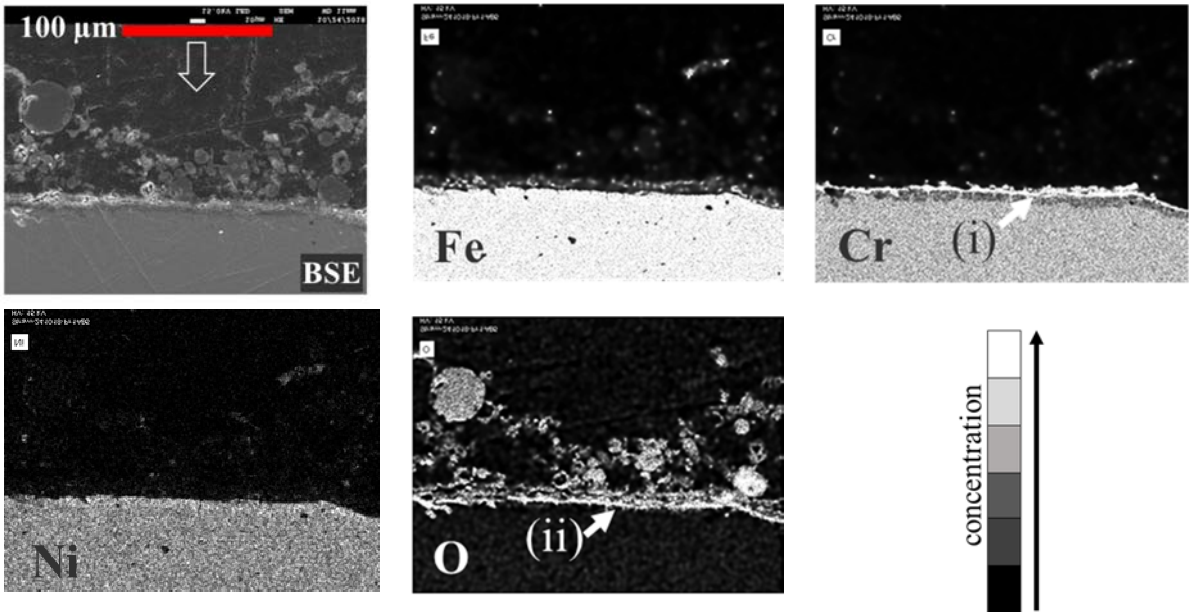


Figure 41: BSE image and element map relevant to oxide scale corresponding to (straw) S case showing (i) chromium depletion and (ii) oxide scale.

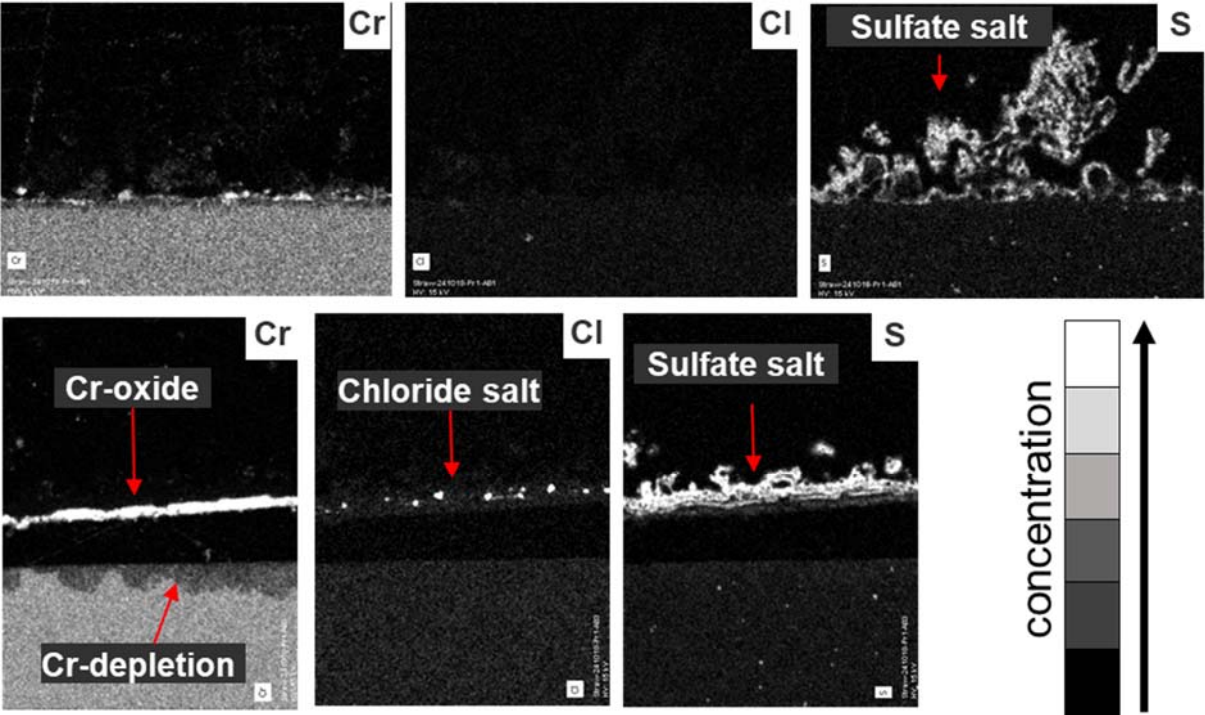


Figure 42: Element maps of Cr, Cl, and S corresponding to S (straw) case without additive.

4.3.1.5.2 Biomass with additive

Martensitic alloy (sample from Test set B)

Figure 43 shows the BSE image and element map relevant to oxide scale and salt deposit species corresponding to M+B case. In contrast to case without additive, see M case in Figure 37, the M+B, see Figure 43, shows a regular oxide scale over the surface suggesting lower corrosion activity. In comparison to the M case, the corrosion activity in the mix M+B case is fundamentally different, i.e. oxide scale is chemically intact which is attributed to the absence of K-chloride in salt deposit.

The attachment of oxide scale with the alloy substrate appears compromised and shows faint presence of sulfur beneath the oxide scale suggesting metal-sulfides, see Figure 43, an observation similar to mix case, see M+W case in Figure 37. From the overall micro-graph observation the author speculates⁴ that the severity of metal-sulfide formation is comparatively lower and is probably the consequence of lower salt deposit growth, attributed to their capture already in the gaseous phase prior to onset of condensation over the sampling surface.

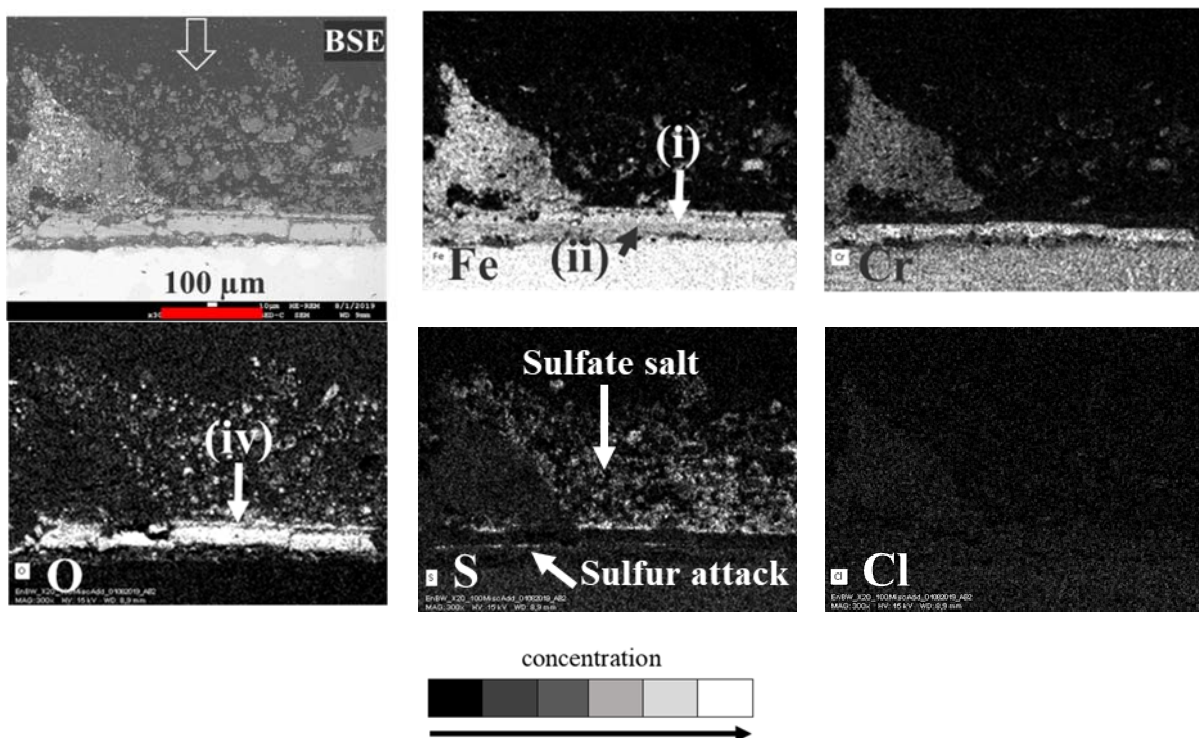


Figure 43: BSE image and element map relevant to oxide scale and salt deposit species corresponding to M+B.

⁴ Qualitative observational conclusion: Sulfur intensity beneath the oxide layer is faint and irregular

Austenitic alloy (sample from Test set C)

The BSE image of probe surface cross-section corresponding to straw case with additive is organized in Annex 2 (see section 8.3.2). The sample surface cross-section in BSE images indicates that the corrosion activity is substantially lower in comparison to the corresponding case without additive. Figure 44 shows the BSE image and element map relevant to oxide scale and salt deposit species corresponding to straw case with additive.

Though thinner and discontinuous, no sign of substrate attack or scale detachment is observed. The overall observation suggests that the corrosion activity in case with additive is fundamentally different in comparison to the corresponding case without additive. The obvious conclusion is that the lower corrosion activity in accordance to the absence of K-chloride and the lesser significance of K-sulfate layer grown over the surface.

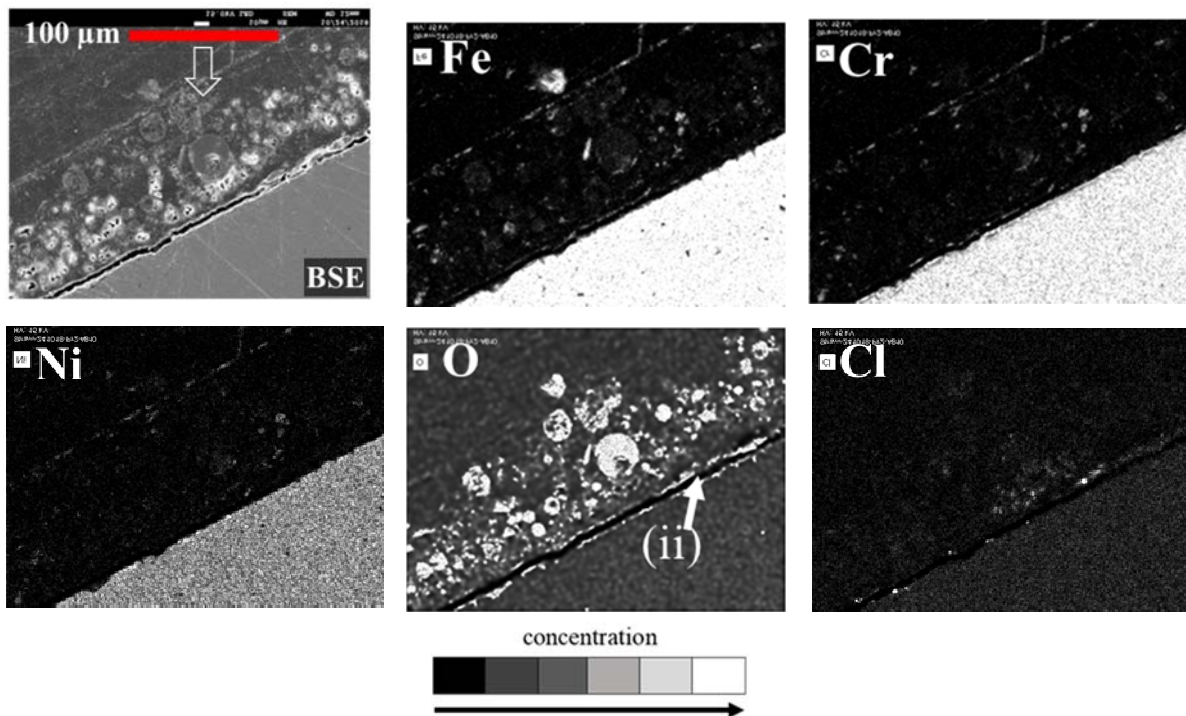


Figure 44: BSE image and element map relevant to oxide scale and salt deposit species corresponding to M+B.

4.3.1.5.3 Discussion: Influence of additive in fireside corrosion

The one to one comparison of case without and with additive, exhibits a certain level of uncertainties and observational bias because all micro-graph observations are qualitative or else semi-quantitative. Additionally, it is noted that in combustion system exposures conditions are not exactly similar among cases throughout the exposure duration. Comparatively lower corrosion severity corresponding to additive cases for both martensitic and austenitic alloy is observed from the samples. How much is contributed by possible differences in sampling boundary conditions and how much is the influence of additive on the ash system chemistry and consequently the suppression of chlorine retention in the deposit, is difficult to state. Nonetheless, it can be confidently said that the difference in corrosion activity as observed in sample is related to the chemical form of K-salt present in deposit. The corrosion severity related to sulfate and chloride salt is well reported in literature [21,79] and can satisfactorily explain the observation made from the samples discussed here.

Both, martensitic and austenitic alloy, do not offer oxide scale protectiveness when KCl is present in salt deposit. The presence of chloride salt establishes a corrosion mechanism characterized by loss of alloy element, i.e. Cr. This corrosion mechanism is explained in the literature as active oxidation. The Cl source to trigger active oxidation could be either HCl released from sulfation of KCl or the direct interaction of KCl with the alloy-metal elements. The direct interaction is more catastrophic.

The presence of chlorine in combination with alloy-metal elements is faintly observed which is apparently due to volatile nature of metal-chlorides in the exposure conditions. The volatile nature of metal chlorides, especially Cr-chlorides, is an explanation provided for the loss of chromium from the substrate or from the oxide scale in many fireside corrosion studies [75,84]. The protectiveness of oxide scale in presence of sulfate salt can be compromised for martensitic alloy while austenitic alloy may provide protectiveness when sulfates are solely the salt component in deposit. Formation of metal-sulfides, mainly Fe-sulfide, beneath the oxide scale weakens its attachment to the substrate. The in-situ sulfation of KCl, i.e. followed after condensation over the sampling surface, prepares sulfur attack. In-situ sulfation is a plausible pathway for the existence of salt melt as salt eutectics. The molten salt then provides the sulfur ion required to establish the hot corrosion mechanism leading to the formation of metal sulfides beneath the oxide scale.

The capture of gaseous alkali species already in high temperature zone prior to the onset of their condensation, reduces the overall salt deposit growth. Especially, the KCl capture and in progress the escape of Cl, in flue gas as HCl, which is a non-condensable component in boiler temperature regime. Thereby the suppression of chlorine retention in ash/deposit is the main influence of additive which results in lower fireside corrosion activity.

4.3.2 Summary discussion: Demonstration of additive mitigating effect

Two different aspects of additive mitigation are observed from deposit samples of the pilot scale tests; the reduction of the molten ash fraction and chloride salts in the deposit. These effects could be demonstrated with results from the pilot scale combustion test facility. The test combustion facility employed in this work simulates the temperature and residence time typical to PF combustion systems. The mitigating effects of additives in reference to tests with the corresponding biomass alone are demonstrated via:

- The decrease in the deposition rate and propensity in relation to the suppression of molten ash species or else fractions.
- An improved deposit and particle morphology in relation to the suppression of molten ash species or else fractions.
- The increase of the ash fusion temperature of bulk ash in relation to high melting aluminosilicatic species.
- The decrease in chlorine retention in deposit in relation to the increase of the KCl-additive capture reaction and consequently the escape of chlorine to the flue gas as HCl.
- The decrease in corrosion activity in relation to the decrease in K-chloride in deposit/ash.

This mitigating chemistry is well agreed and explained by the shift of the biomass ash system chemistry driven by kaolinite, i.e. the aluminosilicate introduced with the additive. Explained by the K-species and kaolinite capture reactions. During combustion, the potassium in fuel is released largely as KOH (g) and KCl (g). The chemical reaction between the K-species and SiO₂, either after the primary release to the gas phase or secondary with the burning fuel char particle prior to release, retains potassium in the silicatic slag phase. This retention forms K-/Ca-silicates as primary silicatic slag precursors. Most biomass fuel contains a considerable amount of silicon, stoichiometrically enough to retain all potassium as silicates. However, most

of the silicon in biomass originates from soil impurities, like quartz, and shows partial surface reactivity or ideally escapes the combustion zone without taking part in chemical interaction. The kaolinite provides the reactive aluminosilicate but it remains outside the burning fuel particle. The aluminosilicate will interfere with the formation of primary silicatic slag precursors that proceeds outside the char particle. In contrast, the silicatic slag evolution proceeding within the burning char particle largely remains unaffected. Once the char particle collapses, physical contact between aluminosilicatic particle and molten silicatic slag droplet is plausible. The inclusion of aluminosilicate on such encounter modifies the solidification (crystallization) behavior of a molten slag droplet. It is expected to exhibit early crystallization of solid compounds out of the molten slag. The increase of the ash fusion temperature of bulk deposit samples justifies that the melting behavior of the ash system is modified by additive. In addition, the quantitative deposit measurements from ODS suggest that the presence of additive substantially suppresses the mass growth as bulk deposit. It is noted that the bulk deposit growth as OD does not directly simulate the boiler deposition scenario, i.e. over the heat exchanger surface. What the lower mass growth signifies is that, the accumulation efficiency of ash particles on impaction is lower if an additive is present because (i) the chemical inhibition of the evolution of molten silicatic slag precursors at its very beginning suppresses the melt induced stickiness of ash particles and (ii) the mitigating effect by the physical inclusion. Further, the fraction of refractory solid components increases with addition of additive which as well exhibits eroding effects and contributes to decrease the bulk deposit growth.

The promoted capture of K-salt species by additives is confirmed by the suppression of salt deposit growth in the ID deposit. This suppression is not only in accordance to the capture of KCl (g) but also according to other gaseous K-species (like KOH). The reaction between K-species and SO_x (sulfation) competes with the K-species and aluminosilicate reaction (capture reaction). Within the combustion zone, the heterogeneous (gas-solid) reaction of alkali capture is more favorable than the homogenous (gas-gas) sulfation reaction. The kinetic drive for sulfation is lower at higher temperature where K₂SO₄ (as solid aerosols) is not favorable. An early capture of gaseous K-species decreases the overall fraction of K-species at the onset of condensation. In accordance, the K-species/SO₂ ratio decreases. This situation promotes sulfation.

The supersession of chlorine retention in ash/deposit relates to the KCl (g) capture reaction which promotes the escape of HCl (g) to the flue gas. The HCl measurement within the combustion chamber confirms the increase of HCl associated with the introduction of additive and thereby confirms the capture reactions in the high temperature zone. Although at the deposit

front, sulfation is still relevant. An additional advantage related to the additive capture reaction is that it proceeds already in the temperature regime of the combustion zone while the sulfation largely occurs along diffusion-condensation or in-situ.

The decrease in fire-side corrosion severity corresponding to the additive cases is attributed to the absence of K-chloride salt in the deposit. The transport and accumulation of unburnt char is argued to be a pathway that brings KCl to the deposit front. It is not clear if this pathway is specific to down fired combustion system where every combustion residue passes through the probe exposure plane. In this test system, the combustion generated ash/unburnt char does not have a size dependent fractionation, like bottom ash and fly ash, as it is typical in industrial PF boilers. Experience shows that fuel characterized by a lower ash fusion temperature typically exhibits unburnt char transport and accumulation in the deposit front. The increase in ash fusion temperature of the bulk ash in presence of additive has an indirect consequence to minimize unburnt char transport and accumulation, thereby also of KCl to the receptive surface. The validation of this argument is limited to the observation made from the given test facility.

The HCl released by the capture of the KCl-additive interaction escapes in the surrounding flue gas stream. In contrast, in case of sulfation; Cl₂ is released at the deposition front near the vicinity of metal surface. At the water vapor (H₂O) rich global flue gas atmosphere, Cl₂ eventually escapes as HCl and may not be of high concern with regard to boiler heat exchanger corrosion. But, the release of Cl₂ (by in-situ sulfation) which occurs in the vicinity of material (probe) surface is relevant with regard to the corrosion activity. The corrosion mechanism explained by *active oxidation* [73]. The observation drawn from this study suggests that in biomass fuel, even if the 2S/Cl ratio is well below to satisfy the sulfation demand, eventual corrosion mechanism is driven by K-sulfate formed over exposure duration. This could establish *hot corrosion* mechanism [73].

The observed, accelerated corrosion is coupled with the presence of K-chloride salt. This is a clear implication of *active oxidation*. However, the source of chlorine which triggers the corrosion in this case is the direct KCl-metal interaction. The presence of KCl salt appears to accelerate the active corrosion resulting in a substantial loss of alloy element, here Cr, from the alloy substrate itself. Even high grade austenitic steel which is considered to provide a reasonable resistance to K-sulfate salt related corrosion fails to provide protectiveness against the direct K-chloride attack. Such observation is also demonstrated in lab corrosion studies with pure salt [78,83].

4.4 Experiments in electrically heated combustion test facility (BTS-VR)

The test set, case identity and combustion boundaries corresponding to the bench scale facility are summarized in Table 22. Each test set refers to similar combustion boundaries. The combustion cases (see also Table 10 in section 3.1.2) refer to fuel or fuel mix as reported in Table 22 are case identities for the result section and graphs, hereafter.

Table 22: Short name index of combustion cases and test system boundary.

Test set	A		B			C		D
Case identity	W	W+C	TS+A	TS+B	TS+D	TS+A	*W+A	S
ϑ_{set} (91 – 95) [°C]	1300-1300 °C		1300-1100 °C					1200-900 °C
\dot{M}_{fuel} [kg/h]	≈ 2		≈ 1			≈ 1.5		≈ 2.3
Additive loading [%]	-	≈ 1.5	0 to ≈ 20			0 to ≈ 12		-
\dot{V}_{CA} [m ³ /h]	≈ 10.5		≈ 5.1			≈ 7.7		≈ 9.5
Test Fuels: Wood (W), Torrefied Straw (TS), KCl doped Wood (*W) and Straw (S)								
Test Additives: A, B, C and D								

The set temperature refers to the inside wall temperature of the combustion chamber (ceramic tube, Figure 7) established by the various heating zones T1 to T5 (see Figure 7). For test set A, each heating zone is set at 1300°C. For test set B and C, T1, T2, T3, T4 and T5 are set respectively at 1300°, 1250°C, 1200°C, 1150°C and 1100°C. For test set D, T1, T2, T3, T4 and T5 are set respectively at 1200°, 1100°C, 1000°C, 950°C and 900°C. For each test set, the stable combustion condition is monitored with $\text{O}_2 \approx 3 - 3.5 \text{ vol.-%}$ and $\text{CO} < 20 \text{ ppmv}$ at the end of the combustion chamber.

Table 23 summarizes the relevant composition and properties of fired fuel. The complete standard analysis of fired fuel is reported in Annex 1.

Table 23: Relevant composition and properties of fired fuel.

Test set	A		B	C		D
	W	W+C	TS	TS	*W	S
γ_{ash} [wt.-%, db.]	1.05	2.4	6.3	4.5	1.5	13
γ_{Cl} [wt.-%, daf.]	0.02	0.02	0.10	0.05	0.14	0.16
Corrosion index	5.5	5.4	2.5	4.0	1.3	1.3
Fusion index	1.4	1.6	3.3	2.9	1.9	4.7
ϑ_{DT} [°C]	1250	-	840	840	1170	1100
Test set A: Wood: W (W2-3) and Wood + 1.5 % additive C: W+C						
Test set B: Torrefied Straw: TS (TS4)						
Test set C: Torrefied Straw: TS (TS1-3) and KCl doped wood: *W						
Test set D: Straw: S (S5)						

The combustion case scenario corresponding to each test set is briefly reported below.

- Test set A:** Wood (W) is the fired fuel. The complete analysis of fired fuel is in Annex 1 (see Table 27, Fuel Name: W2-3). The additive is premixed with pulverized wood (<500 μm) prior to combustion. The additive C (see Table 16) is used to prepare the mixture. The mixing is done manually. To ensure homogeneous mixing, the mixture is prepared in small batches. The additive in the mixture represents $\approx 1.5\%$ of the fuel. W+C refers to the combustion cases when the additive premixed fuel is fired. The calculated composition of W+C as fired is in Annex 1 (see Table 32, Fuel Name: W+C). The uncooled probe sample refers to OD and the cooled probe sample refers to ID. The material for cooled probe is martensitic grade steel. The probe surface temperature is maintained at $\approx 550\text{ }^{\circ}\text{C}$ during sampling exposure. Both deposits are sampled from 1.5 m below the burner injection (residence time of $\approx 3\text{ s}$) and the probe exposure duration is $\approx 3\text{ h}$. The FA was sampled at the end of the combustion chamber at 2.5 m below the burner injection with a residence time of $\approx 4\text{ s}$ with the vertical oil cooled sampling probe. The probe also extracts the gas for continuous combustion monitoring. The result derived from this test set are discussed in section 4.4.1.1.1-2.

- **Test set B:** Torrefied straw (TS) is the fired fuel. The complete analysis of fired fuel is in Annex 1 (Fuel Name: TS4, Annex 1, Table 30). A, B and D refers to the type of additive (see Table 16). The additive is fed independently and combines with fuel in the feeding line and thus fuel-additive mixture is injected through the burner. The fuel feeding and total combustion air injection inside the combustion chamber is kept constant for each test run. The additive amount is varied for a constant fuel fed and corresponding to different additive loading (Eq. 3.1).

The flue gas concentration is continuously measured by FTIR analyzer. The FTIR refers to measurement location I (see Figure 7). The results derived from this test set are discussed in section 4.4.1.2.1-2.

The FA sample corresponding to three different additive loadings, namely TS+5A, TS+6B and TS+20B are reported in section 4.4.1.2 (in Figure 53). The number represents the additive loading (in %) and A, and B the additive type. The FA is sampled from 2.5 m below the burner injection.

- **Test set C:** The fired fuels are torrefied straw (TS) and KCl doped wood (*W). The *W is prepared by spraying the KCl solution (water) over the pulverized wood. The prepared fuel is analyzed (see Table 30, Annex 1). The additive feeding scenario was similar to that of test set B. The flue gas concentration is continuously measured by FTIR analyzer. The FTIR measurements refers to location II (see Figure 7). The result derived from this test set is reported in section 4.4.1.2.3. Additionally, the results discussed in 4.4.1.2 (Figure 55) also derive from this test set.
- **Test set D:** The fired fuel is straw (S). The complete analysis of fired fuel is in Annex 1 (Fuel Name: S5, Annex 1, Table 28). The fly ash is sampled at different locations inside the combustion chamber, namely 2.5 m, 2 m and 1 m below the burner injection (see Figure 7) and in parallel the flue gas concentrations (by FTIR) are measured. The result discussed in section 4.4.1.2 (Figure 52 and Figure 54) derives from this test set.

4.4.1 Result: Mitigative chemistry and optimum additive amount

The results that follow include the evaluation of the OD and ID samples, HCl concentration corresponding to various additive loading and output from equilibrium calculation at different input scenarios.

4.4.1.1 Additive mitigative chemistry in relation to suppression of molten ash

The specific objective is to evaluate the additive mitigative chemistry in relation to silicatic deposit. Basically, the silicatic deposit are ash particles deposited on the surface by inertial impaction. The luv side shows more relevancy for silicatic deposit particles. The morphology and composition of deposit particles or else phases is evaluated with comparative micro-graph observation between samples without additive and with additive. The micro-graphs include BSE images and element maps. Several BSE image (all luv side) were generated with different scales. The BSE images shown here are considered to show representative deposit particles or phases, corresponding to given case.

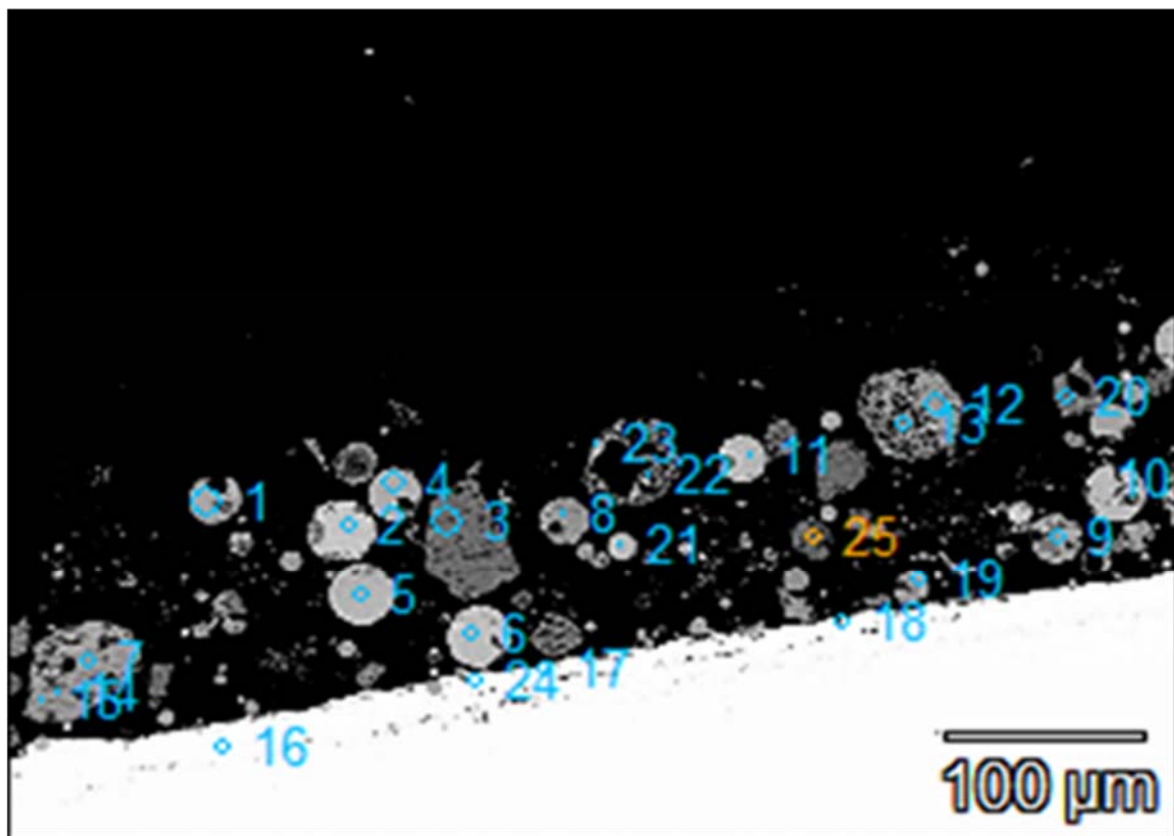


Figure 45: BSE image of ID sample corresponding to W+C case showing various points, as an example of point analysis.

For the selected representative BSE image, the element maps are generated. Corresponding to the same BSE image, the composition of deposit particles or phases are determined by point analysis (see Figure 45). The points were chosen to represent the characteristic particles or phases relevant to silicatic deposit. There is uncertainty (manually chosen) with selecting the characteristic particles or phase. But the author confidently believes that these uncertainties do not impact the discussion and conclusion presented here. The discussion and conclusion are representative to the deposit sample/case. The discussion is presented as comparison between case without additive (W) and case with additive (W+C).

The composition of individual points are organized in Annex 2 (see W case OD and ID respectively in section 8.4.1 and 8.4.3 and W+C case OD and ID respectively in section 8.4.2 and 8.4.4). The composition corresponding to OD sample is grouped as Slag and Silica. While the composition corresponding to ID sample is grouped as Class A, Class B, Class C and Silica. The composition groups are defined as follows.

- **Silica:** Silicon rich ($\text{SiO}_2 > 98$ wt.-%) particles in OD sample as well as in ID sample observed in both cases.
- **Slag:** The fused phase observed in OD sample in both cases.
- **Class A:** The alkali (K_2O) rich phase as coating layer around SiO_2 rich particles observed in W case ID sample.
- **Class B:** Particles (mostly spherical) characterized by composition alkali ($\text{K}_2\text{O} + \text{Na}_2\text{O}$) $<$ earth-alkali ($\text{CaO} + \text{MgO}$) observed in W+C case ID sample.
- **Class C:** Particles (spherical and porous) characterized by alkali ($\text{K}_2\text{O} + \text{Na}_2\text{O}$) $>$ earth-alkali ($\text{CaO} + \text{MgO}$) observed in W+C case ID sample.

From morphology the slag (in OD sample), Class A, Class B and Class C (in ID sample) are believed to have a molten history and are specifically discussed in the following chapters.

4.4.1.1.1 Outer deposit (OD)

The BSE image of OD cross-section corresponding to W case and mix W+C case is shown in Figure 46. The OD from both cases show a similar morphological phase fused to the surface. The fused deposit is understood as the chemical phase which developed from the solid and liquid components accumulating over the ceramic surface. The molten ash component facilitates to incorporate solid ash particles and to develop a complex mixture, the slag. The evolution of slag composition involves solid-liquid reactions which proceed over the collecting surface, here the ceramic probe, where the physical contact is more plausible than in the entrained surrounding. The solid particles are stuck to the slag phase but retain their individual chemical composition and morphology. The solid particles are mostly compact Si-rich particles for the W case. In the W+C case, additional porous aluminosilicate (Si-Al-rich) particles are found.

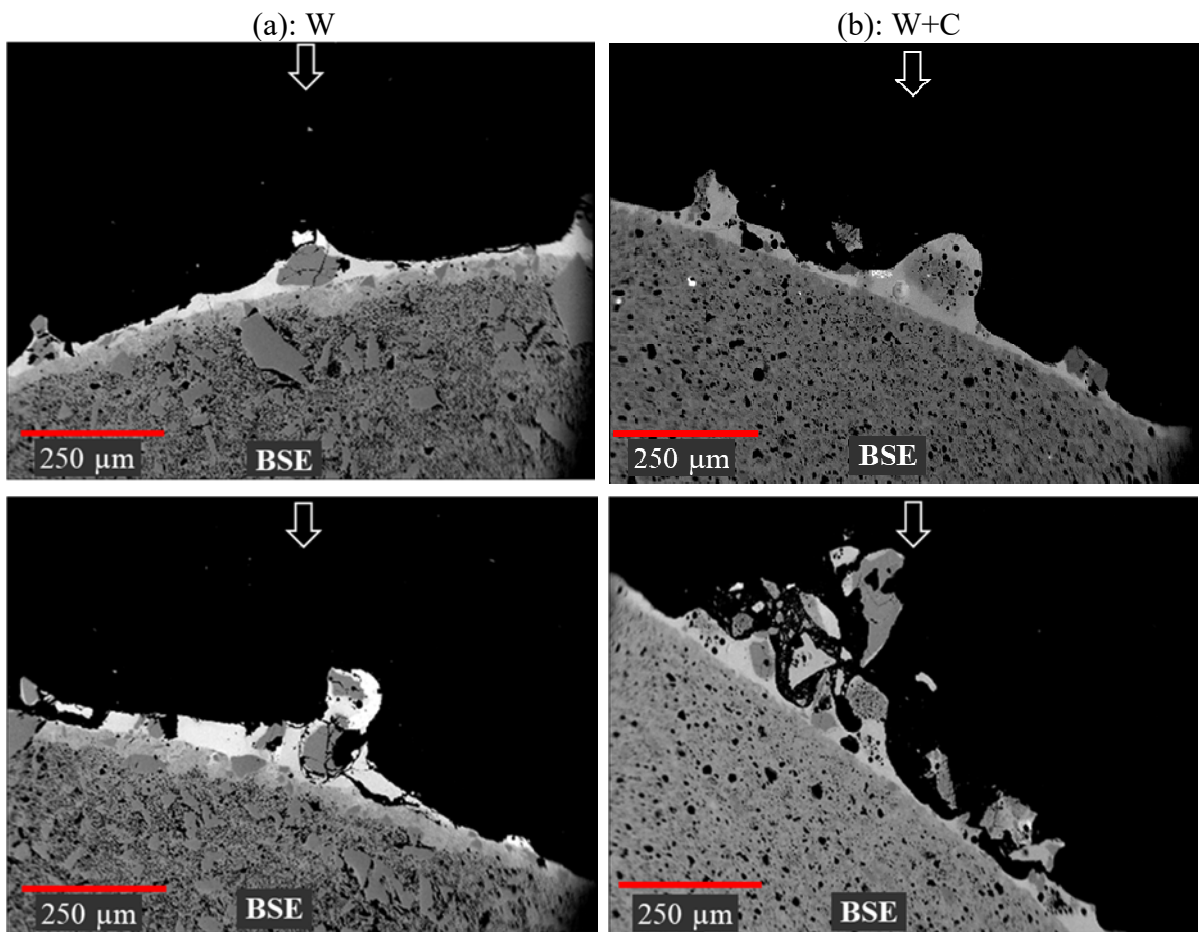


Figure 46: BSE image OD sample corresponding to (a) W case and (b) W+C case.

Figure 47 (a) shows the slag composition as oxide as average composition of various points in the fused layer and corresponding FA composition as oxide from ICP-OES analysis for the W and mix W+C cases. In case W, the SiO_2 and Al_2O_3 content is higher while earth alkali, $\text{CaO}+\text{MgO}$, are lower in slag than in FA. In case W+C, the difference between slag and FA ash composition is comparatively smaller.

It is understood that the slag evolution does not consume all solid components in the system. For example, much of calcium released from the fuel remains entrained as fine CaO particles, for the case W, also as their sulfates and similar with much of silica (SiO_2) present in fuel.

In case W+C, the additive derived minerals, because of their refractory nature, escape melting and remain as individual solid particle and probably do not play a role in slag evolution. From a chemistry point of view, the kaolinite derived aluminosilicates are expected to disturb the evolution of slag by capturing gaseous K-species and thereby hindering the pathway of forming low melting slag precursors, like K-Ca/-silicates. Beside additive mineral kaolinite (67%), muscovite is estimated to account $\approx 10\%$ of additive minerals. The muscovite derived compound, KAlSi_3O_8 , melts above 1150°C . The sampling surrounding is $\approx 1300^\circ\text{C}$. The muscovite fraction in the additive may partly contribute to the slag phase which remains independent to the fuel ash system chemistry.

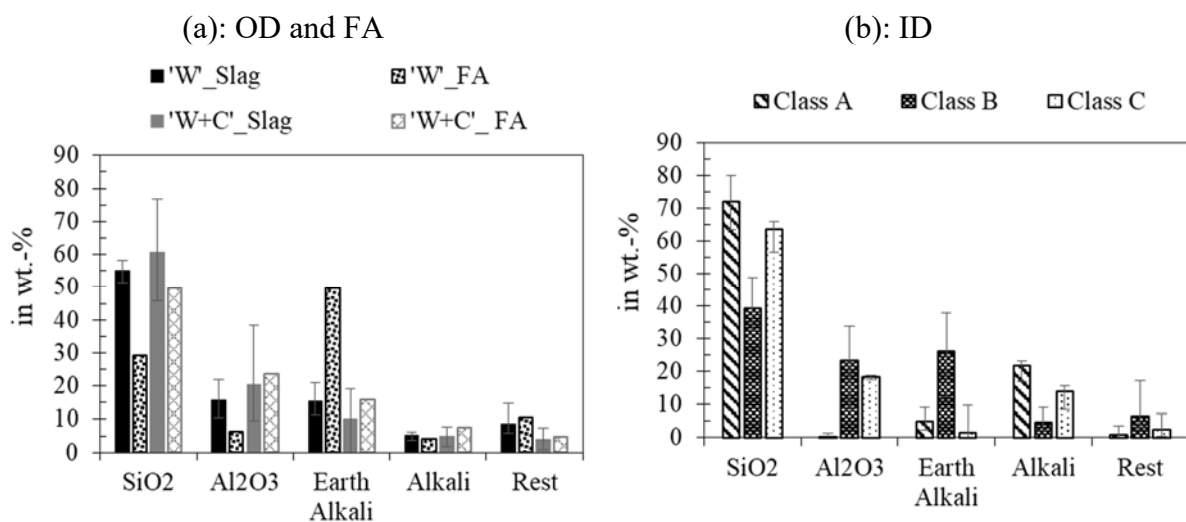


Figure 47: Average oxide composition of (a) slag from OD and corresponding FA and (b) composition Class A, B, and C from ID. The earth alkalis include: CaO and MgO , the alkalis: K_2O and Na_2O , and the rest: P_2O_5 , Fe_2O_3 , TiO_2 , and SO_3 .

4.4.1.1.2 Inner deposit (ID)

The BSE image of an ID cross-section corresponding to case W and mix W+C is shown in Figure 48. The ash content in the fired fuel is 1 wt.-%, db and additive loading in W+C case is 1.5 %. The solid flow inside the combustion chamber in W+C case is almost 2.5 times higher in comparison to corresponding W case. The particles observed in a certain area corresponding to W+C case are relatively abundant, see BSE image Figure 48. The compact irregular particles are observed in both cases. The particle characteristic to W+C case is mostly spherical and of porous structure. These particles are speculated either to derive from the additive minerals or from the fuel ash-additive mineral interaction.

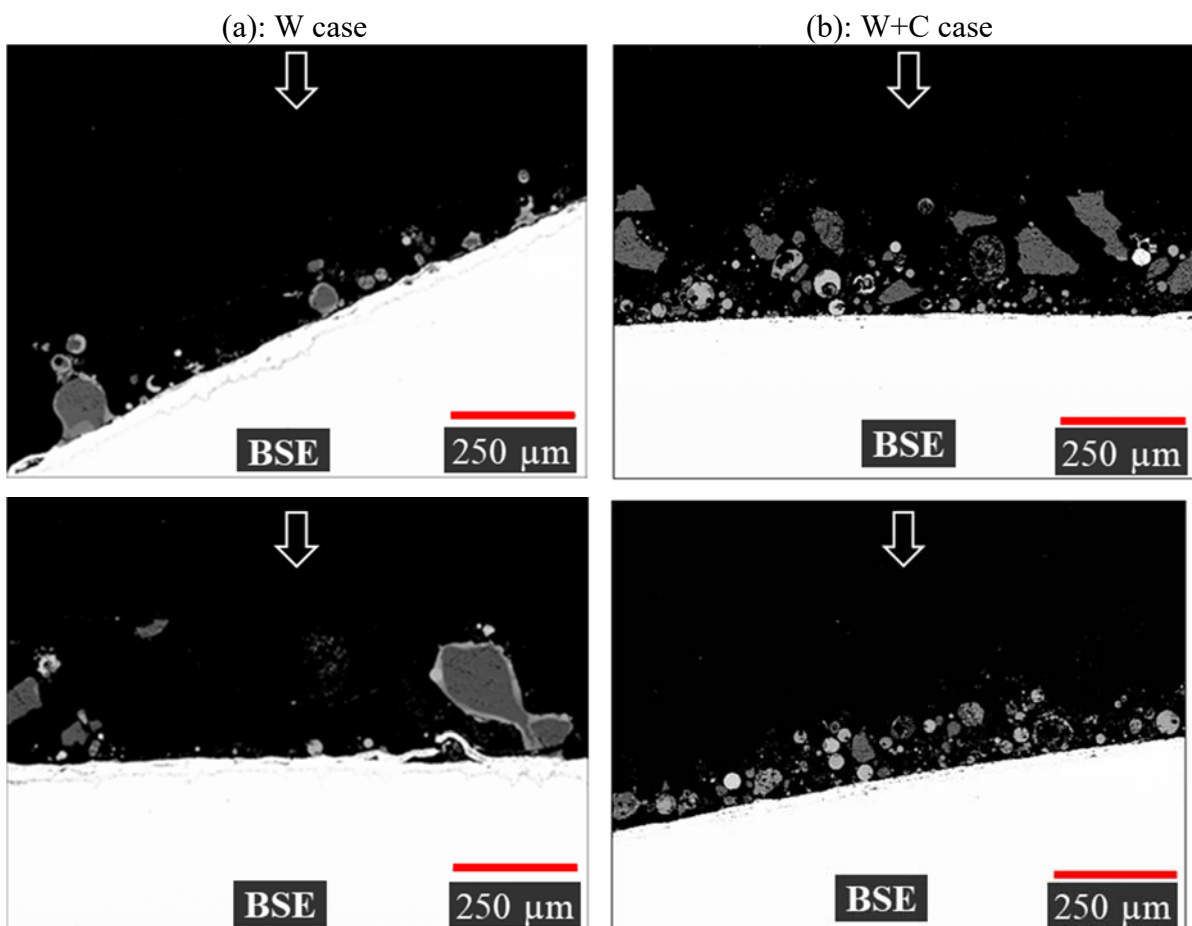


Figure 48: BSE image of ID sample corresponding to case (a) W and (b) W+C.

The element distribution and corresponding BSE image from case W is shown in Figure 49 and from W+C in Figure 50. The most relevant difference between W and W+C case is observed on the surface of irregularly shaped compact silica (SiO_2) particles. In case W, the surface of the particles shows a chemical phase characterized by a potassium distribution, see in Figure

49. The combination suggests it to be K-silicate. Such surface coating appears to connect or bridge particles and facilitates them to stick to the sampling surface. The average composition of coating phase, as Class A, is shown in Figure 47 (b). The silicon rich irregular particles in case W+C have a clean surface, see in Figure 50 and such particles apparently escape the melting.

The characteristic particles to W+C case are spherical and porous (mostly non-spherical) particles. The Al distribution in these particles is as significant as Si. The K and Ca distributions vary from particle to particle. These particles mostly derive from the additive mineral or their interaction with fuel derived components. However, the attempt to differentiate between additive mineral derived particles, particles evolved from fuel ash species, and fuel ash-additive mineral interaction based on micro-graph observation is largely speculative.

The oxide composition (point analysis) of spherical and porous particles has two distinctive compositions, grouped as Class B and C, see Figure 47 (b). The spherical particles are considered to evolve from molten droplets which solidify in the process of deposition. The phase, molten or solid, at the point of surface contact is ambiguous to state. The particles with a porous morphology likely escape the combustion zone as solid.

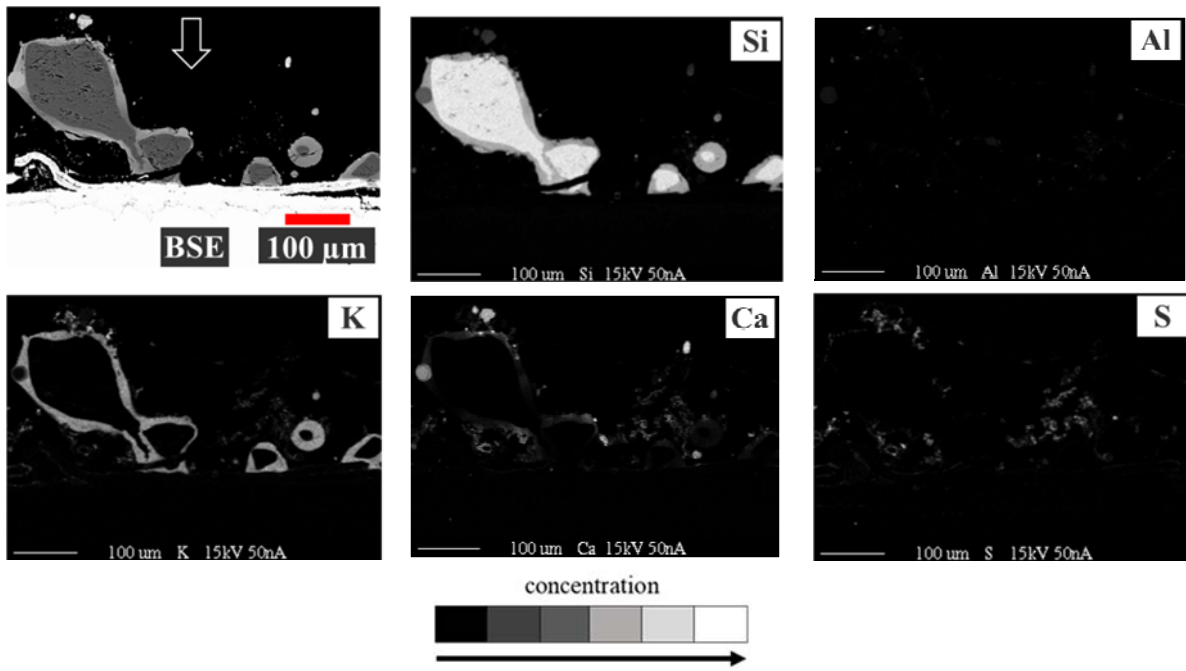


Figure 49: BSE image and element map (WDS) corresponding to case W, ID sample.

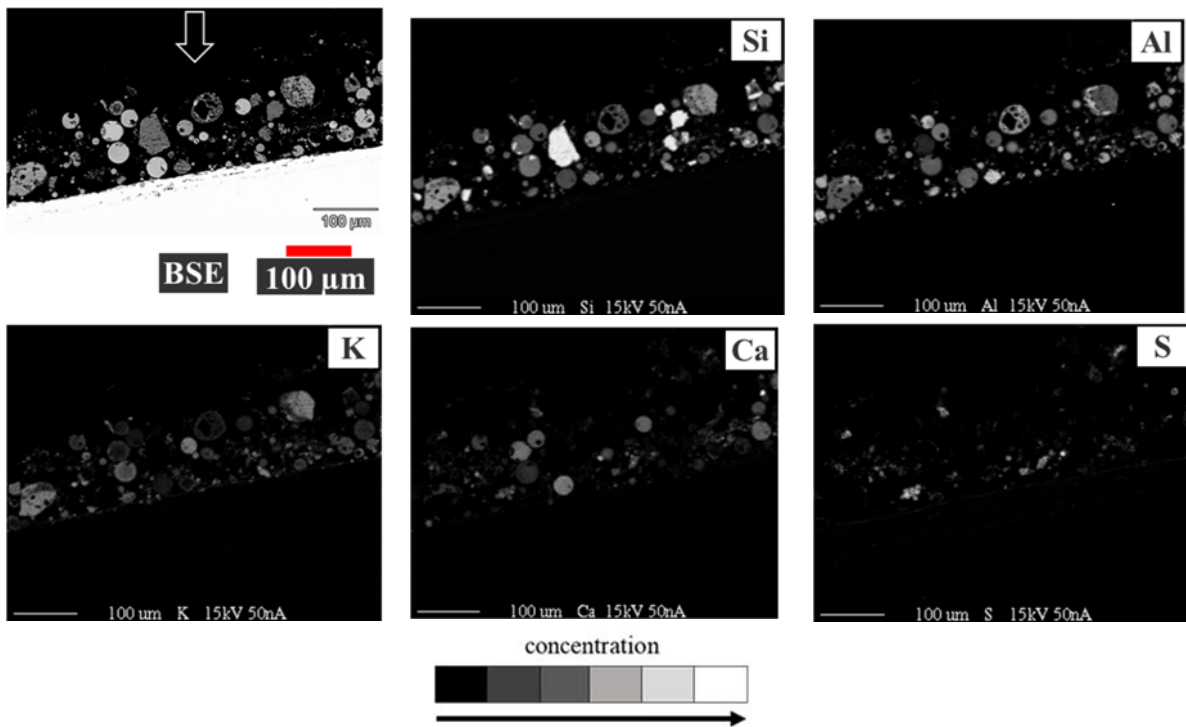


Figure 50: BSE image and element map (WDS) corresponding to case W+C, ID sample. The number in BSE image represents different points chosen for point analysis as wt.-% oxide.

4.4.1.1.3 Molten history of silicatic ash particles

The additive mineral includes mainly kaolinite ($\approx 67\%$), quartz ($\approx 18\%$), and muscovite ($\approx 10\%$). When the kaolinite is injected inside the reactor it loses crystal water. This creates meta-kaolinite which is finally transformed to mullite. In parallel the capture of fuel released K-species proceeds. K-aluminosilicate, KAlSiO_4 and KAlSi_2O_6 , are formed by capture reactions. Both mullite and K-aluminosilicate are refractory compounds which remain solid in the surrounding temperature range of $\approx 1300\text{ }^\circ\text{C}$. The quartz (SiO_2) fraction in the additive also escapes melting. The K-aluminosilicate compound, KAlSi_3O_8 , derives from muscovite transformation and is reported to have incongruent melting above $> 1150\text{ }^\circ\text{C}$. These particles melt or partially melt in the surrounding sampling temperature.

The molten history of a certain particle is relevant to deposit growth. The mitigating effect of additive is reasoned with the decrease of molten/semi-molten ash particle in the system by the presence of additive minerals. This in general is validated by increase in ash fusion temperature of bulk ash and by morphological observation based on micro-graphs.

The compact silicon rich particle except the surface melting suggested by coating in W case and the porous particles from their morphology suggests that they had escaped melting. The spherical particles are considered to be molten droplets which solidify at the boundary layer of the cooled sampling surface, ID, when they fail to solidify, a fused layer/phase is developed, OD.

With the purpose to evaluate the molten history of a given particle or phase composition, the equilibrium calculation is performed using FactSage software and databases. The input for the equilibrium calculation, is the averaged oxide composition rounded to integer of each composition class, including A, B, and C (see Annex 3, Table 40). The temperature range of $550 - 1350\text{ }^\circ\text{C}$ is chosen. The lower end reflects the sampling surface temperature and the upper end reflects the surrounding temperature range. The O_2 (0.3 mole), CO_2 (0.17 mole), and N_2 (0.83 mole) input is chosen which represent the flue gas species O_2 and CO_2 for each equilibrium condition $\approx 3\text{ vol.}\%$, $\approx 17\text{ vol.}\%$, and rest N_2 . The assumption is that the partial pressure of gaseous species are more relevant for equilibrium than their obsolete amount.

Beside the assumption of equilibrium chemistry which is related to the software or else database itself, the following simplified presumptions are made for the discussion.

- The amount of slag liquid at a certain point of equilibrium condition represents the molten fraction of the given class composition corresponding to that temperature.

- The solid compounds are grouped as silicatic which are compounds in association with silicon, aluminosilicatic which are compounds in association with aluminum and silicon, aluminate which are compounds in association with aluminum, rest which is a solid solution corresponding to mullite, and others which are compounds having neither silicon nor aluminum.
- The oxide composition of individual points or particles within the same class differs. The exact temperature at which a certain composition remains completely in slag liquid phase or at which the crystallization of certain solid compound starts may differ with the input oxide composition. The temperature in the following graphs and discussion refers specifically to the average composite of the given class. It is presumed that the equilibrium calculation with the chosen thermodynamic database is a method to evaluate the melting history of deposit particles with reasonable approximation. The variation in composition within the same class does not change the corresponding general conclusion.

The following conclusions are drawn from the equilibrium calculation results in accordance to Figure 51:

- **Class A:** The class A composition is largely silicon, SiO_2 , and alkali oxides, K_2O and Na_2O . The composition remains completely in molten phase above $800\text{ }^\circ\text{C}$. As the temperature drops, the silicatic compounds start to crystallize, followed by the other (SiO_2) after $750\text{ }^\circ\text{C}$. At $550\text{ }^\circ\text{C}$ which is the sampling surface temperature, a significant fraction of $\approx 40\%$ is still liquid slag. The solid compounds corresponding to equilibrium calculation are listed in Figure 51 (a), see below for the respective graph. The coating formation (class A composition), is a consequence of the K-species and SiO_2 particle surface reaction. The fuel released potassium species is largely KOH (g) in given biomass fuel with low chlorine content. The appearance as coating may be related to the size of the silicon particle. The small quartz particles appear to be eventually consumed by the coating chemical phase. The coating of quartz bed particles is also observed for bed combustion/gasification systems firing biomass fuel. The underlying mechanism is explained in [23,125], according to which K-silicates or K-Ca-silicates and their low melting properties are the main reasons of bed agglomeration. With regard to deposition as discussed here bridging among particles and deposit sintering is an issue of concern for bulk mass growth as well as its removability.

- **Class B:** The composition is completely in slag phase above 1250 °C. Below 1250 °C, aluminosilicate compounds start to crystallize, followed by silicate and other compounds below 1150 °C. The slag phase completely disappears below ≈ 950 °C. At sampling surface temperature ≈ 550 °C, the composition is solid. The solid phase corresponding to equilibrium calculation are listed in Figure 51 (b), see below the respective graph. The additive mineral contains very low amounts of CaO. The compositions with substantial CaO content, i.e. class B, either derives from ash species or in interaction with the additive mineral. The Al₂O₃ content of class B supports the assumption that the composition evolves from fuel ash-additive mineral interaction as in the fuel itself the aluminum content is very low. If any, the interaction involving fuel calcium species and additive mineral species, is either a solid or liquid phase reaction. The contact between the two components is prerequisite to proceed the solid or liquid reaction. The contact and inclusion appear feasible in entrained condition and most probably occur during flight. The inclusion of CaO (s) is more plausible with molten KAl₂Si₃O₈ deriving from muscovite than with solid aluminosilicate deriving from kaolinite.
- **Class C:** The composition is completely in the slag phase above 1300 °C. Below 1300 °C, aluminosilicate compounds start to crystallize, first KAlSi₂O₆ then followed by KAlSi₃O₈. Below 1100 °C all K-aluminosilicate exists as KAlSi₃O₈. Until ≈ 900 °C the slag phase is completely replaced by solid compounds. The solid compounds corresponding to equilibrium calculation are listed in Figure 51 (c), see below the respective graph. The class C composition either derives from the additive mineral or from the interaction of the additive derived aluminosilicate and fuel released potassium species. Some of these particles appear to be spherical suggesting to have molten history. Some are porous and relatively large suggesting to remain as solid. The class C composition is likely to be the transformation product of muscovite mineral on the basis of equilibrium calculation that the stable solid compound is KAlSi₃O₈ with ≈ 80 g. The muscovite transformation produces KAlSi₃O₈ while KAlSiO₄ and KAlSi₂O₆ are considered as a product corresponding to gaseous K-species capture by kaolinite derived aluminosilicate.

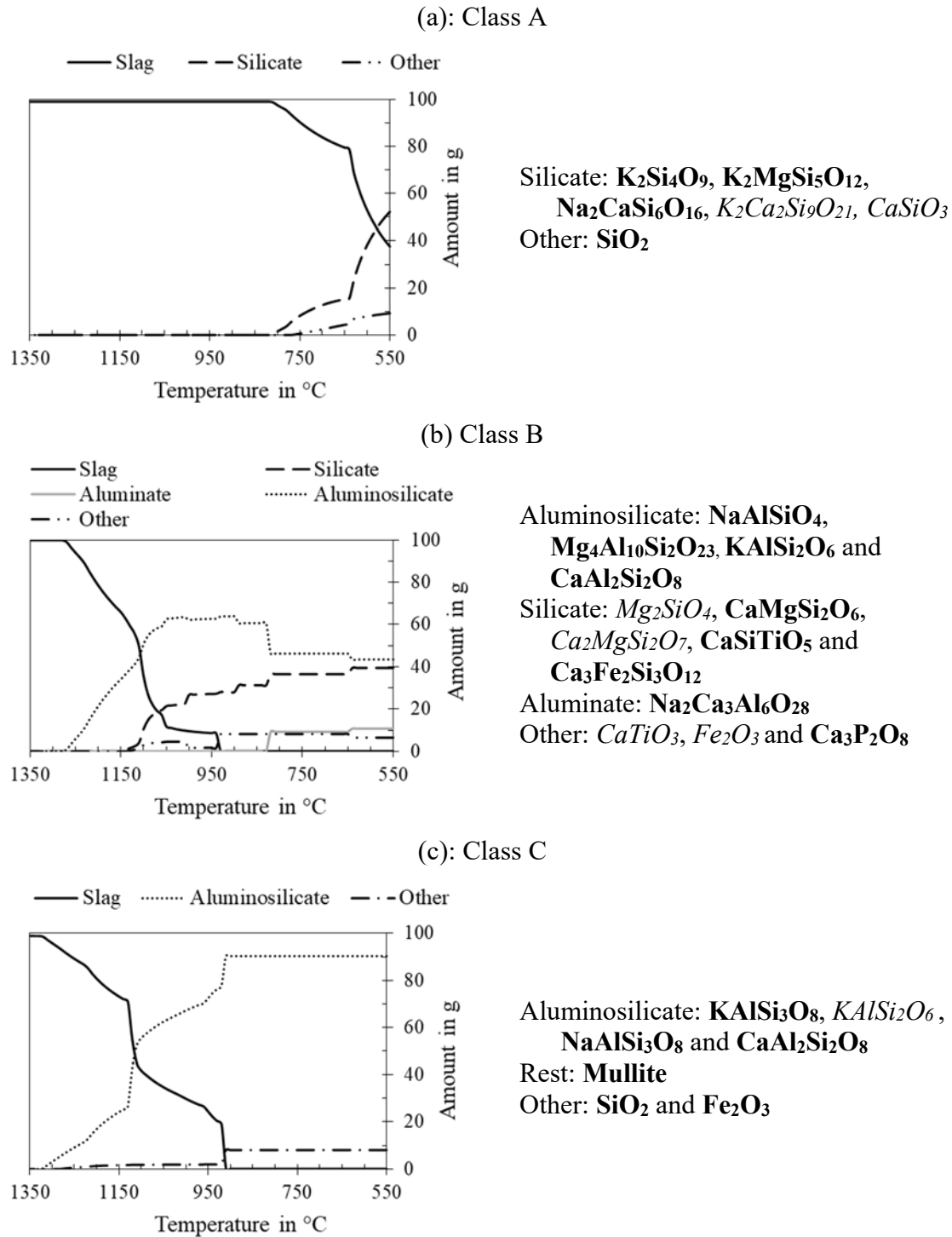


Figure 51: The amount of slag and solid compounds against temperature variation (a) class A, (b) class B, and (c) class C. The solid compound in **bold** exists at 550 °C, while the solid compound as *italic* shows transitional existence, i.e. only for a certain temperature range > 550°C.

The increasing hierarchy of melting temperature is: K-silicate < K-Ca-silicate < Ca-Mg-silicate ≤ K/Ca-aluminosilicate. The crystallization of a given compound within the molten slag

initiates as temperature drops below the melting range. Aluminosilicate compounds are assumed to crystallize earlier than silicate compounds. The argument of improved solidification of slag with increasing fraction of aluminum (Al_2O_3) content is related to this equilibrium chemistry.

The absence of coating, namely class A, in case W+C is attributed to the availability of additive mineral, mainly kaolinite derived aluminosilicate, in the system. The aluminosilicate consumes or rather captures available gaseous alkali species more efficiently than SiO_2 . Consequently, the SiO_2 particle surface is left clean.

The justification of K-aluminosilicate compounds to be the consequence of K-species and kaolinite interaction is difficult to specify. Because the equilibrium also suggests KAlSi_3O_8 which may also derive from the transformation of muscovite present as additive minerals. The most relevant property that differs according to the chemical form of K-aluminosilicate is the melting temperature. KAlSi_3O_8 starts to melt incongruently above > 1150 °C. Other chemical forms of K-aluminosilicate, as KAlSiO_4 and KAlSi_2O_6 , melt above 1500 °C. If one of the awaited effects of using additives is to promote the formation of compounds whose melting temperature exceeds the boiler temperature regime, a fraction of muscovite in given commercial additives may be of concern.

The equilibrium calculation here serves as a method to evaluate and to theoretically explain the molten history of deposit particle/phase composition. The shift in the ash system chemistry and the subsequent decrease in the molten or semi molten ash particles in the system are mainly justified by the absence of class A composition. The class B and class C composition which are characterized as the silicatic deposit are either from fuel ash-additive mineral interaction or simply the transformation product of additive minerals. The equilibrium calculation does not suggest a substantial difference between the melting behavior of class B and class C composition. The particles with porous morphology of class C composition escape the combustion zone as solid particles and is likely more related to their particle size than to the equilibrium chemistry of the composition.

Across biomass fuels with different ash content or composition, the chemistry shift induced by the availability of additive mineral, kaolinite, in the system is expected to be similar. And among additives, the fraction of muscovite (mineral as impurities in commercial additive) and the particle size distribution is relevant for the evolution of silicatic deposit. A similar test with wood (Fuel Name: W1) with additive (A) is published by Paneru et al. [17]. The main conclusion is valid to the observation made from corresponding OD and ID samples. With regard to

the influence of additive on silicatic deposit, similar conclusion can be drawn from the deposit samples from pilot scale tests (see section 4.3). At a mechanistic level, the expected influence of additive mineral on silicatic deposit particle evolution remains similar, irrespective of the size of the combustion system provided that the reaction conditions are comparable, including temperature, residence time, and contact possibility.

4.4.1.2 HCl as a potential additive control and optimization parameter

The chemistry based general understanding of the fate of fuel-Cl is either it remains as KCl or HCl. The main chemistry of additive mineral (kaolinite) is to capture gaseous K-species which includes KCl. The capture of KCl pushes the chlorine out as HCl.

The HCl is a non-condensable gas above the acid dew point. The dew point temperature depends on various other factors. Most important is well below < 180 °C, typical extractive temperature for flue gas measurements. The FTIR device is well established and conveniently implementable for flue gas measurements, including HCl. Further, it has the following practical benefits:

- The HCl measurement with FTIR (continuous measurement) can be conveniently done in any combustion test system.
- Various tests can be repeatedly performed within the close range of additive variation directly and independently with different fuels, additive as well at different combustion and additive injection boundaries.
- The inhomogeneity associated with gas (flue gas) sampling is substantially lower in comparison to solid (fly ash) sampling.

An indirect mass balance is performed to establish the closure between fly ash retained chlorine and of chlorine released to flue gas, i.e. HCl. The objective is to validate that the increase in HCl tallies with the decrease in chlorine retention in ash and vice-versa.

The chlorine retention ($X_{Cl \text{ retention}}$) is calculated according to mathematical formula by Eq.4.5. The $\gamma_{i, \text{ sample}}$ refers to the content (wt.-%, db.) in the given solid sample (FA) while $\gamma_{i, \text{ fuel}}$ refers to the content (wt.-%, db.) in the fired fuel.

$$X_{Cl \text{ retention}} = \frac{\gamma_{\text{ash, fuel}}}{\gamma_{\text{ash, sample}}} \cdot \frac{\gamma_{Cl, \text{ sample}}}{\gamma_{Cl, \text{ fuel}}} \cdot 100 \quad (4.5)$$

The $y_{HCl, \text{ measured}}$ refers to the concentration (average) of HCl (in ppmv) measured in parallel to the fly ash collection duration and location. The $y_{HCl \text{ max}}$ is calculated under the assumption of

a complete conversion of $C \rightarrow CO_2$, $H \rightarrow H_2O$, $N \rightarrow N_2$, $S \rightarrow SO_2$, and $Cl \rightarrow HCl$ and derives from mathematical formula Eq. 4.6. It refers to maximum HCl concentration under the assumption that none of chlorine remains in residual ash. The chlorine release ($x_{Cl \text{ release}}$) is calculated by the mathematical formula shown by Eq. 4.7. Both, measured and maximum concentration, are corrected to the reference of 6 vol-% O_2 and are related to the dry flue gas volume.

$$y_{HCl \text{ max}} = \frac{\frac{Y_{Cl}}{M_{Cl}} \cdot 10^6}{\left(\frac{Y_C}{M_C} + \frac{Y_N}{2M_N} + \frac{Y_S}{M_S} + \frac{Y_{Cl}}{M_{Cl}} + \frac{0.79}{0.21} \left(\frac{Y_S}{M_S} + \frac{Y_C}{M_C} + \frac{Y_H}{4M_H} - \frac{Y_O}{2M_O}\right)\right) \frac{21}{21 - y_{O_2}}} \quad (4.6)$$

$$x_{Cl \text{ release}} = \frac{y_{HCl, \text{ measured}}}{y_{HCl, \text{ max}}} \cdot 100 \quad (4.7)$$

As the solid (FA) sample and the HCl concentration (in flue gas) are obtained from the same sampling duration/location, the assumption made for Eq. 4.5 and 4.7 holds: the sum of $x_{Cl \text{ release}}$ and $x_{Cl \text{ retention}}$ is 100. A similar method is applied with regard to fuel-sulfur. Then, the released fraction is evaluated from the measured SO_2 concentration and the retained fraction derives from the sulfur content in solid sample (FA).

The released versus retention graph corresponding to the straw (S) combustion case from test set D (see Table 22) is shown in Figure 52, corresponding to (a) chlorine and (b) sulfur. Each data point is assigned with the measurement location as distance down the burner (in m).

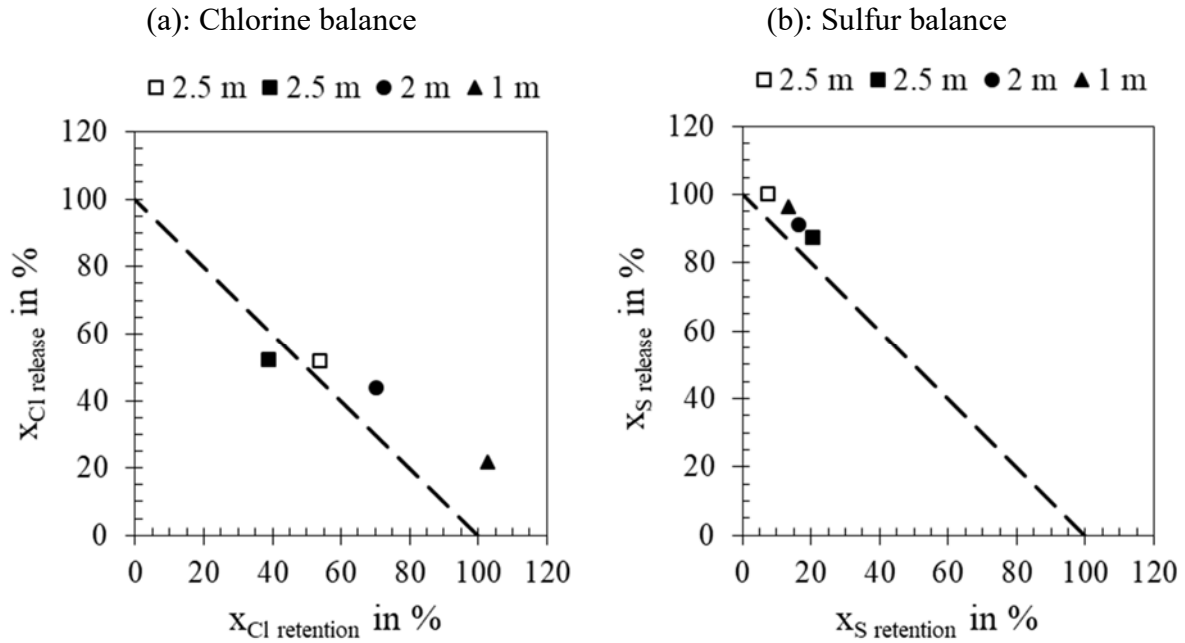


Figure 52: Released versus retention graph corresponding to straw (S) combustion case, corresponding to (a) chlorine and (b) sulfur.

A similar comparison is made with fly ash (FA) samples corresponding to test set B (see Table 22). The FA is sampled by a vertical oil cooled probe at the end of the combustion chamber (2.5 m) while the flue gas HCl is measured outside the combustion chamber in the flue gas duct location I. The fly ash sample was analyzed for ash content (550°C) and for water soluble fraction of chlorine (Cl) and sulfur content (S).

The additive adds solid components therefore dilutes the FA generated from fired fuel. The chlorine content in given solid i.e. FA sample collected during additive case is influenced by this dilution. To consider this dilution the input amount corresponding to ‘fuel+additive’ mix is mathematically corrected by Eq. 4.8. The solid content in the additive increases the resulting ash content while the Cl decreases due to dilution. Under assumption of Eq 4.9, the chlorine retention ($X_{Cl, retention}$) then derives according to Eq. 4.5.

$$\gamma_{i, corrected} = \frac{M_{fuel} \cdot \gamma_{i, fuel} + M_{additive} \cdot \gamma_{i, additive}}{M_{fuel} + M_{additive}} \cdot 100 \quad (4.8)$$

$$\dot{M}_{sample} \cdot \gamma_{ash, sample} = \dot{M}_{fuel} \cdot \gamma_{ash, fuel} \quad (4.9)$$

The fuel feeding is kept constant. The additive fraction does not induce dilution to the flue gas side. Therefore the total flue gas volume is presumed to be similar across various additive loadings. The correction is not required to derive the fraction of chlorine released evaluated from corresponding HCl measurement.

The released versus retention graph is shown in Figure 53 (a) corresponding to chlorine and (b) corresponding to sulfur. Each data point is assigned with combusted fuel (TS) and corresponding additive name (A and B) and loading (5, 6 and 20 %).

Figure 52 and Figure 53 illustrate the proportioning between chlorine release and retention across different cases and conditions. The objective is to establish the transferability of HCl measurement as a valid method to evaluate the extent of chlorine retention in ash.

When the FA sample and HCl measurements are performed parallel, the closure of release and retention is satisfactory. The results shown in Figure 52 and Figure 53 conform a reasonable closure for release (HCl concentration in flue gas) and retention (chlorine content in fly ash) of chlorine. The closure of release (SO₂ concentration in flue gas) and retention (sulfur content in fly ash) is significantly off the closure line corresponding to TS and additive cases, see, Figure 53 (b) while the closure is reasonable for S (straw) case, see Figure 52 (b).

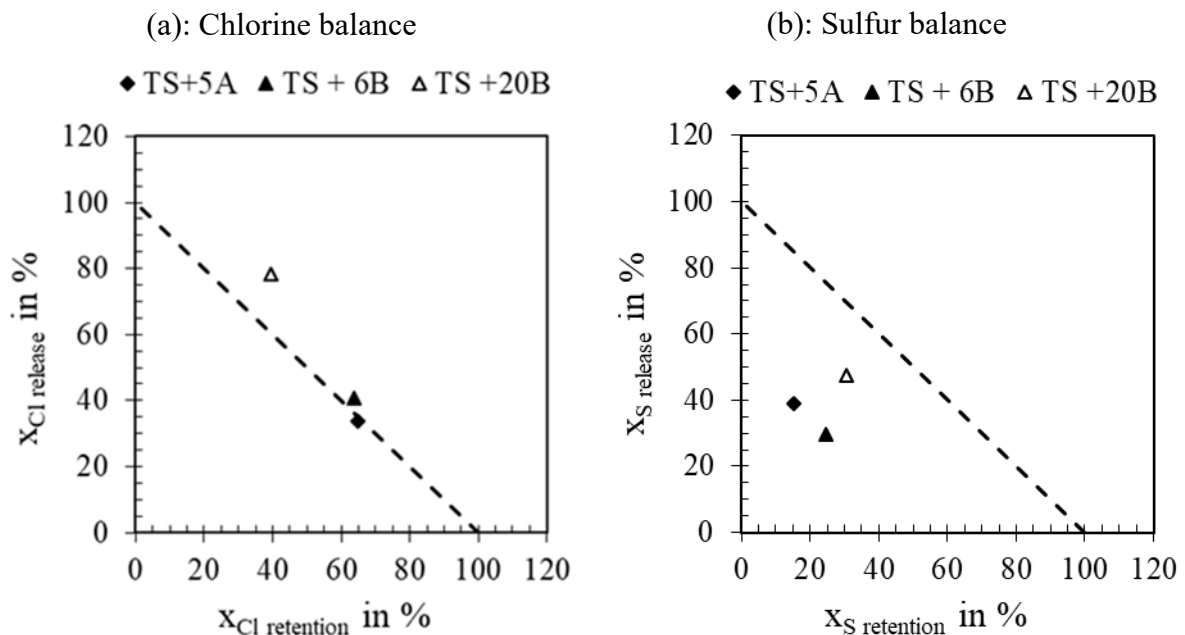


Figure 53: Released versus retention graph corresponding to TS and additive variation case, corresponding to the (a) chlorine and (b) sulfur balance.

Notably, the additional SO₂ capture may occur between combustion chamber outlet and flue gas duct position-I. This is apparently not accounted in the FA samples from test set B, as FA

is sampled at the end of the combustion chamber while the SO₂ is measured outside the combustion chamber. The SO₂ inside the combustion chamber is 17 ppmv in case without additive and stabilizes at maximum average of 67 ppmv with additive in the system. The SO₂ measured outside the combustion chamber at duct position-I is in average 10 ppmv without additive and stabilizes at maximum average of 54 ppmv with additive in the system. Even accounting this, the balance of sulfur release and retention corresponding to TS+additive cases are off the closure line. Another possible reason is the poor solubility of sulfate salts compared to chlorine salts. This may be a reason why closure is achieved for chlorine but not for sulfur. Nonetheless, with additives in the system the fuel borne ash is heavily diluted which as well adds to uncertainty related to FA inhomogeneity along with the simplified assumption made to evaluate the balance.

Experience shows, with many biomass fuels a substantial fraction is molten ash which sticks to the combustion chamber wall, as deposit. In many cases, the molten ash blocks the tip of the FA sampling probe and disturbs the reliable isokinetic and homogeneous extraction of ash from the system. The release and retention balance is not always satisfactory. The failure to closure mostly originates from the solid sampling side (i.e. FA sample).

In contrast, for the extraction of fuel gas the sampling inhomogeneity is not much of concern. The HCl measurement in the flue gas for any given case is convenient, flexible, and repeatable. Therefore HCl is selected as a parameter in this work to evaluate the optimum additive requirement specific to a certain fuel and for the bench mark comparison of capture effectivity of different commercial additives, in a combustion application scenario.

The flue gas extraction location is another concern related to the implementation of HCl as an evaluation parameter. The general assumption is, when flue gas extracted from certain location is quenched to 180 °C any further reaction freezes. This is established along the flue gas extraction line. The acid gases like SO₂ and HCl in the flue gas atmosphere may not strictly follow this assumption. To a certain extent, gas phase sulfation of KCl may occur along quenching duration when the temperature is rapidly dropping. This may influence the measured concentration of HCl when flue gas is extracted from a location where temperature is well above the sulfation temperature > 900°C. Additionally, the HCl (g) may be captured by ash species, especially if free CaO is present, which consequently decreases HCl concentration. This may influence the measured concentration of HCl when the flue gas is extracted from a temperature regime, < 400 °C, where these reactions are favorable.

The temperature inside the combustion zone is well above the optimum sulfation temperature. The flue gas temperature just outside the combustion chamber at the flue gas duct location I drops to the range of 400 – 600 °C. Across different test cases, this temperature varies within this range. The variation is according to the temperature inside the reactor, fuel gas volume, and the false air ingress from reactor bottom. Also, the higher additive loading cases may impact the temperature profile downstream within the combustion chamber and later in the flue gas duct. The temperature at any extraction location downstream to the flue gas duct location I remains < 400 °C. Further downstream the flue gas duct location II, it falls below 200 °C.

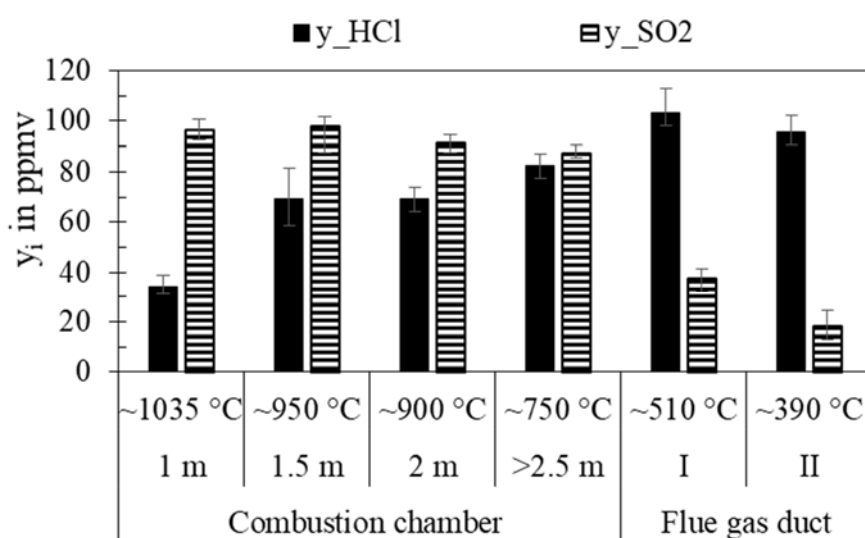


Figure 54: HCl and SO₂ concentration in ppmv, corrected to 6 vol.-% O₂ from different measurement locations corresponding to the S combustion case. The column >2.5 m refers to a position outside the influence of reactor wall heating zone (T5).

Figure 54 shows the HCl and SO₂ concentration measured at different locations corresponding to straw (S) combustion (Test set D). The graph includes the temperature of the measurement location in °C rounded up (thermocouple measurements). The temperature at the sampling location (inside the combustion reactor) is measured by the thermocouple (fitted at the tip of the vertical sampling probe). From inside the combustion reactor, the flue gas was extracted by the vertical (oil cooled, 180°C) probe. For flue gas duct locations, a glass tube with a filter packed head of quartz wool directs the flue gas which is then transported to the FTIR analyzer. This shall keep the ash and flue gas interaction in the extraction location. Further fine aerosols are filtered by a heated ceramic filter, therefore, further in the transport line the interaction that involves solid ash species is minimal. The earlier separation of ash and aerosols is implemented

to avoid the ash-flue gas interaction that may proceed in the sampling line. The flue gas extraction line is ensured to be in equilibrium at the set temperature of 180 °C prior to each measurement run.

Following observations are made corresponding to Figure 54:

- A substantial increase in HCl is observed between 1 m and 1.5 m, further it increases only slightly towards the combustion chamber exit (2.5 m). The SO₂ concentration on the other hand remains similar after 1 m. It implies that the fuel-sulfur release is completed well earlier than the fuel-Cl release. Fly ash sample from 1 m contains a substantial amount of unburnt char ($\gamma_{C \text{ in FA}} \approx 8 \text{ wt.-% db.}$) which indicates that the fuel-chlorine largely retains in char thereby the HCl concentration is lower. Further below (see 1.5 and 2 m in Figure 54) the HCl concentration increases and in this location the char fraction is mostly combusted (at 2 m $\gamma_{C \text{ in FA}} \approx 1.5 \text{ wt.-% db.}$).
- The HCl concentration in the flue gas duct at position I is notably higher than at the combustion chamber exit (2.5 m) and is accompanied by a drop in SO₂. This increase of HCl or decrease of SO₂ corresponding to the change in measurement location mainly signifies the consequence of sulfation. The increase in HCl is caused by the sulfation of KCl. On the other hand, the decrease in SO₂ is not only related to KCl sulfation but may as well include other alkali/earth alkali species.
- Further downstream in the flue gas duct at location II, the HCl concentration drops as well as SO₂. This decrease of SO₂ is associated with the capture saturation. The drop in HCl is apparently related to CaO-HCl capture reactions favored at downstream temperature regime.

Figure 55 shows the comparison between case *W-w/o and *W-w/ for (a) HCl concentration and (b) SO₂ concentration. The cases are referred as *W-without (w/o) additive and *W-with (w/) additive. The graph includes the temperature of the flue gas measurement location in °C. The test boundaries are similar to test set C (see Table 23). The fired fuel is *W-I (Annex1, see Table 31) and additive is A (see Table 16). The additive loading corresponding to test run discussed here is $\approx 10 \%$.

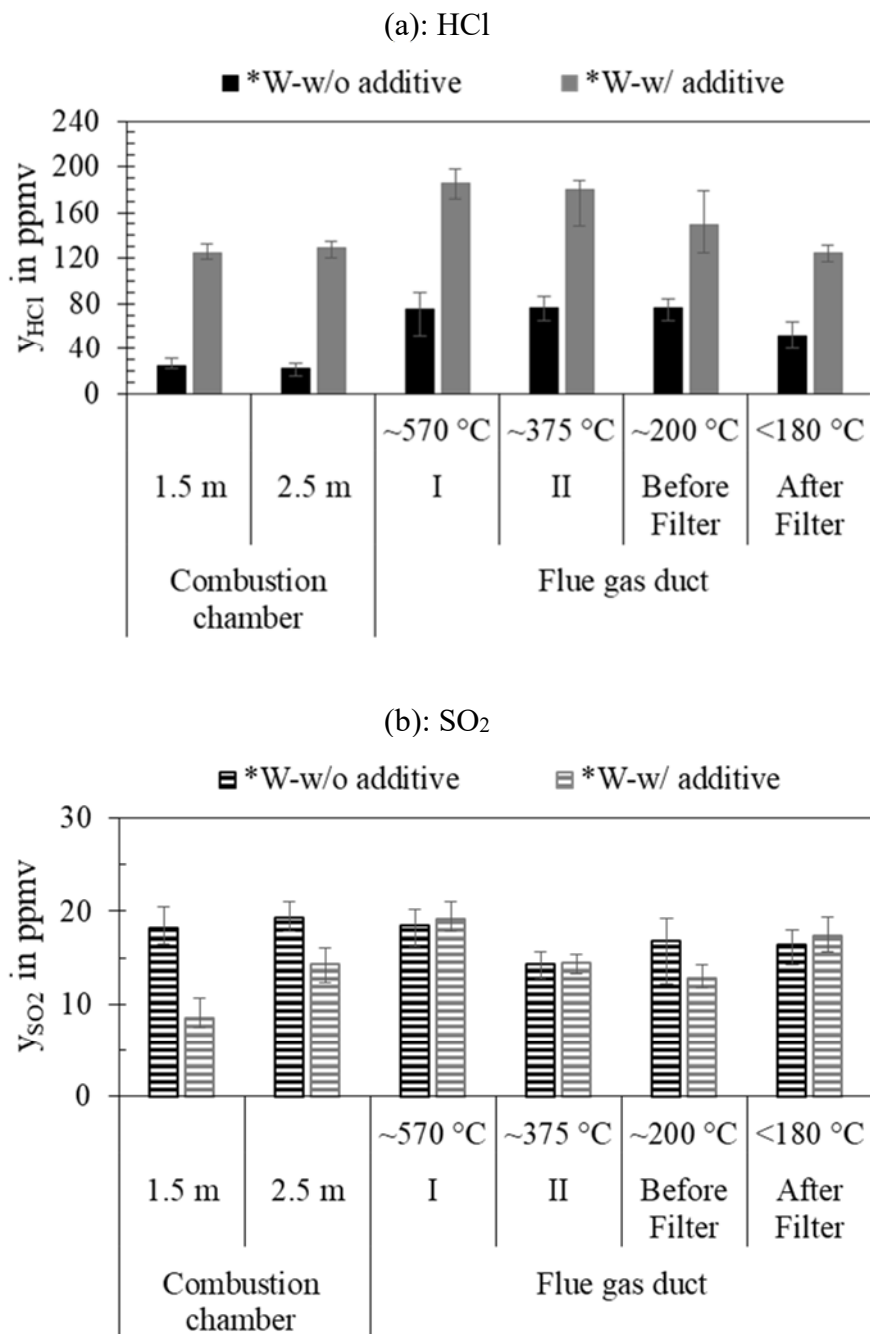


Figure 55: Comparison between case *W-w/o and *W-w/ for (a) HCl concentration and (b) SO₂ concentration in ppmv, corrected to 6 vol.-% O₂.

Following observations are made corresponding to Figure 55.

- The influence of the measurement location on HCl concentration is similar to that of the straw combustion case (discussed earlier) and justified by similar explanation. The SO₂

concentration is overall lower and in either case below 20 ppm. A substantial SO₂ capture is apparently explained by the abundance of sulfur capturing especially CaO in wood ash.

- The HCl concentration is substantially higher corresponding to case *W-w/ in every location. The increase is already observed inside the combustion reactor where the HCl is almost five times higher. In the flue gas duct, it is almost two times higher. Comparable HCl concentration between 1.5 m and 2.5 m, both locations inside the combustion chamber, suggests that the additional availability of reaction time does not promote additional release. The reaction of concern, the KCl-kaolinite capture reaction, is largely proceeding already in the combustion temperature zone and the kinetic limitation is expected to be of low concern provided that the active sorbent, kaolinite derived aluminosilicatic, is available [103].
- The HCl concentration in the flue gas duct location I is higher than inside the combustion chamber for both without and with additive cases. The magnitude of increase is as well similar. It suggests that the KCl sulfation is relevant to the HCl release even in presence of additive. Nonetheless, it remains unclear why a certain fraction of KCl though in presence of additive awaits for sulfation to release HCl.
- The increase in HCl from the location inside the reactor to the location outside the reactor is accompanied by the decrease in SO₂ corresponding to the straw case (discussed earlier). The effect is partly in relation to KCl sulfation. Such observation is not made from the *W test cases though the increase in HCl in the flue gas was clearly registered. In *W case the drop in SO₂ is not registrable and probably relates to the over saturation amount of SO₂ capturing species especially, CaO present in wood ash.
- Further downstream of flue gas duct position II, the HCl drops substantially. This drop is apparently related to the HCl-CaO capture reaction and favored towards the lower temperature end of the test system. The drop is more pronounced corresponding to the additive case when the concentration of HCl upstream in the flue gas is substantially higher. The CaO-HCl capture reactions and the influence of various parameters is published by Mura et al. [126]. The condition downstream the flue gas duct is optimal for such CaO-HCl reaction to proceed.

Following points are made corresponding to the appropriate choice of measurement location for the purpose to use HCl as additive optimization parameter. The measurement location outside the combustion chamber was chosen considering the following points:

- The HCl concentration is highest at flue gas duct position I. KCl which escapes the high temperature interaction, i.e. within the combustion chamber, is sulfated as the temperature drops outside the combustion chamber resulting in HCl increase. Across different fuels, it largely depends on the extent of SO₂ availability and the temperature drop. Downstream of location I, the HCl concentration starts to decrease. The extent of the drop is influenced mainly by ash CaO content and basically relates to the CaO-HCl capture reactions. In most herbaceous fuel, the availability of free CaO is limited. In wood, the availability of free CaO is expected to impact the HCl concentration as the flue gas temperature drops below 400°C. The results support that the flue gas duct location I and II are within the temperature regime where sulfation of KCl is favored but the re-capture of HCl to ash by CaO is limited. For a given case, there is only a minimal increase of HCl from flue gas duct location I to II. It implies that the impact of additional availability of reaction time in these temperature regimes is minimal.
- Across different biomass fuels the 2S/Cl ratio varies which is known to govern the extent of chlorine retention in ash/aerosol, thereby influencing the HCl concentration in the flue gas. To account for the contribution of fuel borne sulfur (S) species, the measurement location in the flue gas duct was chosen. Additionally, the condensation of gaseous alkali species, including KCl is accompanied by its sulfation along diffusion-condensation driven deposition process.

The reactive aluminosilicate mineral from the additive shifts the fate of chlorine in a system from KCl (g) to HCl (g). The underlying KCl-aluminosilicate capture reactions are favored at temperatures within the combustion zone. The increase in HCl concentration to certain additive loadings refers to the achievable KCl-aluminosilicate capture reactions in the given system boundaries and application scenario and well reflects the consequent decrease in the extent of chlorine retention in ash/deposit. The HCl as an additive (amount) optimization parameter is further exploited for the bench mark comparison of capture efficiency among various commercial additives and to evaluate the optimum amount required for a given biomass fuel.

4.4.1.2.1 HCl concentration at different additive loading

The combustion progress inside the test reactor is supported by the heat from the reactor wall, electrical external heating. The influence of additive introduced with it has nominal influence on the combustion progress of fuel particles. The slight decrease in CO at higher additive loadings is observed. Nonetheless, the reference CO which is without additive is substantially lower

to register the variation as additive specific influence. The H₂O concentration increases slightly with additive loadings due to additional input from the additive, apparently related to moisture and crystal water in the additive. In comparison to the reference average concentration of ≈ 11 vol.-%, at higher additive loading it increases up to ≈ 12 vol.-%.

In the implemented electrically heated combustion facility (BTS-VR), the NO shows a trend to increase associated with the additive loading. In test B additive variation cases, the NO in the reference case without additive is ≈ 866 ppmv and increases up to 1144 ppmv, 1082 ppmv and 1012 ppmv corresponding to maximum additive loading of A, B and D cases respectively. The increase in NO is probably related to the increased availability of OH⁻ radicals in the volatile combustion zone originated from the release of crystal water present in additive minerals. A non-staged jet flame is a characteristic flame produced by the burner employed in BTS-VR. The temperature of the combustion chamber is maintained by external electrical heating and the amount of additive probably does not impose the changes in the temperature profile. Therefore any in-flame NO reduction is not expected.

In the pilot scale facility (KSVA) tests, the NO increase in association with additive was not a significant observation (see Table 20, M in comparison to M+B and S in comparison to S+D case) as observed in BTS-VR test cases. The burner (with swirl) employed in the pilot scale facility exhibits in-flame NO reduction. The temperature of the combustion zone is maintained solely by the flame and subject to influence by the amount of additive introduced with the fuel. The influence of additives on the fuel-N related emission species is not within the scope of this work. If any, the significance of NO emission in an additive-fuel co-injection scenario requires further clarification and dedicated study.

For this study, fuel-S and fuel-Cl relevant flue gas species, namely SO₂ and HCl, are of concern. Figure 56 shows the HCl and SO₂ concentration of continuous FTIR measurement corresponding to various additive amount in g/h, as fed, on the right axis. The test run corresponding to additive B is shown as an example. The fuel feeding for a given case is constant while the additive feed is varied independently.

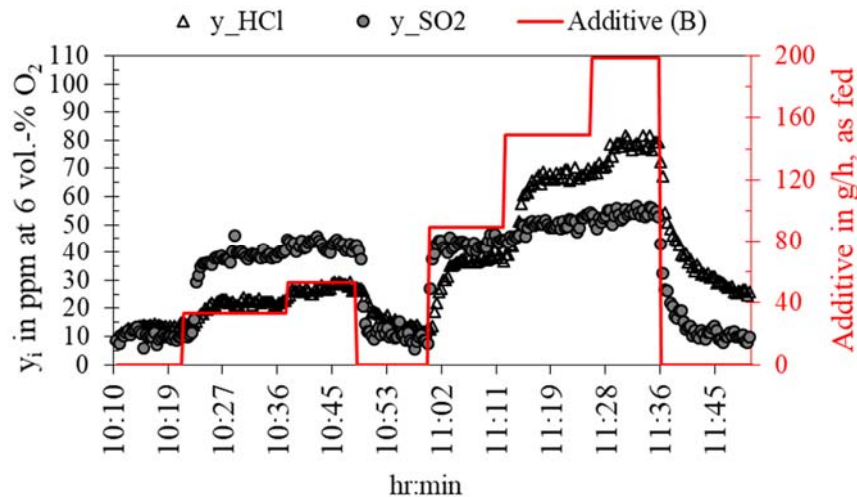


Figure 56: HCl and SO₂ concentration in ppmv on the left axis corresponding to a test run with additive B. The fuel feeding was constant ≈ 1 kg/h. The variation in additive feed in g/h is shown on the right axis.

Following general observations are made from additive variation tests:

- The HCl concentration increases in response to the additive fed to the system and drops down as soon as the additive feeding is stopped. The response of HCl was fast, clear, and repeatable.
- With increase in additive loadings, the HCl concentration in the flue gas increases. For TS4 additive variation cases, the reference HCl (i.e. without additive) is ≈ 15 ppmv and increase up to ≈ 80 ppmv in case with additive (see Figure 56). The additive loading required to approach maximum HCl in the flue gas, depends on the additive in use. Provided, test boundaries are similar, for a given additive variation test run the KCl-aluminosilicate (additive mineral) capture chemistry largely explains the increases in HCl concentration.
- The SO₂ concentration shows a noticeable increase with additives. For TS4 additive variation cases, the reference SO₂ (i.e. without additive) is ≈ 15 ppmv and increase up to ≈ 50 ppmv in case with additive (see Figure 56). The increase in SO₂ is an indirect effect of K-species capture reactions driven by aluminosilicate (additive mineral). The K-species which otherwise consume SO₂ are now captured by the aluminosilicate. The SO₂ consumption i.e. sulfation, is favorable at a lower temperature regime (i.e. outside combustion zone) while K-species capture reactions are favorable already at high temperature (i.e. within the combustion zone). The increase in SO₂ is the consequence of depletion in availability of K-species in the system.

- The main difference to HCl increase and SO₂ increase is that the HCl approaches the allowable maximum (y_{HClmax} : 95 ppmv) while SO₂ saturates well below the allowable maximum ($y_{\text{SO}_2\text{max}}$: 118 ppmv). The availability of CaO (a SO₂ capturing ash component) in the system is probably not depleted by additive minerals and CaO-SO₂ reaction is functional. This probably explains the limit in SO₂ increase.

4.4.1.2.2 Comparison across different commercial additive

If there is no disturbance in feeding (fuel and additive), no blockage of flue gas extraction line, and the flue gas extraction line remains in temperature equilibrium of ≥ 180 °C. Both, HCl and SO₂ concentration, correspond to given additive loading fluctuate in a very close range. The average HCl and SO₂ concentration is expressed as $x_{\text{Cl}\rightarrow\text{HCl}}$ and $x_{\text{S}\rightarrow\text{SO}_2}$ in %. Mathematically, it represents the fraction of fuel-Cl release as HCl and fuel-S release as SO₂. Derived from equation discussed earlier in section 4.4.1.2 (see Eq 4.7), Figure 57 shows the Cl to HCl ($x_{\text{Cl}\rightarrow\text{HCl}}$) and S to SO₂ ($x_{\text{S}\rightarrow\text{SO}_2}$) corresponding to different additive feed rate in g/h db. The reference Cl to HCl conversion, i.e. without additive, is ≤ 20 % and S to SO₂ conversion is ≤ 10 %.

There is initial increase of $x_{\text{S}\rightarrow\text{SO}_2}$ coupled with the introduction of additive to the system. Nonetheless, the SO₂ does not show a further increase with increasing the additive load and it saturates around ≈ 45 % (see Figure 57). This behavior is similar among all additive variation cases. The initial increase in SO₂ is related to the early capture of K-species in the combustion zone. The sulfation reaction is limited in the combustion zone (high temperature). Thereby the capture reaction overtakes. The additive at a lower loading would be consumed by KOH (g) which is supported by the equilibrium chemistry discussed later (in section 4.4.2.2). With a further increase of additive in the system, the SO₂ remains stable apparently because the additive demand to capture KOH (g) is already fulfilled.

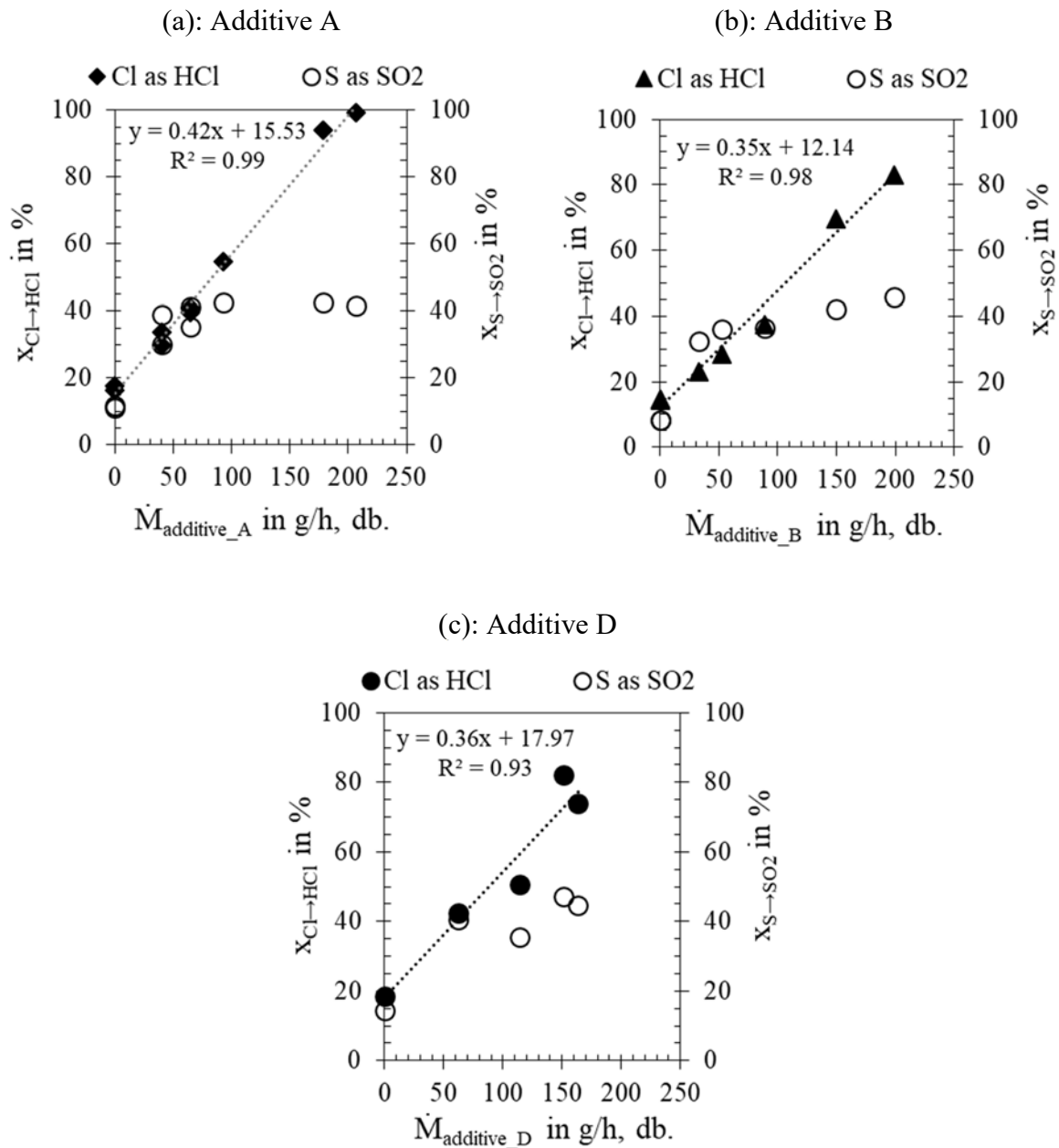


Figure 57: $x_{\text{Cl} \rightarrow \text{HCl}}$ and $x_{\text{S} \rightarrow \text{SO}_2}$ in % corresponding to the different additive feed in g/h, as fed for the variation of (a) additive A, (b) additive B, and (c) additive D. The fuel feeding is constant at ≈ 1 kg/h.

The pathway of the K_2SO_4 (g)-aluminosilicate capture reaction and associated SO_2 increase is less likely. The gas phase stability of KCl and KOH at high temperatures is well established. But, gas phase stability of K_2SO_4 is not well understood owing to its low vapor pressure. The reaction with additives may proceed with solid or liquid K_2SO_4 but in the entrained condition, this pathway may be limited. For all the tested additives similar increase of SO_2 is observed and it saturates around 45 %. The level of release suggests that a substantial fraction of fuel-S still remains in ash. The saturation is probably governed mainly by the availability of free CaO with

escapes the reaction with additive minerals. The physical contact of CaO (solid particle) with additive mineral (solid particle) is expected to be limited. In entrained conditions the solid-solid reactions remain suppressed due to lack of physical contact.

The $x_{\text{Cl} \rightarrow \text{HCl}}$ almost linearly increases in accordance to the amount of additive fed to the system (see Figure 57). It flattens out as it approaches the maximum $> 90\%$. The increase in HCl is a direct consequence of the KCl (g)-aluminosilicate capture reaction. This result justifies that with enough additive in the system, almost all KCl (g) is captured and in the process, chlorine is pushed to the flue gas to remain as HCl. Consequently, with enough additive in the system the KCl (g) capture saturates as well as the HCl concentration in the flue gas saturates near the expected maximum HCl. This behaviour is similar among all additive variation cases.

Figure 58 (a) shows the $x_{\text{Cl to HCl}}$ in % versus additive loading in % corresponding to different additive types and it facilitates a comparison between different commercial additives. To harmonize the variation in moisture content between the additives in use, the additive loading is presented as the amount of additive fed (db.) in reference to the fuel fed (constant: 1 kg/h). The ash content in the given fuel (TS4) is 6.3 wt.-%, db. Substantially higher additive loadings is required to approach maximum HCl.

It is well known that not all the minerals introduced with additive are involved in the capture reaction. Kaolinite derived aluminosilicate minerals drive the capture chemistry. The fraction of kaolinite in the test additive decreases in the following order $B > A > D$ (see Table 16).

Figure 58 (a) shows the $x_{\text{Cl to HCl}}$ in % versus kaolinite loading in % corresponding to different additives and it facilitates the comparison across different commercial additives. The kaolinite loading in % refers to the fraction of kaolinite feed (db.) in reference to fuel feed (constant: 1 kg/h).

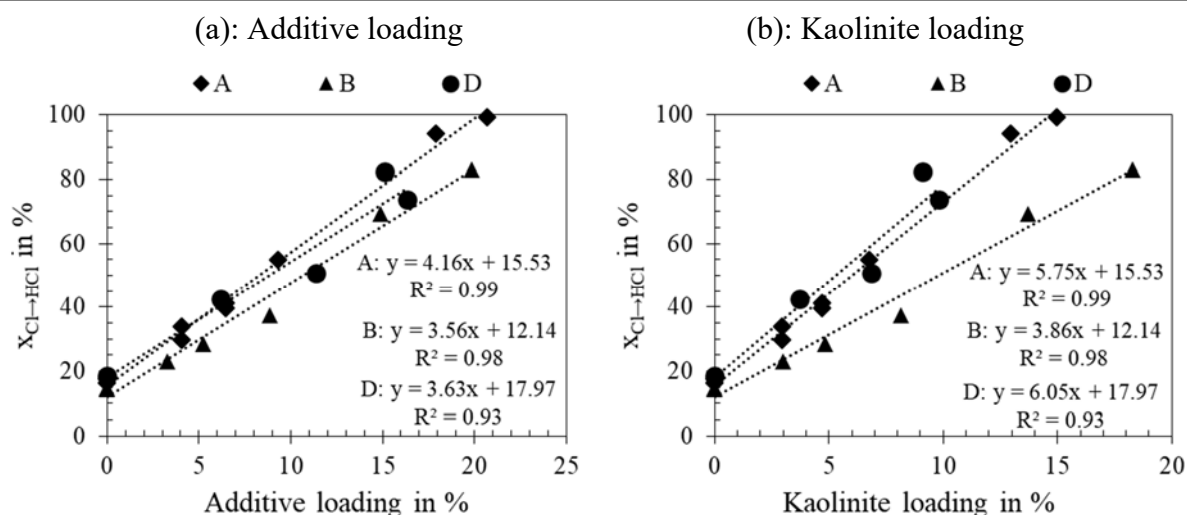


Figure 58: $X_{Cl \rightarrow HCl}$ in % corresponding to (a) additive loading and (b) kaolinite loading (in % of fuel) for different commercial additives in the combustion cases from test set B.

The additional kaolinite fraction in additive B (30-40% higher in comparison to A and D, see Table 16) appears not to add to the overall HCl increase (see Figure 58 (a)). This suggests, the capture efficiency of kaolinite from additive B is compromised in comparison to additive A and D (see Figure 58 (b)). The following general observations regarding the capture efficiency (sorbent utilization) among commercial additive tested during this work are drawn:

- The higher fraction of kaolinite mineral in a given additive does not necessarily mean a better alkali capture (sorbent utilization) efficiency per unit gram. The capture rate is coupled with the transformation rate of the kaolinite particles in a given application scenario. The fuel and combustion boundaries are comparable among different additive cases, therefore the difference is related to the properties of additive and the transformation behavior of kaolinite present in it. The moisture content, particle size distribution and mineralogical composition of additives are relevant to transformation rate. The water content and particle size largely govern the heating rate of a particle. In turn, the heating rate governs the time and temperature a particle experiences prior to the capture reaction. The lower capture efficiency of the kaolinite in additive B is probably related to a faster transformation rate. The transfer rate is possibly faster owing to smaller particle size distribution in given additive B, in comparison to other two additives (see Table 16). Additionally, the presence of mineral impurities like muscovite and quartz are known to modify the transformation of kaolinite. Zhou et al. [98] pointed out that mullite forms more readily from pure kaolinite than from kaolinite with other impurities. To note, additive B is mostly Kaolinite (see Table 16). For either both of the stated

reasons, the slip to the mullite phase is faster with additive B so the capture efficiency is compromised.

- Among kaolin group minerals halloysite is argued to be a better a capture sorbent than kaolinite [94,97]. The BET surface area of halloysite containing additive is higher with 60 – 70 m²/g than kaolinite containing additives with 10 – 13 m²/g. For solid sorbents, higher BET surface area is an indication of better adsorption capacity. Considering the reactive aluminosilicate fraction as Al₂Si₂O₅(OH)₄ among additives, the slope of HCl increase in case of additive D is marginally steeper than for additive A and clearly steeper than for additive B. The steeper slope indicates a better capture performance. In a combustion application scenario, the halloysite or kaolinite itself is not the actual component to be involved in the capture reaction. Rather the amorphous meta-kaolin Al₂Si₂O₇ which is formed after losing the crystal water, drives the capture reaction. The formation of meta-kaolin is commenced in the range of 450°C-600°C [98,127]. The kaolinite injected to the combustion chamber can see temperature up to 1300 °C. This is well above the optimum range for meta-kaolin stability. Further, any additional reaction related to the structure or properties as raw mineral particle probably exhibit shorter-life as the surrounding condition, namely the temperature, favors transformation to the spinel and mullite phase. The higher capture efficiency with halloysite in high temperature application scenarios requires further justification.

4.4.1.2.3 Comparison across different biomass fuels

Figure 59 shows the $x_{\text{Cl} \rightarrow \text{HCl}}$ and $x_{\text{S} \rightarrow \text{SO}_2}$ in % corresponding to additive A feed rate in g/h, db., from test set C, (a) TS1 combustion case, and (b) *W combustion case. The average HCl and SO₂ concentration is expressed as $x_{\text{Cl} \rightarrow \text{HCl}}$ and $x_{\text{S} \rightarrow \text{SO}_2}$ in %. The maximum concentration of HCl and SO₂ under assumption of complete conversion is, respectively, 50 ppmv and 93 ppmv for TS1 and 136 ppmv and 87 ppmv for *W.

For the TS1 combustion case, see Figure 59 (a), the $x_{\text{S} \rightarrow \text{SO}_2}$ saturates at $\approx 40\%$ already without additive and the $x_{\text{Cl} \rightarrow \text{HCl}}$ is nearly at 50 % and approaches 100 % with increasing amounts of additive fed to the system. In comparison to the observations of test set B, see Figure 57 (b), the response of SO₂ to additive is non substantial while the response to HCl shows similar trend. Corresponding to the *W case, see Figure 59 (b), the $x_{\text{S} \rightarrow \text{SO}_2}$ is almost zero and the $x_{\text{Cl} \rightarrow \text{HCl}}$ is nearly $\approx 40\%$. It approaches 100 % with increasing amounts of additive fed to the system. The saturation of SO₂ without additive may be partly related to the fuel ash composition (mainly

availability of free CaO) which supports the capture of released SO₂ and partly to downstream measurement location (flue gas duct position I) which provides enough time for the SO₂ capture to saturate. The zero SO₂ in case of wood is probably related to the excess availability of CaO in original wood ash.

In the temperature regime along the flue gas duct, the KCl which escapes sulfation largely remains as solid aerosol particles. These are formed as the flue gas temperature drops. The solid phase capture pathway of KCl is presumably largely limited and most of the HCl increase corresponds to the KCl (g)-additive interaction which occurs predominantly inside the combustion chamber.

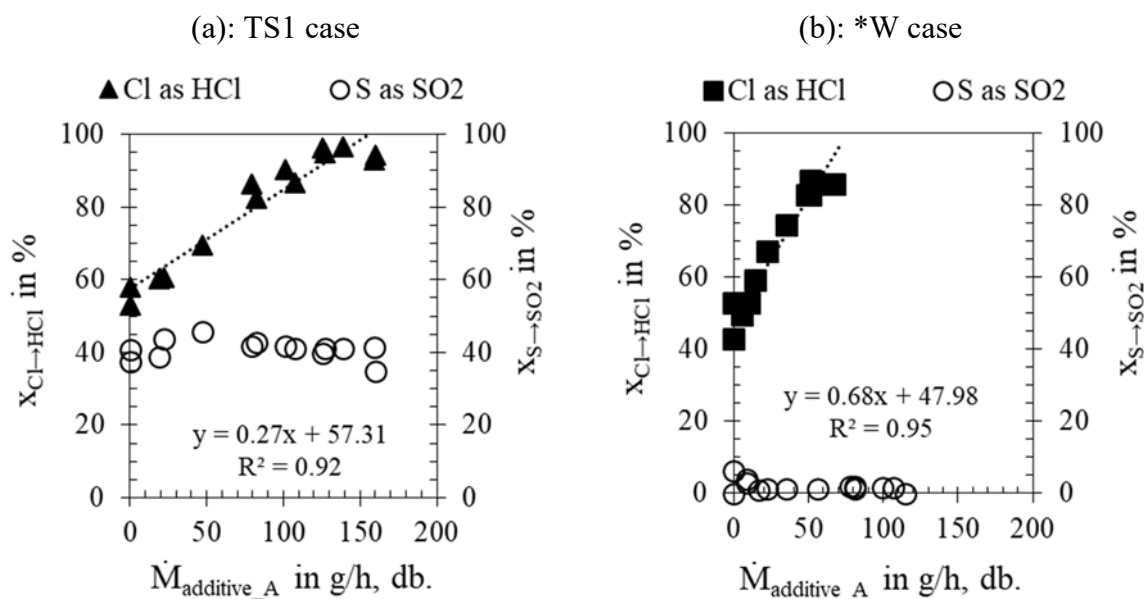


Figure 59: $x_{\text{Cl} \rightarrow \text{HCl}}$ and $x_{\text{S} \rightarrow \text{SO}_2}$ in % corresponding to additive (A) feed rate in g/h, db for the combustion case (a) TS1 and (b) *W. The fuel feeding was constant at ≈ 1.5 kg/h.

Figure 60 shows the $x_{\text{Cl} \rightarrow \text{HCl}}$ in % versus (a) additive loading and (b) kaolinite loading (in % of fuel) for different fuel combustion cases with the same additive A and facilitates the comparison across different biomass fuels. In case of TS1 it is ≈ 8.0 % and it for the *W case it is ≈ 6.6 % of additive loading corresponding to the maximum HCl release. The test boundaries are comparable across the cases. The difference in response to the additive loading is not related to the additive mineralogy and transformation but to the fuel composition and chemistry of the fired fuel.

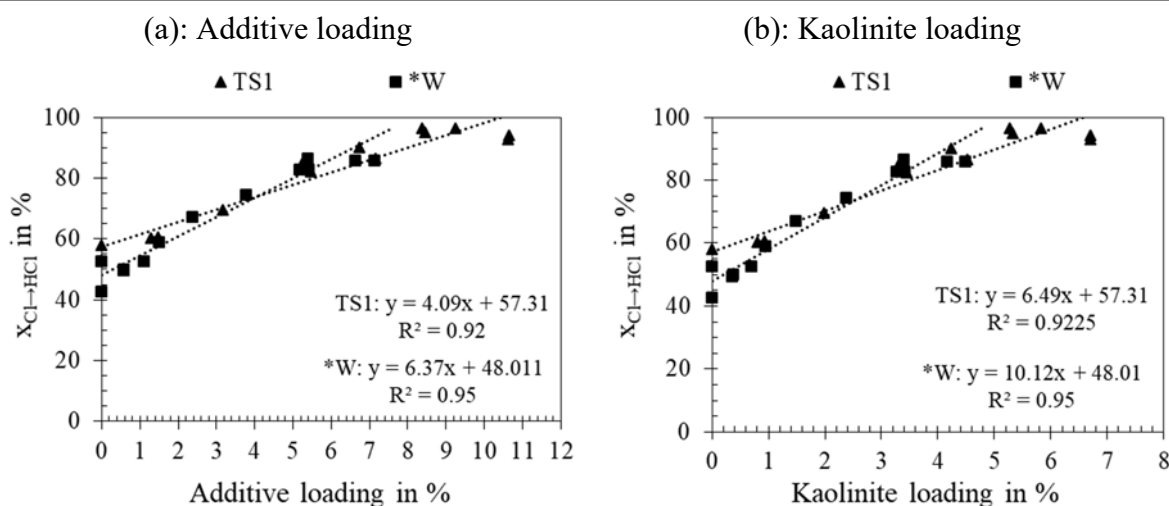


Figure 60: $X_{Cl \rightarrow HCl}$ in % corresponding to (a) additive loading and (b) kaolinite loading (in % of fuel) for different biomass fuels and additive A from test set C.

The ash and potassium contents in *W fuel are substantially lower (1.7 and 0.23 wt.-%, db., respectively) than in TS1 (4.5 and 1.24 wt.-%, db., respectively) which does not justify a close range among them in terms of additive loading. The total amount of K content per kg fuel in *W is almost 4 – 5 times lower than in TS1. However, almost 65 % of the potassium corresponds to KCl in *W while in TS1 it is only 7 %, under assumption that all chlorine in fuel is present in form of KCl. The higher loading in the *W case is probably related to higher amounts of chlorine (0.14 wt.-%, db.) in comparison to TS1 (0.05 wt.-%, db.) or in other words; the chemical form of K in the fuel. This implies, the capture of KCl proceeds less effectively than with other chemical forms of K.

4.4.1.2.4 Equilibrium chemistry and comparability with experimental results

Figure 61 shows the distribution of potassium as fraction of total input K against the variation of temperature, (a) phase distribution and (b) K-species distribution. The input to the calculation corresponds to the composition of torrefied straw, Fuel Name: TS4.

Towards the higher temperature > 1050 °C, potassium prefers to be either in liquid or gaseous phase. Towards the lower temperature < 1050 °C, the solid phase increases in expense of liquid phase. Among K-species, KCl prefers to remain in the gaseous phase and moves to the solid phase < 700 °C, see Figure 61 (a) on the left axis. KOH moves to the gas phase above 1050 °C mainly in expense of the liquid phase. The gas phase stability of K_2SO_4 is low and remains in a narrow temperature range. Sulfur prefers to remain as SO_2 in the gas phase above 1050 °C. HCl slightly increases with temperature, and at equilibrium most of chlorine prefers to stay as KCl, see Figure 61 (b).

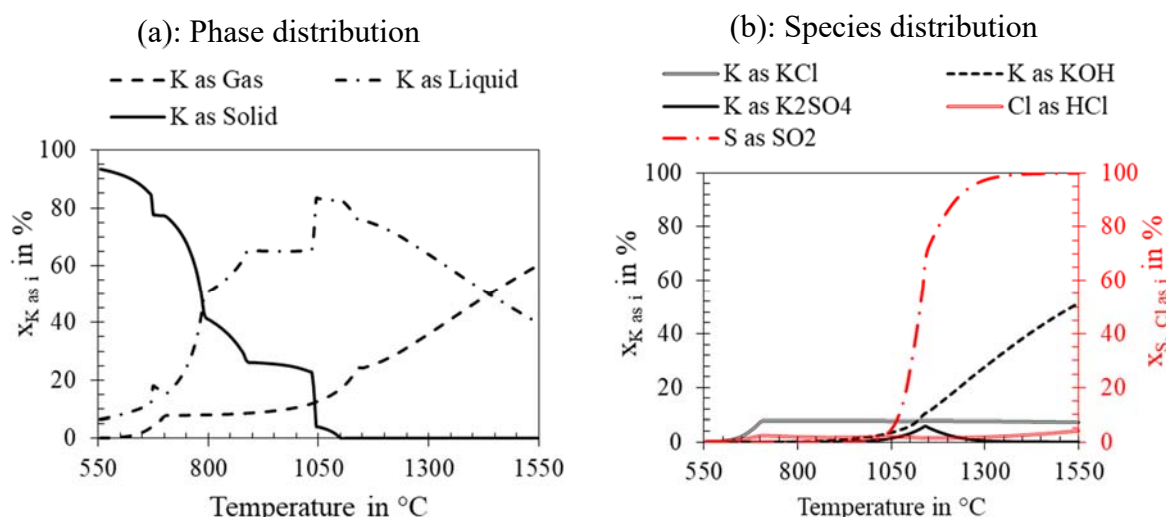


Figure 61: The distribution of potassium $X_{K, as i}$ in % against temperature variation derived from the FactSage equilibrium calculation: (a) phase distribution and (b) species distribution. The $X_{S, Cl, as i}$ refers to the fraction in reference to the respective input.

This equilibrium chemistry related to biomass fuel inorganics is well reported [22,27,128] and a similar discussion is published by the author with input composition corresponding to wood [17]. The amount of a certain phase or species and the temperature range of their existence, varies mainly with the amount of calculation input (amount of individual elements in fuel) and their relative ratio.

Most important to understand is that at combustion temperature regime, the potassium exists either in the gas phase and/or as liquid phase. KOH and KCl are the main gaseous species which is confirmed [32,90].

To evaluate the equilibrium chemistry in the combustion temperature regime, for the further discussion presented here, a temperature of 1200 °C is chosen.

It is well agreed that only a certain fraction of Si from the fuel takes part in ash formation reactions. The input amount of silicon in the equilibrium calculation run is varied in steps of 5 % of total silicon present in fuel. The silicon (Si) input variation shall represent the scenario of variation in the reactive fraction of silicon. Figure 62 shows the distribution of potassium plotted against the variation of silicon (a) the phase distribution and (b) the species distribution. The amount of Si in the equilibrium system significantly influences the phase distribution of K-species, as K-gas, K-liquid, or K-solid. The increasing Si amount decreases the K-gas while it increases K-liquid. The most important message of this equilibrium chemistry is that the reactive fraction of silicon substantially influences the released amount of K as gaseous species.

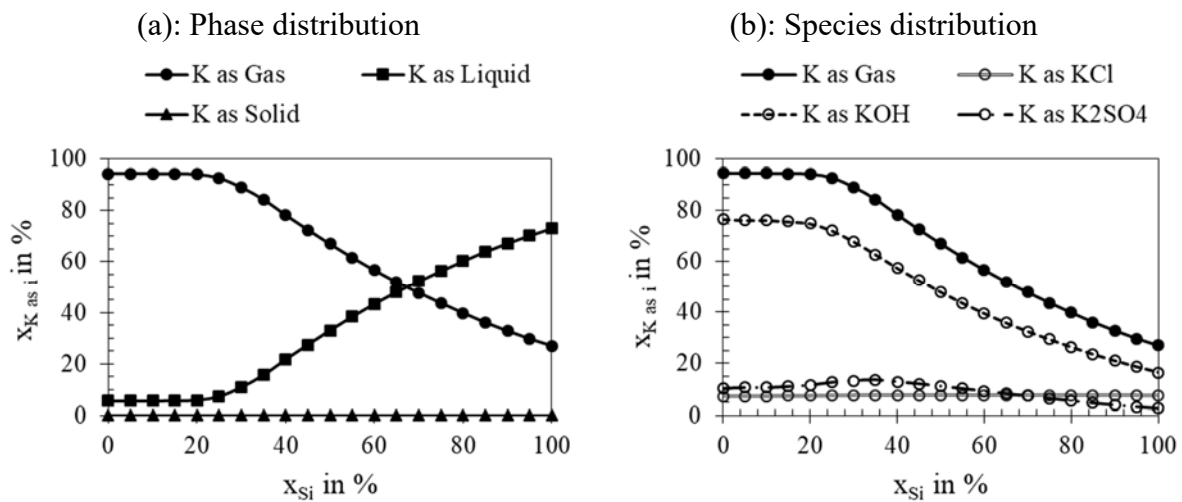


Figure 62: The distribution of potassium $x_{K \text{ as } i} \text{ in } \%$ against the variation of silicon in % derived from the FactSage equilibrium calculation for (a) phase distribution and (b) species distribution.

Among different gas phase K-species, KOH is most effected by the increase in silicon in expense of which the K-liquid is formed. K₂SO₄ starts to decrease after the KOH. While, the fraction of KCl remains almost stable and shows no response to the increasing amount of Si. A similar discussion as above is also published by the author [17] with an input composition corresponding to wood.

KOH represents the main gaseous K-species. The amount of KCl is limited by the amount of chlorine in the fuel and is a stable gas phase species at high temperature. The gas phase stability of K₂SO₄ at high temperatures is lower. Therefore most of S, in the equilibrium prefers to remain as SO₂ rather than as K₂SO₄.

Many authors consider [27,29] the soluble fraction of silicon present in given biomass fuel to represent the reactive fraction. Nonetheless, the soluble fraction is very much fuel specific and also depends on the type of solvent use, water, buffer, and/or acid. There is no common agreement on the approach of defining the reactive fraction of silicon. But in general, the reactive silicon fraction in herbaceous fuel is expected to be higher than in woody fuels.

Figure 63 shows the distribution of K in fraction of the total input-K against the variation of kaolinite loading (a) phase distribution and (b) species distribution. The input to the equilibrium calculation corresponds to the composition of torrefied straw, Fuel Name: TS4. The amount of kaolinite as Al₂Si₂O₅(OH)₄ varies up to 200 g with steps of 1 g. The input amount corresponding to fuel is constant 1000 g. The variation is presented as kaolinite loading in % and represents the fraction of kaolinite in reference to the fuel input amount.

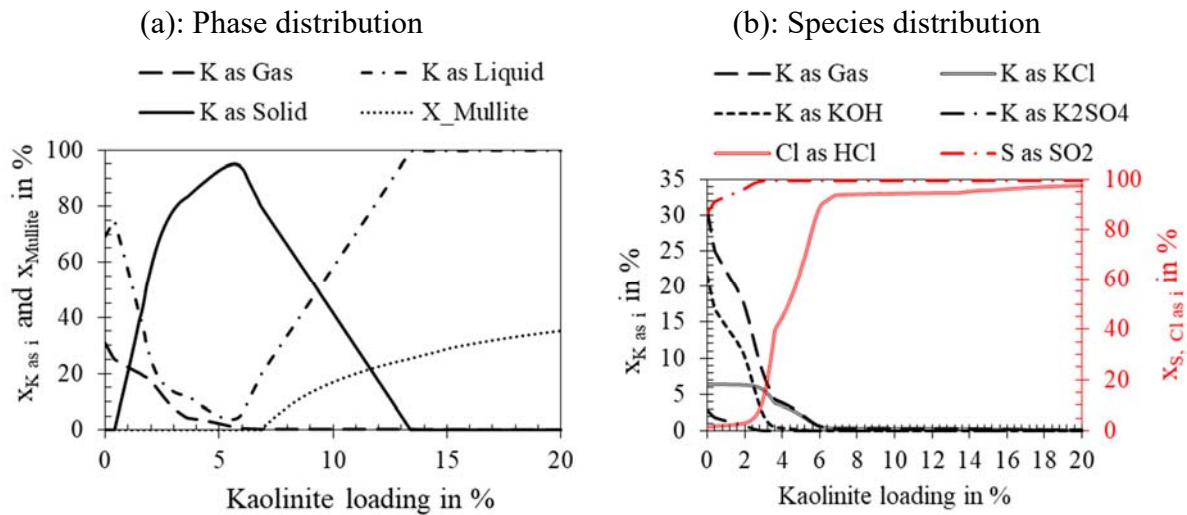


Figure 63: The distribution of potassium $X_{K \text{ as } i}$ in % against kaolinite loading derived from FactSage equilibrium calculation for (a) phase distribution and (b) species distribution. The $X_{S, Cl \text{ as } i}$ refers to the fraction in reference to the respective input.

Both, K-liquid and K-gas, decrease towards higher kaolinite loading. Comparatively, K-liquid drops more rapidly than K-gas. With a substantial amount, almost all potassium moves to the K-solid phase. The appearance of mullite signifies that the amount of kaolinite is in excess which is also characterized by re-increase in the K-liquid phase.

Kaolinite is known to capture alkali species and keep them in the solid phase, apparently as K-aluminosilicate. The equilibrium reflects the ash-additive chemistry and provides the theoretical, chemistry based justification of the additive mitigating effect which means to reduce the fraction of K-gas phase in the system as well as the amount of K-liquid phase.

Table 24 shows the *equilibrium optimum* derived corresponding to Figure 63 (a). The equilibrium optimum refers to the amount of kaolinite loading corresponding to which the desirable situation is achieved.

Table 24: Equilibrium optimum defined corresponding to Figure 63 (a).

Desirable situation	increase or decrease range [%]	Kaolinite loading [%]
Minimum K-Gas	≈ 27 to 0	9.3
Minimum K-liquid	≈ 73 to 6	7.2
Maximum K-Solid	≈ 0 to 92	7.5
Mullite	> 1	9.7

Among different gas phase K-species, KOH and K_2SO_4 decrease, followed by KCl which starts to decrease only after the other two are consumed. The slope of decrease for KOH in comparison to other K-species, namely KCl and K_2SO_4 , is higher. Table 25 shows the equilibrium optimum derived corresponding to Figure 63 (b). To note, SO_2 maximum and K_2SO_4 minimum should theoretically tally. Similar, for the HCl maximum and the KCl minimum. The difference relates to rounding the % to integer values against which the equilibrium optimum is defined.

Table 25: Equilibrium optimum defined corresponding to Figure 63 (b).

Desirable situation	increase or decrease range [%]	Kaolinite loading [%]
Minimum KOH	≈ 17 to 0	5
Minimum K_2SO_4	≈ 3 to 0	3
Minimum KCl	≈ 8 to 0	9.3
Maximum HCl	≈ 1 to 94	12
Maximum SO_2	≈ 86 to 99	3.8

Qualitatively the equilibrium calculation validates the experimental results discussed in earlier sections and provides equilibrium chemistry based justification to the increase in HCl concentration as well as for SO_2 concentration. The following general comments regarding the equilibrium chemistry corresponding to the variation of kaolinite loading and its comparability with experimental results of corresponding fuel (TS4) discussed in earlier section are drawn:

- The equilibrium optimum corresponding to maximum SO_2 is 3.8 %. A similar behavior of SO_2 increase is observed during the experiment. But, the experimental results show that $S \rightarrow SO_2$ release stabilizes well below 50 % while the equilibrium results show almost a complete release. Corresponding to the higher temperature 1200 °C chosen for equilibrium calculation, the thermodynamic possibility of sulfates is low. Thereby, in equilibrium condition almost all sulfur accounts for SO_2 . In contrast, the temperature at the fuel gas extraction location in the experimental case is in a temperature regime which ensures the formation and stability (s, l) of sulfates. Additionally, in an equilibrium system most of the ash inorganics, like Ca and Mg, remain a part of the slag liquid while in the actual reaction system they as well form Ca/Mg-sulfates.
- The equilibrium shows an initial lag in HCl increase, related to preference of K-liquid and KOH decrease prior to KCl. But the experimental results do not show this initial

lag of HCl increase. It suggests that in the actual application scenario, the KCl (g)-additive (s) interaction commence in parallel or even more favorably in comparison to liquid-solid reactions. Liquid-solid reactions are probably limited due to lack of physical contact owing to entrained flow condition. The observation made from the deposit morphology and composition with additive cases indicates that the silicatic slag is lower but not completely suppressed. This means, the magnitude of decrease in K-liquid as suggested by equilibrium calculation is not completely transferable to the actual application scenario.

- Highest additive loading (among other *equilibrium optimum*) is required when most of chlorine is kept as HCl. The difference in temperature of equilibrium calculation and flue gas extraction location from the experimental result does not limit the comparability with regard to HCl saturation. Because the KCl-additive reaction largely occurs already inside the combustion chamber (high temperature zone) and HCl being a non-condensable species remains in the flue gas also outside the combustion zone.
- The decrease of K-liquid and K-solid flips after the appearance of mullite. This flip indicates that the excess amount of additive in the system is probably non-beneficial. From equilibrium chemistry point of view, this flip is related to the excess availability of silicon in the system.
- Among different equilibrium optimums reported in Table 24 and Table 25, the highest kaolinite loading is 12 % corresponding to which maximum HCl is achieved. From 0 to 9.1 % kaolinite loading induces an HCl increase from 0 up to 90 %. The increase from 9.1 to 12 % loading accounts only for an increase from 90 to 94 %. In the equilibrium results and during the experiment measurement, it is observed that the increase of HCl above a certain threshold is rather difficult. To compare equilibrium and experimental results a reference of $x_{\text{Cl as HCl}} \geq 90\%$ is chosen.
- The additive loading corresponding to when application optimum is reached $x_{\text{Cl} \rightarrow \text{HCl}} \geq 90\%$, is estimated from the linear increase in Figure 58 (a). It is 17.9, 21.9, and 19.8 % for additive A, B, and D, respectively. In equilibrium, $x_{\text{Cl} \rightarrow \text{HCl}} \geq 90\%$ is reached with a kaolinite loading of 9.1 %. In reference to 9.1 % kaolinite loading, the sorbent utilization efficiency of additive A, B, and D is estimated 51, 42, and 46 % respectively.
- The $\text{Al}_2\text{Si}_2\text{O}_5(\text{OH})_4$ is the main chemical form of reactive aluminosilicate mineral in additive. The kaolinite loading corresponding to the application optimum of

$x_{\text{Cl} \rightarrow \text{HCl}} \geq 90\%$ is derived from the linear assumption in Figure 58 (b). It is 13.0, 20.1, and 11.9 for additive A, B, and D, respectively. In reference to 9.1 % kaolinite loading, the utilization efficiency of kaolinite in additive A, B, and D could be estimated 70, 45, and 76 %, respectively.

An exact comparability between equilibrium and experimental result cannot be expected. It only serves as a benchmark comparison across different fuels and additive types. In application scenarios, the equilibrium is achieved either partially or selectively. Furthermore, the compromised capture efficiency related to the transformation state of kaolinite and/or additional efficiency in relation to the mineralogy (kaolinite and/or halloysite), physical properties (particle size, moisture content), and application conditions (heating rate and peak temperatures) is not reflected by the equilibrium. Additionally, the estimation of kaolinite as reactive aluminosilicate fraction present in given additive and other variation in experimental application, e.g. feeding rate, generates uncertainties for a direct quantitative comparison.

Nonetheless, the equilibrium result provides a theoretical, chemistry based justification to the experimental results and a method for a benchmark comparison across various kaolin based commercial additives. Further, the equilibrium calculation provides a reasonable guess for additive loadings across different biomass fuel and additive types. The optimization is necessary for the individual fuel and additive application cases for which HCl concentration could be a reasonable control parameter.

4.4.1.2.5 Equilibrium chemistry and optimum additive loading

Wan et al. [102,103] suggests that the K-species as individual components and the additive interaction is largely in the equilibrium prediction regime. In an actual biomass ash system, the synergies or competition from other ash elements exists. The role of ash elements, mainly silicon (Si) and earth alkalis (Ca+Mg), is of most interest regarding biomass ash systems. The underlying methodology and algorithm of the FactSage equilibrium calculation is the minimization of Gibbs free energy of a system. All input components involve without kinetic limitation and the physical contact limitation. An equilibrium calculation is proceeded for torrefied straw (TS4) under different input scenarios. All equilibrium calculation corresponds to temperature of 1200 °C and uses the following input:

- All input: including all ash elements
- w/o Si: excluding only Si
- w/o Ca+Mg: excluding only Ca+Mg

- w/o Si+Ca+Mg: excluding only Si+Ca+Mg

This equilibrium calculation is done to evaluate the interference or synergy of the ash elements, Si, and Ca+Mg, in the equilibrium additive demand. Figure 64 (a) shows the equilibrium calculation results summarized as $x_{\text{Cl}^{\text{ash}} \text{HCl}}$ versus the additive loading. In reference to the All input scenario, the equilibrium results suggest when silicon (Si) is not available in the system, the equilibrium additive demand is higher and when earth alkalis, Ca+Mg, are not available in the system the additive demand is lower. This equilibrium chemistry suggests that the availability of Si in the system decreases the additive demand while availability of Ca and Mg increases the additive demand.

When all elements, Si+Ca+Mg, are excluded, the additive loading is comparable to the All input scenario and a characteristic delay in increase of HCl as $x_{\text{Cl}^{\text{as}} \text{HCl}}$ is observed similar to the w/o Si scenario. This delay is likely related to the thermodynamic consideration that species other than KCl is consumed first. The chlorine prefers to remain as KCl until aluminum and silicon, both input from kaolinite variations, in the system cross a certain threshold.

Not all silicon present in biomass fuel is reactive. The reactive amount of silicon present in fuel directly governs the portioning between K-release as gas and K-retention as solid/liquid and consequently the demand of kaolinite. Additionally, the possible interference posed by the availability of calcium/magnesium species depends on the physical contact with additive derived minerals as both are expected to be largely released as solid particle. That means, the partial reactivity of the fuel ash species and the possibility of physical contact when the fuel derived species is solid or liquid. Both exhibit the influence on the actual requirement of kaolinite loading in the actual application scenario. Also, the sorbent utilization of a given additive or the kaolinite utilization efficiency is also subject to vary depending on the application conditions as well as with the choice of additive.

In a co-feeding scenario of additive with the fuel, the release of fuel ash inorganic species, the transformation of additive minerals, and the interaction between ash inorganic species and additive derived minerals proceeds in parallel over a temperature range. To evaluate the influence of the temperature, the equilibrium calculation is done at various temperatures for the All input scenario. The general understanding drawn from the comparison of equilibrium results is that higher temperature results in higher additive demand. The higher demand reflects the thermodynamic drive for potassium species to remain a gas and liquid species is higher at higher temperatures. To counter act this, a higher additive loading is required.

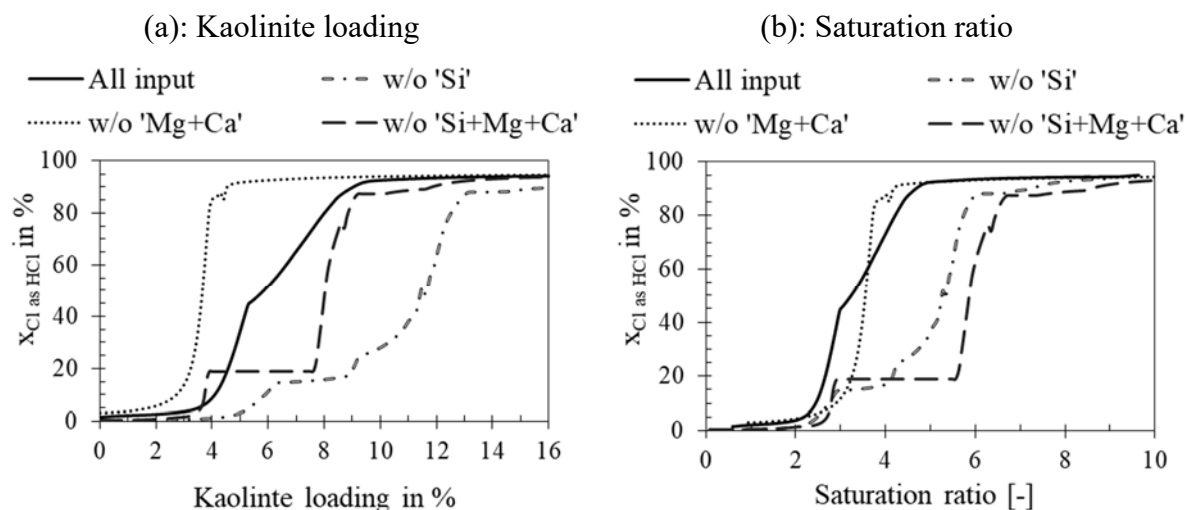


Figure 64: $X_{Cl \text{ as HCl}}$ versus (a) the additive loading and (b) the saturation ratio derived from equilibrium results corresponding to different input scenario.

The main aim of the additive is to capture the gaseous alkali species. The availability of aluminosilicate minerals directly in the combustion zone is a way to ensure that the gaseous alkali species are captured prior to any further reaction and/or their condensation as K-chlorides/sulfates. The amount of alkalis (K+Na) in a given fuel basically increases the additive demand. Equilibrium calculation shows that the additive amount is lower for input case without Mg+Ca (see w/o 'Mg+Ca' in Figure 64 (a)) which means the amount of Mg+Ca in given fuel increases the additive demand. While for input case without Si (see w/o 'Si' in (a) Figure 64) shows higher additive amount which means the amount of silicon (Si) in given fuel decreases the additive demand. When the objective is to push all fuel-chlorine as HCl in the flue gas, the amount of chlorine in given fuel increases the additive demand. The sulfur (S) content in given fuel on the other hand decrease the additive demand. The additive loading is basically governed by the interrelated ash system chemistry.

A ratio including additive and fuel-ash components may be useful to define the additive loading at which the equilibrium optimum is reached. The optimum is considered when all chlorine remains as HCl in the resulting equilibrium system. The ratio is referred to as saturation ratio and is defined by Eq. 4.11. The fuel ash elements Si, Al and S are as the numerator and their availability lowers the additive amount. The K, Na, Ca, Mg and Cl are as denominator and their availability rises additive demand. For a given input scenario the amount of additive 'Z' thereby varies to reach an equilibrium optimum. Across different input scenarios the amount of additive as kaolinite loading (see Figure 64 (a)) varies in range of 4 to 14%. In terms of saturation ratio (corresponding to respective kaolinite loading) the equilibrium optimum is reached in the range

of $\geq 4 - 6$ (see (b) Figure 64). With respect to the amount of input fuel component, the amount of Z varies to saturate HCl at maximum level, see Figure 64 (a) owing to the interrelated ash system chemistry discussed earlier.

$$\text{Saturation ratio} = \frac{M_Z + M_{(\text{Si+Al})} + M_S}{M_{(\text{K+Na})} + M_{(\text{Ca+Mg})} + M_{\text{Cl}}} \quad (4.11)$$

where Z refers to the amount of kaolinite (in g) and other the amount of each relevant element (corresponding to fuel composition) (in g per kg Fuel) as input to the equilibrium calculation.

Figure 65 (a) shows the $x_{\text{Cl as HCl}}$ corresponding to various kaolinite loadings derived from the equilibrium calculation corresponding to three different biomass test fuels composition ‘All input’ scenario.

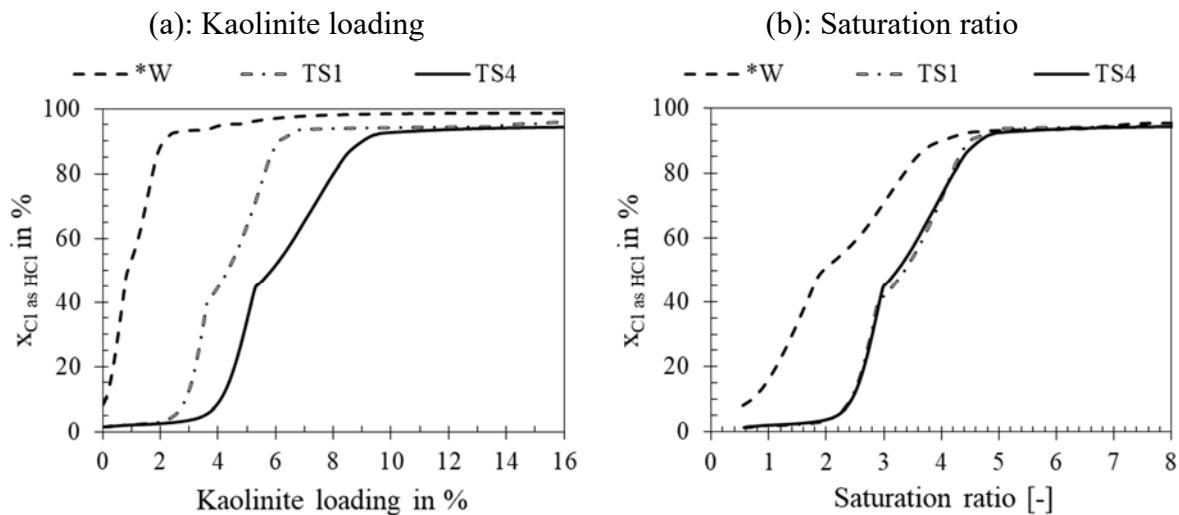


Figure 65: $x_{\text{Cl as HCl}}$ versus (a) the additive loading and (b) the saturation ratio.

The kaolinite loading to approach maximum HCl in equilibrium condition shows a hierarchy similar to ash content in fuel. The kaolinite loading for a given fuel to approach maximum HCl is $\approx 2\%$ for *W, $\approx 6\%$ for TS1, and $\approx 9\%$ for TS4, and the ash content (wt.-%, db.) in a given fuel is 1.5% for *W, 4.4% for TS1, and 6.3% for TS4. Even with equilibrium assumptions and as 100% kaolinite, the optimum additive amount exceeds the ash content in respective fuels. Considering the kaolinite fraction in most commercial additives and their sorbent utilization efficiency of 40 – 60% in a combustion application scenario, the actual additive demand is approximately in the range of 1 – 2 times the ash content for a given woody fuel and 2 – 3 times the ash content for a given herbaceous biomass fuel. The higher additive demand corresponding

to herbaceous biomass fuels is owing mainly to the higher potassium content. Additionally, the chlorine content in most herbaceous biomass fuels is higher which results in additional additive demand.

The equilibrium chemistry based saturation ratio is a theoretical reference. Across test biomass fuels, wood and torrefied straw, the saturation ratio appears to be ≥ 5 , see Figure 65 (a). The equilibrium chemistry remains the same. Therefore, comparable saturation ratios are expected for different biomass fuels.

In this work, the additive optimization is focusing on HCl concentration individually for different biomass fuels and commercially available aluminosilicate based mineral additives. The additive is applied with the fuel directly in the combustion zone. The additive loading in an actual application scenario is fuel specific and generally higher than suggested by equilibrium.

4.4.2 Summary discussion: Mitigative chemistry and optimum additive amount

The mitigative chemistry of kaolin based mineral additive relies on its efficiency to capture the gaseous potassium species at its origin of the release. The consequence of this reaction is the formation of high melting and stable K-aluminosilicate (K-solid) instead of liquid K-slag, thereby the stickiness associated with the impacting ash particle is reduced. Another consequence is the escape of chlorine in the flue gas as HCl, thereby the possible retention of chlorine in ash/deposit is reduced. The mitigating effect is confirmed not only against the bulk ash properties but also from individual ash deposit particles and the increase in HCl associated with additive confirms the later mitigative chemistry.

The central role of the K-species-additive capture reaction is well established and the mechanism behind is well studied. Nonetheless, the amount of additive required for certain biomass fuel is not straight forward. Publications on this question are to the author's knowledge rather limited. The required additive loading is of most concern when it comes to its application in relation to operational economics, e.g. additional cost of additive, and an issue that may create operational challenges, e.g. high solid flow in the system.

The chemical compounds promoted by additive are K-aluminosilicates. Among various chemical forms, namely KAlSiO_4 , KAlSi_2O_6 , and KAlSi_3O_8 , the molar ratio of K/Al remains 1. One approach to define the optimum amount is to keep the molar ratio of K/Al ratio in the system ≥ 1 . With Kaolinite as additive, the ratio derives 3.33 g of kaolinite per g of fuel-K. This amount

refers to the stoichiometric optimum. Another theoretical approach may be based on the saturation ratio ≥ 5 , as discussed earlier in the section 4.4.1.2.5. The saturation ratio refers to equilibrium optimum demand and for the condition when all Cl in the equilibrium remains as HCl. The equilibrium reaction system differs from the actual reaction system in many ways. Not all ash species, i.e. inorganic elements, present in a given fuel involve equally in the reaction. Additionally, the kinetics and the physical contact when necessary may limit the desirable mitigative reactions. The capture efficiency of additive mineral, kaolinite, deviates and is rather dynamic in application scenario depending upon temperature and the available transformation and reaction time.

The alkali (K) capture level of kaolin (kaolinite) additive in entrained conditions is in detail studied by Wang et al. [102,103]. The alkali salt species namely, KOH, K₂CO₃, KCl, and K₂SO₄, are individually mixed with additive and methanol and thus prepared a slurry which are injected as atomized slurry droplets inside the heated reactor. The vaporization of salt species and their capture by kaolin are evaluated corresponding to a residence time of 1.2 s and in the temperature range of 800 – 1450 °C. The evaluation was made from the solid product collected by cyclone/filter at the outlet of the reactor. The relevant conclusions of Wang et al. [102,103] are listed below:

- The capture level of KOH, K₂CO₃, and KCl in entrained condition are comparable to equilibrium prediction at temperature > 1100 °C. It is argued that the capture reactions at higher temperature > 1100 °C are largely thermodynamically driven and exhibit lower kinetic limitation. The K₂SO₄ is the only species that shows the capture level far lower than predicted by the equilibrium. This is argued to be related to the lower evaporation rate of K₂SO₄.
- The capture level of KOH and K₂CO₃ are approximately 0.24 g of K per gram of kaolin additive. For KCl and K₂SO₄, it is approximately 0.12 g of K per gram of kaolin additive. This suggests that KCl and K₂SO₄ are captured less effectively. Wang et al. [102,103] argue that with KCl and K₂SO₄, the main K-aluminosilicate species is KAlSi₂O₆ while for KOH and K₂CO₃, it is KAlSiO₄. The additional requirement of SiO₂ in former K-aluminosilicate is a possible reason for lower capture level.

Clery et al. [90] measures the gas phase potassium release profile in a single particle of 5 mm diameter of a combustion experiment with flame emission spectroscopy. Three different biomasses namely, wood, wheat straw, and olive cakes, are used. For each fuel, the effect of

additive on potassium release is investigated corresponding to various additive loading including: 5, 10, 15, and 25 %. The relevant conclusion of Cley et al. [90] are:

- For wood, the first K-release peak is observed in volatile combustion stage. A higher peak in the char combustion stage is observed, for wheat straw. Instead of a peak release, the release profile extends throughout the ash cooking stage while for olive cake the release peak is observed mainly in the char combustion stage. Irrespective to difference in the potassium release profile among fuels, the presence of additive substantially decreases the overall amount of potassium release. They argue that the K-release during volatile combustion is less sensitive to the addition of additive while in the char combustion and the ash cooking stage, the influence of additive is more prominent.
- The additive loading of 5, 10, 15, and 25 % was examined with each fuel. For reference, the ash content in fuel (γ_{Ash}) is 0.9, 5.7, and 8.7 wt.-%, the chlorine content (γ_{Cl}) 0.02, 0.0, and 0.15 wt.-% and the alkali content ($\gamma_{\text{K+Na}}$) is 0.11, 0.66, and 3.08 wt.-% in wood, wheat straw, and olive cake all as wt.-%, db. in fuel, respectively. With wood and wheat straw, the total K-release is already minimal at 5 % while olive cake shows a linear decrease until 25 %. They state that the ash system chemistry determines the quantity of gas phase potassium released corresponding to fuel and thereby the required quantity of additive. It implies that the quantity of additive for a given fuel requires individual optimization.

This work proposes an additive optimization method: to measure the HCl concentration in the flue gas against various additive loading. A fast, clear and repeatable response in HCl concentration is associated with the introduction of additive to the system. With increasing additive loadings, the HCl concentration in the flue gas increases and stabilizes at certain maximum. On a chemistry basis, the following presumptions are made:

- The amount of additive corresponding to which the HCl concentration in the fuel gas approaches the theoretical maximum HCl concentration, refers to the optimum amount.
- Corresponding to this optimum amount, the KCl in the system is captured by the additive derived aluminosilicate and in the process the chlorine is pushed to flue gas to remain as HCl. The consumption of KCl ensures that any other gaseous potassium species are as well already consumed owing to the fact that KCl is most difficult species to capture among all.

The concern of additive effectivity in a higher temperature regime of PF boilers, is the slip of meta-kaolinite to mullite phase, prior to the capture reaction. The higher additive demand corresponding to high KCl containing biomass fuels relates to the fact that thermodynamically and also kinetically KCl capture is less favorable in comparison to other alkali species. Additionally, most of the KCl releases during the char combustion stage until most of meta-kaolinite probably slips to the mullite phase. As a consequence, higher additive loading is required.

With KCl, the K-silicate formation is not favored. KCl is considered to be limited by the amount of fuel-Cl and to remain in the gas phase at high temperature. As flue gas temperature drops, the KCl nucleates to form aerosol particles in parallel to sulfation supported by fuel-S born SO_x species. The presence of kaolinite, aluminosilicate, intervenes in the fate of KCl. The KCl (g) is preferably captured by kaolinite derived aluminosilicate and in the process chlorine escapes to flue gas as HCl. With fuel and additive co-feeding the following scenario exists for the capture reaction to proceed:

- The transformation level of kaolinite particles is dynamic and it is apparently the particle heating rate that governs this process. The amorphous meta-kaolinite, $\text{Al}_2\text{Si}_2\text{O}_7$, is the most reactive aluminosilicate that derives from the initial transformation of kaolinite. On further heating, the amorphous meta-kaolinite structurally re-arranges to a crystalline form, chemically mullite. The aluminosilicate as mullite is known to be less reactive than meta-kaolinite [99,102].
- The KOH releases earlier mostly during de-volatilization while KCl releases later mostly during char oxidation [35]. Also, there is interference or else competition from ash species other than KCl to react with aluminosilicate available in the system.

It is reported that the capture efficiency of kaolinite particle decreases towards its higher transformation level, i.e. mullite is less reactive than meta-kaolin [102,104,107]. Wang et al. [102] argue if the temperature is high enough, the mullite particles are melted and the capture reaction changes from slow gas-solid diffusion to faster gas-liquid diffusion. Most importantly, the capture rate with a specific transformation form of kaolinite does not picture the actuality. The application temperature window (in combustion zone) is well above the temperature for the stability of meta-kaolinite but well below the melting range of mullite. The transformation level of kaolinite particles at a given time is associated with the particle size and the temperature seen by the particle (or heating rate). In contrast, the temperature of the surrounding varies according to the distance down the injection point and is not precisely known. Most of kaolinite particles

probably experience the peak temperature of 1200 – 1300 °C prior to the interaction with alkali species.

The experimental and modeling study of Teklay et al. [127,129] on flash calcination of clay minerals containing kaolinite and of comparable particle size range as test additive in a suspension calciner system, suggests that the kaolinite to meta-kaolinite transformation is achieved within less than 0.5 s. Teklay et al. [127] report that conditions of particles with a mean size of 14 µm at 950 °C for about 0.5 s is the optimum for kaolinite to meta-kaolinite transformation. A high temperature range > 1000 °C facilitates the transformation but also speeds up crystallization of meta-kaolin to the spinel and further to the mullite phase. In reference to the flash calcination studies, the kaolinite particle (see PSD of test additive in Table 16) are likely to slip to the spinel-mullite within the residence time range where most of the capture reactions proceed.

The size of biomass particles is in a range less < 500 µm. With biomass fuel particles of this range, the drying and primary volatile release completes before 1 s. This is followed by combustion which is typically completed in a range of 2 – 3 sec. The alkali species from the fuel release early during de-volatilization and follow further in char oxidation. The amount of total alkali release is largely fuel specific and is impacted by the ash system chemistry [90]. The early species are primarily KOH and later, at the char combustion stage, KCl follows [35]. The KOH may primarily react with meta-kaolinite in the surrounding while KCl probably gets spinel and/or mullite in the surrounding.

Mwabe et al. [107] point out that the temperature range of 900 – 1100 °C is the optimum temperature range to capture alkali (sodium) species, in their experimental work, in an entrained condition. They argue that the optimum temperature window is linked to the onset of condensation of alkali species on the lower temperature side and to the transformation of meta-kaolin to mullite in the higher temperature side. The later work from Wang et al. [102,103] also provides a similar conclusion.

5 Summary and Conclusion

Within this work, deposition, namely slagging and fouling, and corrosion problems related to biomass fuels are investigated as well as the option of using aluminosilicate based additives to mitigate these problems. Both, deposition and corrosion problems, are related to fuel-ash species and their properties. The inorganic composition of biomass and their interactive chemistry along the combustion progress is the root to these problems. The problematic ash species generated in biomass fired systems can be divided into silicatic species and salt species. The silicatic species mainly derive from the interaction between silicon (Si), alkalis (mainly K), and earth alkali (mainly Ca) and have a molten history (as silicatic slag). The salt species (mainly KCl and K₂SO₄) derive from the gaseous alkali species and their subsequent condensation accompanied by sulfation reactions.

Demonstration of additive mitigative effect

The biomass from woody feedstock sources and herbaceous feedstock sources are investigated during this study. The severity related to silicatic species deposition is quantitatively measured by ODS. The deposit growth in the ODS probe (ceramic) surface is largely by inertial impaction without phase change. This deposit growth does not directly simulate the boiler heat exchanger surface deposition situation but a scenario of bulk deposit growth when the temperature at the deposit front approaches the surrounding flue gas temperature. This deposit is referred to as outer deposit (OD). In a real boiler situation, the OD growth is largely avoided by boiler cleaning operations, mainly soot blowing. There removability is related to the level of fusion and sintering of the deposit.

The severity related to fouling deposit is qualitatively evaluated from deposit collected over a temperature-controlled metal (probe) surface. The silicatic ash species on the surface accumulate by inertial impaction accompanied by the phase transfer from molten state to solid. The salt ash species grow mainly by diffusion-condensing accompanied by sulfation reactions. The fine and aerosol particles may as well be transported by thermophoresis (temperature gradient between surrounding and receptive surface). Such deposit is referred to as inner deposit (ID).

The silicatic particle morphology and the chemical form of salt species were comparatively evaluated among all cases via EMPA generated micro-graphs, including BSE images and element maps relevant to ash elements. The corrosion severity associated with the salt ash species were comparatively assessed from one to other case against the physical and chemical integrity

of surface oxide scale via EMPA generated micro-graphs, including BSE images and Element maps relevant to alloy-metal elements.

The deposition rate (OD) is directly coupled with the ash content in the fired fuel. Higher ash flow directly results in a higher deposition rate. However, the deposit rate of biomass fuels in comparison to coal in a similar temperature regime is clearly higher, despite of lower ash content in fired biomass compared to the substantially high ash content in the coal. Additives increase the ash (solid) flow in the system in reference to biomass alone but the magnitude of increase does not essentially increase the deposition rate. This is mostly because the additive dilutes the system with refractory solid minerals which on one hand increases the eroding effect and on the other interferes with the biomass ash system chemistry and further demoting or hindering the formation of low melting silicatic species. One of the main concerns with additive use is the increasing ash flow in the system which makes it difficult to judge the mitigative effect of additive in terms of deposition rate. The mitigative chemistry of additive is much demonstrated by lower deposition propensity corresponding to the additive cases. The morphology of deposit bulk is also improved in the presence of additives, i.e. absence of fused and heavily sintered deposits. Nonetheless, in reference to quantitative deposition measurements, it is difficult to distinguish the contribution of mitigative chemistry and that of simple physical dilution of additional refractory solid minerals.

The external availability of additive minerals cannot interfere with the evolution chemistry of silicatic species that proceed within the char particle surface. But any reaction outside the char particle is shifted in favor to the formation of less problematic K-aluminosilicate. The higher the ash fusion temperature of bulk ash is, earlier the solidification behavior as individual deposit particles, and the morphologically of less sintering/bridging among particles is characteristic to additive cases. This demonstrates the significance of mitigative chemistry, i.e. interference/hindrance of the evolution of problematic silicatic ash species. Overall, the additive contributes to the reduction of the ash melt fraction in the biomass ash-additive system. Thereby, the stickiness of impacting ash particles is substantially lower which eventually contributes to minimize deposition.

The existence of KCl as salt deposit not only relates to the available KCl (g) in the system, but in whole to the amount of total gas phase alkali species. KCl (g) reaching the heat exchanger surfaces are eventually sulfated either along diffusion-condensation or in-situ. KCl will escape the sulfation when other competing species, like KOH, are abundant. Beside the diffusion-condensation, a transport pathway of KCl by internal impaction may exist for fired herbaceous

fuels which are characterized by low ash fusion temperatures. The transport occurs along with unburnt char particles incorporated in the molten ash droplets or the receptive surface is sticky by molten ash droplets to accumulate unburnt char particles. The KCl transport via this pathway largely escapes sulfation and so exhibits higher corrosion risks.

The availability of additive mineral already in the combustion zone is an advantage. It captures the gaseous species, including KCl, and thereby reduces their flux reaching the heat exchanger surfaces. This hinders the formation of low melting K-silicates as well. Consequently, the risk of KCl reaching the heat exchanger surface is reduced. Even for high chlorine containing fuels, like straw, the risk of chlorine in ash/deposit is lower when an optimum amount of additive minerals are available in the system. The major advantage of additive mineral driven capture reaction over sulfation is that it effectively occurs in the high temperature zone and in the process the chlorine escapes to flue gas as HCl, a non-condensable species in boiler temperature regime. This mitigating effect of additive is demonstrated from the comparative evaluation of ID samples corresponding to biomass fired cases versus biomass with additive cases.

The corrosion severity is not only related to the extent of salt species in deposit ash and to their chemical form but also to the sulfation that proceeds near the material surface. The KCl sulfation that occurs near the heat exchanger surface is a risk to the material as the HCl released (near the surface vicinity) in the process could be the source to trigger chlorine induced active oxidation. Further, if the converted K_2SO_4 exhibits a transitional existence as melt, it can trigger sulfur/sulfate induced hot corrosion. The direct KCl-material interaction is of most risk as it provides chlorine directly inside the material matrix to establish cyclic mechanism of active oxidation. The tested biomass cases clearly show each type of corrosion risk within a short exposure time. Both, martensitic and austenitic grade material (boiler tube material), fail to provide oxide scale protectiveness against the corrosion related to KCl salt. Corrosion mitigative effect in presence of additive is directly related to the suppression of KCl in salt deposit. This mitigating effect of additives is demonstrated from the comparative evaluation of the material surface (ID probe cross-section) corresponding to biomass fired cases versus biomass with additive cases.

Mitigative chemistry and optimum additive loading

During this work a methodology is derived for a benchmark comparison of fuel specific demand of additive loadings and to compare the effectivity of different additive types directly in a combustion application scenario. The methodology was validated in an electrically heated combustion test facility. The amount of additive introduced to the system correlates with the increase

of HCl concentration in the flue gas owing to KCl-additive capture reactions. The HCl concentration in the flue gas can be a reliable parameter to optimize or control additive loadings. The flue gas extraction location for HCl measurement should be chosen carefully.

Nonetheless, the methodology is applicable for biomass fuels with a chlorine content above a certain minimum threshold. For woody biomass of lower fuel-Cl content, the range of the HCl increase is probably narrower as an effect, but for herbaceous fuel, the methodology is largely applicable. Furthermore, it is principally applicable only with a biomass fuel whose ash system chemistry prefers to keep fuel-Cl as KCl.

The fuel specific demand of additive loading is influenced by the biomass ash system chemistry. This equilibrium chemistry relates to the relative ratio of relevant ash components rather than to their individual content. Out of the FactSage equilibrium calculation, a saturation ratio is defined by Eq. 4.11.

From this saturation ratio a fuel specific additive demand is calculated which represents the optimum additive loading under equilibrium assumption. Corresponding to the saturation ratio most of the Cl in the equilibrium system remains as HCl which apparently means keeping almost all potassium, as K-aluminosilicate.

Generally, the equilibrium additive demand for woody fuel is 1 – 2 times the ash content in the fuel of concern and for herbaceous biomass 2 – 3 times the ash content in the fuel of concern. The higher demand in herbaceous fuels is mainly related to the higher ash content and consequently higher potassium content. The chlorine content is generally higher in most herbaceous fuels which additionally increases the equilibrium additive demand. Considering the additional cost of additive and increased ash flow in the system, the application amount of additive is reasonable to keep within the limit of the equilibrium optimum. Further, the excess additive moves the equilibrium chemistry again to favor molten slag phase mainly due to excess of silicon species originating from the additive minerals.

The equilibrium scenario does not cover the whole complexity of an actual application scenario but works for a reference around which the application optimum could be found. The capture demand of alkali, K/Na species, which remain in the gas phase are argued to be satisfactorily predicted by the equilibrium chemistry but due to the interference or competition with other fuel ash components the actual optimum in a combustion (fuel) application scenario differs from the equilibrium optimum. The variation in the reactive fraction of silicon (Si) in a given fuel and contact possibility of fuel derived ash species, mostly Ca/Mg species, with additive

borne reactive minerals in entrained conditions contribute to the variation of the application optimum from equilibrium optimum.

The major concern is the content of chlorine in a given fuel which increases the demand of additive far more than the predictions corresponding to the equilibrium situation. A higher demand is not only related to the KCl capture chemistry but as well to the time KCl is released along the fuel combustion stage coupled with the level of kaolinite (additive mineral) transformation. As most of fuel-KCl is released during char combustion, its capture effectivity is compromised due to the slip of meta-kaolin to the spinel and mullite phase. This transformation rate is specific to the additive in relation to its properties, including particle size distribution, additive moisture content, and mineralogy which means the presence of minerals other than kaolinite, even when application boundaries, like surrounding temperature and available residence time, are similar. Nonetheless, the high temperature, the short residence time, and entrained conditions characteristic to the pulverized combustion zone is not a limitation to capture the gaseous alkali species in competition with other fuel ash species provided that the slip of meta-kaolin to mullite phase is minimal within the reaction zone.

6 Limitations and Recommendations

The mitigative effect of additive is demonstrated with results from the down fired combustion test facility. The test combustion facility employed in this work simulates the temperature and residence time typical to PF combustion systems. Mechanistically, the mitigative effect of additive is transferable irrespective to the size but the magnitude of the effect may vary. Especially, the influence of flow dynamics and geometry induced eddies would be completely different for the regime in real boilers. This would directly affect the actual deposition behavior. Additionally, in real pulverized combustion systems, a substantial fraction of silicatic ash ends up as bottom ash. The load of silicatic particles reaching the boiler zone and the extent of unburnt char transport outside the furnace zone would be substantially lower than suggested by down fired test rigs. Additionally, the peak temperature experienced by additive derived mineral particles in large pulverized flames/furnaces and associated deactivation owing to meta-kaolin to mullite transformation would influence the performance of mitigative chemistry. Both, the magnitude of risk with biomass and the magnitude of mitigative effect with additive, may differ in real boiler situations.

The comparative advantage of using additive is an attractive option for biomass retrofit boiler to extend the range of fuel they can handle. The following are recommendations which require further research work:

- Additives fed directly with the fuel through the burner may create issues with the flame stability and burner performance at higher additive loadings. Various options of additive injection to the boiler requires additional research in order to reduce the unwanted wastage of additive mineral reactivity imposed by flame zone peak temperatures.
- The optimization of additive amounts in relation to the physical properties of additive, e.g. particle size, moisture content, influence of different application location within the combustion zone, and the influence of combustion boundaries, e.g. staged and unstaged cases, are some open areas which require further dedicated work.
- The cost and benefit of additive use as well as the negative or positive impact of higher solid flow in the system and the utilization of fly ash generated from ash additive mix requires further dedicated work.

7 Annex 1

7.1 Standard analysis of test fuels

- Sample I refers to pellets
- Sample II refers to supplied as milled <1 mm
- Sample III refers to milled <1 mm and sieved < 0.5 mm
- The Laser particle size analyzer (Malvern Master Sizer 3000) is used to determine the characteristics PSD of coal (EC).
- Sieve analysis (DIN EN ISO 17827-2) is used to determine the characteristic PSD of biomass fuels.

Table 26: Standard analysis of bituminous coal.

Test facility	KSVA
Test set	A
Sample	II
Fuel Name	EC
H_u [an, MJ/kg]	27.0
Proximate analysis [wt.-%]	
$\gamma_{\text{Moisture (an.)}}$	2.4
$\gamma_{\text{Volatile (daf.)}}$	36
$\gamma_{\text{Ash (db.)}}$	12
Ultimate analysis [wt.-%, daf.]	
γ_{C}	79
γ_{Hf}	5
γ_{N}	1.60
γ_{S}	0.79
γ_{Cl}	0.02
Ash oxides [wt.-%, normalized]	
$X_{\text{Al}_2\text{O}_3}$	30.2
X_{CaO}	5.6
$X_{\text{Fe}_2\text{O}_3}$	7.6
$X_{\text{K}_2\text{O}}$	1.4
X_{MgO}	1.4
$X_{\text{Na}_2\text{O}}$	0.4
$X_{\text{P}_2\text{O}_5}$	1.4
X_{SO_3}	5.4
X_{SiO_2}	44.8
X_{TiO_2}	1.7
Ash fusion temperature [°C]	
ϑ_{IDT}	NA
ϑ_{DT}	1310
ϑ_{FT}	1460
Fuel Indices	
Corrosion Index	88
Fusion Index	1.3
Particle size distribution	
D10 in μm	4
D50 in μm	23
D90 in μm	55

Table 27: Standard analysis of woody biomass fuel (Wood 'W').

Test facility	BTS				KSVA		
Test set	A				B		
Sample	III	I	III	II	III	II	II
Fuel Name	W1	W2	W3	W4	W5	W6	W7
H_u [an, MJ/kg]	17.3	17.3	NA	17.4	17.0	17.1	17.3
Proximate analysis [wt.-%]							
γ_{Moisture} (an.)	6.5	7.9	6.0	8.0	7.7	7.8	7.3
γ_{Volatile} (daf.)	80	81	81	80	79	81	81
γ_{Ash} (db.)	2.6	1.2	0.9	1.4	1.0	1.4	1.3
Ultimate analysis [wt.-%, daf.]							
γ_C	52	51	50	51	51	51	52
γ_{Hf}	5	5	6	5	6	6	6
γ_N	0.02	0.35	0.35	0.63	0.58	0.17	0.16
γ_S	0.09	0.04	0.05	0.07	0.01	0.02	0.02
γ_{Cl}	0.02	0.02	0.02	0.03	0.03	0.03	0.02
Ash oxides [wt.-%, normalized]							
$X_{Al_2O_3}$	7.0	3.7	4.5	5.7	4.1	8.8	8.5
X_{CaO}	12.5	25.4	29.8	19.7	25.6	19.2	18.7
$X_{Fe_2O_3}$	3.9	2.1	5.3	12.9	6.9	4.4	3.9
X_{K_2O}	6.3	9.3	13.6	7.7	10.5	7.7	7.2
X_{MgO}	4.5	6.5	8.3	5.9	7.2	4.0	3.9
X_{Na_2O}	1.3	1.9	2.0	1.3	1.8	1.9	1.7
$X_{P_2O_5}$	1.8	2.9	3.3	2.5	3.1	1.1	1.1
X_{SO_3}	1.1	2.6	3.8	5.0	7.1	1.4	1.4
X_{SiO_2}	61.2	44.4	27.9	37.9	32.1	50.9	53.2
X_{TiO_2}	0.3	1.3	1.4	1.5	1.6	0.5	0.4
Ash fusion temperature [°C]							
ϑ_{IDT}	1170	1000	NA	960	1050	1150	1160
ϑ_{DT}	1210	1250	NA	1170	1170	1170	1180
ϑ_{FT}	1270	1300	NA	1190	1220	1220	1230
Fuel Indices							
Corrosion Index	9.2	6.1	4.9	5.5	0.9	1.8	2.0
Fusion Index	2.9	1.6	1.1	1.6	1.3	1.9	2.0
Particle size distribution							
D10 in μm			63			55	
D50 in μm			184			305	
D90 in μm			350			623	

Table 28: Standard analysis of herbaceous biomass fuel (Straw 'S').

Test facility		KSVA			BTS	KSVA
Test set		A			D	C
Sample	I	II	II	II	III	II
Fuel Name	S1	S2	S3	S4	S5	S6
H_u [an, MJ/kg]	15.0	14.5	13.9	NA	13.7	13.7
Proximate analysis [wt.-%]						
$\gamma_{\text{Moisture (an.)}}$	5.8	6.7	5.3	9.1	10.4	10.1
$\gamma_{\text{Volatile (daf.)}}$	80	80	80	79	81	81
$\gamma_{\text{Ash (db.)}}$	11	10	11	10	13	13
Ultimate analysis [wt.-%, daf.]						
γ_{C}	49	49	50	49	49	51
γ_{Hf}	6	6	6	6	6	6
γ_{N}	1.04	0.94	1.08	0.91	0.91	1.44
γ_{S}	0.18	0.15	0.13	0.31	0.09	0.16
γ_{Cl}	0.31	0.27	0.34	0.41	0.16	0.31
Ash oxides [wt.-%, normalized]						
$X_{\text{Al}_2\text{O}_3}$	4.5	6.0	4.8	6.2	5.1	5.9
X_{CaO}	10.1	12.6	10.8	9.4	9.4	8.9
$X_{\text{Fe}_2\text{O}_3}$	2.5	3.1	2.2	2.6	2.2	1.9
$X_{\text{K}_2\text{O}}$	15.3	18.8	16.4	18.9	10.2	11.3
X_{MgO}	2.9	3.3	3.1	5.5	2.4	2.5
$X_{\text{Na}_2\text{O}}$	0.7	0.9	0.8	1.0	0.7	0.8
$X_{\text{P}_2\text{O}_5}$	3.1	3.2	3.5	3.1	2.1	2.2
X_{SO_3}	2.3	1.9	1.5	1.5	1.8	2.6
X_{SiO_2}	58.4	50.0	56.7	51.6	66.0	63.7
X_{TiO_2}	0.2	0.3	0.2	0.2	0.2	0.2
Ash fusion temperature [°C]						
ϑ_{IDT}	700	NA	740	NA	730	730
ϑ_{DT}	1070	NA	1090	NA	1100	1130
ϑ_{FT}	1300	NA	1240	NA	1280	1240
Fuel Indices						
Corrosion Index	1.3	1.2	0.9	1.7	1.3	1.2
Fusion Index	4.4	3.3	4.1	3.5	4.7	4.5
Particle size distribution						
D10 in μm		57			54	
D50 in μm		272			185	
D90 in μm		622			365	

Table 29: Standard analysis of herbaceous biomass fuel (Miscanthus 'M').

Test facility	KSVA			
Test Set	B			
Sample	I	II	II	III
Fuel Name	M1	M2	M3	M4
H_u [an, MJ/kg]	15.4	16.1	16.7	16.6
Proximate analysis [wt.-%]				
γ_{Moisture} (an.)	8.4	8.0	5.7	6.4
γ_{Volatile} (daf.)	81	81	81	81
γ_{Ash} (db.)	6.7	3.4	2.4	2.2
Ultimate analysis [wt.-%, daf.]				
γ_C	49	50	50	49
γ_{Hf}	5	6	6	6
γ_N	0.74	0.36	0.35	0.26
γ_S	0.11	0.08	0.06	0.07
γ_{Cl}	0.09	0.09	0.05	0.03
Ash oxides [wt.-%, normalized]				
$X_{\text{Al}_2\text{O}_3}$	2.9	1.7	0.6	0.7
X_{CaO}	4.0	10.1	8.8	8.3
$X_{\text{Fe}_2\text{O}_3}$	0.5	1.2	0.4	0.4
$X_{\text{K}_2\text{O}}$	14.0	17.2	27.7	25.7
X_{MgO}	1.7	1.4	2.0	1.4
$X_{\text{Na}_2\text{O}}$	0.1	0.1	0.1	0.6
$X_{\text{P}_2\text{O}_5}$	3.8	6.7	9.1	9.3
X_{SO_3}	3.3	3.4	3.7	1.6
X_{SiO_2}	69.6	58.0	47.5	51.9
X_{TiO_2}	0.1	0.1	0.1	0.0
Ash fusion temperature [°C]				
ϑ_{IDT}	NA	700	700	790
ϑ_{DT}	970	920	830	870
ϑ_{FT}	1340	1310	1260	1390
Fuel Indices				
Corrosion Index	2.7	1.9	2.7	4.5
Fusion Index	10.1	6.2	7.4	8.4
Particle size distribution				
D10 in μm	44			
D50 in μm	200			
D90 in μm	465			

Table 30: Standard analysis of herbaceous biomass fuel (Torrefied Straw‘TS’).

Test facility	BTS			
Test set		C		B
Sample	II	III	III	III
Fuel Name	TS1	TS2	TS3	TS4
H_u [an, MJ/kg]	16.9	17.0	17.5	17.5
Proximate analysis [wt.-%]				
γ_{Moisture} (an.)	10.0	9.8	7.9	6.7
γ_{Volatile} (daf.)	75	76	76	76
γ_{Ash} (db.)	4.5	4.4	4.4	6.3
Ultimate analysis [wt.-%, daf.]				
γ_C	54	54	53	52
γ_{Hf}	5	5	5	6
γ_N	0.52	0.52	0.52	0.67
γ_S	0.09	0.09	0.09	0.11
γ_{Cl}	0.05	0.05	0.06	0.10
Ash oxides [wt.-%, normalized]				
$X_{Al_2O_3}$	1.6	1.6	1.7	2.0
X_{CaO}	19.6	19.8	19.6	17.5
$X_{Fe_2O_3}$	3.1	3.7	3.3	2.2
X_{K_2O}	17.6	17.3	25.1	25.8
X_{MgO}	2.9	2.8	3.0	2.5
X_{Na_2O}	0.6	0.6	0.5	1.6
$X_{P_2O_5}$	2.5	2.4	2.7	2.3
X_{SO_3}	2.7	2.6	4.3	4.1
X_{SiO_2}	49.1	48.9	39.8	42.1
X_{TiO_2}	0.3	0.3	0.1	0.1
Ash fusion temperature [°C]				
ϑ_{IDT}	740	740	720	780
ϑ_{DT}	840	840	840	840
ϑ_{FT}	1160	1160	1160	1060
Fuel Indices				
Corrosion Index	4.0	4.1	3.3	2.5
Fusion Index	2.9	2.9	2.8	3.3
Particle size distribution				
D10 in μm		97		
D50 in μm		231		
D90 in μm		368		

Table 31: Standard analysis of biomass mix (Miscanthus/Wood: 50/50, 'M+W'), straw pre-mixed with additive (S+D) and KCl doped wood (*W).

Test facility	KSVA			BTS		
Test set	B		C	C		
Sample	II	II	II	III	III	III
Fuel Name	M+W	M+W	S+D	*W	*W	*W-I
H_u [an, MJ/kg]	17.0	17.0	14.0	NA	NA	17.5
Proximate analysis [wt.-%]						
γ _{Moisture} (an.)	6.7	6.4	7.5	7.2	7.5	6.1
γ _{Volatile} (daf.)	81	81	80	79	79	79
γ _{Ash} (db.)	1.5	1.9	13.9	1.5	1.5	1.3
Ultimate analysis [wt.-%, daf.]						
γ _C	49	51	49	52	52	53
γ _{Hf}	6	6	6	5	5	5
γ _N	0.29	0.32	1.17	0.64	0.63	0.62
γ _S	0.04	0.04	0.13	0.08	0.07	0.06
γ _{Cl}	0.05	0.05	0.33	0.14	0.13	0.17
Ash oxides [wt.-%, normalized]						
X _{Al2O3}	3.3	3.1	12.2	4.9	6.2	4.0
X _{CaO}	17.0	16.9	8.3	18.5	17.5	28.5
X _{Fe2O3}	1.7	1.8	8.3	10.8	10.3	6.9
X _{K2O}	18.9	16.5	11.7	17.3	19.3	30.8
X _{MgO}	4.3	4.1	2.3	5.3	5.0	7.8
X _{Na2O}	0.7	0.7	0.6	1.5	1.4	1.8
X _{P2O5}	6.7	6.5	3.0	2.5	2.4	3.4
X _{SO3}	3.2	3.2	1.0	5.4	5.4	8.4
X _{SiO2}	44.0	47.1	51.5	32.7	31.2	6.9
X _{TiO2}	0.2	0.2	1.1	1.1	1.3	1.6
Ash fusion temperature [°C]						
ϑ _{IDT}	820	810	820	930	950	NA
ϑ _{DT}	1080	1080	1210	1160	1180	NA
ϑ _{FT}	1250	1240	1310	1230	1230	NA
Fuel Indices						
Corrosion Index	1.5	1.9	0.9	1.3	1.2	0.7
Fusion Index	2.9	2.9	2.9	1.9	1.9	1.1
Particle size distribution						
D10 in μm	84		125	63		
D50 in μm	332		647	184		
D90 in μm	601		929	350		

Table 32: Calculated composition of 'coal+biomass' blend and 'biomass+additive' mix.

Test facility	KSVA				BTS
Test set	A			B	A
Fuel Name	25S	40S	60S	M+B	W+C
Proximate analysis [wt.-%]					
$\gamma_{\text{Moisture (an.)}}$	4.0	4.7	5.6	6.0*	7.0*
$\gamma_{\text{Volatile (daf.)}}$	52	59	68	80	81
$\gamma_{\text{Ash (db.)}}$	11.4	11.1	10.7	5.7**	2.4**
Ultimate analysis [wt.-%, daf.]					
γ_{C}	68	63	57	50	51
γ_{Hf}	5	6	6	6	6
γ_{N}	1.36	1.25	1.11	0.35	0.35
γ_{S}	0.56	0.46	0.32	0.06	0.04
γ_{Cl}	0.11	0.15	0.21	0.05	0.02
Ash oxides [wt.-%, normalized]					
$X_{\text{Al}_2\text{O}_3}$	23	19	14	26	23
X_{CaO}	8	9	10	3	10
$X_{\text{Fe}_2\text{O}_3}$	6	6	5	1	2
$X_{\text{K}_2\text{O}}$	7	10	13	11	5
X_{MgO}	2	2	3	1	3
$X_{\text{Na}_2\text{O}}$	1	1	1	0	1
$X_{\text{P}_2\text{O}_5}$	2	2	3	4	1
X_{SO_3}	4	4	3	1	1
X_{SiO_2}	46	47	48	53	53
X_{TiO_2}	1	1	1	0	1
Fuel Indices					
Corrosion Index	11.1	6.6	3.4	2.7	5.4
Fusion Index	1.7	2.0	2.5	2.2	1.6

*Includes crystal water from additive
**db. also means crystal water free additive

7.1.1 Additional information on fuels

Table 33: Supplier information

Fuel	Supplier information
Wood (W)	W1 supplied during DEBCO project W2-W5 in frame of industrial project W6-W7 supplied in frame of industrial project
Straw (W)	Acquired from SO.PR.ED, Italy in frame of OnCord project. Main feedstock cereal straw.
Miscanthus (M)	Supplied in frame of industrial project
Torrefied straw (TS)	TS1-TS3: Supplied in frame of Sector project (2011-2015) by CENER, Spain. TS4: Supplied in frame of industrial project (2017) by CENER, Spain Wheat straw is feed stock for both torrefied straw

7.2 Normalized composition of additives and estimation of mineral fraction

Table 34: Normalized dry (moisture free) composition of additives.

wt.-%, db., normalized	A	B	C	D
$\gamma_{\text{Crystal water}}$	14	14	13	15
$\gamma_{\text{Al}_2\text{O}_3}$	32.6	36.7	30.3	24.5
γ_{CaO}	0.1	0.0	0.2	0.6
$\gamma_{\text{Fe}_2\text{O}_3}$	1.3	0.5	0.8	17.2
$\gamma_{\text{K}_2\text{O}}$	2.3	0.1	1.2	0.2
γ_{MgO}	0.3	0.0	0.2	0.3
$\gamma_{\text{Na}_2\text{O}}$	0.1	0.0	0.0	0.2
$\gamma_{\text{P}_2\text{O}_5}$	0.1	0.0	0.0	0.6
γ_{SO_3}	0.0	0.0	0.2	0.0
γ_{SiO_2}	49.4	48.0	54.1	38.9
γ_{TiO_2}	0.1	0.5	0.4	2.4
Ash fusion temperature [°C]				
ϑ_{IDT}	990	990	970	900
ϑ_{DT}	NR	NR	NR	1430
ϑ_{FT}	NR	NR	NR	NR

The estimation is performed with following assumptions:

- The aluminum in a given additive remains only as muscovite and kaolinite. The muscovite with chemical formula $\text{KA}_3\text{Si}_3\text{O}_{10}(\text{OH})_2$ and for kaolinite with chemical formula $\text{Al}_2\text{Si}_2\text{O}_5(\text{OH})_4$.
- At first the Al_2O_3 demand corresponding to muscovite is satisfied. The fraction of muscovite is limited by the amount of K_2O in given additive.
- From remaining amount of Al_2O_3 , the fraction of kaolinite derives.
- The excess SiO_2 that remains after muscovite and kaolinite is considered to be quartz.
- The remaining (difference to 100) is referred as others.
- The estimated fraction serves the purpose of comparison across additive in terms of available reactive aluminosilicate as $\text{Al}_2\text{Si}_2\text{O}_5(\text{OH})_4$ in given mineral additive. It carries the uncertainty borne to given assumptions.

8 Annex 2

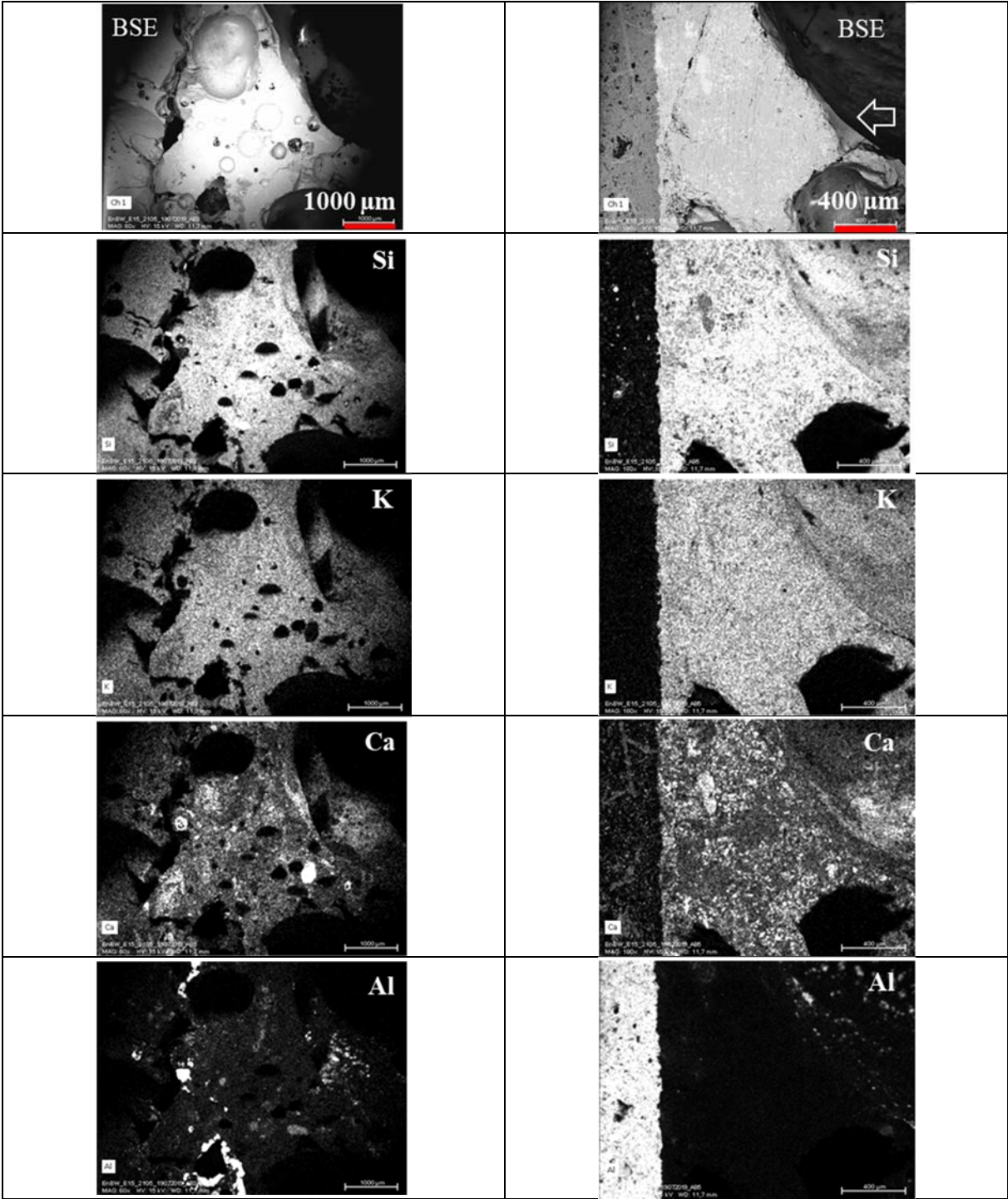
8.1 Composition of deposit and fly ash

Table 35: Normalized ash oxide composition of outer deposit (OD) and fly ash (FA).

wt.-%, Norm.	OD_L11				OD_L15				FA_L27			
	W	M+W	M	M+B	W	M+W	M	M+B	W	M+W	M	M+B
X _{Al2O3}	8.6	5.0	2.7	12.4	7.8	4.5	3.7	11.0	10.3	3.6	3.4	25.1
X _{CaO}	12.5	16.9	12.6	7.7	16.9	17.1	13.6	8.0	37.1	23.4	12.2	3.1
X _{Fe2O3}	3.7	1.7	1.7	0.7	3.3	1.7	1.7	0.7	4.5	1.5	2.0	0.7
X _{K2O}	5.6	11.9	10.8	13.2	9.3	13.9	12.6	16.0	8.6	12.8	11.9	12.6
X _{MgO}	2.6	3.4	1.4	1.3	3.0	3.6	1.5	1.5	5.8	3.6	1.4	0.7
X _{Na2O}	1.8	0.8	0.3	0.1	1.9	0.8	0.4	0.1	2.0	1.2	0.8	0.4
X _{P2O5}	0.8	6.0	4.6	4.8	1.1	6.3	5.3	6.0	2.7	6.7	5.6	3.4
X _{SO3}	0.0	0.1	0.3	0.0	0.1	0.5	0.7	0.1	2.1	1.1	0.8	0.3
X _{SiO2}	63.8	54.1	65.1	59.6	56.1	51.6	60.1	56.3	26.3	46.0	61.6	53.1
X _{TiO2}	0.4	0.2	0.4	0.2	0.4	0.2	0.5	0.2	0.6	0.2	0.4	0.4
Oxide ratio in wt.-%/wt.-%												
Relevant ratio	0.3	0.5	0.7	0.7	0.4	0.6	0.7	0.8	0.2	0.5	0.8	0.4
Fusion Index	3.0	2.9	4.8	3.6	2.5	2.9	4.2	3.8	0.7	2.2	4.7	2.4
Ash fusion temperature in °C												
g _{IDT}	1160	910	840	1160	NA	1010	1020	1040	1160	NA	850	1320
g _{DT}	1170	1140	1100	1390	NA	1110	1080	1300	1180	NA	1070	1360
g _{FT}	1430	1330	1320	1430	NA	1270	1360	1440	1250	NA	1370	1460

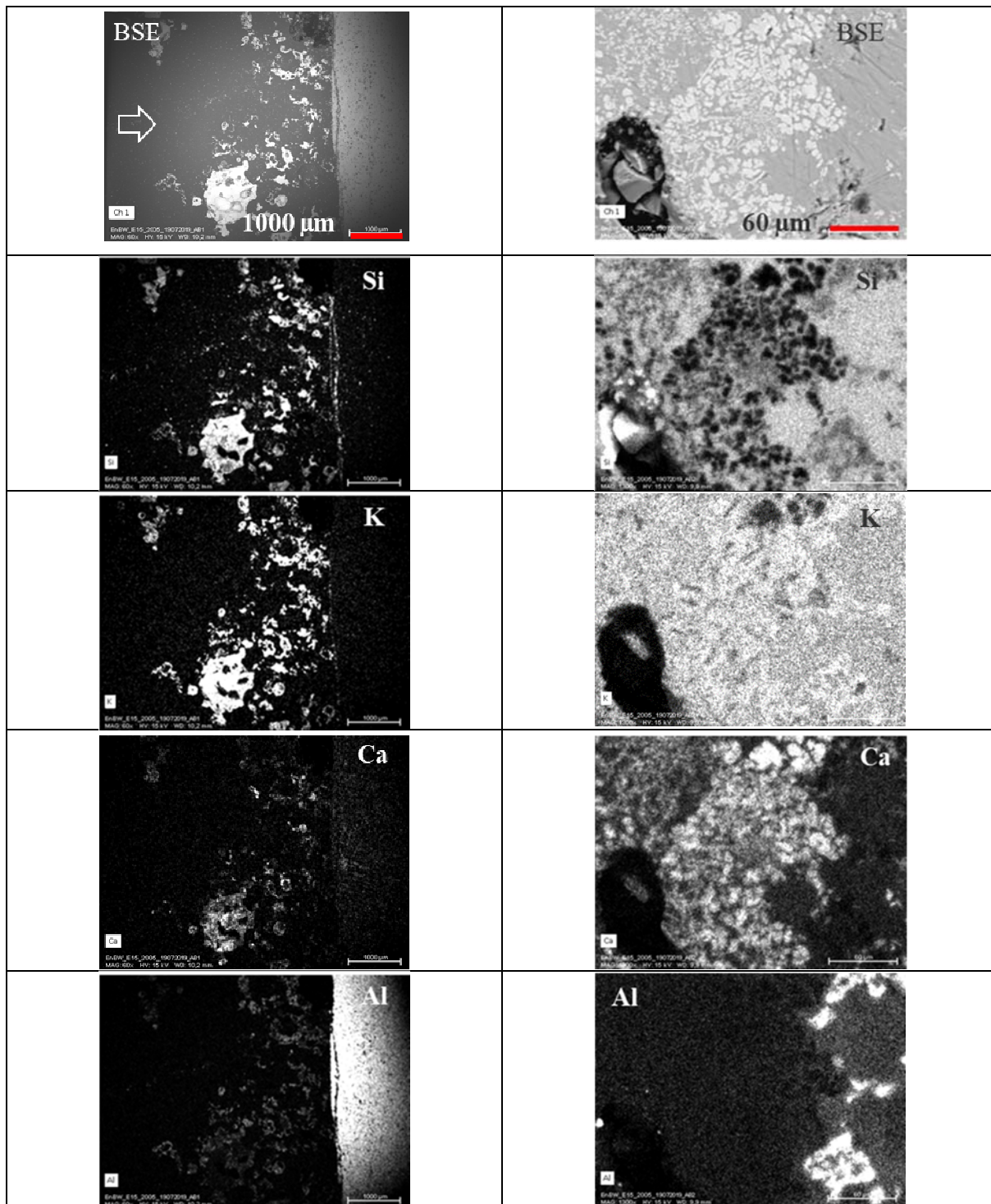
8.2 BSE image and element maps of deposit samples from test set B (KSVA)

8.2.1 Outer deposit (OD) from M case



Continue to next page

8.2.2 Outer deposit (OD) from M+B case



Continue in next page

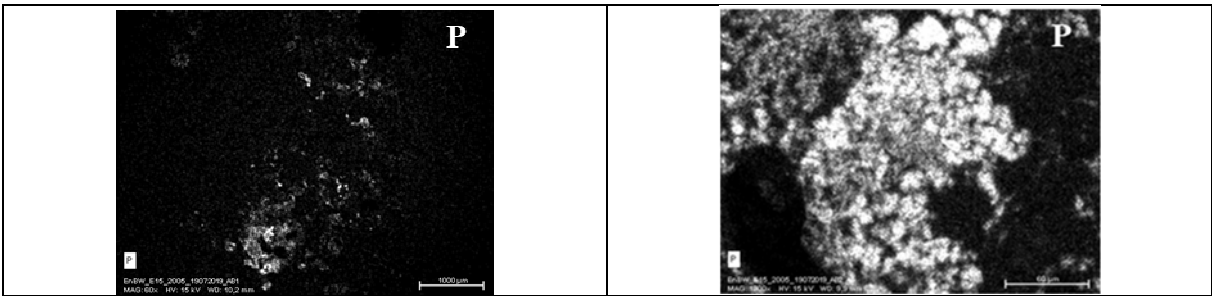


Figure 67: BSE Image (top) and element maps (below) of OD_L15 sample from M+B case.

8.2.3 Inner deposit (ID) from wood (W) case

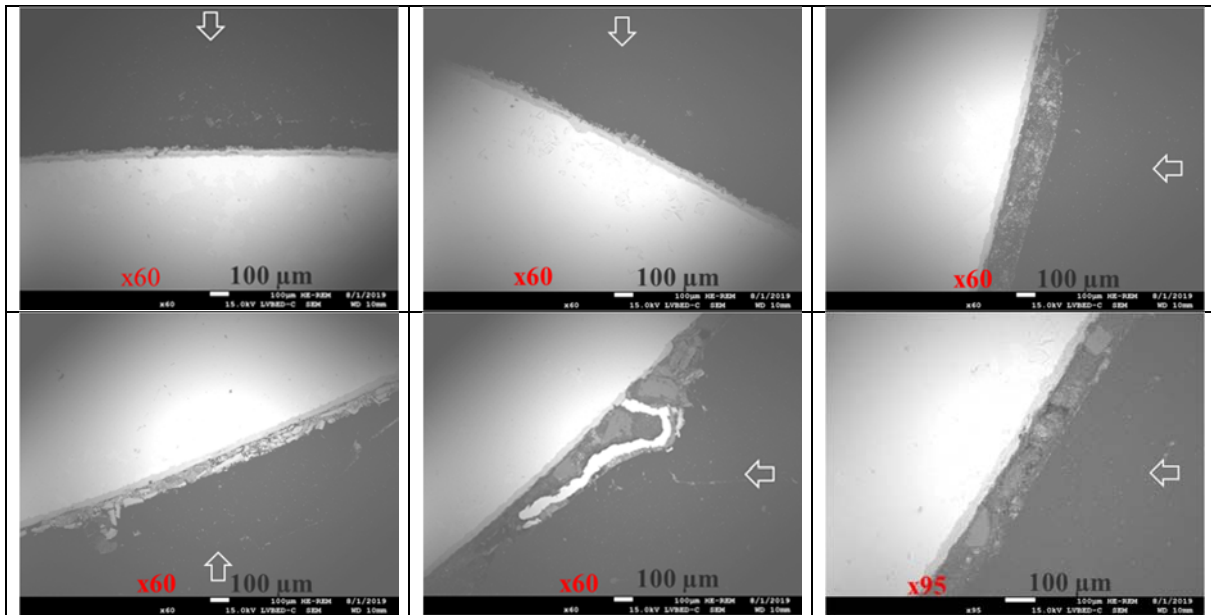
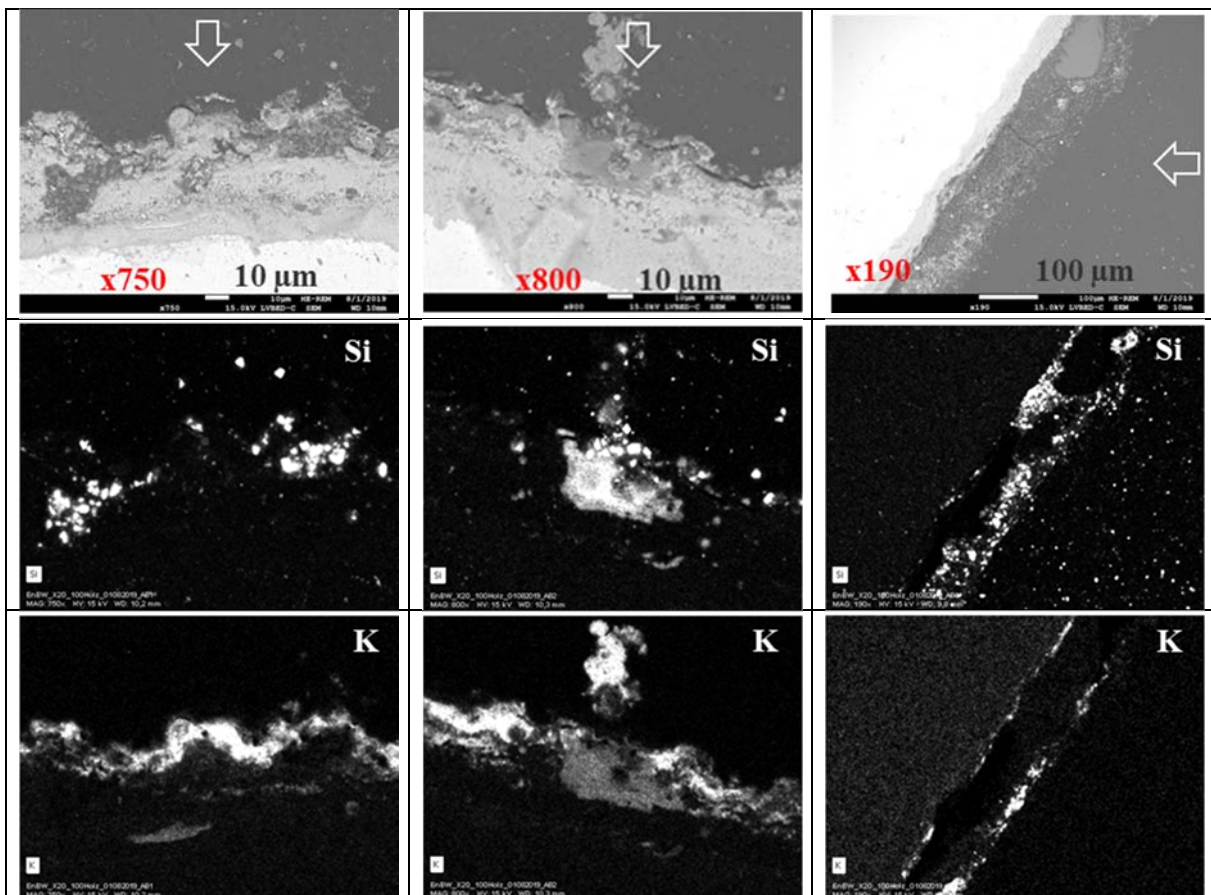
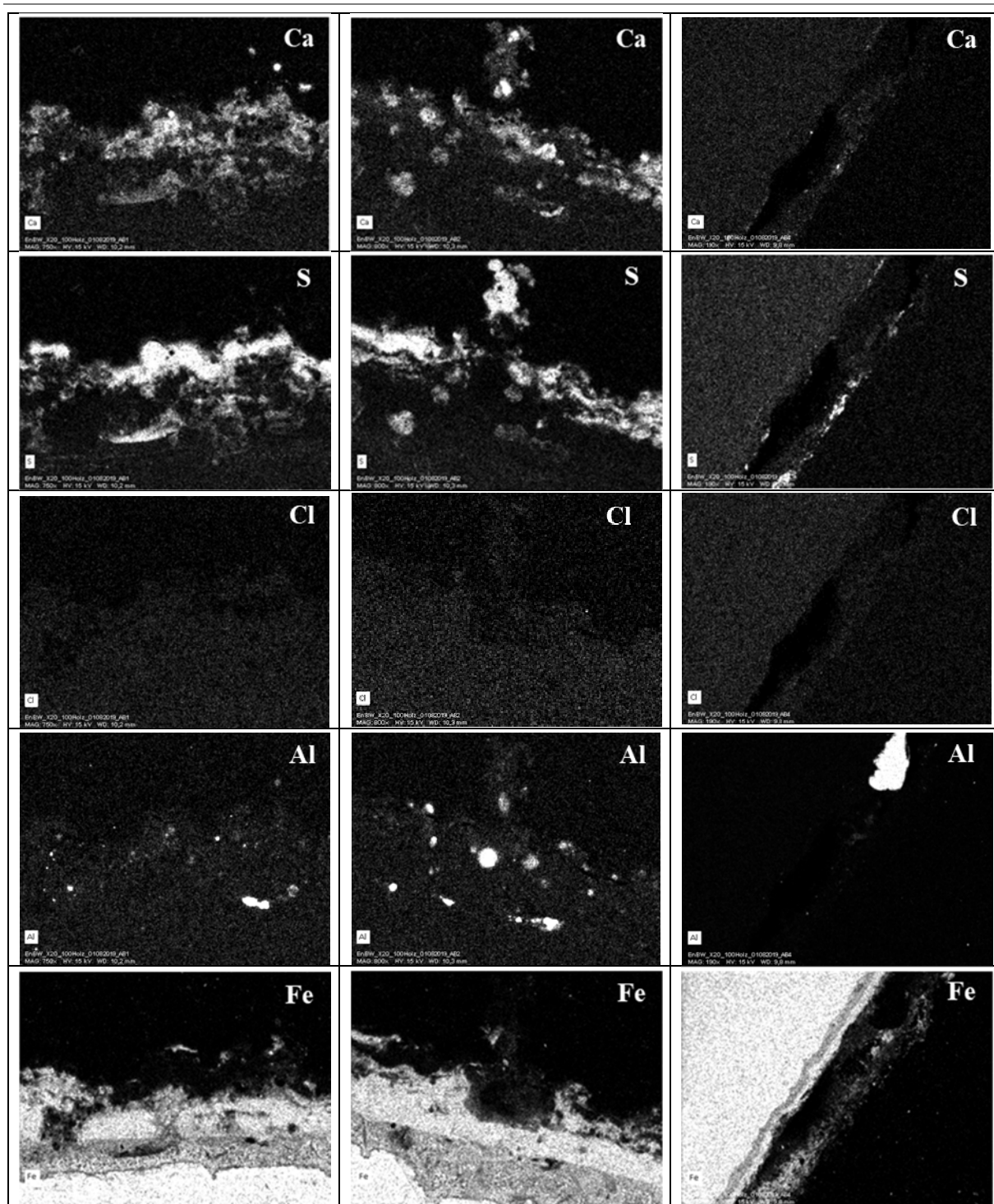


Figure 68: BSE Image of ID L15 sample from W case.



Continue to next page



Continue to next page

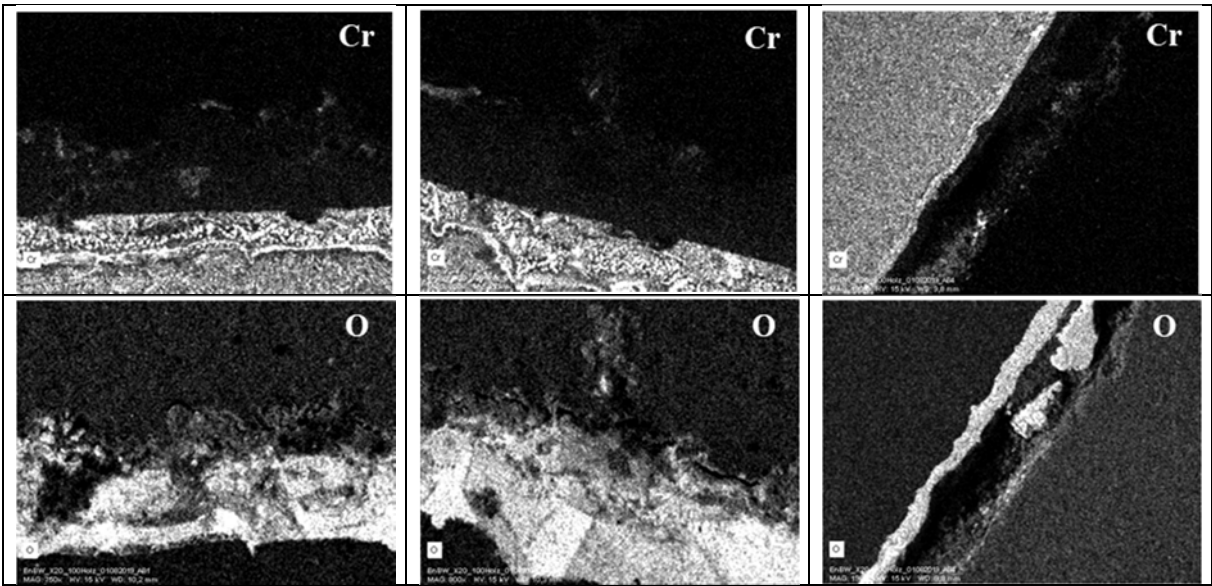


Figure 69: BSE Image (top) and element map (below) of ID L15 sample from W case.

8.2.4 Inner deposit from mix (M+W) case

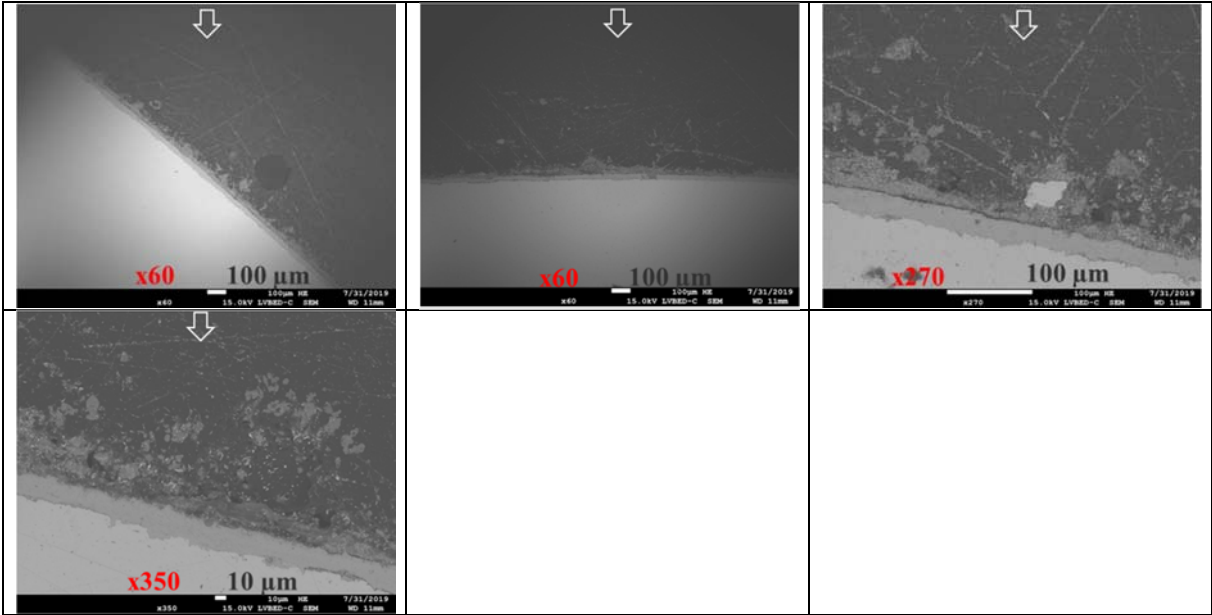
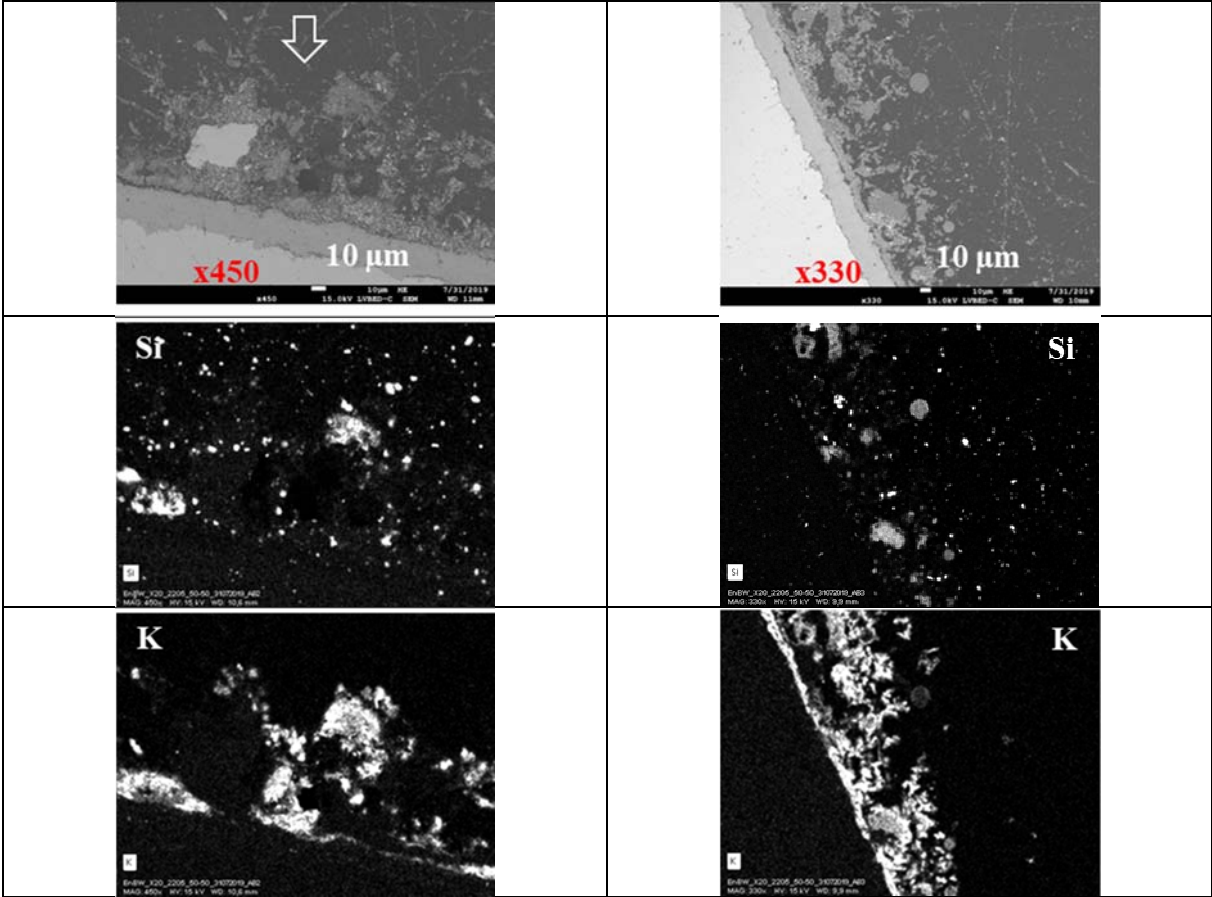
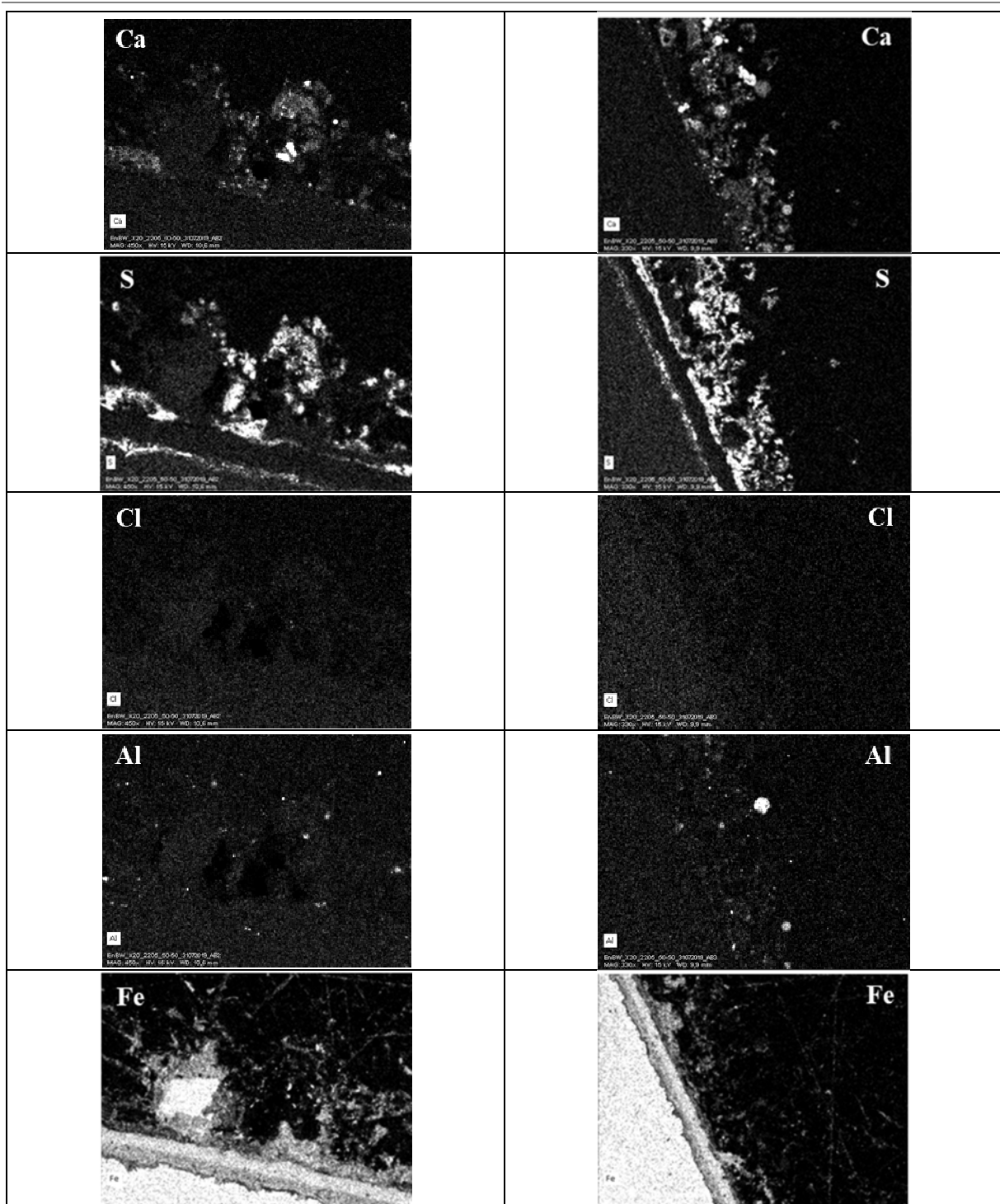


Figure 70: BSE Image of ID L15 sample from M+W case.



Continue to next page



Continue to next page

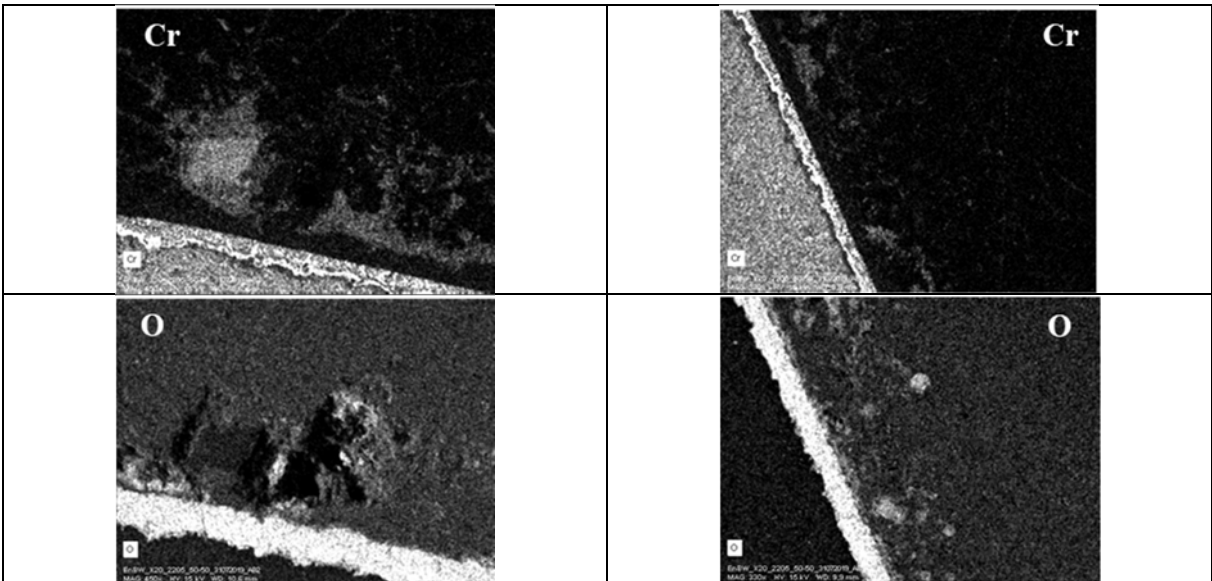


Figure 71: BSE Image and element map of ID L15 sample from M+W case.

8.2.5 Inner deposit (ID) from Miscanthus (M) case

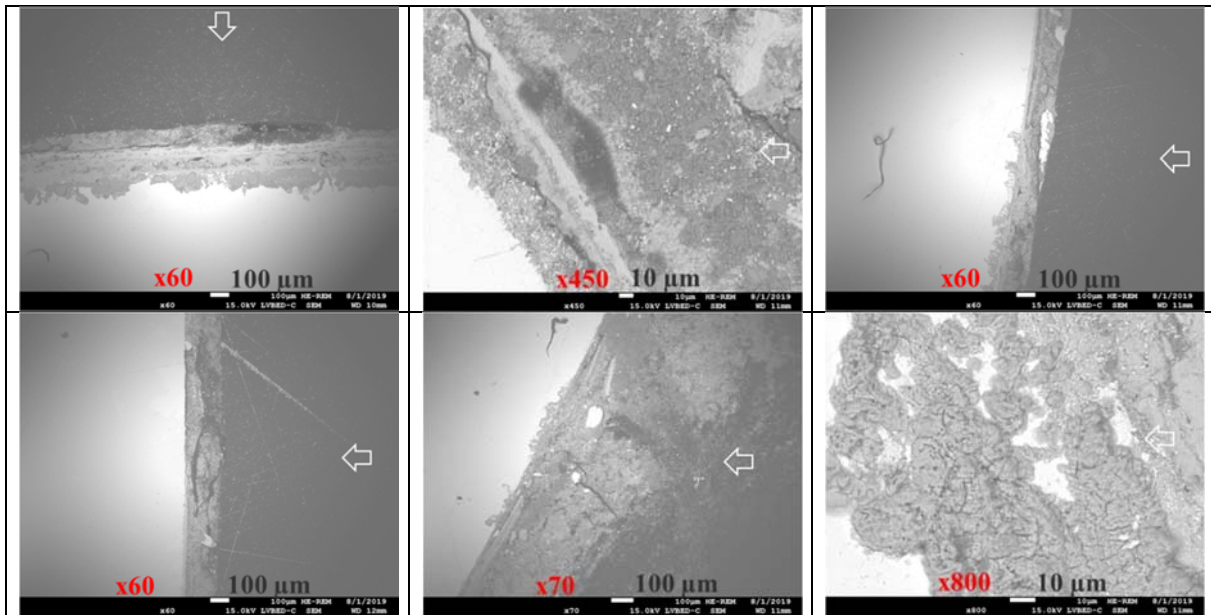
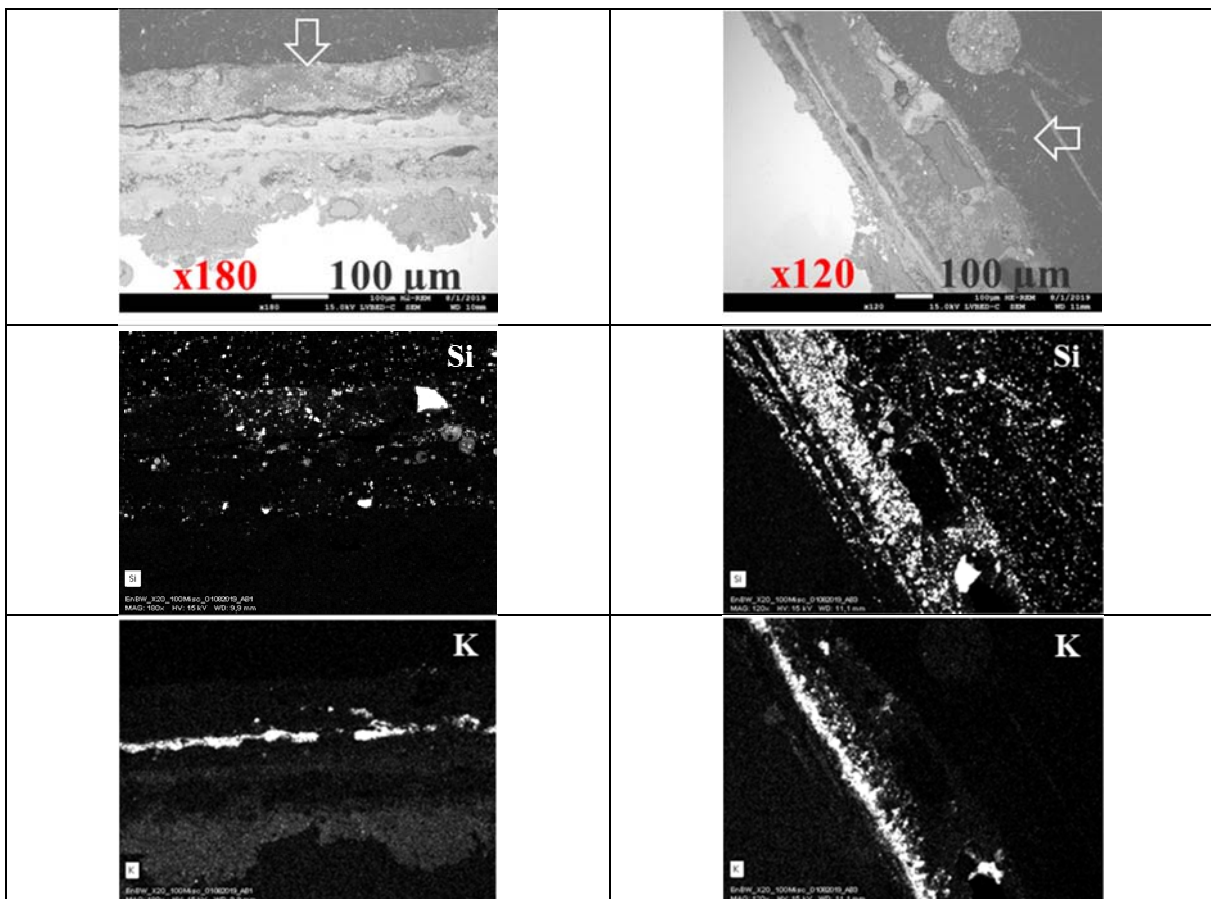
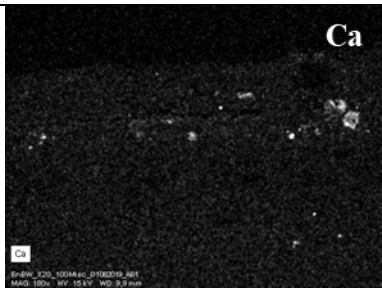
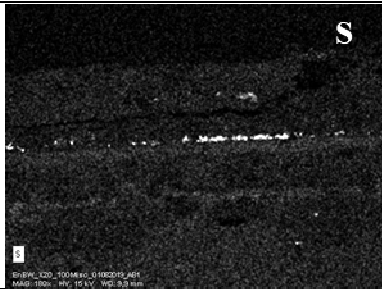
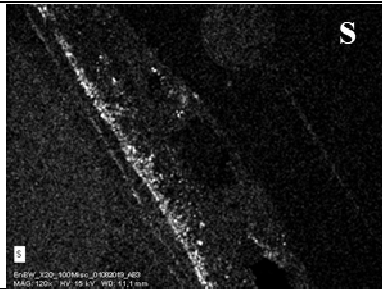
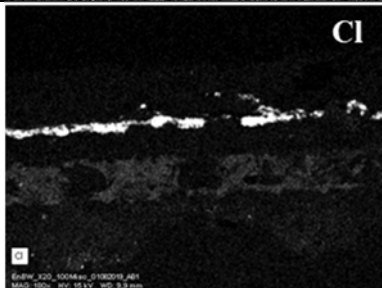
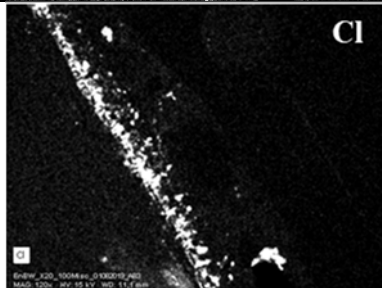


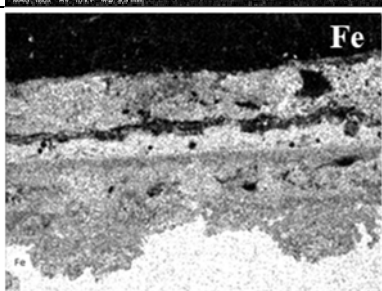
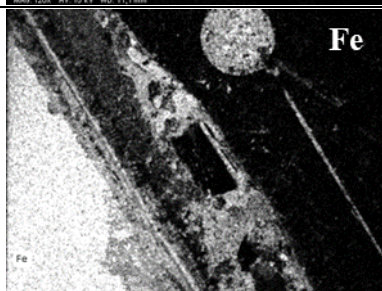


Figure 72: BSE Image of ID L15 sample from M case.



Continue to next page

	<p>NA</p>
	
	
	
	

Continue to next page

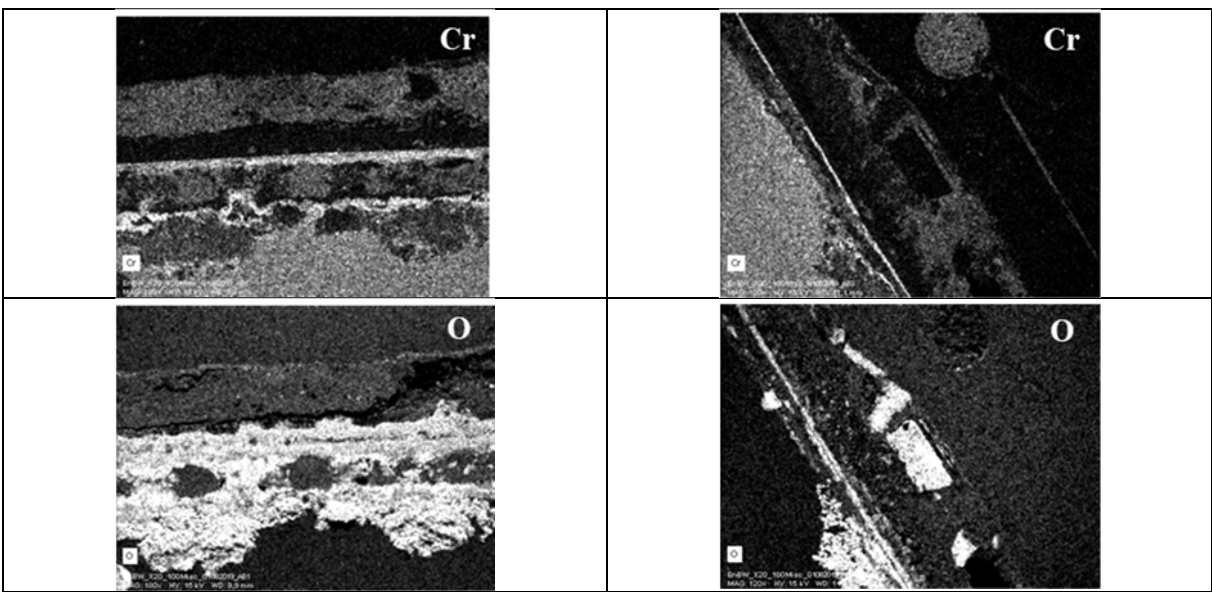


Figure 73: BSE Image and element map of ID L15 sample from M case.

8.2.6 Inner deposit (ID) from miscanthus with additive (M+B) case

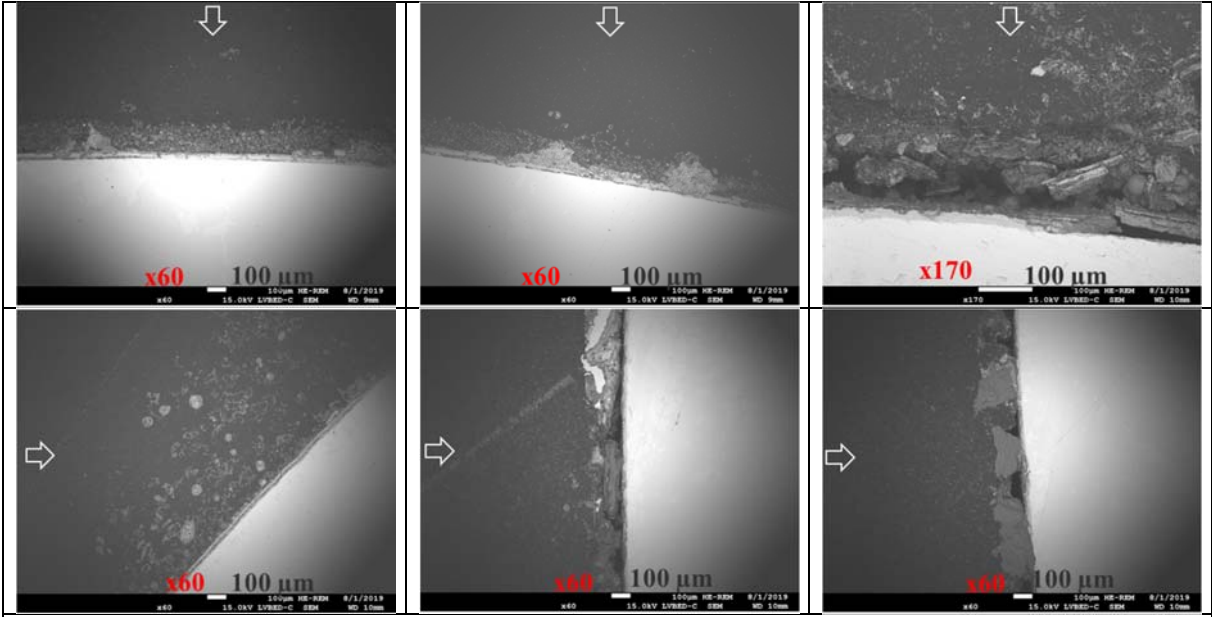


Figure 74: BSE Image showing of ID L15 sample from M+B case.

8.3 BSE image and element maps of deposit samples from test set C (KSVA)

8.3.1 Inner deposit (ID) from straw (S) case

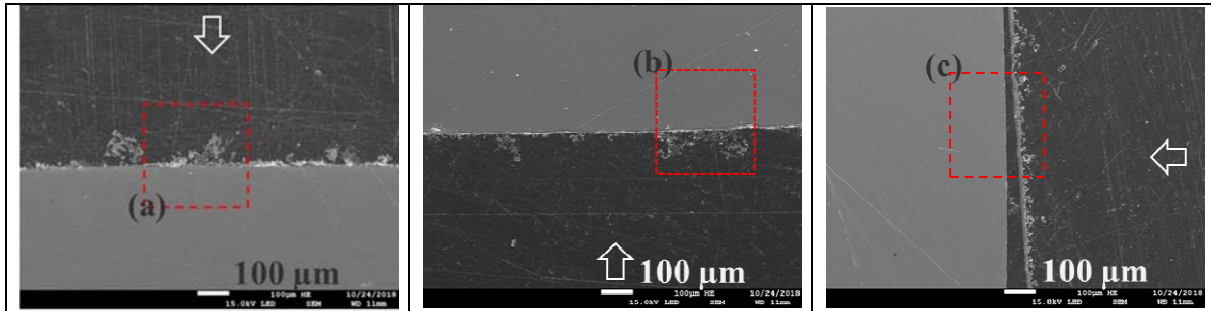
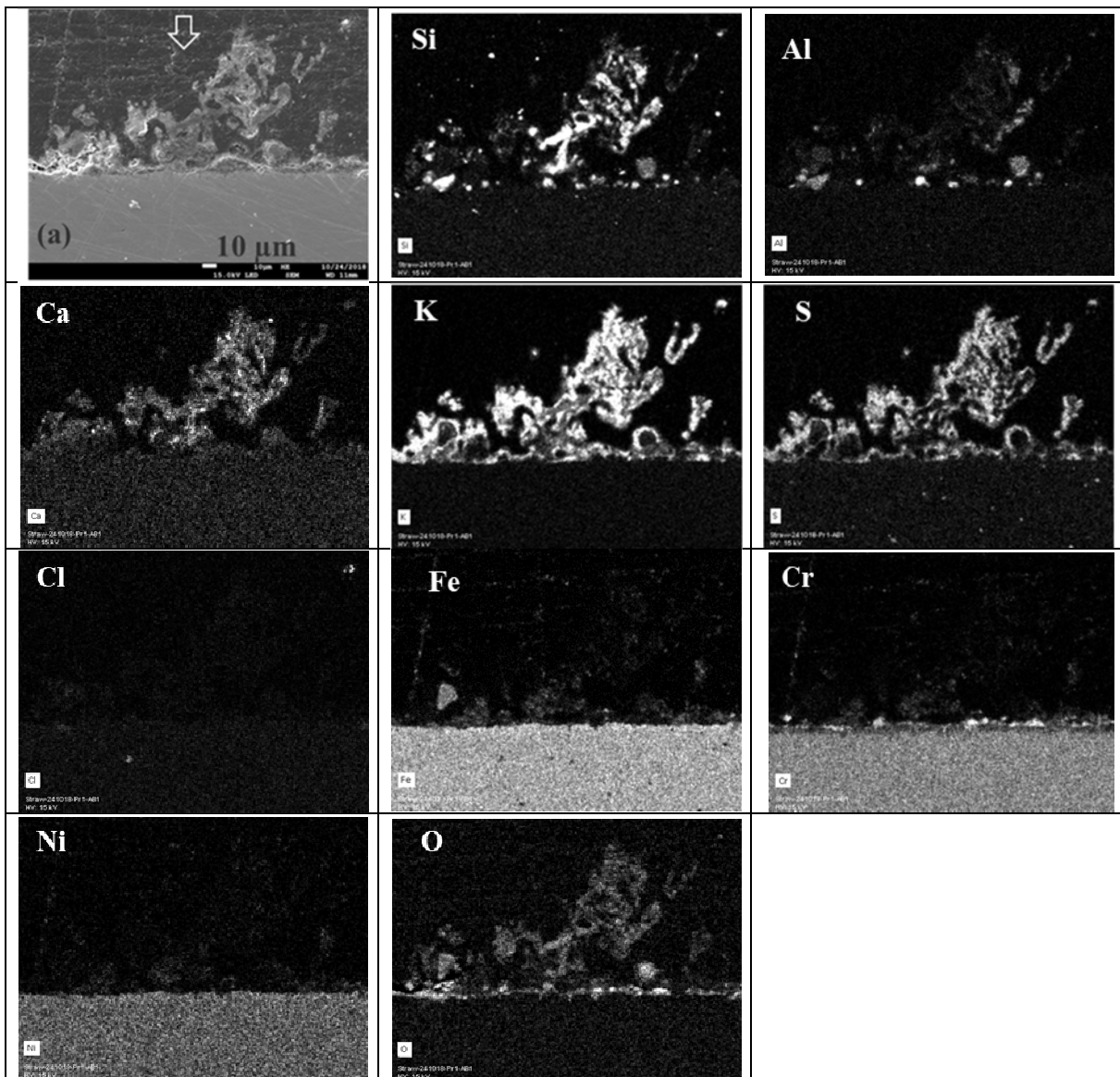
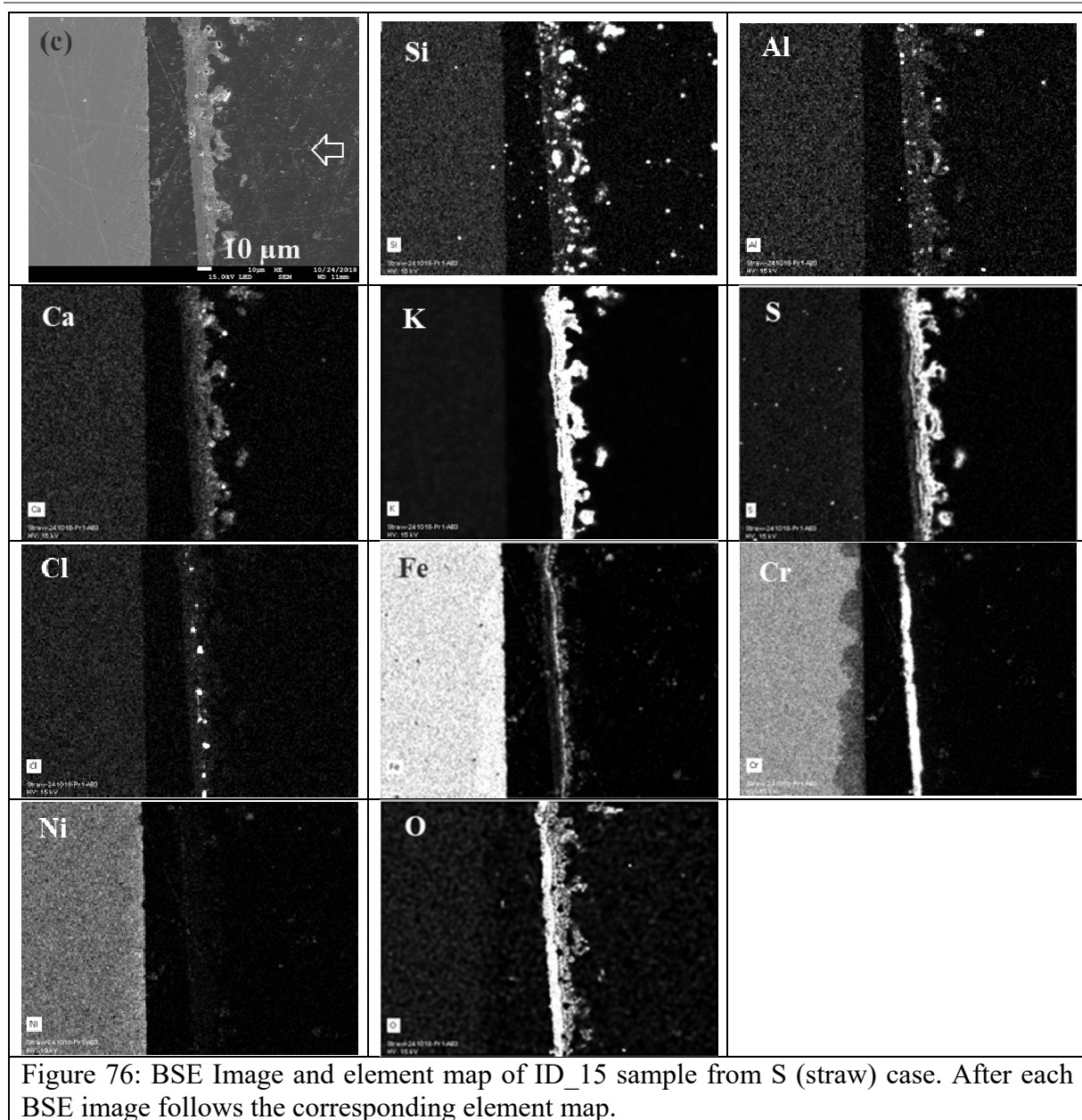


Figure 75: BSE Image of ID L15 sample form straw (S) case.



Continue in next page



8.3.2 Inner deposit from straw with additive (S+D) case

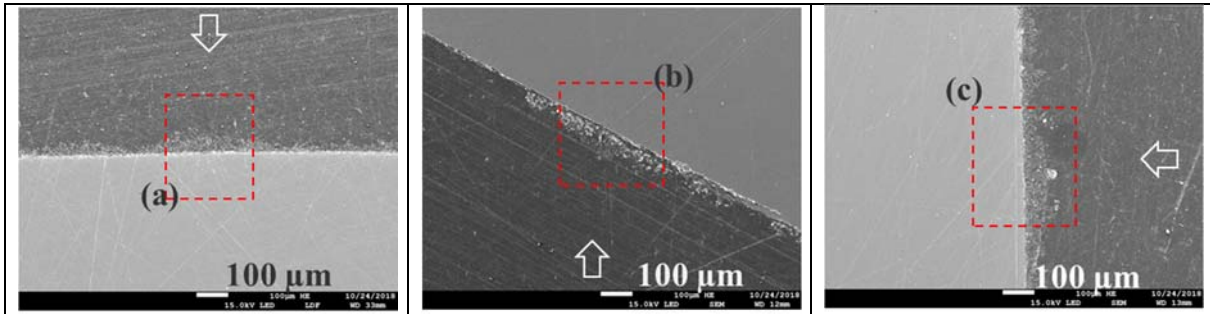
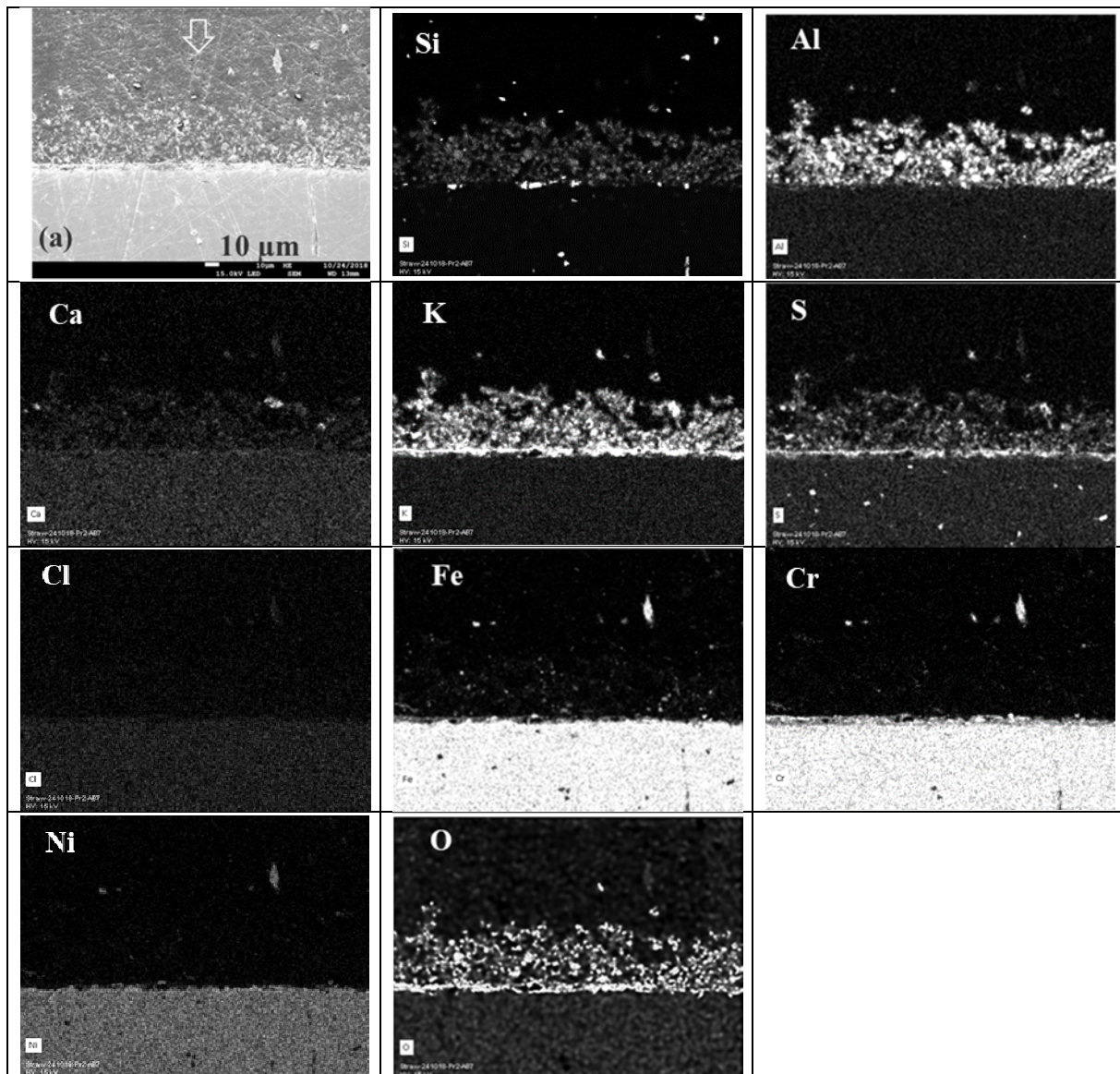
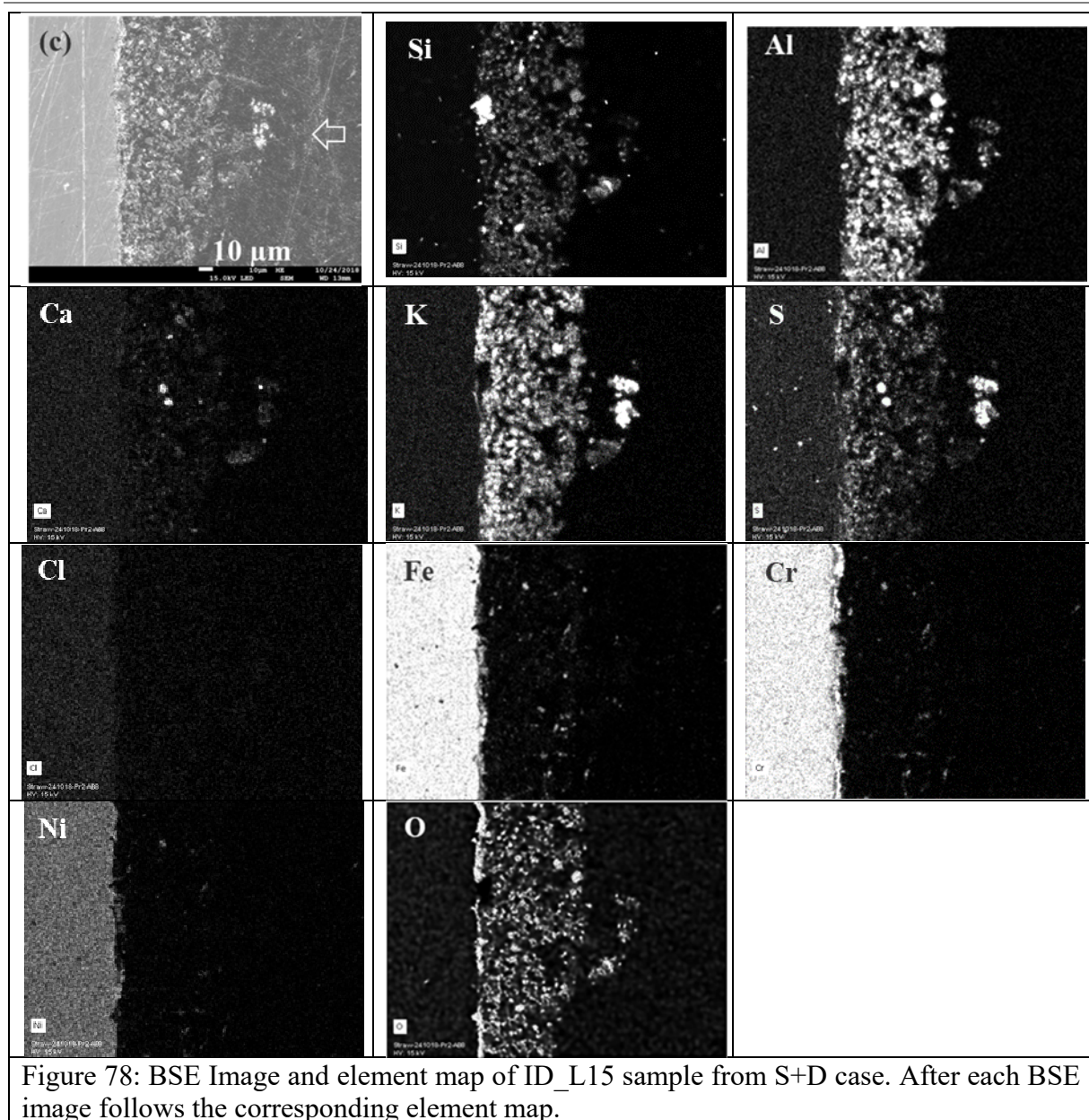


Figure 77: BSE Image showing surface cross-section of probe metal ring corresponding to straw with additive (S+D) case. (b) Corresponds to the BSE image shown in chapter 4.3.1.5.2 (Figure 44).



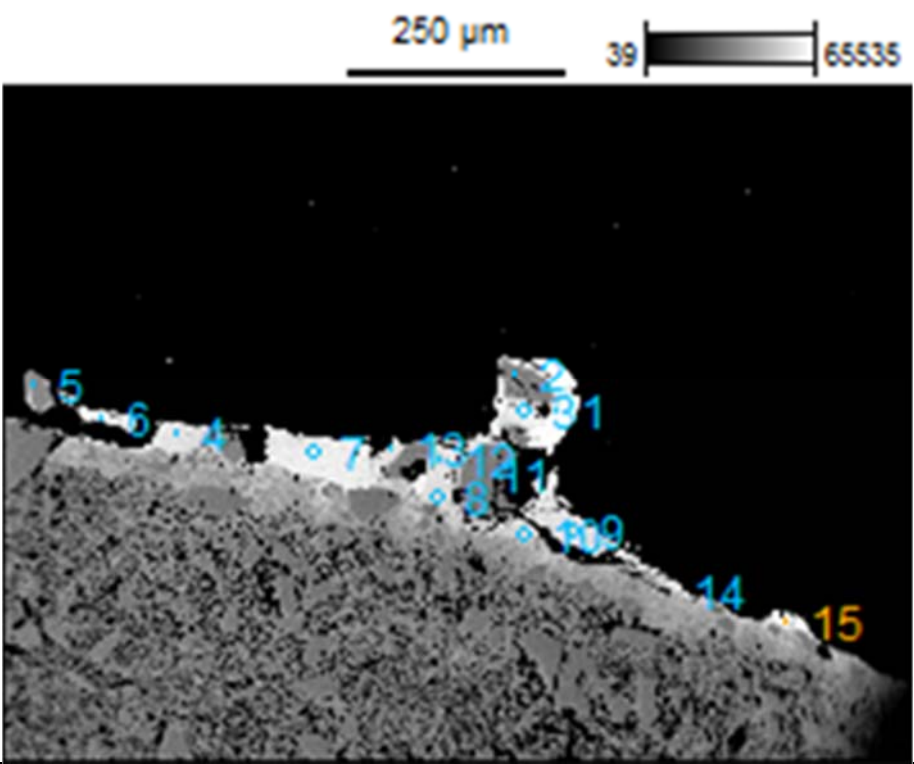
Continue in next page



8.4 Composition of deposit ash particle/phases corresponding to test set A (BTS)

8.4.1 Outer deposit (OD) from wood (W) case

Table 36: Point analysis of OD sample corresponding to W case.

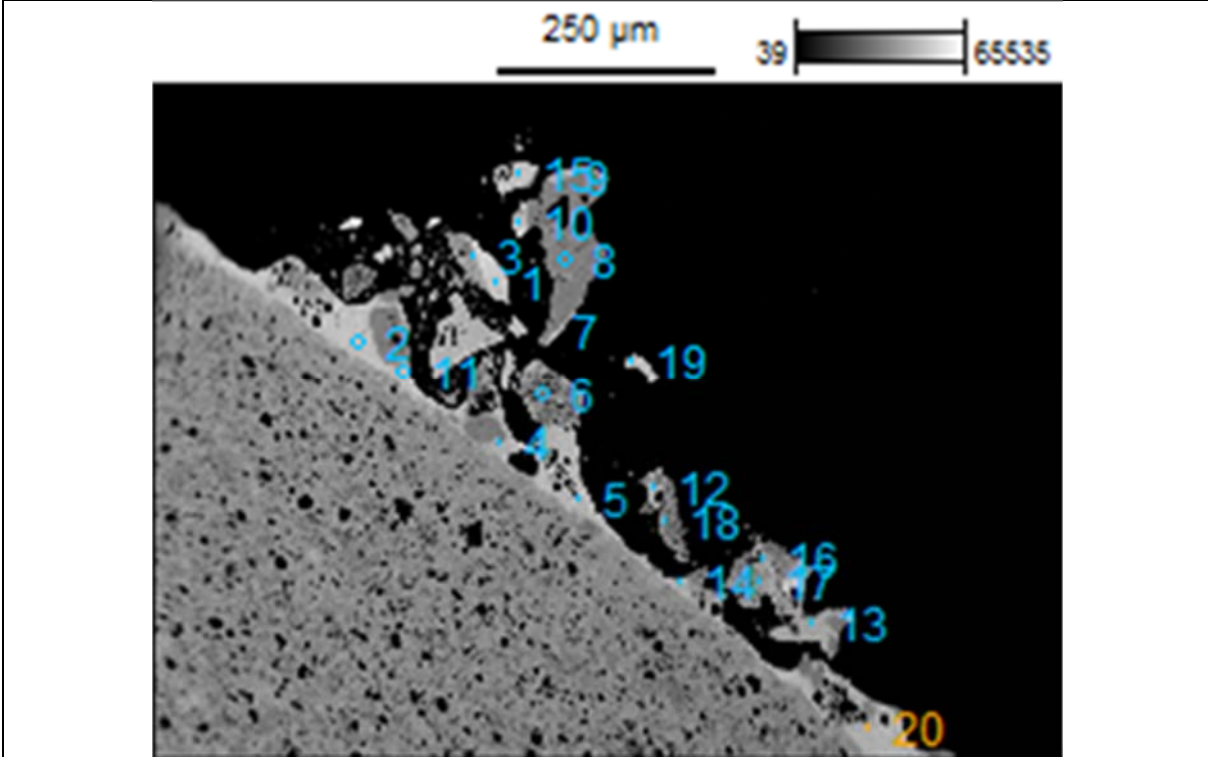


Points	SiO ₂	Al ₂ O ₃	CaO	MgO	K ₂ O	Na ₂ O	P ₂ O ₅	Fe ₂ O ₃	TiO ₂	SO ₃	Composition
1	28.65	6.36	5.54	1.50	2.39	0.62	0.64	0.73	53.55	0.04	Other
2	99.16	0.00	0.00	0.01	0.00	0.14	0.20	0.00	0.07	0.43	Silica
3	57.25	10.46	9.13	2.24	5.17	1.03	0.85	1.17	12.61	0.08	Slag
4	58.15	13.87	11.60	2.93	4.24	1.12	1.51	2.78	3.75	0.06	Slag
5	99.06	0.00	0.00	0.08	0.00	0.19	0.17	0.02	0.04	0.42	Silica
6	53.21	16.33	12.71	2.69	3.72	1.19	2.18	2.44	5.41	0.13	Slag
7	53.24	14.29	18.00	3.06	2.89	0.93	1.33	3.12	3.02	0.11	Slag
8	54.78	17.18	12.77	2.84	4.24	1.10	1.47	2.54	3.04	0.06	Slag
9	52.60	17.01	12.97	2.90	3.92	1.04	1.50	1.53	6.45	0.08	Slag
10	51.21	21.92	15.34	2.06	2.90	0.82	1.18	1.75	2.77	0.06	Slag
11	98.98	0.00	0.00	0.00	0.00	0.14	0.39	0.06	0.03	0.39	Silica
12	57.19	14.57	11.62	2.77	4.42	1.09	1.31	2.60	4.32	0.09	Slag
13	57.94	14.36	11.53	2.33	4.84	1.08	1.46	2.70	3.69	0.07	Slag
14	41.32	41.61	13.82	0.00	0.74	1.03	0.29	0.61	0.45	0.14	Slag
15	31.89	20.91	10.16	1.24	1.76	0.78	0.67	1.23	31.30	0.06	Other

	SiO ₂	Al ₂ O ₃	CaO	MgO	K ₂ O	Na ₂ O	P ₂ O ₅	Fe ₂ O ₃	TiO ₂	SO ₃	
Fly ash	28.99	6.18	40.44	8.92	3.24	0.86	4.46	3.45	1.55	1.11	0.80 (Cl)

8.4.2 Outer deposit (OD) from wood with additive (W+C) case

Table 37: Point analysis of OD sample from W+C case.

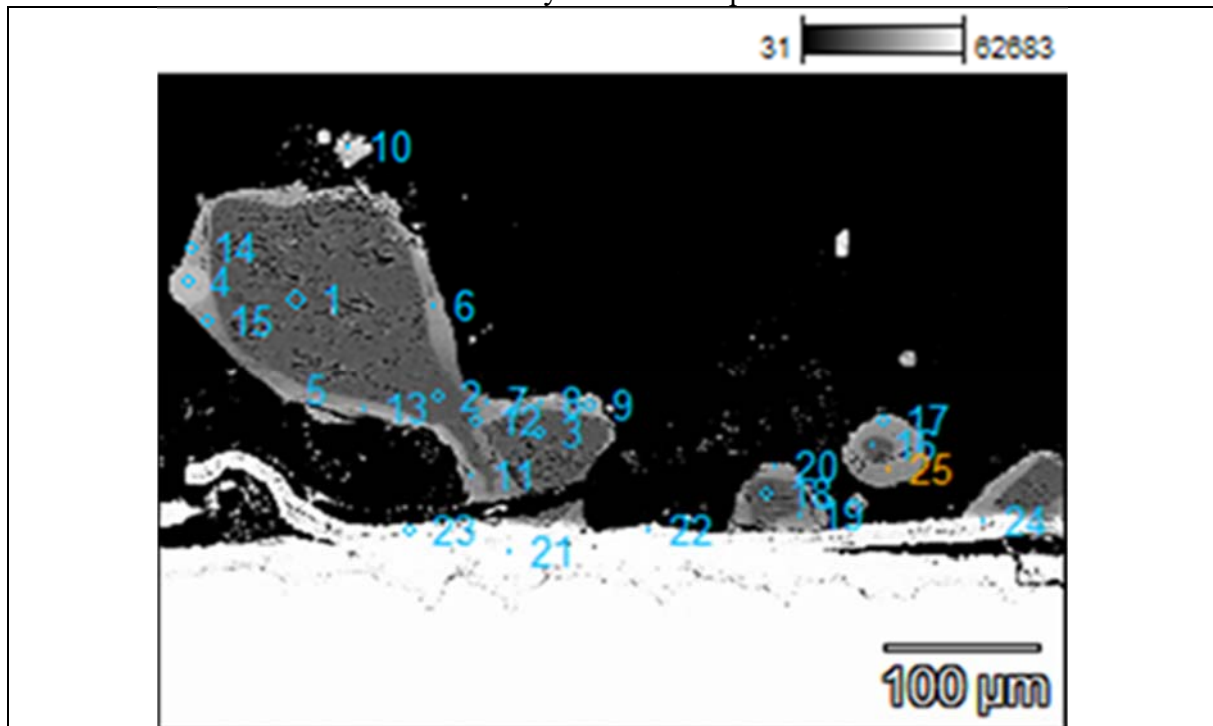


Points	SiO ₂	Al ₂ O ₃	CaO	MgO	K ₂ O	Na ₂ O	P ₂ O ₅	Fe ₂ O ₃	TiO ₂	SO ₃	Composition
1	56.30	16.60	12.67	3.04	3.72	0.56	2.03	3.11	1.89	0.08	Slag
2	55.11	18.26	10.26	4.60	3.95	0.56	2.56	2.89	1.75	0.06	Slag
3	45.90	38.39	9.66	0.39	2.49	0.38	0.61	1.28	0.87	0.03	Slag
4	59.56	19.79	7.66	2.23	5.70	0.80	1.91	1.58	0.63	0.11	Slag
5	48.99	26.65	17.34	1.83	1.31	0.33	1.58	1.37	0.58	0.01	Slag
6	53.27	40.94	0.04	0.00	2.66	0.40	0.27	1.33	0.82	0.23	Other
7	98.37	0.29	0.02	0.14	0.39	0.25	0.30	0.12	0.07	0.04	Silica
8	99.09	0.00	0.00	0.00	0.00	0.05	0.43	0.04	0.08	0.28	Silica
9	75.78	9.77	6.48	1.34	4.54	0.50	0.45	0.87	0.17	0.09	Slag
10	76.63	9.40	5.42	1.26	4.43	0.54	0.89	1.06	0.28	0.08	Slag
11	57.42	18.05	7.66	3.64	4.99	0.70	2.49	3.60	1.38	0.05	Slag
12	84.12	7.25	1.13	0.53	4.43	0.58	0.40	1.10	0.23	0.18	Silica
13	58.74	24.81	9.66	0.00	4.82	1.00	0.17	0.66	0.11	0.03	Slag
14	56.24	23.53	5.24	1.87	6.82	0.87	2.61	1.88	0.88	0.07	Slag
15	59.76	16.64	12.03	3.14	3.63	0.54	1.94	1.66	0.61	0.05	Slag
16	54.83	33.10	1.87	0.20	6.21	0.67	1.29	1.54	0.25	0.04	Other

Points	SiO ₂	Al ₂ O ₃	CaO	MgO	K ₂ O	Na ₂ O	P ₂ O ₅	Fe ₂ O ₃	TiO ₂	SO ₃	Composition
17	65.34	26.63	1.02	0.01	4.83	0.47	0.58	0.80	0.22	0.09	Slag
18	76.65	20.40	0.04	0.00	1.49	0.20	0.28	0.67	0.17	0.10	Slag
19	60.60	15.97	9.76	2.84	4.97	0.55	2.80	1.64	0.85	0.03	Slag
20	55.05	21.09	8.52	3.40	4.55	0.62	2.29	2.78	1.63	0.06	Slag
Fly ash	48.69	23.29	12.85	2.71	6.22	1.12	1.98	1.58	0.72	0.44	0.39 (Cl)

8.4.3 Inner deposit (ID) from wood (W) case

Table 38: Point analysis of ID sample from W case



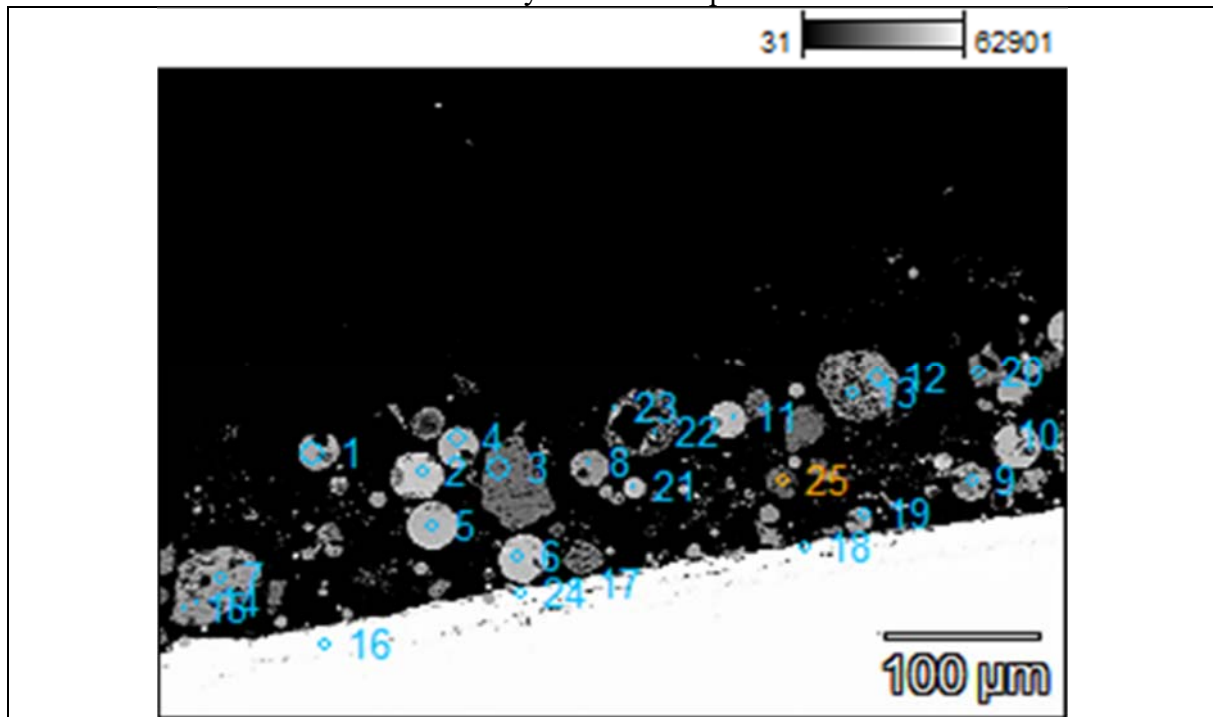
Points	SiO ₂	Al ₂ O ₃	CaO	MgO	K ₂ O	Na ₂ O	P ₂ O ₅	Fe ₂ O ₃	TiO ₂	SO ₃	Composition
1	99.26	0.00	0.07	0.01	0.00	0.07	0.41	0.18	0.00	0.00	Silica
2	99.36	0.00	0.05	0.02	0.00	0.02	0.50	0.05	0.00	0.00	Silica
3	99.42	0.00	0.00	0.06	0.01	0.04	0.41	0.06	0.00	0.00	Silica
4	39.90	5.53	33.05	11.00	0.99	1.53	4.48	2.40	1.11	0.01	Class B
5	74.24	0.00	3.35	0.08	16.19	5.68	0.17	0.28	0.01	0.00	Class A
6	70.56	0.34	5.70	0.21	17.07	5.39	0.39	0.27	0.07	0.00	Class A
7	66.41	0.53	5.14	3.18	18.42	4.29	0.31	0.71	0.07	0.94	Class A
8	69.00	0.02	9.50	0.42	15.97	4.06	0.55	0.43	0.04	0.00	Class A
9	55.14	5.01	17.66	5.72	10.63	2.19	0.56	2.45	0.64	0.00	Class B
10	20.66	1.34	43.42	3.02	1.22	0.92	27.17	2.09	0.16	0.00	Class B
11	74.75	0.00	3.52	0.06	15.91	4.94	0.20	0.59	0.02	0.00	Class A
12	79.99	0.06	2.41	0.25	12.78	4.17	0.27	0.00	0.07	0.00	Class A
13	74.08	0.00	4.55	0.05	16.12	5.04	0.15	0.00	0.00	0.00	Class A
14	67.80	0.12	7.20	0.55	16.92	5.46	0.43	1.51	0.00	0.00	Class A
15	73.90	0.00	2.01	0.46	17.15	5.96	0.24	0.28	0.00	0.00	Class A
16	99.21	0.00	0.01	0.03	0.02	0.07	0.46	0.20	0.00	0.00	Silica

Continue in next page

Points	SiO ₂	Al ₂ O ₃	CaO	MgO	K ₂ O	Na ₂ O	P ₂ O ₅	Fe ₂ O ₃	TiO ₂	SO ₃	Composition
17	71.18	0.00	6.28	0.35	17.14	4.74	0.31	0.00	0.00	0.00	Class A
18	98.85	0.00	0.02	0.08	0.09	0.04	0.53	0.39	0.00	0.00	Silica
19	75.18	0.00	2.23	0.01	16.25	5.44	0.26	0.56	0.03	0.04	Class A
20	63.39	1.30	6.49	2.57	18.04	4.72	1.80	1.15	0.16	0.38	Class A
21	0.55	0.09	0.05	0.00	0.00	0.08	0.07	98.97	0.07	0.12	Alloy element
22	11.29	0.24	1.86	0.85	1.41	0.07	0.20	83.72	0.00	0.36	Alloy element
23	0.43	0.05	0.02	0.00	0.06	0.10	0.03	99.23	0.00	0.08	Alloy element
24	3.85	0.07	0.08	0.00	1.92	0.68	0.03	92.58	0.00	0.79	Alloy element
25	73.39	0.18	2.10	0.53	17.58	5.65	0.16	0.41	0.00	0.00	Class A

8.4.4 Inner deposit from wood with additive (W+C) case

Table 39: Point analysis of ID sample from W+C case



Points	SiO ₂	Al ₂ O ₃	CaO	MgO	K ₂ O	Na ₂ O	P ₂ O ₅	Fe ₂ O ₃	TiO ₂	SO ₃	Composition
1	41.69	27.02	14.65	5.46	4.75	0.76	1.22	3.56	0.85	0.05	Class B
2	40.49	8.71	27.88	3.56	1.96	0.22	12.87	3.86	0.45	0.00	Class B
3	98.91	0.03	0.05	0.05	0.00	0.05	0.40	0.47	0.05	0.00	Silica
4	35.92	25.40	22.50	8.96	2.21	0.18	2.73	1.46	0.61	0.03	Class B
5	48.98	20.23	11.53	3.01	7.87	1.18	0.67	5.56	0.96	0.02	Class B
6	32.72	22.52	30.12	7.71	2.35	0.11	2.09	1.65	0.69	0.06	Class B
7	65.36	18.67	0.37	0.00	14.09	0.90	0.19	0.29	0.11	0.01	Class C
8	65.96	18.46	0.22	0.00	13.68	1.15	0.13	0.29	0.09	0.00	Class C
9	56.55	17.86	6.95	2.80	7.93	0.60	1.82	4.79	0.70	0.00	Class C
10	34.65	22.77	24.52	7.53	4.27	0.19	3.75	1.76	0.57	0.00	Class B
11	33.03	24.09	24.39	9.41	4.05	0.44	2.57	1.77	0.20	0.06	Class B
12	65.20	18.30	0.14	0.00	14.53	1.11	0.18	0.48	0.06	0.00	Class C
13	65.33	18.80	0.16	0.03	13.46	0.97	0.08	1.14	0.04	0.00	Class C
14	61.56	17.58	0.10	0.01	13.86	0.87	0.16	5.72	0.12	0.00	Class C
15	65.35	18.49	0.19	0.00	14.19	0.95	0.24	0.54	0.05	0.00	Class C
16	2.48	0.03	0.00	0.00	0.09	0.12	0.00	97.28	0.00	0.00	Alloy element

Continue in next page

Points	SiO ₂	Al ₂ O ₃	CaO	MgO	K ₂ O	Na ₂ O	P ₂ O ₅	Fe ₂ O ₃	TiO ₂	SO ₃	Composition
17	0.74	0.07	0.22	0.00	0.22	0.11	0.02	98.54	0.00	0.07	Alloy element
18	12.17	10.09	1.79	1.07	3.82	1.02	0.26	69.14	0.16	0.49	Alloy element
19	42.80	33.77	9.50	2.88	6.76	0.95	1.09	2.06	0.18	0.02	Class B
20	42.41	20.79	0.29	0.07	1.53	0.64	0.09	33.37	0.17	0.63	Other
21	43.16	26.10	19.20	2.13	3.06	1.16	0.21	4.78	0.20	0.00	Class B
22	44.95	37.16	0.47	0.28	3.22	1.08	0.11	11.47	0.53	0.74	Other
23	40.15	33.12	0.22	0.12	5.57	0.43	0.24	1.32	18.83	0.00	Other
24	3.81	3.21	0.09	0.01	0.89	0.09	0.15	91.58	0.00	0.17	Other
25	98.44	0.31	0.02	0.05	0.05	0.04	0.50	0.59	0.00	0.00	Silica

9 Annex 3

9.1 Input for FactSage calculation

Table 40: Average oxide composition of characteristics 'silicatic' deposit particle/phases categorized here as; Class A, Class B and Class C composition.

Sample	W case	W+C case	
	Class A K ₂ O+Na ₂ O rich	Class B (K ₂ O+Na ₂ O)<(CaO+MgO)	Class C (K ₂ O+Na ₂ O)>(CaO+MgO)
Points	Table 38 5, 6, 7,8, 11, 12, 13, 14, 15, 17, 19, 20 and 25	Table 39 1, 2, 4, 5, 6, 10, 11, 19 and 21	Table 39 7, 8, 9, 12, 13, 14 and 15
Morphology/shape	Coating	Spherical	Spherical/porous
SiO ₂	72	39	64
Al ₂ O ₃	0	23	18
CaO	5	20	1
MgO	1	6	0
K ₂ O	17	4	13
Na ₂ O	5	1	1
P ₂ O ₅	0	3	0
Fe ₂ O ₃	0	3	2
TiO ₂	0	1	0
SO ₃	0	0	0

Table 41: FactSage equilibrium input as amount of each component in g per Kg of given fuel (derive from standard analysis of respective fuel).

Fuel Name	TS4	TS1	*W
Fuel components			
H ₂ O	67.40	78.90	73.50
C	456.00	468.00	471.50
H	52.91	43.13	46.68
N	5.86	4.60	5.79
S	1.00	0.75	0.72
Cl	0.89	0.50	1.26
Al	0.60	0.36	0.44
Ca	7.24	5.69	1.94
Fe	0.88	0.93	1.11
K	12.40	8.43	2.29
Mg	0.88	0.72	0.47
Na	0.68	0.15	0.16
P	0.58	0.47	0.16
Si	11.40	7.55	2.25
Ti	0.03	0.03	0.11
O _{diff}	381.25	379.79	391.63
Combustion Air			
O ₂	1512	1458	1489
N ₂	4636	4470	4565

10 References

- [1] IEA, Coal 2018, 2018. <https://www.iea.org/reports/coal-2018>.
- [2] S. van Loo, J. Koppejan (Eds.), The handbook of biomass combustion and co-firing, Earthscan, London, 2009.
- [3] M.S. Roni, S. Chowdhury, S. Mamun, M. Marufuzzaman, W. Lein, S. Johnson, Biomass co-firing technology with policies, challenges, and opportunities: A global review, *Renewable and Sustainable Energy Reviews* 78 (2017) 1089–1101. <https://doi.org/10.1016/j.rser.2017.05.023>.
- [4] DIN EN ISO 17225-1: Solid biofuels-Fuel specification and classes-Part 1 General requirements, 2014.
- [5] F. Al-Mansour, J. Zuwala, An evaluation of biomass co-firing in Europe, *Biomass and Bioenergy* 34 (2010) 620–629. <https://doi.org/10.1016/j.biombioe.2010.01.004>.
- [6] M. Sami, K. Annamalai, M. Wooldridge, Co-firing of coal and biomass fuel blends, *Progress in Energy and Combustion Science* 27 (2001) 171–214. [https://doi.org/10.1016/S0360-1285\(00\)00020-4](https://doi.org/10.1016/S0360-1285(00)00020-4).
- [7] DIN EN ISO 17225-2: Solid biofuels-Fuel specification and classes-Part 2 Graded wood, 2014.
- [8] C. Ndibe, Characterization of torrefied fuels for direct co-firing in large pulverized fuel boilers, Dissertation, Universität Stuttgart, 2019.
- [9] R.W. Bryers, Fireside slagging, fouling, and high-temperature corrosion of heat-transfer surface due to impurities in steam-raising fuels, *Progress in Energy and Combustion Science* 22 (1996) 29–120. [https://doi.org/10.1016/0360-1285\(95\)00012-7](https://doi.org/10.1016/0360-1285(95)00012-7).
- [10] R.P. Gupta, T.F. Wall, L. Baxter (Eds.), *Impact of Mineral Impurities in Solid Fuel Combustion*, Kluwer Academic Publishers, Boston, MA, 2002.
- [11] M. Lackner, F. Winter, A.K. Agarwal, *Handbook of Combustion*, Wiley-VCH Verlag GmbH & Co. KGaA, Weinheim, Germany, 2010.
- [12] S.V. Vassilev, D. Baxter, L.K. Andersen, C.G. Vassileva, T.J. Morgan, An overview of the organic and inorganic phase composition of biomass, *Fuel* 94 (2012) 1–33. <https://doi.org/10.1016/j.fuel.2011.09.030>.
- [13] S.V. Vassilev, D. Baxter, C.G. Vassileva, An overview of the behaviour of biomass during combustion: Part I. Phase-mineral transformations of organic and inorganic matter, *Fuel* 112 (2013) 391–449. <https://doi.org/10.1016/j.fuel.2013.05.043>.

- [14] S.V. Vassilev, D. Baxter, L.K. Andersen, C.G. Vassileva, An overview of the composition and application of biomass ash. Part 1. Phase–mineral and chemical composition and classification, *Fuel* 105 (2013) 40–76. <https://doi.org/10.1016/j.fuel.2012.09.041>.
- [15] S.V. Vassilev, D. Baxter, C.G. Vassileva, An overview of the behaviour of biomass during combustion: Part II. Ash fusion and ash formation mechanisms of biomass types, *Fuel* 117 (2014) 152–183. <https://doi.org/10.1016/j.fuel.2013.09.024>.
- [16] S.V. Vassilev, C.G. Vassileva, Y.-C. Song, W.-Y. Li, J. Feng, Ash contents and ash-forming elements of biomass and their significance for solid biofuel combustion, *Fuel* 208 (2017) 377–409. <https://doi.org/10.1016/j.fuel.2017.07.036>.
- [17] M. Paneru, S. Babat, J. Maier, G. Scheffknecht, Role of potassium in deposit formation during wood pellets combustion, *Fuel Processing Technology* 141 (2016) 266–275. <https://doi.org/10.1016/j.fuproc.2015.10.008>.
- [18] T. Heinzl, V. Siegle, H. Spliethoff, K. Hein, Investigation of slagging in pulverized fuel co-combustion of biomass and coal at a pilot-scale test facility, *Fuel Processing Technology* 54 (1998) 109–125. [https://doi.org/10.1016/S0378-3820\(97\)00063-5](https://doi.org/10.1016/S0378-3820(97)00063-5).
- [19] S.C. Stultz, J.B. Kitto (Eds.), *Steam: Its generation and use*, 40th ed., Babcock & Wilcox, Barberton, Ohio, 1992.
- [20] U. Kleinhans, C. Wieland, F.J. Frandsen, H. Spliethoff, Ash formation and deposition in coal and biomass fired combustion systems: Progress and challenges in the field of ash particle sticking and rebound behavior, *Progress in Energy and Combustion Science* 68 (2018) 65–168. <https://doi.org/10.1016/j.pecs.2018.02.001>.
- [21] H.P. Nielsen, F.J. Frandsen, K. Dam-Johansen, L.L. Baxter, The implications of chlorine-associated corrosion on the operation of biomass-fired boilers, *Progress in Energy and Combustion Science* 26 (2000) 283–298. [https://doi.org/10.1016/S0360-1285\(00\)00003-4](https://doi.org/10.1016/S0360-1285(00)00003-4).
- [22] L.L. Baxter, T.R. Miles, B.M. Jenkins, T. Milne, D. Dayton, R.W. Bryers, L.L. Oden, The behavior of inorganic material in biomass-fired power boilers: Field and laboratory experiences, *Fuel Processing Technology* 54 (1998) 47–78. [https://doi.org/10.1016/S0378-3820\(97\)00060-X](https://doi.org/10.1016/S0378-3820(97)00060-X).
- [23] L.L. Baxter, T.R. Miles, T.R. Miles JR., B.M. Jenkins, D.C. Dayton, T.A. Milne, R.W. Bryers, L.L. Oden, Alkali deposits found in biomass boilers: The behavior of inorganic material in biomass-fired power boilers -- Field and laboratory experiences. Volume 2, 1996.

- [24] Yves Ryckmans, Experience with biomass firing for large scale power, 2017.
http://task32.ieabioenergy.com/wp-content/uploads/2017/03/08-Yves_Ryckmans.pdf.
- [25] Y. Niu, H. Tan, S. Hui, Ash-related issues during biomass combustion: Alkali-induced slagging, silicate melt-induced slagging (ash fusion), agglomeration, corrosion, ash utilization, and related countermeasures, *Progress in Energy and Combustion Science* 52 (2016) 1–61. <https://doi.org/10.1016/j.pecs.2015.09.003>.
- [26] W.R. Livingston, J. Middelkamp, W. Willeboer, S. Madrali, The status of large scale biomass firing: The milling and combustion of biomass materials in large pulverized coal boilers, 2016. https://www.ieabioenergy.com/wp-content/uploads/2016/03/IEA_Bioenergy_T32_cofiring_2016.pdf.
- [27] D. Boström, N. Skoglund, A. Grimm, C. Boman, M. Öhman, M. Broström, R. Backman, Ash Transformation Chemistry during Combustion of Biomass, *Energy Fuels* 26 (2012) 85–93. <https://doi.org/10.1021/ef201205b>.
- [28] F.E. Huggins, Overview of analytical methods for inorganic constituents in coal, *International Journal of Coal Geology* 50 (2002) 169–214. [https://doi.org/10.1016/S0166-5162\(02\)00118-0](https://doi.org/10.1016/S0166-5162(02)00118-0).
- [29] J. Werkelin, B.-J. Skrifvars, M. Zevenhoven, B. Holmbom, M. Hupa, Chemical forms of ash-forming elements in woody biomass fuels, *Fuel* 89 (2010) 481–493.
<https://doi.org/10.1016/j.fuel.2009.09.005>.
- [30] M. Zevenhoven, P. Yrjas, B.-J. Skrifvars, M. Hupa, Characterization of Ash-Forming Matter in Various Solid Fuels by Selective Leaching and Its Implications for Fluidized-Bed Combustion, *Energy Fuels* 26 (2012) 6366–6386. <https://doi.org/10.1021/ef300621j>.
- [31] M.J. Wornat, R.H. Hurt, N.Y. Yang, T.J. Headley, Structural and compositional transformations of biomass chars during combustion, *Combustion and Flame* 100 (1995) 131–143. [https://doi.org/10.1016/0010-2180\(94\)00055-W](https://doi.org/10.1016/0010-2180(94)00055-W).
- [32] D.C. Dayton, R.J. French, T.A. Milne, Direct Observation of Alkali Vapor Release during Biomass Combustion and Gasification. 1. Application of Molecular Beam/Mass Spectrometry to Switchgrass Combustion, *Energy Fuels* 9 (1995) 855–865.
<https://doi.org/10.1021/ef00053a018>.
- [33] D.C. Dayton, B.M. Jenkins, S.Q. Turn, R.R. Bakker, R.B. Williams, D. Belle-Oudry, L.M. Hill, Release of Inorganic Constituents from Leached Biomass during Thermal Conversion, *Energy Fuels* 13 (1999) 860–870. <https://doi.org/10.1021/ef980256e>.

- [34] K.O. Davidsson, B.J. Stojkova, J.B.C. Pettersson, Alkali Emission from Birchwood Particles during Rapid Pyrolysis, *Energy Fuels* 16 (2002) 1033–1039. <https://doi.org/10.1021/ef010257y>.
- [35] P.E. Mason, L.I. Darvell, J.M. Jones, A. Williams, Observations on the release of gas-phase potassium during the combustion of single particles of biomass, *Fuel* 182 (2016) 110–117. <https://doi.org/10.1016/j.fuel.2016.05.077>.
- [36] J.M. Johansen, M. Aho, K. Paakkinen, R. Taipale, H. Egsgaard, J.G. Jakobsen, F.J. Frandsen, P. Glarborg, Release of K, Cl, and S during combustion and co-combustion with wood of high-chlorine biomass in bench and pilot scale fuel beds, *Proceedings of the Combustion Institute* 34 (2013) 2363–2372. <https://doi.org/10.1016/j.proci.2012.07.025>.
- [37] J.M. Johansen, J.G. Jakobsen, F.J. Frandsen, P. Glarborg, Release of K, Cl, and S during Pyrolysis and Combustion of High-Chlorine Biomass, *Energy Fuels* 25 (2011) 4961–4971. <https://doi.org/10.1021/ef201098n>.
- [38] J.N. Knudsen, P.A. Jensen, K. Dam-Johansen, Transformation and Release to the Gas Phase of Cl, K, and S during Combustion of Annual Biomass, *Energy Fuels* 18 (2004) 1385–1399. <https://doi.org/10.1021/ef049944q>.
- [39] S.C. van Lith, P.A. Jensen, F.J. Frandsen, P. Glarborg, Release to the Gas Phase of Inorganic Elements during Wood Combustion. Part 2: Influence of Fuel Composition, *Energy Fuels* 22 (2008) 1598–1609. <https://doi.org/10.1021/ef060613i>.
- [40] S.C. van Lith, V. Alonso-Ramírez, P.A. Jensen, F.J. Frandsen, P. Glarborg, Release to the Gas Phase of Inorganic Elements during Wood Combustion. Part 1: Development and Evaluation of Quantification Methods, *Energy Fuels* 20 (2006) 964–978. <https://doi.org/10.1021/ef050131r>.
- [41] E. Björkman, B. Strömberg, Release of Chlorine from Biomass at Pyrolysis and Gasification Conditions 1, *Energy Fuels* 11 (1997) 1026–1032. <https://doi.org/10.1021/ef970031o>.
- [42] S. Arvelakis, P.A. Jensen, K. Dam-Johansen, Simultaneous Thermal Analysis (STA) on Ash from High-Alkali Biomass 18 1066–1076. <https://doi.org/10.1021/ef034065+>.
- [43] H. Zhao, W. Xu, Q. Song, J. Zhuo, Q. Yao, Effect of Steam and SiO₂ on the Release and Transformation of K₂CO₃ and KCl during Biomass Thermal Conversion, *Energy Fuels* 32 (2018) 9633–9639. <https://doi.org/10.1021/acs.energyfuels.8b02269>.
- [44] D.L. Perry (Ed.), *Handbook of inorganic compounds*, CRC Press, Boca Raton, 1995.

- [45] D. Pham Minh, A.R. Sane, N. Semlal, P. Sharrock, A. Nzihou, Alkali polyphosphates as new potential materials for thermal energy storage, *Solar Energy* 157 (2017) 277–283. <https://doi.org/10.1016/j.solener.2017.08.030>.
- [46] N. Skoglund, A. Grimm, M. Öhman, D. Boström, Effects on Ash Chemistry when Co-firing Municipal Sewage Sludge and Wheat Straw in a Fluidized Bed: Influence on the Ash Chemistry by Fuel Mixing, *Energy Fuels* 27 (2013) 5725–5732. <https://doi.org/10.1021/ef401197q>.
- [47] A. Grimm, Experimental studies of ash transformation processes in combustion of phosphorus-rich biomass fuels, Dissertation, Luleå University of Technology, 2012.
- [48] R.L. Frost, M.L. Weier, Thermal treatment of whewellite—a thermal analysis and Raman spectroscopic study, *Thermochimica Acta* 409 (2004) 79–85. [https://doi.org/10.1016/S0040-6031\(03\)00332-0](https://doi.org/10.1016/S0040-6031(03)00332-0).
- [49] M. Földvári, Handbook of thermogravimetric system of minerals and its use in geological practice, Geological Inst. of Hungary, Budapest, 2011.
- [50] F. Frandsen, Ash formation, deposition and corrosion when utilizing straw for heat and power production, Dissertation, DTU Chemical Engineering, 2011.
- [51] P. Holmgren, D.R. Wagner, A. Strandberg, R. Molinder, H. Wiinikka, K. Umeki, M. Broström, Size, shape, and density changes of biomass particles during rapid devolatilization, *Fuel* 206 (2017) 342–351. <https://doi.org/10.1016/j.fuel.2017.06.009>.
- [52] O. Sippula, T. Lind, J. Jokiniemi, Effects of chlorine and sulphur on particle formation in wood combustion performed in a laboratory scale reactor, *Fuel* 87 (2008) 2425–2436. <https://doi.org/10.1016/j.fuel.2008.02.004>.
- [53] W. Weng, S. Chen, H. Wu, P. Glarborg, Z. Li, Optical investigation of gas-phase KCl/KOH sulfation in post flame conditions, *Fuel* 224 (2018) 461–468. <https://doi.org/10.1016/j.fuel.2018.03.095>.
- [54] P. Glarborg, P. Marshall, Mechanism and modeling of the formation of gaseous alkali sulfates, *Combustion and Flame* 141 (2005) 22–39. <https://doi.org/10.1016/j.combustflame.2004.08.014>.
- [55] A. Grimm, N. Skoglund, D. Boström, M. Öhman, Bed Agglomeration Characteristics in Fluidized Quartz Bed Combustion of Phosphorus-Rich Biomass Fuels, *Energy Fuels* 25 (2011) 937–947. <https://doi.org/10.1021/ef101451e>.

- [56] J. Fagerström, E. Steinvall, D. Boström, C. Boman, Alkali transformation during single pellet combustion of soft wood and wheat straw, *Fuel Processing Technology* 143 (2016) 204–212. <https://doi.org/10.1016/j.fuproc.2015.11.016>.
- [57] D. Nordgren, H. Hedman, N. Padban, D. Boström, M. Öhman, Ash transformations in pulverised fuel co-combustion of straw and woody biomass, *Fuel Processing Technology* 105 (2013) 52–58. <https://doi.org/10.1016/j.fuproc.2011.05.027>.
- [58] B.-M. Steenari, A. Lundberg, H. Pettersson, M. Wilewska-Bien, D. Andersson, Investigation of Ash Sintering during Combustion of Agricultural Residues and the Effect of Additives, *Energy Fuels* 23 (2009) 5655–5662. <https://doi.org/10.1021/ef900471u>.
- [59] H. Wu, M.S. Bashir, P.A. Jensen, B. Sander, P. Glarborg, Impact of coal fly ash addition on ash transformation and deposition in a full-scale wood suspension-firing boiler, *Fuel* 113 (2013) 632–643. <https://doi.org/10.1016/j.fuel.2013.06.018>.
- [60] M.S. Bashir, P.A. Jensen, F. Frandsen, S. Wedel, K. Dam-Johansen, J. Wadenbäck, S.T. Pedersen, Ash transformation and deposit build-up during biomass suspension and grate firing: Full-scale experimental studies, *Fuel Processing Technology* 97 (2012) 93–106. <https://doi.org/10.1016/j.fuproc.2012.01.018>.
- [61] B. Kutchko, A. Kim, Fly ash characterization by SEM–EDS, *Fuel* 85 (2006) 2537–2544. <https://doi.org/10.1016/j.fuel.2006.05.016>.
- [62] L.L. Baxter, Ash deposition during biomass and coal combustion: A mechanistic approach, *Biomass and Bioenergy* 4 (1993) 85–102. [https://doi.org/10.1016/0961-9534\(93\)90031-X](https://doi.org/10.1016/0961-9534(93)90031-X).
- [63] H. Nielsen, Deposition of potassium salts on heat transfer surfaces in straw-fired boilers: A pilot-scale study, *Fuel* 79 (2000) 131–139. [https://doi.org/10.1016/S0016-2361\(99\)00090-3](https://doi.org/10.1016/S0016-2361(99)00090-3).
- [64] T. Heinzl, Ascheseitige Probleme bei der Mitverbrennung von Biomasse in Kohlenstaubfeuerungen, Dissertation, Universität Stuttgart, 2003.
- [65] M.S. Bashir, P.A. Jensen, F. Frandsen, S. Wedel, K. Dam-Johansen, J. Wadenbäck, S.T. Pedersen, Suspension-Firing of Biomass. Part 1: Full-Scale Measurements of Ash Deposit Build-up, *Energy Fuels* 26 (2012) 2317–2330. <https://doi.org/10.1021/ef201680k>.
- [66] A.L. Robinson, H. Junker, L.L. Baxter, Pilot-Scale Investigation of the Influence of Coal–Biomass Cofiring on Ash Deposition, *Energy Fuels* 16 (2002) 343–355. <https://doi.org/10.1021/ef010128h>.

- [67] H. Wu, P. Glarborg, F.J. Frandsen, K. Dam-Johansen, P.A. Jensen, Dust-Firing of Straw and Additives: Ash Chemistry and Deposition Behavior, *Energy Fuels* 25 (2011) 2862–2873. <https://doi.org/10.1021/ef200452d>.
- [68] H. Zhou, P.A. Jensen, F.J. Frandsen, Dynamic mechanistic model of superheater deposit growth and shedding in a biomass fired grate boiler, *Fuel* 86 (2007) 1519–1533. <https://doi.org/10.1016/j.fuel.2006.10.026>.
- [69] P.A. Jensen, M. Stenholm, P. Hald, Deposition Investigation in Straw-Fired Boilers, *Energy Fuels* 11 (1997) 1048–1055. <https://doi.org/10.1021/ef960154t>.
- [70] C. Mueller, M. Selenius, M. Theis, B.-J. Skrifvars, R. Backman, M. Hupa, H. Tran, Deposition behaviour of molten alkali-rich fly ashes—development of a submodel for CFD applications, *Proceedings of the Combustion Institute* 30 (2005) 2991–2998. <https://doi.org/10.1016/j.proci.2004.08.116>.
- [71] S. Srinivasachar, J.J. Helble, A.A. Boni, An experimental study of the inertial deposition of ash under coal combustion conditions, 23rd Symposium (International) on Combustion (1991) 1305–1312. [https://doi.org/10.1016/S0082-0784\(06\)80394-2](https://doi.org/10.1016/S0082-0784(06)80394-2).
- [72] M.S. Bashir, P.A. Jensen, F. Frandsen, S. Wedel, K. Dam-Johansen, J. Wadenbäck, Suspension-Firing of Biomass. Part 2: Boiler Measurements of Ash Deposit Shedding, *Energy Fuels* 26 (2012) 5241–5255. <https://doi.org/10.1021/ef300611v>.
- [73] P. Kofstad, High temperature corrosion, Elsevier Applied Science Publishers, Crown House, Linton Road, Barking, Essex IG 11 8 JU, UK, 1988 (1988).
- [74] N. Eliaz, G. Shemesh, R.M. Latanision, Hot corrosion in gas turbine components, *Engineering Failure Analysis* 9 (2002) 31–43. [https://doi.org/10.1016/S1350-6307\(00\)00035-2](https://doi.org/10.1016/S1350-6307(00)00035-2).
- [75] H.J. Grabke, E. Reese, M. Spiegel, The effects of chlorides, hydrogen chloride, and sulfur dioxide in the oxidation of steels below deposits, *Corrosion Science* 37 (1995) 1023–1043. [https://doi.org/10.1016/0010-938X\(95\)00011-8](https://doi.org/10.1016/0010-938X(95)00011-8).
- [76] Y.S. Li, M. Spiegel, S. Shimada, Corrosion behaviour of various model alloys with NaCl–KCl coating, *Materials Chemistry and Physics* 93 (2005) 217–223. <https://doi.org/10.1016/j.matchemphys.2005.03.015>.
- [77] S. Enestam, D. Bankiewicz, J. Tuiremo, K. Mäkelä, M. Hupa, Are NaCl and KCl equally corrosive on superheater materials of steam boilers?, *Fuel* 104 (2013) 294–306. <https://doi.org/10.1016/j.fuel.2012.07.020>.

- [78] M. Paneru, G. Stein-Brzozowska, J. Maier, G. Scheffknecht, Corrosion Mechanism of Alloy 310 Austenitic Steel beneath NaCl Deposit under Varying SO₂ Concentrations in an Oxy-fuel Combustion Atmosphere, *Energy Fuels* 27 (2013) 5699–5705. <https://doi.org/10.1021/ef4005626>.
- [79] G. Sorell, The role of chlorine in high temperature corrosion in waste-to-energy plants, *Materials at High Temperatures* 14 (1997) 207–220. <https://doi.org/10.1080/09603409.1997.11689546>.
- [80] F. Abe, Research and Development of Heat-Resistant Materials for Advanced USC Power Plants with Steam Temperatures of 700 °C and Above, *Engineering* 1 (2015) 211–224. <https://doi.org/10.15302/J-ENG-2015031>.
- [81] F. Masuyama, Advances in Physical Metallurgy and Processing of Steels. History of Power Plants and Progress in Heat Resistant Steels, *ISIJ International* 41 (2001) 612–625. <https://doi.org/10.2355/isijinternational.41.612>.
- [82] M. Uusitalo, P. Vuoristo, T. Mäntylä, High temperature corrosion of coatings and boiler steels below chlorine-containing salt deposits, *Corrosion Science* 46 (2004) 1311–1331. <https://doi.org/10.1016/j.corsci.2003.09.026>.
- [83] J. Pettersson, N. Folkesson, L.-G. Johansson, J.-E. Svensson, The Effects of KCl, K₂SO₄ and K₂CO₃ on the High Temperature Corrosion of a 304-Type Austenitic Stainless Steel, *Oxid Met* 76 (2011) 93–109. <https://doi.org/10.1007/s11085-011-9240-z>.
- [84] H.J. Grabke, M. Spiegel, A. Zahs, Role of alloying elements and carbides in the chlorine-induced corrosion of steels and alloys, *Mat. Res.* 7 (2004) 89–95. <https://doi.org/10.1590/S1516-14392004000100013>.
- [85] R.A. Antunes, M.C. Lopes de Oliveira, Corrosion in biomass combustion: A materials selection analysis and its interaction with corrosion mechanisms and mitigation strategies, *Corrosion Science* 76 (2013) 6–26. <https://doi.org/10.1016/j.corsci.2013.07.013>.
- [86] J. Lehmusto, P. Yrjas, B.-J. Skrifvars, M. Hupa, High temperature corrosion of superheater steels by KCl and K₂CO₃ under dry and wet conditions, *Fuel Processing Technology* 104 (2012) 253–264. <https://doi.org/10.1016/j.fuproc.2012.05.020>.
- [87] L. Wang, J.E. Hustad, Ø. Skreiberg, G. Skjevraak, M. Grønli, A Critical Review on Additives to Reduce Ash Related Operation Problems in Biomass Combustion Applications, *Energy Procedia* 20 (2012) 20–29. <https://doi.org/10.1016/j.egypro.2012.03.004>.

- [88] F. Li, H. Fan, M. Guo, Q. Guo, Y. Fang, Influencing Mechanism of Additives on Ash Fusion Behaviors of Straw, *Energy Fuels* 32 (2018) 3272–3280.
<https://doi.org/10.1021/acs.energyfuels.7b04012>.
- [89] S. Kalisz, S. Ciukaj, K. Mroczek, M. Tymoszuik, R. Wejkowski, M. Pronobis, H. Kubiczek, Full-scale study on halloysite fireside additive in 230 t/h pulverized coal utility boiler, *Energy* 92 (2015) 33–39. <https://doi.org/10.1016/j.energy.2015.03.062>.
- [90] D.S. Clery, P.E. Mason, C.M. Rayner, J.M. Jones, The effects of an additive on the release of potassium in biomass combustion, *Fuel* 214 (2018) 647–655.
<https://doi.org/10.1016/j.fuel.2017.11.040>.
- [91] L.J. Roberts, P.E. Mason, J.M. Jones, W.F. Gale, A. Williams, A. Hunt, J. Ashman, The impact of aluminosilicate-based additives upon the sintering and melting behaviour of biomass ash, *Biomass and Bioenergy* 127 (2019) 105284. <https://doi.org/10.1016/j.biombioe.2019.105284>.
- [92] H. Schürmann, S. Unterberger, K.R. Hein, P.B. Monkhouse, U. Gottwald, The influence of fuel additives on the behaviour of gaseous alkali-metal compounds during pulverised coal combustion, *Faraday Discuss.* (2001) 433-44; discussion 445-59.
<https://doi.org/10.1039/B102122M>.
- [93] F. Bergaya, G. Lagaly (Eds.), *Handbook of clay science*, 2nd ed., Elsevier, Amsterdam, 2013.
- [94] B. Bauluz, Halloysite and Kaolinite: Two Clay Minerals with Geological and Technological Importance, 2015. <http://www.raczar.es/webracz/ImageServlet?mod=publicaciones&subMod=revistas&car=revista70&archivo=07Bauluz.pdf>.
- [95] E. Raask, *Mineral impurities in coal combustion: Behavior, problems, and remedial measures*, Hemisphere, Washington, 1985.
- [96] S. Babat, *Untersuchungen zur Belagsbildung und Charakterisierung der Ascheablagerungen in steinkohlegefeuerten*, Dissertation, Universität Stuttgart, 2016.
- [97] K. Mroczek, S. Kalisz, M. Pronobis, J. Softys, The effect of halloysite additive on operation of boilers firing agricultural biomass, *Fuel Processing Technology* 92 (2011) 845–855. <https://doi.org/10.1016/j.fuproc.2010.11.020>.
- [98] H.M. Zhou, X.C. Qiao, J.G. Yu, Influences of quartz and muscovite on the formation of mullite from kaolinite, *Applied Clay Science* 80-81 (2013) 176–181.
<https://doi.org/10.1016/j.clay.2013.04.004>.

- [99] P.O. Mwabe, Mechanisms governing alkali metal capture by kaolinite in a down-flow combustor, Dissertation, The University of Arizona, 1993.
- [100] Nanosized Tubular Clay Minerals - Halloysite and Imogolite, Elsevier, 2016.
- [101] Y. Zheng, P.A. Jensen, A.D. Jensen, A kinetic study of gaseous potassium capture by coal minerals in a high temperature fixed-bed reactor, *Fuel* 87 (2008) 3304–3312. <https://doi.org/10.1016/j.fuel.2008.05.003>.
- [102] G. Wang, P.A. Jensen, H. Wu, F.J. Frandsen, B. Sander, P. Glarborg, Potassium Capture by Kaolin, Part 1: KOH, *Energy Fuels* 32 (2018) 1851–1862. <https://doi.org/10.1021/acs.energyfuels.7b03645>.
- [103] G. Wang, P.A. Jensen, H. Wu, F.J. Frandsen, B. Sander, P. Glarborg, Potassium Capture by Kaolin, Part 2: K₂CO₃, KCl, and K₂SO₄, *Energy Fuels* 32 (2018) 3566–3578. <https://doi.org/10.1021/acs.energyfuels.7b04055>.
- [104] K.-Q. Tran, K. Iisa, B.-M. Steenari, O. Lindqvist, A kinetic study of gaseous alkali capture by kaolin in the fixed bed reactor equipped with an alkali detector, *Fuel* 84 (2005) 169–175. <https://doi.org/10.1016/j.fuel.2004.08.019>.
- [105] B.-M. Steenari, O. Lindqvist, High-temperature reactions of straw ash and the anti-sintering additives kaolin and dolomite, *Biomass and Bioenergy* 14 (1998) 67–76. [https://doi.org/10.1016/S0961-9534\(97\)00035-4](https://doi.org/10.1016/S0961-9534(97)00035-4).
- [106] K.O. Davidsson, B.-M. Steenari, D. Eskilsson, Kaolin Addition during Biomass Combustion in a 35 MW Circulating Fluidized-Bed Boiler, *Energy Fuels* 21 (2007) 1959–1966. <https://doi.org/10.1021/ef070055n>.
- [107] P.O. Mwabe, J.O. Wendt, Mechanisms governing trace sodium capture by kaolinite in a downflow combustor, 26th Symposium (International) on Combustion (1996) 2447–2453. [https://doi.org/10.1016/S0082-0784\(96\)80075-0](https://doi.org/10.1016/S0082-0784(96)80075-0).
- [108] M.F. Llorente, P.D. Arocas, L.G. Nebot, J.C. García, The effect of the addition of chemical materials on the sintering of biomass ash, *Fuel* 87 (2008) 2651–2658. <https://doi.org/10.1016/j.fuel.2008.02.019>.
- [109] T. Madhiyanon, P. Sathitruangsak, S. Sungworagarn, S. Fukuda, S. Tia, Ash and deposit characteristics from oil-palm empty-fruit-bunch (EFB) firing with kaolin additive in a pilot-scale grate-fired combustor, *Fuel Processing Technology* 115 (2013) 182–191. <https://doi.org/10.1016/j.fuproc.2013.05.018>.

- [110] K. Kubica, M. Jewiarz, R. Kubica, A. Szlęk, Straw Combustion: Pilot and Laboratory Studies on a Straw-Fired Grate Boiler, *Energy Fuels* 30 (2016) 4405–4410.
<https://doi.org/10.1021/acs.energyfuels.5b02693>.
- [111] K.O. Davidsson, L.-E. Åmand, B.-M. Steenari, A.-L. Elled, D. Eskilsson, B. Leckner, Countermeasures against alkali-related problems during combustion of biomass in a circulating fluidized bed boiler, *Chemical Engineering Science* 63 (2008) 5314–5329.
<https://doi.org/10.1016/j.ces.2008.07.012>.
- [112] M. Öhman, A. Nordin, The Role of Kaolin in Prevention of Bed Agglomeration during Fluidized Bed Combustion of Biomass Fuels, *Energy Fuels* 14 (2000) 618–624.
<https://doi.org/10.1021/ef990198c>.
- [113] S.B. Hansen, P.A. Jensen, F.J. Frandsen, H. Wu, M.S. Bashir, J. Wadenbäck, B. Sander, P. Glarborg, Deposit Probe Measurements in Large Biomass-Fired Grate Boilers and Pulverized-Fuel Boilers, *Energy Fuels* 28 (2014) 3539–3555.
<https://doi.org/10.1021/ef500442z>.
- [114] M. Paneru, I. Polyzois, J. Maier, G. Scheffknecht, Use of additive to mitigate deposition and corrosion problems during biomass combustion. In: 27. Deutscher Flammentag, VDI-Berichte Nr. 2267, 2015, pp. 87–96.
- [115] TOPAS SAG 410 Manual: Topas SAG 410. <https://www.topas-gmbh.de/en/produkte/sag-410/>.
- [116] M. Stein-Cichoszewska, Fireside corrosion of superheater alloys in ultra-supercritical coal-fired boilers, Dissertation, Universität Stuttgart, 2016.
- [117] "Patent DE: 10 2013 205 645.1 " Verfahren und Vorrichtung zur Bestimmung der Deposition in Kraftwerkskesseln und Hochtemperaturöfen 10 2013 205 645.1, 2013.
- [118] Gasmet FTIR. <https://www.gasmet.com/products/category/portable-gas-analyzers/dx4000/>.
- [119] G. Zwick und P. Basmer, Theorie der FT-IR Spektroskopie: GASMET FT_IR Analysator CALCMET Software. https://www.ffb.kit.edu/download/CD-FFB_IMK_Ber._Nr._137_Theorie_der_FT-IR_Spektroskopie.pdf.
- [120] J.I. Goldstein, D.E. Newbury, J.R. Michael, N.W. Ritchie, J.H.J. Scott, D.C. Joy, Scanning Electron Microscopy and X-Ray Microanalysis, fourth ed, Springer New York, New York, NY, 2018.
- [121] C.W. Bale, E. Bélisle, P. Chartrand, S.A. Deckerov, G. Eriksson, A.E. Gheribi, K. Hack, I.-H. Jung, Y.-B. Kang, J. Melançon, A.D. Pelton, S. Petersen, C. Robelin, J.

- Sangster, P. Spencer, M.-A. van Ende, Reprint of: FactSage thermochemical software and databases, 2010–2016, *Calphad* 55 (2016) 1–19. <https://doi.org/10.1016/j.calphad.2016.07.004>.
- [122] D. Lindberg, R. Backman, P. Chartrand, M. Hupa, Towards a comprehensive thermodynamic database for ash-forming elements in biomass and waste combustion — Current situation and future developments, *Fuel Processing Technology* 105 (2013) 129–141. <https://doi.org/10.1016/j.fuproc.2011.08.008>.
- [123] P. Sommersacher, T. Brunner, I. Obernberger, Fuel Indexes: A Novel Method for the Evaluation of Relevant Combustion Properties of New Biomass Fuels, *Energy Fuels* 26 (2012) 380–390. <https://doi.org/10.1021/ef201282y>.
- [124] K.A. Christensen, M. Stenholm, H. Livbjerg, The formation of submicron aerosol particles, HCl and SO₂ in straw-fired boilers, *Journal of Aerosol Science* 29 (1998) 421–444. [https://doi.org/10.1016/S0021-8502\(98\)00013-5](https://doi.org/10.1016/S0021-8502(98)00013-5).
- [125] E. Brus, M. Öhman, A. Nordin, Mechanisms of Bed Agglomeration during Fluidized-Bed Combustion of Biomass Fuels, *Energy Fuels* 19 (2005) 825–832. <https://doi.org/10.1021/ef0400868>.
- [126] G. Mura, A. Lallai, On the kinetics of dry reaction between calcium oxide and gas hydrochloric acid, *Chemical Engineering Science* 47 (1992) 2407–2411. [https://doi.org/10.1016/0009-2509\(92\)87068-2](https://doi.org/10.1016/0009-2509(92)87068-2).
- [127] A. Teklay, C. Yin, L. Rosendahl, L.L. Köhler, Experimental and modeling study of flash calcination of kaolinite rich clay particles in a gas suspension calciner, *Applied Clay Science* 103 (2015) 10–19. <https://doi.org/10.1016/j.clay.2014.11.003>.
- [128] D. Nutalapati, R. Gupta, B. Moghtaderi, T.F. Wall, Assessing slagging and fouling during biomass combustion: A thermodynamic approach allowing for alkali/ash reactions, *Fuel Processing Technology* 88 (2007) 1044–1052. <https://doi.org/10.1016/j.fuproc.2007.06.022>.
- [129] A. Teklay, C. Yin, L. Rosendahl, Flash calcination of kaolinite rich clay and impact of process conditions on the quality of the calcines: A way to reduce CO₂ footprint from cement industry, *Applied Energy* 162 (2016) 1218–1224. <https://doi.org/10.1016/j.apenergy.2015.04.127>.